



HAL
open science

Mechanical and Molecular Regulation of Periodic Cortical Waves of Contraction

Özge Özgüç

► **To cite this version:**

Özge Özgüç. Mechanical and Molecular Regulation of Periodic Cortical Waves of Contraction. Cellular Biology. Sorbonne Université, 2021. English. NNT : 2021SORUS482 . tel-03720085

HAL Id: tel-03720085

<https://theses.hal.science/tel-03720085>

Submitted on 11 Jul 2022

HAL is a multi-disciplinary open access archive for the deposit and dissemination of scientific research documents, whether they are published or not. The documents may come from teaching and research institutions in France or abroad, or from public or private research centers.

L'archive ouverte pluridisciplinaire **HAL**, est destinée au dépôt et à la diffusion de documents scientifiques de niveau recherche, publiés ou non, émanant des établissements d'enseignement et de recherche français ou étrangers, des laboratoires publics ou privés.

Sorbonne Université
École doctorale Complexité du Vivant (ED515)
Institut Curie / Génétique et Biologie du Développement

Mechanical and Molecular Regulation of Periodic Cortical Waves of Contraction

Par Özge ÖZGÜÇ

Thèse de doctorat de Biologie Cellulaire et du Développement

Dirigée par Jean-Léon MAÎTRE

Présentée et soutenue publiquement le 28/09/2021

Devant un jury composé de :

Pr. Sophie LOUVET-VALLEE, Sorbonne Université

Présidente du jury

Dr. Jérôme COLLIGNON, Institut Jacques Monod

Rapporteur

Dr. Peter LENART, Max Planck Institute for Biophysical Chemistry

Rapporteur

Dr. Cécile SYKES, Ecole Normale Supérieure

Examinatrice

Dr. Kevin CHALUT, University of Cambridge

Examineur

Dr. Anne-Cécile REYMANN, Institut de Génétique et de Biologie Moléculaire et Cellulaire Membre invité

Dr. Jean-Léon MAÎTRE, Institut Curie

Directeur de thèse

ACKNOWLEDGEMENTS

There are many people without whom this thesis wouldn't be possible. I would like to take this opportunity to thank them shortly;

First of all; I would like to start from my PhD supervisor **Jean-Léon MAÎTRE**. I have been very fortunate, both at the professional and personal levels, to be the “crêpe de chef” and have worked alongside with you. I appreciate in particular the friendly, and the accessible manner in which you communicated with me whenever I needed. Thank you for making this challenging long-term race into an enriching experience.

I would also like to thank both past and current members of the Maître lab. Starting from our two lab heroes: **Francesca TORTORELLI**, and **Ludmilla de PLATER**, this thesis (and also the lab) wouldn't be as it is without all your affords. To the post docs of the lab; **Julien DUMORTIER**, **Diane PELZER**, **Edgar Herrera Delgado** for all the encouragements through the ups and downs of my PhD and showing me the light at the end of the tunnel when I needed. To following PhDs to come from Maître Lab: Thank you **Markus SCHLIFFKA** for all the “Tea” and the Shade, and **Julie FIRMIN**, for the French support and the new perspective in the project. Thank you all for all the scientific discussions that helped to shape this research and at personal level for making the environment and these 4 years amazing and unforgettable for me.

Next, many thanks to the members of my thesis committee : **Sophie Louvet-Vallée**, **Julie Plastino**, and **Claire Fournier-Thibault**. Your advice, support, and insights into the project have been exceptionally important to complete this thesis.

Many thanks for our outstanding imaging platform (PICT-IBiSA@BDD); **Olivier RENOUD**, **Olivier LEROY**, **Aurelian DAUPHINE**, **Varun KAPOOR** for their outstanding support and afford. Also to the animal facility of the Institut Curie for keeping the mice happy.

I would like to thank **Ido LAVI** with whom we started a collaboration aimed at developing a physical model of the PeCoWaCo to understand how the decoupling of PeCoWaCo period and velocity could be explained. Many thanks to **Victoire CACHOUX** for our fruitful tea-time discussions and ending my sufferings with MatLab. To **Andrew CLARK**, for his interest in my research, insightful comments, and also his help with cortex thickness measurements. Equal thanks go to the team of **Herve TURLIER**, specially **Matthieu Le VERGE-SERANDOUR**, with whom we had interesting discussions on the physical aspect of my project. Discussing with you was always (and still is) a lot of fun.

Many thanks to **Ayşegül DEDE-EREN**, **İpek AKOL**, and **Oğuz BOLGI** for critical reading of my thesis and their important editorial touches!

I also want to thank my **IC3i Family**. Going through the PhD journey all together was a great experience and you all made this journey much more easier and enjoyable. Equal thanks go to other amazing people in my life; **Penelope, Jenny, Pelin, Ayşegül, Onur, Burcu, Esin, Bolgi, İpek**. Even if we were separated by kilometers, and borders, thank you all simply for being there! I am so lucky to have you in my life!

Very importantly, I want to thank **Tristan** for being the crash test of all my presentations and still wanting to be with me after all he has seen during the writing of this thesis. Many thanks also goes to our cats **Chivers** and **Pixel** for their much appreciated warm cuddles and stress relieving purrs.

Finally my last thanks goes to all my family and specifically to my parents;

Canım **annem**, Canım **babam**, bana doğruyu yanlış ayırabilmeyi, hayatta her zaman güçlü, pozitif, ve mutlu olmayı öğrettiğiniz için ve bana olan güven ve inancınız için size minnettarım. Kilometrelerce uzaktan bile varlığınızı hissettirerek bana hep moral ve güç verdiniz. Her şey için çok ama çok teşekkür ederim. Sizsiz hiçbir şey mümkün olmazdı.

Tezimi doktora yolculuğum sırasında kaybettiğim iki dedeme adıyorum.

I dedicate this thesis to my two grandfathers whom I lost during this journey.

TABLE OF CONTENTS

ACKNOWLEDGEMENTS	3
RÉSUMÉ/SUMMARY/ÖZET	8
INTRODUCTION	14
1. MOUSE PREIMPLANTATION DEVELOPMENT	17
2. ACTOMYOSIN CORTEX AND ITS CONTRACTILITY	21
3. PERIODIC CONTRACTIONS AND CONTRACTION WAVES	27
4. REVIEW ARTICLE: MULTISCALE MORPHOGENESIS OF THE MOUSE BLASTOCYST BY ACTOMYOSIN CONTRACTILITY.....	32
METHODS	40
1. MOUSE HUSBANDRY	42
2. EMBRYO MANIPULATIONS.....	42
2.1. BLOCKING CYTOKINESIS	43
2.2. BLOCKING ZYGOTIC GENOME ACTIVATION.....	43
2.3. ZONA PELLUCIDA REMOVAL	44
2.4. DISSOCIATION	44
2.5. CELLULAR FRAGMENTATION	45
2.6. CELLULAR FUSION	45
2.7. MICROPIPETTE ASPIRATION AND SURFACE TENSION MEASUREMENTS.....	46
2.8. PHARMACOLOGICAL MANIPULATIONS OF CONTRACTILITY	47
2.9. MICROINJECTION.....	47
3. mRNA PREPARATION.....	48
4. FLUORECENT IMMUNOSTAINING	48
5. MICROSCOPY	49
6. IMAGE ANALYSIS.....	50
6.1. PECoWACo ANALYSIS	50
6.2. CORTEX THICKNESS.....	53
7. STATISTICS	53
RESULTS.....	54
1. PECoWACo THROUGHOUT CLEAVAGE STAGES.....	56

INITIATION OF PeCoWaCo	57
ROLE OF CELL SIZE ON THE RISE OF PeCoWaCo DETECTION	59
ROLE OF ZYGOTIC GENOME ACTIVATION ON THE RISE OF PeCoWaCo DETECTION	62
CHANGES IN ACTOMYOSIN CORTEX THROUGH CLEAVAGE STAGES	64
2. REGULATION OF PeCoWaCo	68
2.1. GEOMETRICAL REGULATION	69
CELL SIZE DOES NOT INFLUENCE THE PROPERTIES OF PeCoWaCo	70
CONSTRICTION OF THE AREA DOES NOT CHANGE THE PERIOD OF THE OSCILLATIONS	73
MECHANICAL STRESS REDUCES WAVE VELOCITY.....	76
2.2. MOLECULAR REGULATION	78
ROLE OF MYOSIN-II MOTOR	79
ROLE OF ACTIN FILAMENTS	84
ROLE OF APKC.....	86
<u>RESEARCH PAPER 1 : ZYGOTIC CONTRACTILITY AWAKENING DURING MOUSE PREIMPLANTATION DEVELOPMENT</u>	<u>90</u>
<u>RESEARCH PAPER 2: MULTISCALE ANALYSIS OF SINGLE AND DOUBLE MATERNAL-ZYGOTIC MYH9 AND MYH10 MUTANTS DURING MOUSE PREIMPLANTATION DEVELOPMENT</u>	<u>108</u>
<u>DISCUSSION.....</u>	<u>138</u>
1. PeCoWaCo REVEALS MATURATION OF ACTOMYOSIN CORTEX	141
2. ROBUSTNESS OF PeCoWaCo PERIOD AND VELOCITY.	145
3. MOLECULAR REGULATION OF PeCoWaCo.....	148
<u>CONCLUSION.....</u>	<u>150</u>
<u>REFERENCES</u>	<u>154</u>

RESUME/SUMMARY/ÖZET

Résumé

Au cours du développement préimplantatoire, l'embryon de mammifère forme le blastocyste, qui est la structure fixant l'embryon dans l'utérus. La formation du blastocyste repose en grande partie sur les forces contractiles générées par le cortex d'actomyosine. Chez la souris, sur des échelles de temps de quelques secondes, nous observons des impulsions de contractions d'actomyosine voyageant périodiquement autour du périmètre cellulaire. Nous appelons ce phénomène **vagues de contraction corticale périodique (PeCoWaCo)**, une manifestation fascinante et mal comprise de la contractilité. Dans cette étude, nous profitons du développement lent de l'embryon de souris pour étudier des milliers d'impulsions de contraction. Nous mettons également à profit la robustesse de ce développement pour explorer les propriétés biophysiques des PeCoWaCo pendant les étapes de clivage précédant la morphogenèse précoce des mammifères.

Nous constatons que, lors des étapes de clivage, des mouvements périodiques apparaissent occasionnellement au stade zygote et 2-cellules puis deviennent systématiques après le 2ème cycle de divisions de clivage. Fait intéressant, la période des oscillations diminue progressivement de 200s au stade zygote à 80s au stade 8-cellules. Étant donné que les cellules deviennent de plus en plus petites avec des divisions de clivage successives, la taille des cellules pourrait être un déterminant important dans l'initiation et la régulation des PeCoWaCo. Nous manipulons la taille des cellules sur une large gamme de rayons cellulaires (10-40 μm) en utilisant la fragmentation et la fusion des cellules et constatons que l'initiation, la persistance ou les propriétés des PeCoWaCo ne dépendent pas de la taille des cellules. Après la période des PeCoWaCo, on découvre que les tensions de surface des blastomères diminuent progressivement jusqu'au stade de 8-cellules et que l'assouplissement artificiel des cellules augmente prématurément les PeCoWaCo. Par conséquent, lors des étapes de clivage, l'assouplissement cortical réveille la contractilité zygotique avant la morphogenèse préimplantatoire. En plus, en manipulant la contractilité de l'actomyosine à l'aide de mutants et des drogues, nous avons montré que la période des PeCoWaCo peut être contrôlée par la régulation du taux de polymérisation de l'actine filamenteuse et de l'activité motrice de la myosine.

Dans l'ensemble, nos résultats sur les aspects biophysiques et moléculaires du PeCoWaCo nous aident à comprendre comment la contractilité de l'actomyosine s'éveille avant la morphogenèse préimplantatoire et comment elle est régulée au niveau mécanique et moléculaire.

Summary

During pre-implantation development, the mammalian embryo forms the blastocyst, which is the structure embedding the embryo into the uterus. The shaping of the blastocyst relies in large part on contractile forces generated by the actomyosin cortex. In the mouse, on timescales of seconds, we observe pulses of actomyosin contractions traveling periodically around the cell perimeter. We call this phenomenon periodic cortical waves of contraction (PeCoWaCo), a fascinating and poorly understood manifestation of contractility. In this study, we take advantage of the slow development of the mouse embryo to study thousands of contraction pulses and of the robustness of the mouse embryo to size manipulation to explore the biophysical properties of PeCoWaCo during the cleavage stages preceding early mammalian morphogenesis.

We find that, during cleavage stages, periodic movements appear occasionally at the zygote and the 2-cell stage and become systematic after the 2nd round of cleavage divisions. Interestingly, the period of oscillations progressively decreases from 200 s at the zygote stage to 80 s at the 8-cell stage. Since cells become successively smaller with successive cleavage divisions, cell size could be an important determinant in the initiation and regulation of PeCoWaCo. We manipulate cell size on a broad range of cell radii (10-40 μm) using fragmentation and fusion of cells and find that the initiation, persistence or properties of PeCoWaCo do not depend on cell size. Following the period of PeCoWaCo, we discover that blastomeres gradually decrease their surface tensions until the 8-cell stage and that artificially softening cells enhances PeCoWaCo prematurely. Therefore, during cleavage stages, cortical softening awakens zygotic contractility before preimplantation morphogenesis. In addition, by manipulating actomyosin contractility using mutants and drugs, we showed that the period of PeCoWaCo can be tuned by F-actin polymerization rate and myosin motor activity.

Altogether our results on biophysical and molecular aspects of PeCoWaCo help us understand how actomyosin contractility awakens before preimplantation morphogenesis and how it is regulated both mechanically and molecularly.

Özet

İmplantasyon öncesi gelişim sırasında, memeli embriyosu, embriyoyu rahim içine yerleştiren yapı olan blastosisti oluşturur. Blastosistin şekillendirilmesi büyük ölçüde aktomiyozin korteks tarafından oluşturulan kasılma kuvvetlerine dayanır. Farede, saniyelik zaman ölçeklerinde, hücre çevresinde periyodik olarak dolaşan aktomiyozin kasılmalarının darbeleri gözlemlenebilir. Bu fenomene, kasılmanın büyüleyici ve yeterince anlaşılmamış bir tezahürü olan periyodik kortikal kasılma dalgaları (periodic cortical waves of contraction: PeCoWaCo) diyoruz. Bu çalışmada, erken memeli morfogenezinden önceki bölünme aşamaları sırasında PeCoWaCo'nun biyofiziksel özelliklerini keşfetmek ve binlerce kasılma darbesini inceleyebilmek için fare embriyosunun yavaş gelişiminden ve fare embriyosunun boyut manipülasyonuna dayanıklılığından faydalandık.

Bölünme aşamaları sırasında, zigotta ve 2 hücreli aşamada periyodik hareketlerin zaman zaman ortaya çıktığını ve ikinci tur bölünmeden sonra bu hareketlerin sistematik hale geldiğini bulduk. İlginç bir şekilde, salınım periyodunun zigot aşamasında 200 saniyeden, 8 hücreli aşamada 80 saniyeye sistematik olarak azaldığını gözlemledik. Hücreler ardışık bölünmeleriyle sürekli küçüldüğünden, hücre boyutu PeCoWaCo'nun başlatılmasında ve düzenlenmesinde önemli bir belirleyici olabilir. Hücreleri geniş bir hücre yarıçapı aralığında (10-40 μm) küçük parçalara bölerek veya birbirleriyle birleştirerek PeCoWaCo'nun başlatılmasının, kalıcılığının veya genel özelliklerinin hücre boyutuna bağlı olmadığını bulduk. PeCoWaCo periyodunu takiben, embriyo hücrelerinin zigottan 8 hücreli aşamaya kadar yüzey gerilimini kademeli olarak azalttığını ve yapay olarak korteksleri yumuşatılan hücrelerin PeCoWaCo'yu zamanından önce geliştirdiğini keşfettik. Bu sonuçlarla bölünme aşamaları sırasında, kortikal yumuşama, ilke implantasyon öncesi morfogenezinden önce zigotik kasılmaları uyandırdığını gösterdik. Ayrıca, genetik mutantlar ve kimyasallar kullanarak aktomiyozin kasılmasını manipüle ederek, PeCoWaCo periyodunun F-aktin polimerizasyon hızı ve miyozin motor aktivitesinin düzenlenmesi ile ayarlanabileceğini gösterdik.

Sonuç olarak, PeCoWaCo'nun biyofiziksel ve moleküler yönleriyle ilgili bulgularımız, aktomiyozin kontraktilesinin implantasyon öncesi morfogenezinden önce nasıl uyandığını, ayrıca hem mekanik hem de moleküler olarak nasıl düzenlendiğini anlamamıza yardımcı olur.

INTRODUCTION

At the very beginning of their life, every multicellular organism goes through a marvelous transformation. Over the course of hours, days, or months, the organism turns from a single cell called the zygote into a huge, organized collection of cells, tissues, and organs. In order for this to happen, for tissues to form, change their shape, and become an organism, individual cells produce mechanical forces. The first shape-changing event, called **morphogenesis**, happens during the **pre-implantation stages** in the first days of an embryo.

Pulsatile contractions of **the acto-myosin cortex** accompanied by cell shape deformation have been observed in diverse systems, from nematodes to mammals. Interestingly duration of these pulses is similar over these diverse systems suggesting common underlying machinery. The problem with mainly used organisms for contractility studies is that they develop fast. **Periodic cortical waves of contraction (PeCoWaCo)** observed on pre-implantation mouse embryos serve as a great tool to uncover this machinery as the mouse embryo develops slower. For example, PeCoWaCo has a ~80s period, whereas the fastest morphogenetic event in mouse pre-implantation takes hours.

In this thesis, by taking advantage of the slow development and easy manipulation of cells of the mouse embryo, I investigated when and why pre-implantation mouse embryos start showing PeCoWaCo and how PeCoWaCo is regulated both mechanically and molecularly via mechanical manipulations of cell size and shape as well as genetic and chemical disruptions of actomyosin contractility.

1. MOUSE PREIMPLANTATION DEVELOPMENT

The pre-implantation phase of mammalian development prepares the embryo to attach to the uterine wall of the mother. For an embryo to implant successfully, the formation of a blastocyst structure is crucial. The blastocyst consists of a squamous epithelium enveloping a cluster of pluripotent stem cells and a fluid-filled lumen. The journey of an embryo to form this structure starts with the fusion of 2 unique types of cells, sperm, and oocyte, in the oviduct. This fusion triggers a cascade of reactions known as “fertilisation” this reaction results in a change of the oocyte surface and prevents other sperms from fusing. After this point, the fertilized oocyte is called a “zygote”. Mouse embryos are usually staged by the number of days since the mating. The day after the mating will be Embryonic day 0.5 (E0.5) as the mating occurs at night or by the number of cells such as; 2-cell-stage, 4-cell-stage. From fertilization to implantation takes five days, and at day ~20 a mouse will be born.

The Zygote is encapsulated by the zona pellucida (ZP), a rigid glycoprotein shell that plays an essential role in fertilization but is no longer needed for further development. After fertilization, the embryo is no longer attached to the ZP, and it is freely floating within the ZP until the blastocyst cavity is formed and big enough, except for the 2-cell-stage. At the 2-cell-stage, the embryo pushes the ZP from 2 sides and deforms the ZP creating an oblong shape. When the blastocyst is formed, this deformation of the ZP drives the orientation of the blastocyst’s embryonic/abembryonic (Ab) axis (with the ICM at the embryonic pole and the cavity at the (Ab) pole) (Motosugi et al., 2005).

Upon fertilization, the maternal and paternal chromosomes become enclosed in two separate pronuclei in the periphery of the zygote. The pronuclei subsequently migrate to the zygote's center, where they meet, and later undergo nuclear breakdown and cell division (Clift & Schuh, 2014). As for other animals, mammalian embryos' initial divisions occur without cell growth during interphase; therefore, they are called "cleavage divisions". After each division, cell volume gets halved and creates smaller and smaller cells after each division (Fig. 1, Movie 1) (Aiken et al., 2004; Lehtonen, 1980; Niwayama et al., 2019). The first two cell cycles last ~20 h, then the cell cycle gets shorter (~11h for third and fourth) (Artus & Cohen-tannoudji, 2008).

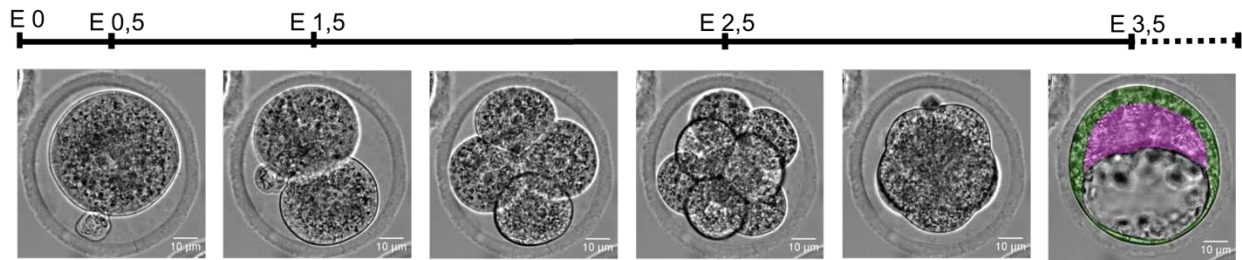


FIGURE 1: PREIMPLANTATION DEVELOPMENT OF MOUSE EMBRYO.
Trophectoderm (TE) in green, Inner Cell Mass (ICM) in magenta.

The oocyte is full of maternally provided mRNAs and proteins for the early embryo to have basic biosynthesis to survive and direct its first cell division. Through the first steps of its development, an embryo undergoes maternal to zygotic transition. This transition takes different times for different animal species (Tadros & Lipshitz, 2009). In mice, maternally supplied mRNAs are starting to be eliminated upon fertilization, and large amount of it is already degraded by the 2-cell-stage. Up to the middle of the 2-cell-stage, the embryo still mainly relies on proteins and mRNA supplied by the mother. At this stage, the embryo activates its own genome, marked as major zygotic genome activation (ZGA) (Hamatani et al., 2004) resulting in the transfer of developmental control from the maternal to the zygotic genome.

The blastomeres, cells of the embryo, are relatively round and identical in appearance until the late 8-cell stage (Fig. 1, Movie 1). At the 8-cell stage, the embryo undergoes a morphogenetic process called compaction. This morphogenetic event is driven by increasing contractility (Maître et al., 2015). As cells increase their contractile forces, they start pulling their neighbors with greater forces, resulting in the increased cell-cell contact area. During the 8-cell stage, blastomeres also become apico-basally polarized with an apical domain occupying only a portion of the contact-free surface (Fig 2A). The apical domain is enriched in microvilli (Ducibella et al., 1977) and apical proteins such as aPKC, Par3, and Par6 (Dard et al., 2009; Korotkevich et al., 2017; Niwayama et al., 2019; Zenker et al., 2018) whereas, it is depleted in actomyosin (Maître et al., 2016).

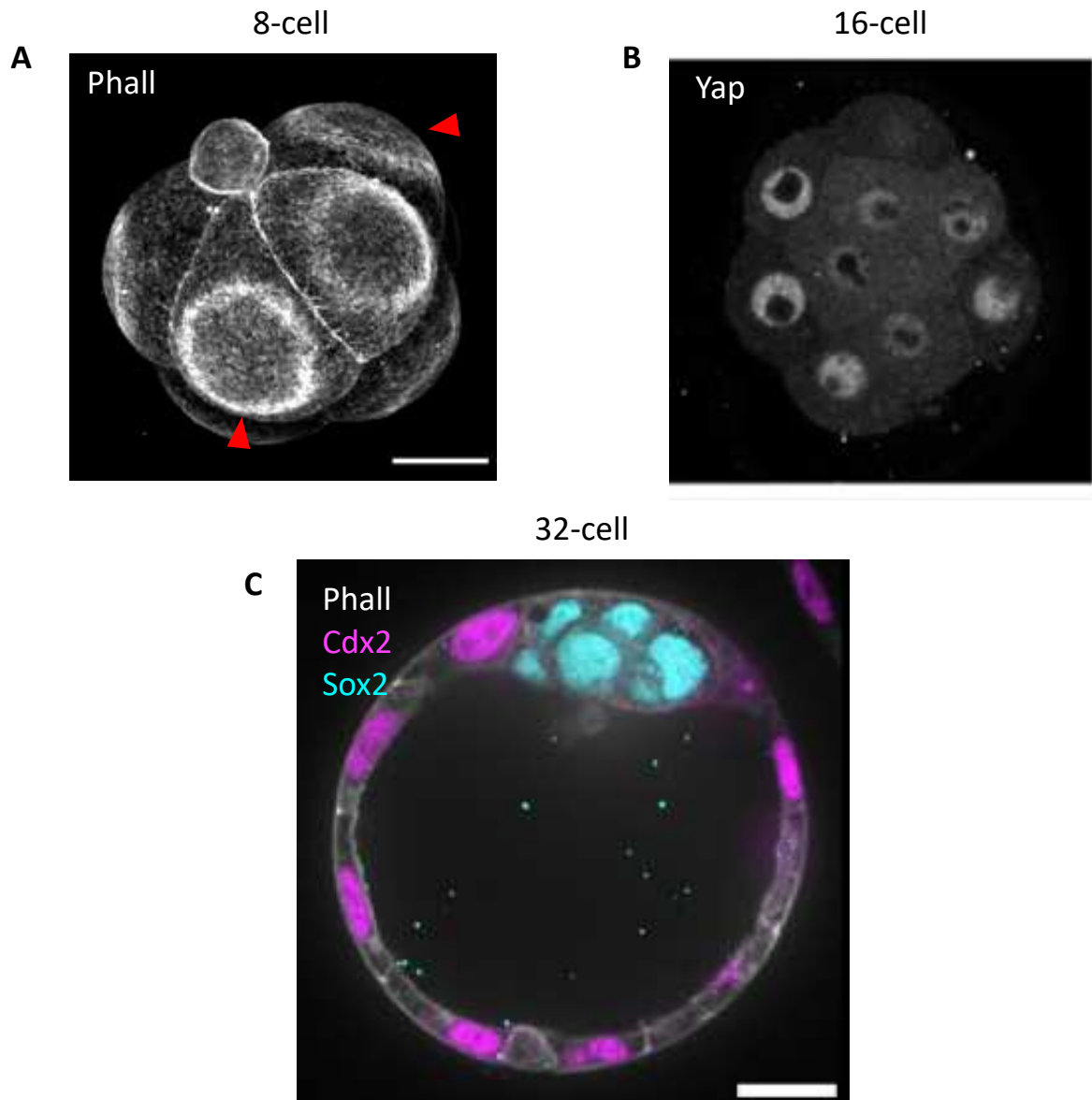


FIGURE 2 : IMMUNOFLOURESCENCE IMAGES OF POLARIZED 8-CELL STAGE, 16-CELL STAGE AND BLASTOCYST STAGE MOUSE EMBRYOS

A) Immuno staining of a polarized 8-cell-stage embryo stained for F-actin. red arrows showing apical domains observable with actin. Image from Francesca Tortorelli **B)** Immuno staining of a 16-cell stage embryo stained for Yap showing Yap localization differences between inner and outer cells. Image adapted from (Royer et al., 2020) **C)** Immuno staining of an E3.5 blastocyst stained for F-actin, Cdx2 (TE marker), and Sox2 (ICM marker) with ICM shown in Blue, TE shown in magenta. Image taken from Schliffka & Tortorelli et. al. 2021 (Schliffka et al., 2021)

The presence of the apical domain causes some of the 4th round divisions to be asymmetric (Dard et al., 2009; Plusa et al., 2009) as it can recruit one of the poles of the mitotic spindle (Korotkevich et al., 2017). The division can be asymmetric both in terms of inheritance of molecular content and volume. Asymmetric partitioning of the apical domain results in asymmetric distribution of contractility (Maître et al., 2016). Differences in contractility segregate cells into different positions, causing them to differentiate into two different cell types: polar cells on the outside and apolar cell inside (Maître et al., 2016; Samarage et al., 2015). This enforces the differentiation of the cells into ICM or TE fate as polar and apolar cells differentially control the subcellular localization of the Yes-associated protein (Yap) by its phosphorylation through the Hippo pathway (Fig. 2B) (Cockburn et al., 2013; Hirate et al., 2013). The Hippo Pathway is active in ICM and prevents Yap from entering the nucleus by phosphorylation; therefore, Yap cannot interact with Tead4 (Transcriptional enhancer activator domain family 4) and cannot induce the expression of TE-specific genes (Nishioka et al., 2008). Further in the 16-cell-stage, the apical domain expands and covers all the contact-free surfaces of the outside cells and merges with apical domains of neighbor cells like a zipper (Zenker et al., 2018). This is followed by the recruitment of tight junction protein ZO1 (zona occludens 1) and seals the embryo (Zenker et al., 2018).

The final morphogenetic event to build the blastocyst is the formation of the blastocoel. At E3.5, when the embryo reaches to 32-cell-stage, fluid is drawn between cell-cell contacts as a result of osmotic changes coming from ion pumping (Dumortier et al., 2019; Madan et al., 2007; Watson et al., 2004) and pressurized with the help of the sealing of embryo with tight junctions (Torres et al., 2002; Wang et al., 2008). The pressurized fluid then fractures cell-cell contacts into hundreds of micrometer-sized lumens (Madan et al., 2007). These microlumens eventually discharge their volumes, with the guidance of actomyosin contractility differences between the cells, into a single dominant lumen creating the first axis of symmetry of the mouse embryo (Fig. 2C) (Dumortier et al., 2019). While the cavity forms, the blastomeres of the ICM split into two populations: epiblast (Epi) and primitive endoderm (PrE) with the Epi against the polar TE and the PrE lining the cavity. Once it is all set, blastocyst hatches from ZP and implants into the uterus.

The success of a pre-implantation embryo is measured by its ability to implant. Its ability to implant depends on its ability to form the structure that will invade the maternal uterus: The Blastocyst. Shaping the blastocyst relies on the cellular properties and behaviors that can modify tissue architecture, such as cell deformations and rearrangements. All these cell deformations and rearrangement processes require the generation of forces and changing the mechanical properties of cells and the tissue.

2. ACTOMYOSIN CORTEX AND ITS CONTRACTILITY

One of the outstanding questions in developmental biology is how a single cell (zygote) can develop and shape itself into a complex organism? The shape of animal cells and tissues largely relies on the contractility of the actomyosin cortex and the developing embryo is not an exception (Coravos et al., 2018; Levayer & Lecuit, 2012; Maître et al., 2015; Maître et al., 2016; Murrell et al., 2015). The morphogenetic events, processes by which multicellular organisms change their shape, are driven by forces generated by molecular motors and transmitted via cytoskeletal elements and adhesion molecules within and between cells (Heisenberg & Bellaïche, 2013).

The cytoskeleton of animal cells is a system of filaments that functions at various biological processes from pulling chromosomes, cleaving cells to supporting the cell to bear stress and migrate. It consists of semiflexible protein polymers, including microtubules, intermediate filaments, and actin (Wen & Janmey, 2012). The actin and microtubules are polymers of ubiquitously expressed globular proteins: globular actin and α - and β -tubulin. Intermediate filaments are polymers of fibrous proteins such as vimentin, keratin, or lamin, which vary over cell types. When compared to microtubules and actin filaments that have ~ 30 (in vitro)- 500 (in vivo) nm/s (Brugués et al., 2012; Tournebize et al., 1997) and ~ 7 - 170 nm/s (Vallotton et al., 2005; Watanabe & Mitchison, 2002) assembly/disassembly rate respectively. Intermediate filaments are relatively stable structures with a growth rate ~ 100 nm/min (Windoffer et al., 2004). Microtubules gives the general architecture of the cells by organising the organelles and play an essential role in chromosome segregation and protein trafficking. The actin filaments, on the other hand, are associated with cell

shape changes and movement. Moreover, actin filaments play a central role in shaping the preimplantation mouse embryo (Özgüç & Maître, 2020). Therefore I focus my discussion on actin filaments.

The actin cytoskeleton is a dynamic network of actin filaments and its associated proteins. It encompasses all cytoplasm and connects nucleus, organelles, and cellular membrane to one another. As a profoundly dynamic structure and connecting all the parts of the cell together, the actin cytoskeleton can alter the morphology of a cell simply by reorganizing itself together with associated proteins and myosin motors. This adaptability in organization empowers cells to adopt a wide scope of shapes and helps directing diverse range of processes such as muscle contraction, lamellipodia extrusion, cell locomotion, cytokinesis, and cytoplasmic streaming. In animal cells, a micron-thin layer of crosslinked actin filaments, a part of the actin cytoskeleton, is put under tension by non-muscle myosin II motors, and this assembly is called the actomyosin cortex. (Fig. 3D) (G. Charras & Paluch, 2008). In order to create mechanical stress, the system requires assembly and disassembly of actin filament and myosin motors coupling (Fig. 3C). To better understand how this functions, we first need to look into the structure and dynamics of actin filaments and myosin motors. Actin filaments, consisting of polymerized globular actin monomers, are formed and breakdown in a dynamic steady-state manner (Fig. 3A) (Plastino & Blanchoin, 2018) (Fig. 1A). For the formation of mechanical forces, in addition to the rate of polymerization and depolymerization of actin filaments, nucleation and crosslinking of the filaments also play an important role. In addition to their connection with the organelles, the cortex filaments are also tethered the plasma membrane by proteins such as ezrin, radixin, and moesin (ERM) (Fehon et al., 2010). Non-muscle myosin II (NM II) is the key motor generating cortical contractility as its cyclic interaction with F-actin, driven by ATP hydrolysis, produces force and movement. NM-II consists of two “heads” containing a conserved motor domain, the very long tail of the two heavy chains (NMHCs) supercoiling, thus forming a head-to-tail dimer (Fig. 3B) (Vicente-manzanares et al., 2010). They also possess one regulatory light chain (MRLCs) and one essential light chain (MLSCs), associated with each “head” making a “neck” region (Vicente-manzanares et al., 2010). For NM II motors to retain their normal, native, and active conformations, the light chains must be bound to the heavy chains. The myosin

head binds to F-actin and uses ATP hydrolysis to generate force. The neck domain acts as a lever arm to amplify head rotation while the chemical energy of ATP is converted into the mechanical movement of the myosin head. MRLCs are responsible for the assembly of filaments and increasing ATPase activity (Uyeda et al., 1996). NMHCs, on the other hand, are responsible for generating the power stroke. They also interact with actin filaments (F-actin) and convert chemical energy (ATP) into mechanical energy (movement of myosin head on F-actin), pulling F-actins closer creating actomyosin contractility (Fig. 3B) (Vicente-manzanares et al., 2010).

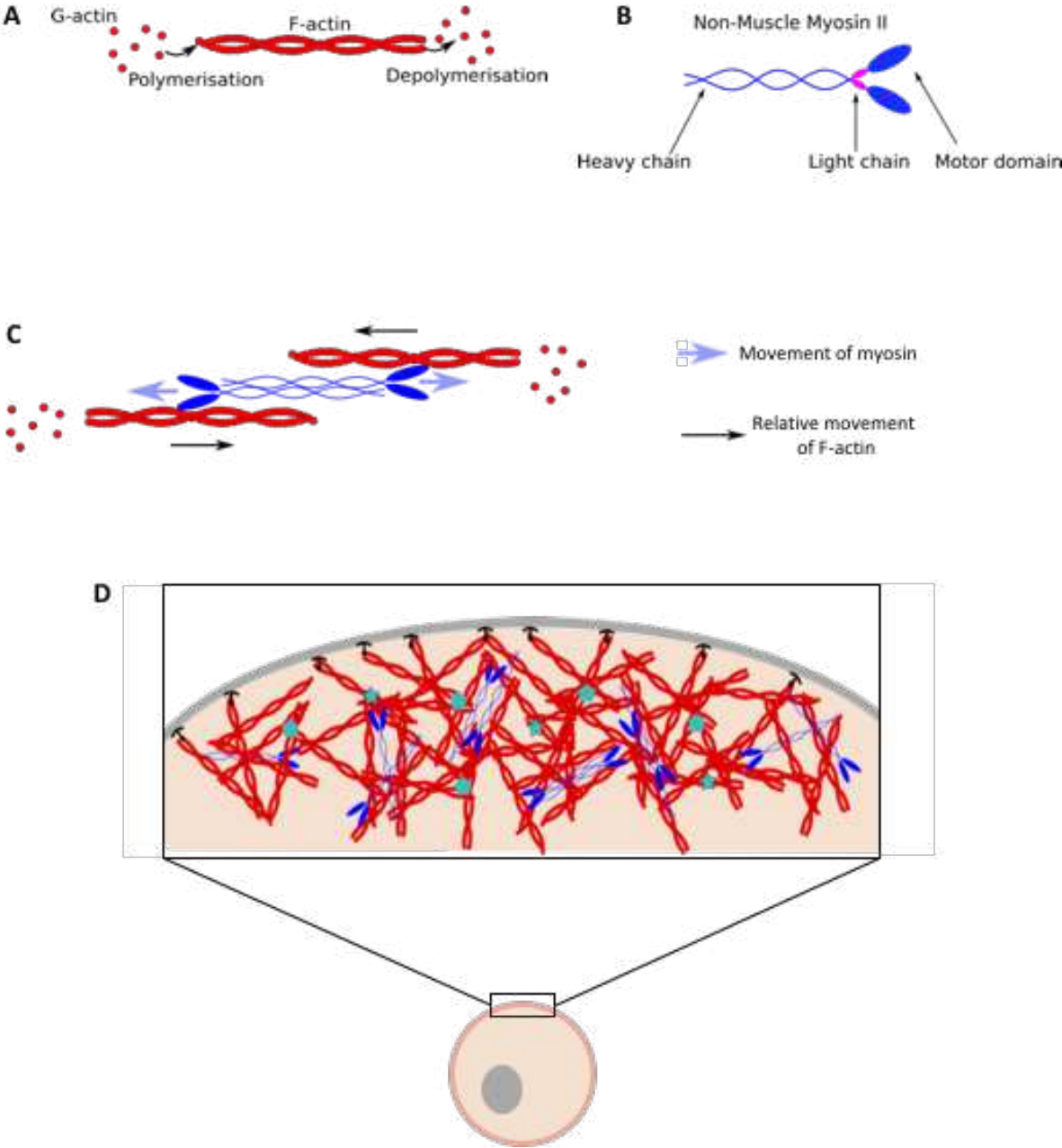


FIGURE 3 : COMPONENT OF ACTOMYOSIN CORTEX AND ITS CONTRACTILITY

Schematic diagram of **A)** polymerization and depolymerization actin filament **B)** components of non-muscle myosin II motor **C)** formation of actomyosin contractility, and **D)** localization and structure of actomyosin cortex under the cellular membrane.

The composition, architecture, and properties of the actomyosin cortex vary largely between cell types and even at subcellular levels and between different states of the same cells (Svitkina, 2020). Thanks to the advancements in the imaging and image analysis, we now know that average cortex thickness 50-400nm depending on cell type and stage of the cell cycle, being typically thicker in less spread cells and reaching the maximal thickness in rounded cells except mitotic cells (Chugh & Paluch, 2018; Clark et al., 2013).

Actomyosin contractility is regulated in space, time, and magnitude. This regulation is achieved at the level of cortex architecture (thickness, density, crosslinking, etc.) and by the activity of myosin II motor (phosphorylation state, conformation, etc.). The contractome analysis done by Zaidel-Bar and colleagues presents us with a map of the network of proteins that generate and regulate actomyosin contractility. The proteins with the highest number of potential interactions in the contractome, in addition to F-actin and myosin II motor, are RhoA, Rho kinase (ROCK), myosin phosphatase (MYPT1), Myosin light chain kinase (MLCK), and protein kinase C (PKC) (Zaidel-Bar et al., 2015). ROCK and MLCK are kinases that phosphorylate and activate MLCs. RhoA is a Rho GTPase that controls both actin filaments nucleation via formins and non-muscle myosin II activation via kinases (Bement et al., 2015; Graessl et al., 2017; Munjal et al., 2015; Zaidel-Bar et al., 2015). In contrast, PKC inhibits Myosin light chain phosphatase (MLCP) resulting in inhibition of actomyosin contractility (Bitar et al., 2012). In this thesis, I focus on F-actin, Myosin II, PKC, RhoA, and MLCK. Schematic description of their function on actomyosin contractility and chemicals used to inhibit their function can be found in figure 4.

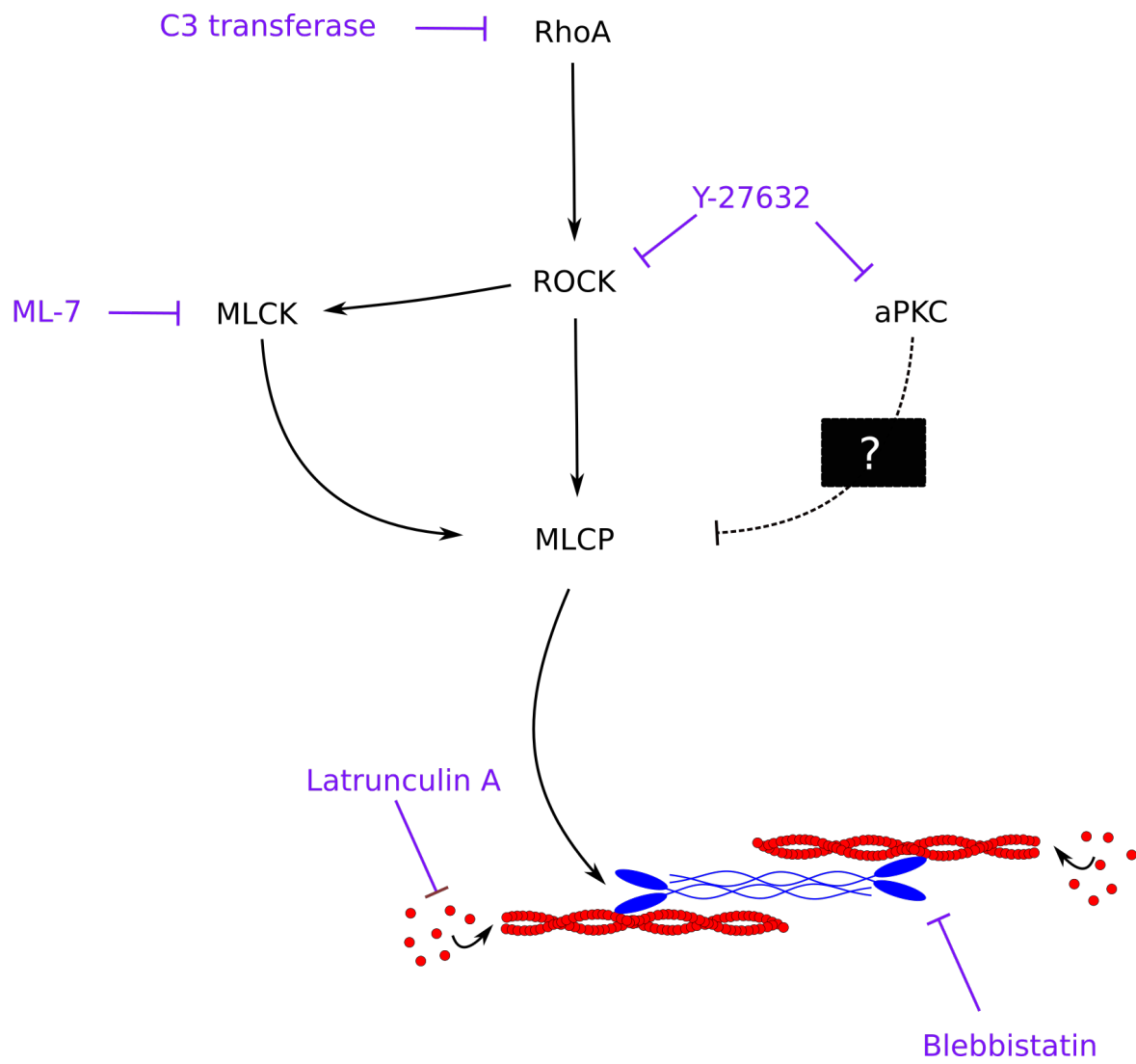


FIGURE 4: SCHEMATIC DIAGRAM OF ACTOMYOSIN CONTRACTILITY REGULATORY PATHWAYS AND THEIR INHIBITORY DRUGS.

The Spatio-temporal regulation of the contractility leads to the deformation of animal cells by generating surface stresses. For example, higher contractility at the cleavage furrow cleaves cells into two during cytokinesis (Fujiwara & Pollard, 1976; Straight et al., 2003), higher contractility at the back of migrating cells help them retract their cell body that is dragged by lamellipodia (Eddy et al., 2000; Tsai et al., 2019), lower contractility at cell-cell contacts relaxes them and promotes their spreading (Wakatsuki et al., 2003). The resting magnitude of contractility also sets the surface tension of cells, which elevates the hydrostatic pressure of the cytoplasm. For example, both increase prior to cytokinesis to force cells to round up against their environment (Stewart et al., 2011); pressure drives membrane blebs which are then retracted by locally increased contractility (Charras et al., 2006; Taneja & Burnette, 2019). Cell surface tension and hydrostatic pressure are a good readout of the contractility of cells and can be measured using different techniques such as atomic force microscopy or micropipette aspiration.

At the tissue scale, spatiotemporal changes in actomyosin contractility drive apical constriction (Martin et al., 2009) or the remodeling of cell-cell contacts (Maitre et al., 2012). Although tissue remodeling takes place on timescales from tens of minutes to hours or days, the action of the actomyosin cortex is manifest on shorter timescales of tens of seconds (Coravos et al., 2018). It has been shown that pulsed contractions are better for protecting the integrity of the tissue, as this way, cell-cell contacts can adapt, and they do not break with one big contraction to change the shape of the tissue (Vasquez et al., 2014). In fact, actomyosin is often found to act via pulses of contraction during morphogenetic processes among different animal species from nematodes to human cells that we will discuss in the next section (Baird et al., 2017; Blanchard et al., 2010; Kim & Davidson, 2011; Maître et al., 2015; Roh-Johnson et al., 2012; Solon et al., 2009).

3. PERIODIC CONTRACTIONS AND CONTRACTION WAVES

Actomyosin contractility is often found to act via pulses of contraction in diverse morphogenetic processes among different animal species, from nematodes to human cells. A pulse of actomyosin begins with the polymerization of actin filaments and the sliding of myosin mini-filaments until maximal contraction of the local network within about 30 s (Dehapiot et al., 2020; Ebrahim et al., 2013). Then, the actin cytoskeleton disassembles, and myosin is inactivated, relaxing the local network for another 30 s (Munjal et al., 2015; Vasquez et al., 2014). In instances where a sufficient number of pulses occur, pulses of contraction show an apparent periodicity. The oscillation period of pulsed contractions is interestingly similar, ranging from 60 to 200 s, over diverse systems suggesting a common underlying machinery (Baird et al., 2017; Bement et al., 2015; Maître et al., 2015; Solon et al., 2009). Moreover, periodic contractions can propagate like traveling waves. Such periodic cortical waves of contraction (PeCoWaCo) were observed in different systems from cell culture to embryos (Bement et al., 2015; Driscoll et al., 2015; Hubatsch et al., 2019; Kapustina et al., 2013; Maître et al., 2015).

Understanding the mechanism of action of PeCoWaCo can help decipher their function at the cellular and tissue levels. PeCoWaCo are observed as a “traveling wave”; however, how these contractions occurred at cortex level and how they “travel” remains unknown. The formation of contraction waves is considered to be resulting from the actomyosin cortex being an excitable matrix. The excitability of the cortex is carried by the cortical cytoskeleton and its regulators (Bement et al., 2015; Bretschneider et al., 2009; Iglesias & Devreotes, 2012). The formation of the contractions could be imagined to be resulting from polymerization and depolymerization of actin filaments or local contraction/relaxation mechanisms. Traveling motion of these contractions, on the other hand, requires more of a physical aspect. Excitable dynamics are often modeled as reaction-diffusion systems. In these systems, an activator stimulates more of its own production via positive feedback while also stimulating the production of an inhibitor responsible for negative feedback (Michaud et al., 2021). The contractions could be traveling through the cell surface by directional assembly and disassembly of membrane-anchored actin filaments in waves

through positive and negative feedbacks. For example, signaling for actin polymerization advances the wavefront, and the signaling for actin depolymerization stops the wave at the wave rear leading to the translocation of actin filaments and associated proteins (Fig. 5A) (Katsuno et al., 2015). The balance between these positive and negative feedback loops will give the wavelength and frequency characteristics of the traveling waves. On another aspect, it could appear to be traveling due to kinetic phase shift in local oscillations with activator/inhibitor relationship. Contraction waves could be made up of “stationary” components. The sequential assembly and disassembly of these components give the illusion of a propagating wave (Fig. 5B) (Bretschneider et al., 2009). This means that it is not the actin and/or the myosin which travels but the cortex contract patches sequentially, resulting in a contraction wave.

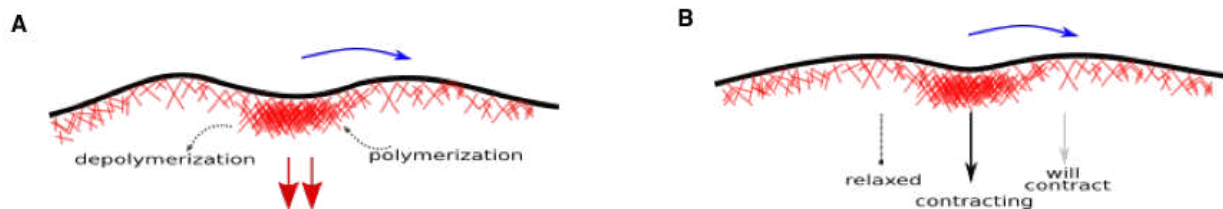


FIGURE 5: MODELS OF TRAVELING CONTRACTION WAVES

A) Contraction wave propagation by positive feedback loop and actin polymerization / depolymerization **B)** Coordinated contraction of cortex patches creating a traveling wave. Cell membrane depicted in black, actomyosin cortex in red. Blue arrow shows the traveling orientation of the contraction wave.

Different characteristics and functions of PeCoWaCo had been described in a variety of model organisms, from cell lines to developing embryos. PeCoWaCo in Chinese hamster ovary (CHO) cells propagates by repeated cycles of cortical compression and dilation that lead to periodic protrusions of the cell boundary (Fig. 6A) (Driscoll et al., 2015; Kapustina et al., 2013). The osteosarcoma cells show local pulses with a period of 2–7 min; however, when Rho activity artificially increases, these pulses transform into a wave with a velocity of 0.3–0.4 $\mu\text{m/s}$ (Graessl et al., 2017). Waves observed in starfish and frog oocytes have a period of 80 s, speed of 0.22 $\mu\text{m/s}$, and they appear when Rho becomes activated in a cell cycle-dependent manner (Fig. 6B) (Bement et al., 2015). Rho activation wavefront is shown to be coupled to the local curvature of the cell surface (Bischof et al., 2017a) which is then proposed to serve as

a mechanism for cells to sense their shape (Wigbers et al., 2021). In *Drosophila* germline cells, PeCoWaCo are described to regulate cytoplasmic transport from nurse cells during oocyte formation with a velocity of $\sim 0.3 \mu\text{m/s}$ (Fig. 6C-D), a speed comparable to Rho-actin contraction waves, observed in frog and starfish oocytes and embryos (Alsous et al., 2021; Bement et al., 2015). In *C. elegans* embryos, pulsed contractions move towards the anterior pole of the zygotes as a result of tension anisotropies triggered by local downregulation of contractility ensuing signals mediated by the sperm entry (Mayer et al., 2010; Munro et al., 2004). This cortical flow advects polarity proteins as it couples to the cytoplasm and induces its streaming (Goehring et al., 2011; Mittasch et al., 2018). In mouse embryos, PeCoWaCo were observed at the 8-cell stage with a period of 80 s (Fig. 6E-F, Movie 2) (Maître et al., 2015; Maître et al., 2016) similar to the ones of periodic contractions observed in other early embryos such as in the fly (Martin 2009, Munjal 2015), frog or starfish (Bement et al., 2015). In cells isolated from the embryo, PeCoWaCo can be observed circulating freely as two waves following each other during interphase (Movie 3) (Maître et al., 2015). The wave velocity is calculated as $0.8 \pm 0.1 \mu\text{m/s}$ by dividing the cell perimeter by the oscillation period and further dividing this by two as there are two waves traveling around the cell (Maître et al., 2015). PeCoWaCo in mouse pre-implantation embryo are shown to require intact actin and myosin function and, as such, resemble waves of compression and dilations of the actomyosin cortex (Driscoll et al., 2015; Kapustina et al., 2013). When the cells are in contact, PeCoWaCo are locally weakened by adhesion molecules. The apical domain also shows reduced actomyosin levels, and PeCoWaCo becomes further confined. At the 16- cell stage, PeCoWaCo can be used to predict the fate of the blastomeres earlier than any known fate markers as ICM precursors show it with higher amplitude than TE precursors (Maître et al., 2016).

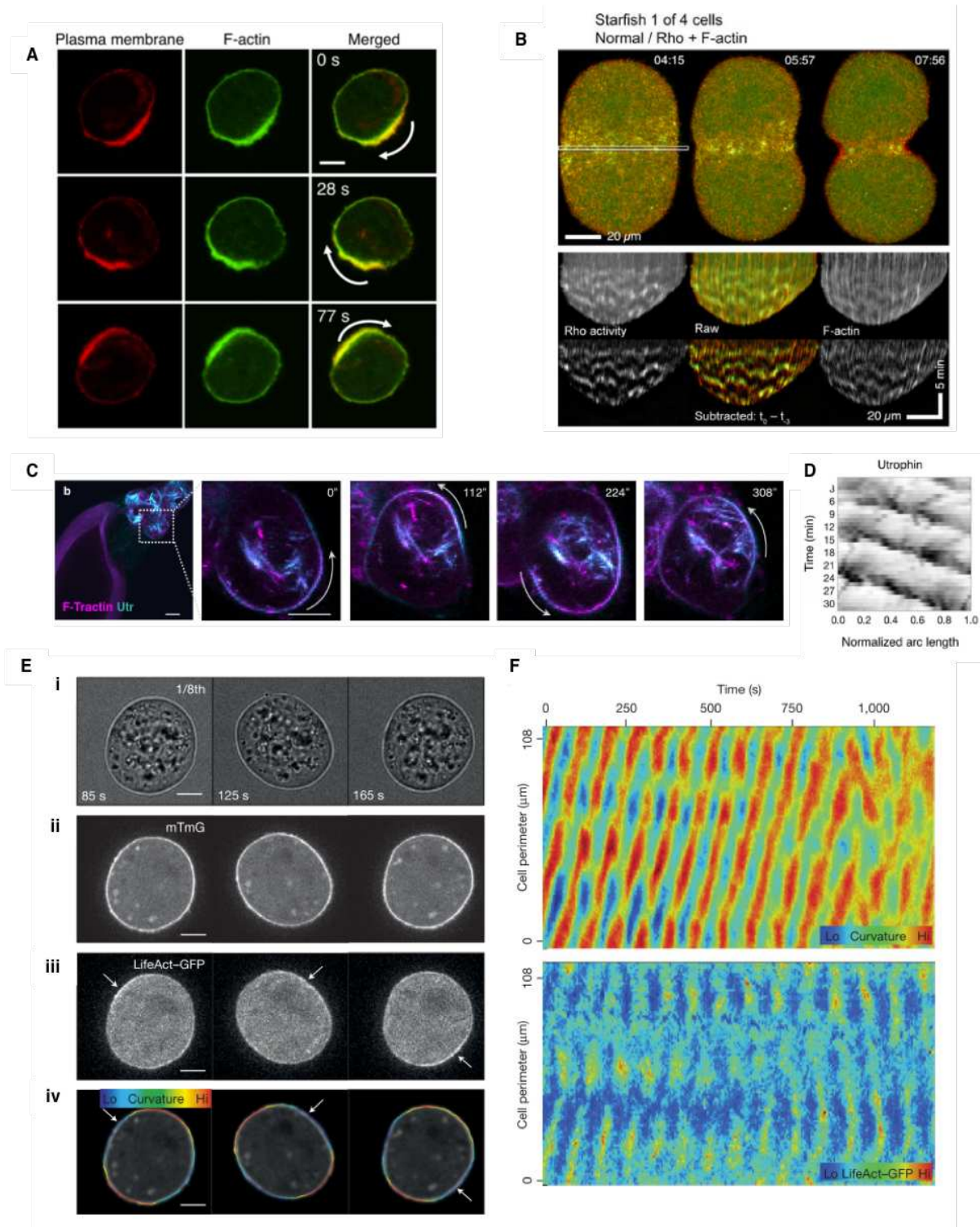


FIGURE 6: PeCoWaCo OBSERVED IN DIFFERENT SYSTEMS

A) Still images of PeCoWaCo observed on rounded CHO cell. Plasma membrane in red, F-actin in green. Image taken from (Driscoll et al., 2015) **B)** Still images of a starfish blastomere undergoing cytokinesis on top, and at the bottom, subtracted kymographs of the the timelapse made from outlined area showing waves of Rho activity rises and falls. Rho activity shown in green, and F-actin in red. Images taken

from (Bement et al., 2015) **C)** Still images from timeplapse movie of *Drosophila* egg chamber showing PeCoWaCo during nurse cell (NC) dumping. F-tractin in magenta and F-actin in cyan. Scale bars =20 μm . **D)** Intensity Kymograph of F-actin wave dynamics during NC dumping. Images (C-D) taken from (Alsous et al., 2021) **E)** Still images from timelapse movie in i) bright-field ii) membrane iii) F-actin, and iv) the local curvature overlaid on membrane images of an isolated blastomere of an 8-cell-stage mouse embryo showing PeCoWaCo. Scale bars = 10 μm . **F)** Kymographs showing local curvature (top) and cortical F-actin intensity (bottom) extracted from timeplase images. Images (E-F) are taken from (Maître et al., 2015).

Although pulsatile contractions and contraction waves are widely studied, what controls the properties like its period, amplitude, and propagation velocity of such an evolutionarily conserved phenomenon is unclear. PeCoWaCo observed on preimplantation mouse embryos serve as a great tool to uncover this machinery as the mouse embryo develops slower. Allowing us to decouple the slow morphogenesis from the PeCoWaCo which one cannot do when timescales of morphogenesis and pulsed contractions are too similar. For example, PeCoWaCo at 8-cell-stage mouse embryo have a $\sim 80\text{s}$ period, whereas the fastest morphogenetic event in mouse preimplantation takes hours. Therefore, we can take advantage of the slow development of the mouse embryo to study thousands of pulsed contractions and the robustness of the mouse embryo to size manipulation to explore the mechanical and molecular regulation of PeCoWaCo. Moreover, by characterizing the regulatory machinery behind PeCoWaCo, we are hoping to increase our understanding of mechanochemical characteristics of the early embryonic cortex. As it was said by Cheer et al in 1987, “observations on the wave characteristics can be used as a ‘diagnostic’ of cortical properties; that is, the waves can provide a ‘map’ of the mechanochemical characteristics of the cortex” (Cheer et al., 1987).

4. REVIEW ARTICLE: MULTISCALE MORPHOGENESIS OF THE MOUSE BLASTOCYST BY ACTOMYOSIN CONTRACTILITY

Shaping the blastocyst relies on the cellular properties and behaviors that can modify tissue architecture, such as cell deformations and rearrangements. All these cell deformations and rearrangement processes require the generation of forces and changing the mechanical properties of cells and the tissue. In this review, we discussed the role of actomyosin contractility in preimplantation mouse development at different scales in time and space.



Multiscale morphogenesis of the mouse blastocyst by actomyosin contractility

Özge Özgüç and Jean-Léon Maître

Abstract

During preimplantation development, the mouse embryo forms the blastocyst, which consists of a squamous epithelium enveloping a fluid-filled lumen and a cluster of pluripotent cells. The shaping of the blastocyst into its specific architecture is a prerequisite to implantation and further development of the embryo. Recent studies identified the central role of the actomyosin cortex in generating the forces driving the successive steps of blastocyst morphogenesis. As seen in other developing animals, actomyosin functions across spatial scales from the subcellular to the tissue levels. In addition, the slow development of the mouse embryo reveals that actomyosin contractility operates at multiple timescales with periodic cortical waves of contraction every ~80 s and tissue remodeling over hours.

Addresses

Institut Curie, 26, rue d'Ulm - 75248 Paris Cedex 05 - France

Corresponding author: Maître, Jean-Léon (jean-leon.maitre@curie.fr)

Current Opinion in Cell Biology 2020, 66:123–129

This review comes from a themed issue on Cell Dynamics

Edited by Diane Barber and Xavier Trepat

For a complete overview see the [Issue](#) and the [Editorial](#)

<https://doi.org/10.1016/j.ceb.2020.05.002>

0955-0674/© 2020 Published by Elsevier Ltd.

Keywords

Actomyosin contractility, Early mammalian development, Tissue mechanics.

Mouse preimplantation development

Within 4 days after fertilization, the mouse embryo forms the blastocyst, a structure that mediates implantation in the uterus [1,2]. From the zygote stage, blastomeres undergo cleavage divisions, producing smaller cells after each successive round. Blastomeres remain spherical and of equivalent size until they reach the 8-cell stage on the 3rd day. Then, the mouse embryo undergoes compaction, a morphogenetic process during which blastomeres draw themselves into closer contact (Figure 1a). Concomitantly, blastomeres gather their apical material into an apical domain [3–5]. This domain affects the divisions from the 8- to 16-cell stage

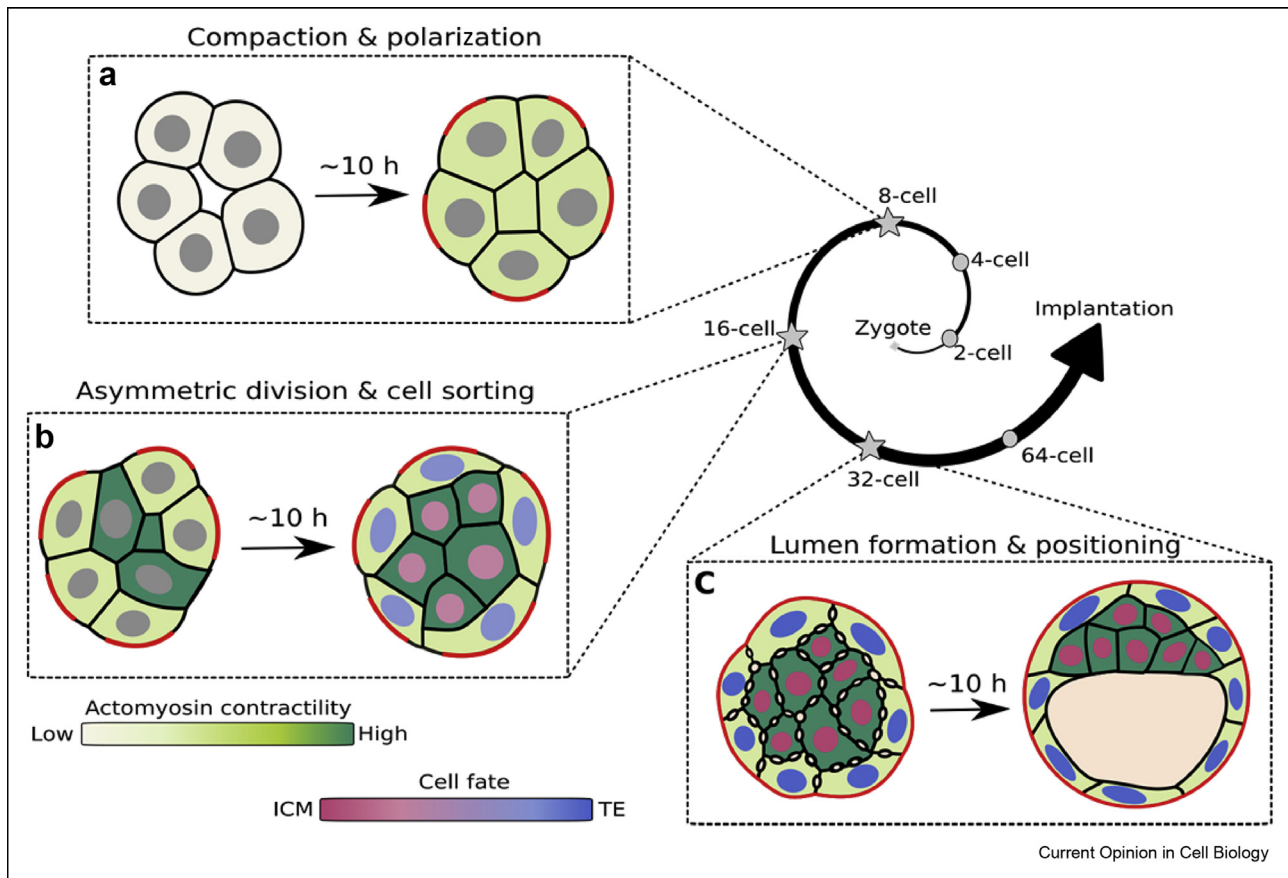
by tethering one pole of the mitotic spindle, which can result both in the asymmetric partitioning of the apical domain among sister cells and in divisions oriented perpendicularly to the embryo surface [4,6–8]. During the 16-cell stage (Figure 1b), cells adopt inner or outer positions causing them to initiate distinct differentiation processes: inner cell mass (ICM) and trophoblast (TE) [4,8–12]. TE cells progressively epithelialize, and during the 32-cell stage (Figure 1c), pump fluid into the intercellular space to create the first mammalian lumen called the blastocoel [13–15]. The formation of this lumen is accompanied with further differentiation of the ICM, turning either into epiblast or primitive endoderm. Eventually, epiblast cells become sandwiched between the TE and primitive endoderm cells, which line the lumen [16]. When the blastocyst reaches its full expansion, it consists of nearly a hundred cells and is ready to implant.

Shaping the blastocyst relies on the deformation of cells and the rearrangement of their contacts (Figure 1). These result from the generation of forces and changes in the mechanical properties of cells and tissues. In animals, cell shape and mechanics are controlled in large part by the actomyosin cortex. As reported in several recent studies, the early mammalian embryo is no exception.

Contractility of the actomyosin cortex

The actomyosin cortex consists of a cross-linked meshwork of dynamic actin filaments that are tethered to the plasma membrane [19]. The contractility of the actomyosin cortex is controlled by the dynamics and cross-linking of actin filaments as well as the activity of the myosin motor nonmuscle myosin II [20–22]. The spatiotemporal regulation of contractility patterns the stresses at the surface of animal cells and drives several key cellular processes. For example, stronger contractility at the cleavage furrow cleaves cells into two during cytokinesis [23]; contractility at the back of migrating cells help them retract their cell body [24]; weaker contractility at cell–cell contacts relaxes them and promotes their spreading [25,26]. Importantly, surface stresses generated by contractility can be controlled across multiple scales, from the subcellular [27] to the tissue levels [28] and from seconds [29] to hours [17].

Figure 1



Morphogenetic events during mouse preimplantation development. Mouse morphogenesis begins on the 3rd day after fertilization with compaction and polarization (a) driven by increased contractility (green) and accumulation of apical material in a restricted domain (red), respectively [4,5,17] (b) Some 16-cell stage blastomeres inherit the apical domain from symmetric or asymmetric divisions and remain at the embryo surface [4,7,8]. Cells without apical material further increase their contractility until they pull themselves inside the embryo. As this cell sorting takes place, cells initiate lineage specification into either TE (blue) or ICM (red) [8,9] (c) When tight junctions of the TE seal, microlumens filled with intercellular fluid appear at cell–cell contacts [15]. Contractility repairs these fractures [18] and pushes the fluid into a single large lumen [15].

The first description of actomyosin during preimplantation development dates to 1983 [30]. Since then, actomyosin was found to be involved in all of the morphogenetic processes forming the blastocyst (Figure 1). Here, we elaborate on how actomyosin contractility acts at multiple spatial and temporal scales to shape the early mouse embryo.

Tempos of the beating blastocyst

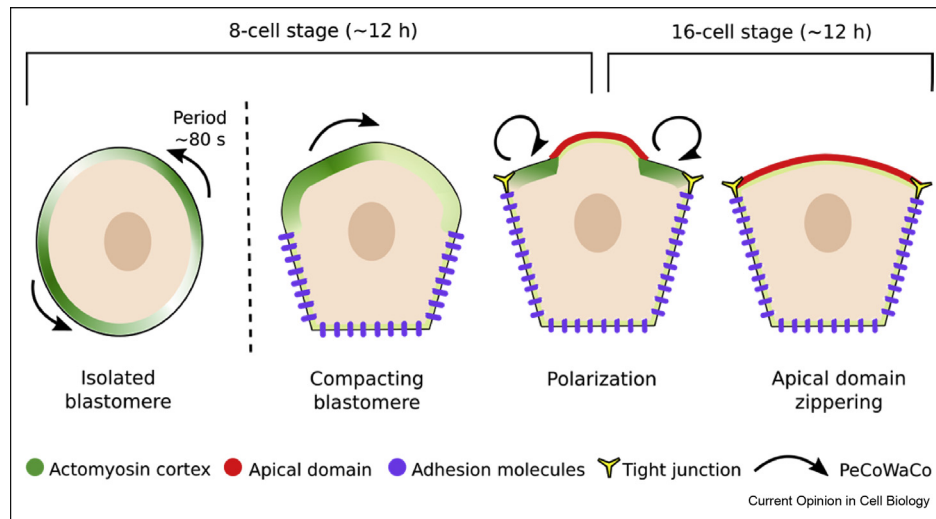
Unlike other model organisms typically used to study animal morphogenesis, the mouse embryo develops slowly (Figure 1). However, actomyosin keeps beating with the same tempo in the mouse as it does in fast-developing organisms. In this section, we discuss how contractility acts at short and long timescales.

Seconds to minutes

Morphogenetic processes such as compaction, cell internalization, or lumen formation take ~10 h each,

while actomyosin contractility typically acts within seconds to minutes. On such short timescale, mouse blastomeres show rapid and reversible deformations. Initially spotted in 1980 [31], these movements were later identified as Periodic Cortical Waves of Contraction—in short, ‘PeCoWaCo’ [17]. PeCoWaCo consists of a surface deformation that propagates around the cell with a speed of $\sim 0.8 \mu\text{m s}^{-1}$ (Figure 2). It requires intact actin and myosin function and, as such, resembles waves of compression and dilations of the actomyosin cortex [32,33] rather than pure actin waves [34], which were both described in cell lines. The ~ 80 s oscillation period of PeCoWaCo is similar to the ones of periodic contractions observed in other early embryos such as in the fly [35,36], frog, or starfish [37]. In fly embryos, actomyosin turnover, the architecture of the meshwork, and a mechanical feedback on Rho GTPases are thought to regulate the duration of pulsed contractions [36,38,39]. However, what sets the traveling motion of

Figure 2



Spatiotemporal control of contractility during the 8- and 16-cell stages. *PeCoWaCo* (black arrows) is most visible on the most contractile regions of the cortex (dark green) [8,17]. In cells isolated from the embryo, *PeCoWaCo* can be observed circulating freely [17]. When in contact, *PeCoWaCo* is locally weakened by adhesion molecules (purple) [8,17]. The apical domain (red), also shows reduced actomyosin levels and *PeCoWaCo* becomes further confined [8]. As polarized cells enlarge their apical domains [4], the most contractile part of the cortex disappears when eventually the apical domain reaches tight junctions (yellow) [13].

contractions observed in mouse, frog, and starfish embryos remain unknown [17,37]. In *Caenorhabditis elegans* embryos, pulsed contractions move toward the anterior pole of the zygotes as a result of tension anisotropies triggered by local downregulation of contractility ensuing signals mediated by the sperm entry [40,41]. This cortical flow advects polarity proteins as it couples to the cytoplasm and induces its streaming (Figure 3) [42,43]. However, such cytoplasmic streaming is not observed in mouse blastomeres. This could be explained by weak coupling of the cortex with the cytoplasm and/or by the absence of cortical flow altogether. Indeed, it remains to be established whether *PeCoWaCo* involves any movement of material or if they simply consist of a local deformation that would occur successively in adjacent parts of the cortex.

Hours to days

In mouse embryos, *PeCoWaCo* can be detected most often from the 8-cell stage onwards [8,17], when actomyosin begins a slower, longer-term reorganization. This reorganization is mirrored by changes in surface tension and leads to the compaction of the embryo over a timescale of ~ 10 h [5,17]. As in other species [25,44–46], compaction of the mouse embryo is set by the ratio of surface tensions between cell–cell contacts and the embryo surface [17,47]. During mouse compaction, the tension ratio gradually changes primarily thanks to the elevation of contractility throughout the 8-cell stage (Figure 1a) [17]. What controls contractility increase and, therefore, the timing of compaction? As noted in

the 1980s, protein synthesis inhibitors applied from the late 2-cell stage on do not block compaction. Moreover, this treatment could induce compaction as early as at the 2- or 4-cell stage, suggesting the presence of an inhibitor of compaction that would be continuously produced [48,49]. The timing of compaction could be controlled by PKC signaling because PKC activators trigger premature compaction at the 4-cell stage [50,51]. Recently, Protein Kinase C (PKC) activation was proposed to activate actomyosin contractility via the Rho GTPase [5], which was earlier found to be required for compaction [52]. What would occur downstream of Rho remains unclear since Rho kinase (Rock), the usual suspect for controlling actomyosin contractility, does not seem to be involved in compaction as neither Rock inhibitors [13,53,54], nor Rock knockout [55] shows a compaction phenotype (or other signs of contractility inhibition). What controls the onset of contractility and kick-starts preimplantation morphogenesis remains unclear.

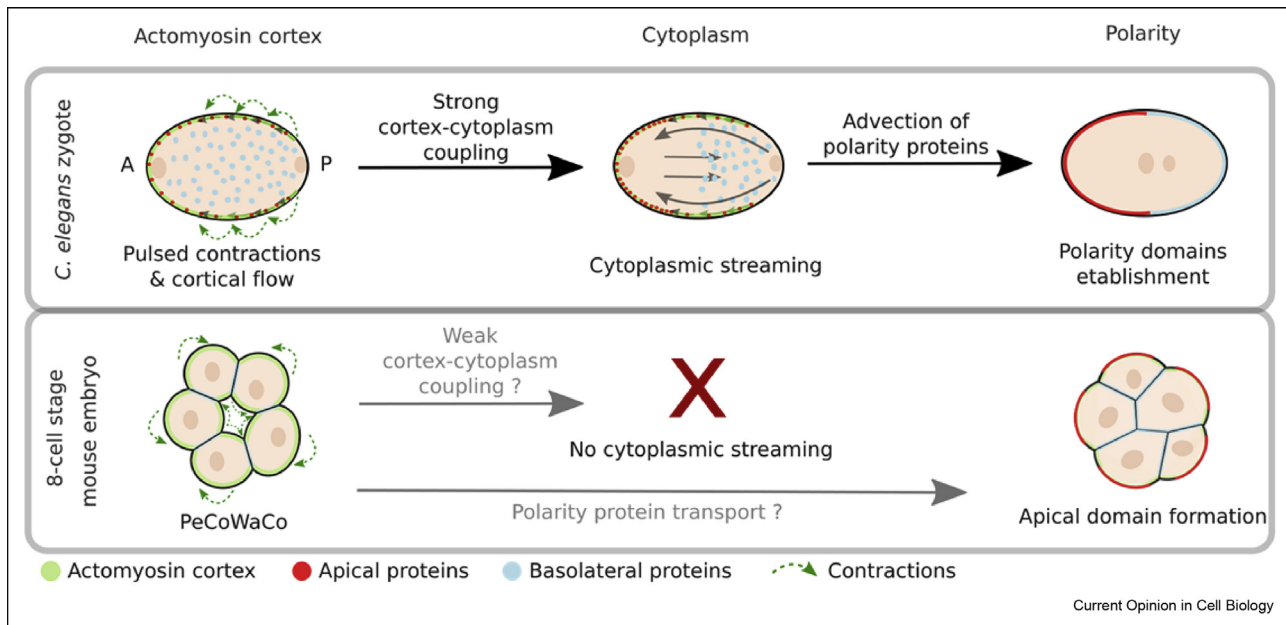
Spatial control of actomyosin contractility

While contractility rises during the 8-cell stage, it becomes spatially patterned at the cellular and tissue levels, definitively transforming a loosely organized cluster of cells into an elaborate cyst.

Subcellular scale

During the 8-cell stage, blastomeres gather their apical material into the apical domain, a master regulator of preimplantation development. Indeed, the apical

Figure 3



Contractility and de novo polarity establishment in early embryos of *C. elegans* and mouse. Early *C. elegans* (top) and mouse (bottom) embryos undergo de novo polarization at the zygote and 8-cell stage respectively. In *C. elegans*, anisotropic pulsed contractions (green) produce cortical flows that entrain the cytoplasm, which starts streaming (middle) [40,41]. These help segregating polarity proteins into distinct domains (red and blue) [42]. In the 8-cell stage mouse embryo (bottom), contractility gradually rises and generates PeCoWaCo (left, green) [8,17]. Concomitantly, cells undergo cell-autonomous de novo polarization but, contrary to *C. elegans*, no cytoplasmic streaming is observed (middle) and contractility seems unnecessary to form the apical domain (right) [5,8].

domain provides positional information that guides cell differentiation by sequestering regulators of the TE fate promoting Yap co-transcriptional regulator [9]. It also determines cell positioning by orienting the spindle during the 4th and 5th cleavages [4,7,56] and by controlling contractility [8]. While enriched in microvilli [3] and apical proteins [4,7,13,56], the apical domain is depleted in actomyosin (Figure 2) [8]. The absence of actomyosin at the apical domain seems to depend on the apical kinase aPKC, as double mutants for the zeta and iota isoforms of aPKC show ectopic actomyosin enrichments at what remains of their apical domain [8]. Because the apical domain can be asymmetrically distributed during the 8- to 16-cell stage division, sister cells inherit distinct contractility [8]. This translates into distinct amplitudes of PeCoWaCo on the short timescale and into the sorting of cells on the long timescale with the most contractile cells being internalized [8,54]. After their spatial allocation, outer cells initiate their differentiation in TE, while inner cells opt for the ICM fate (Figure 1b). This differentiation relies in part on the Yap co-transcriptional activator, which responds to mechanical stimuli [57,58], including the ones generated by actomyosin contractility [59]. During the internalization of the ICM, surface cells become stretched, and Yap becomes nuclear, whereas it remains cytoplasmic in the rounder inner cells [8]. Interestingly, myosin function is essential for both the positioning of

cells and the correct localization of Yap [8]. Whether this phenomenon is controlled by mechanosensing requires further experiments.

What controls the formation of the apical domain at the 8-cell stage? Interestingly, de novo polarization in *C. elegans* zygotes relies on actomyosin contractility (Figure 3) [40–43]. Inhibiting actomyosin contractility in the mouse embryo leads to conflicting results when it comes to apical domain establishment. Blebbistatin, a direct inhibitor of nonmuscle myosin II [60], efficiently blocks cell division, PeCoWaCo, and lowers surface tension [17] but does not affect apical domain formation [5]. Similarly, heterozygous knockout of the myosin heavy chain isoform Myh9 or homozygous knockout of another isoform Myh10 does not seem to affect polarity because these mutants successfully go through processes requiring polarity (they form a blastocyst with TE, ICM, and a blastocoel) [8]. Nevertheless, Zhu et al. conclude that contractility is required for apical domain establishment [5,61] based on the effect of ML7, an inhibitor of the myosin regulatory light chain kinase [62], which prevents the formation of the apical domain. From these conflicting observations, we suspect that ML7 affects mouse blastomeres beyond their contractility, and we do not think that contractility is required for apical polarity establishment in the early mouse embryo.

Tissue scale

Additionally to the apical domain, cell–cell contacts also downregulate contractions (Figure 2). Originally discovered in the compacting mouse embryo [63], the cell–cell adhesion molecule E-cadherin (or Cdh1) signals to reduce contractility locally at contacts between cells [25,64,65] as well as globally [23]. The control of contractility by cadherins can be mediated via regulators of the small GTPase Rho, which are recruited by p120-catenin, a core component of adherens junctions [66,67]. During compaction, actomyosin levels decrease at cell–cell contacts as compared with the cell medium interface in a Cdh1-dependent manner [17]. On the long timescale, the local downregulation of contractility could account for up to 1/4 of the entire compaction of the mouse embryo [17].

As actomyosin is reduced at cell–cell contacts and at the apical domain, PeCoWaCo becomes confined to the nonapical part of the noncontact interface (Figure 2). This contractile interface disappears when embryos develop further at 16-cell stage, as cells which do not inherit the apical domain from their mother cell internalize [8], and polarized cells enlarge their apical domain [4,5] until the most contractile part of the exposed surface disappears [13]. This is concomitant with the sealing of the tight junctions when the apical domains of contacting cells zip together and seal the embryo (Figure 2) [13]. Zenker et al. conclude that the expansion of the apical domain does not result from the difference in contractility between the apical and nonapical part of the cell. This is based on experiments with drugs that were thought to inhibit contractility. However, as stated by the authors [13], these drugs did not affect cell shape, which is inconsistent with a number of other studies in which contractility is inhibited [5,8,14,15,17]. At that point, it is worth highlighting a technical note on Blebbistatin, a potent contractility inhibitor, which is, as many other drugs, hydrophobic, and not compatible with usual mouse embryo culture conditions under mineral oil [8,15,17]. Therefore, it remains conceivable that the expansion of the apical domain results from the different contractility between the apical and nonapical part of the exposed cell surface.

Once tight junctions are sealed [68], intercellular fluid becomes trapped within the intercellular space [13] and accumulates to form the blastocoel. This occurs after the fracturing of cell–cell contacts by pressurized fluid leading to the formation of micron-size water pockets (Figure 1c) [15]. As observed *in vitro* [18], contractility mediates the healing of these fractures and can redistribute the extra-cellular fluid. The higher contractility of the ICM, as compared with the TE, squishes the fluid away from the ICM and progressively coarsens the many smaller water pockets into a larger one until there is only one lumen remaining [15]. Interestingly, on short time

scales, water pockets seem to pulse at a rhythm close to the one of PeCoWaCo [15,17]. After a few hours of expansion, the blastocoel undergoes cycles of collapse and re-growth reaching a long-term steady state [69]. Collapses seem to result from transient seal rupture because of cell division within the TE [14,70]. Once again, tight junction repair is aided by contractility [14], which could be recruited by Rho, as observed in the surface epithelium of *Xenopus* gastrula [71].

Concluding remarks

After the many discoveries on actomyosin contractility during worm, fly, or fish development, the mammalian embryo finally joined the club. With its comparably slow development, the mammalian embryo can now provide unique information on the different timescales at which actomyosin functions. This will become possible thanks to the advancements in imaging technologies, which will require preserving long-term viability while enabling high temporal resolution. In this regard, light-sheet microscopy will be key to put the multiple scales of contractility under the spotlight [72,73].

Conflict of interest statement

Nothing declared.

Acknowledgements

The authors thank J. Firmin and D. Pelzer for critical reading of the manuscript. Ö.Ö. is funded from the European Union's Horizon 2020 research and innovation program under the Marie Skłodowska-Curie grant agreement No 666003. Research in the lab of J.-L.M., who is supported by the Institut Curie and the CNRS, is funded by the FSER via the FRM, the INSERM transversal program HuDeCA, an ERC-2017-StG 757557, QLife grants and Labex DEEP (ANR-11-LBX-0044) which are part of the IDEX PSL (ANR-10-IDEX-0001-02 PSL).

References

Papers of particular interest, published within the period of review, have been highlighted as:

- * of special interest
- ** of outstanding interest

1. Maître J-L: **Mechanics of blastocyst morphogenesis**. *Biol Cell* 2017, **109**:323–338.
2. Chazaud C, Yamanaka Y: **Lineage specification in the mouse preimplantation embryo**. *Development* 2016, **143**:1063–1074.
3. Ducibella T, Ukena T, Karnovsky M, Anderson E: **Changes in cell surface and cortical cytoplasmic organization during early embryogenesis in the preimplantation mouse embryo**. *J Cell Biol* 1977, **74**:153–167.
4. Korotkevich E, Niwayama R, Courtois A, Friese S, Berger N, Buchholz F, Hiragi T: **The apical domain is required and sufficient for the first lineage segregation in the mouse embryo**. *Dev Cell* 2017, **40**:235–247. e7.
5. Zhu M, Leung CY, Shahbazi MN, Zernicka-Goetz M: **Actomyosin polarisation through PLC-PKC triggers symmetry breaking of the mouse embryo**. *Nat Commun* 2017, <https://doi.org/10.1038/s41467-017-00977-8>.
- ** Describe how PKC and PIPs regulate the exclusion of actomyosin from the apical domain.
6. Dard N, Louvet-Vallée S, Maro B: **Orientation of mitotic spindles during the 8- to 16-cell stage transition in mouse embryos**. *PLoS One* 2009, **4**, e8171.

7. Niwayama R, Moghe P, Liu Y-J, Fabrèges D, Buchholz F, Piel M, Hiiragi T: **A tug-of-war between cell shape and polarity controls division orientation to ensure robust patterning in the mouse blastocyst.** *Dev Cell* 2019, <https://doi.org/10.1016/j.devcel.2019.10.012>.
8. Maître J-L, Turlier H, Illukkumbura R, Eismann B, Niwayama R, Nédélec F, Hiiragi T: **Asymmetric division of contractile domains couples cell positioning and fate specification.** *Nature* 2016, **536**:344–348.
- Determine the mechanisms by which apical domain asymmetric inheritance induces inner and outer cells sorting by controlling contractility.
9. Hirate Y, Hirahara S, Inoue K, Suzuki A, Alarcon VB, Akimoto K, Hirai T, Hara T, Adachi M, Chida K, *et al.*: **Polarity-dependent distribution of angiotonin localizes Hippo signaling in pre-implantation embryos.** *Curr Biol* 2013, **23**:1181–1194.
10. Stephenson RO, Yamanaka Y, Rossant J: **Disorganized epithelial polarity and excess trophectoderm cell fate in preimplantation embryos lacking E-cadherin.** *Development* 2010, **137**:3383–3391.
11. Cockburn K, Biechele S, Garner J, Rossant J: **The Hippo pathway member Nf2 is required for inner cell mass specification.** *Curr Biol* 2013, **23**:1195–1201.
12. Hirate Y, Cockburn K, Rossant J, Sasaki H: **Tead4 is constitutively nuclear, while nuclear vs. cytoplasmic Yap distribution is regulated in preimplantation mouse embryos.** *Proc Natl Acad Sci USA* 2012, **109**:E3389–90— author reply E3391–2.
13. Zenker J, White MD, Gasnier M, Álvarez YD, Lim HYG, Bissiere S, Biro M, Plachta N: **Expanding actin rings zipper the mouse embryo for blastocyst formation.** *Cell* 2018, <https://doi.org/10.1016/j.cell.2018.02.035>.
- Describe mutual exclusion between actin and microtubules at the apical domain. Propose that contractility fastens tight junctions after apical domain expansion.
14. Chan CJ, Costanzo M, Ruiz-Herrero T, Mönke G, Petrie RJ, Bergert M, Diz-Muñoz A, Mahadevan L, Hiiragi T: **Hydraulic control of mammalian embryo size and cell fate.** *Nature* 2019, **571**:112–116.
- Describe antagonistic effects of contractility on lumen size. Too much contractility would cause tight junction leakage, yet reduced contractility causes slower lumen expansion.
15. Dumortier JG, Le Verge-Serandour M, Tortorelli AF, Mielke A, de Plater L, Turlier H, Maître J-L: **Hydraulic fracturing and active coarsening position the lumen of the mouse blastocyst.** *Science* 2019, **365**:465–468.
- Identify how contractility positions the first mammalian lumen by closing water pockets that initially appeared by hydraulic fracturing of cell–cell contacts.
16. Plusa B, Piliszek A, Frankenberg S, Artus J, Hadjantonakis A-K: **Distinct sequential cell behaviours direct primitive endoderm formation in the mouse blastocyst.** *Development* 2008, **135**:3081–3091.
17. Maître J-L, Niwayama R, Turlier H, Nédélec F, Hiiragi T: **Pulsatile cell-autonomous contractility drives compaction in the mouse embryo.** *Nat Cell Biol* 2015, **17**:849–855.
18. Casares L, Vincent R, Zalvidea D, Campillo N, Navajas D, Arroyo M, Trepas X: **Hydraulic fracture during epithelial stretching.** *Nat Mater* 2015, **14**:343–351.
19. Clark AG, Wartlick O, Salbreux G, Paluch EK: **Stresses at the cell surface during animal cell morphogenesis.** *Curr Biol* 2014, **24**:R484–R494.
20. Bovellan M, Romeo Y, Biro M, Boden A, Chugh P, Yonis A, Vaghela M, Fritzsche M, Moulding D, Thorogate R, *et al.*: **Cellular control of cortical actin nucleation.** *Curr Biol* 2014, <https://doi.org/10.1016/j.cub.2014.05.069>.
21. Chugh P, Clark AG, Smith MB, Cassani DAD, Dierkes K, Ragab A, Roux PP, Charras G, Salbreux G, Paluch EK: **Actin cortex architecture regulates cell surface tension.** *Nat Cell Biol* 2017, **19**:689–697.
22. Naganathan SR, Fürthauer S, Rodriguez J, Fievet BT, Jülicher F, Ahringer J, Cannistraci CV, Grill SW: **Morphogenetic degeneracies in the actomyosin cortex.** *eLife* 2018, **7**.
23. Padmanabhan A, Zaidel-Bar R: **Non-junctional E-cadherin clusters regulate the actomyosin cortex in the *C. elegans* zygote.** *Curr Biol* 2017, **27**:103–112.
24. Tsai TY-C, Collins SR, Chan CK, Hadjitheodorou A, Lam P-Y, Lou SS, Yang HW, Jorgensen J, Ellett F, Irimia D, *et al.*: **Efficient front-rear coupling in neutrophil chemotaxis by dynamic myosin II localization.** *Dev Cell* 2019, **49**:189–205.e6.
25. Maître J-L, Berthoumieux H, Krens SFG, Salbreux G, Jülicher F, Paluch E, Heisenberg C-P: **Adhesion functions in cell sorting by mechanically coupling the cortices of adhering cells.** *Science* 2012, **338**:253–256.
26. Heuzé ML, Sankara Narayana GHN, D'Alessandro J, Cellerin V, Dang T, Williams DS, Van Hest JC, Marq P, Mège R-M, Ladoux B: **Myosin II isoforms play distinct roles in adherens junction biogenesis.** *eLife* 2019, **8**, e46599.
27. Sun Z, Amourda C, Shagirov M, Hara Y, Saunders TE, Toyama Y: **Basolateral protrusion and apical contraction cooperatively drive *Drosophila* germ-band extension.** *Nat Cell Biol* 2017, **19**:375–383.
28. Bailles A, Collinet C, Philippe J-M, Lenne P-F, Munro E, Lecuit T: **Genetic induction and mechanochemical propagation of a morphogenetic wave.** *Nature* 2019, **572**:467–473.
29. Armon S, Bull MS, Aranda-Díaz A, Prakash M: **Ultrafast epithelial contractions provide insights into contraction speed limits and tissue integrity.** In *Proceedings of the national academy of sciences of the United States of America*, vol. 115; 2018. E10333–E10341.
30. Sobel JS: **Localization of myosin in the preimplantation mouse embryo.** *Dev Biol* 1983, **95**:227–231.
31. Lehtonen E: **Changes in cell dimensions and intercellular contacts during cleavage-stage cell cycles in mouse embryonic cells.** *J Embryol Exp Morphol* 1980, **58**:231–249.
32. Kapustina M, Elston TC, Jacobson K: **Compression and dilation of the membrane-cortex layer generates rapid changes in cell shape.** *J Cell Biol* 2013, **200**:95–108.
33. Driscoll MK, Losert W, Jacobson K, Kapustina M: **Spatiotemporal relationships between the cell shape and the actomyosin cortex of periodically protruding cells.** *Cytoskeleton* 2015, **72**:268–281.
34. Xiao S, Tong C, Yang Y, Wu M: **Mitotic cortical waves predict future division sites by encoding positional and size information.** *Dev Cell* 2017, **43**:493–506.e3.
35. Martin A, Kaschube M, Wieschaus E: **Pulsed contractions of an actin-myosin network drive apical constriction.** *Nature* 2009, **457**:495–499.
36. Munjal A, Philippe J-M, Munro E, Lecuit T: **A self-organized biomechanical network drives shape changes during tissue morphogenesis.** *Nature* 2015, **524**:351–355.
37. Bement WM: **Activator-inhibitor coupling between Rho signalling and actin assembly makes the cell cortex an excitable medium.** *Nat Cell Biol* 2015, **17**:1471–1483.
38. Vasquez CG, Tworoger M, Martin AC: **Dynamic myosin phosphorylation regulates contractile pulses and tissue integrity during epithelial morphogenesis.** *J Cell Biol* 2014, **206**:435–450.
39. Coravos JS, Martin AC: **Apical sarcomere-like actomyosin contracts nonmuscle *Drosophila* epithelial cells.** *Dev Cell* 2016, <https://doi.org/10.1016/j.devcel.2016.09.023>.
40. Munro E, Nance J, Priess J: **Cortical flows powered by asymmetrical contraction transport PAR proteins to establish and maintain anterior-posterior polarity in the early *C. elegans* embryo.** *Dev Cell* 2004, **7**:413–424.
41. Mayer M, Depken M, Bois JS, Jülicher F, Grill SW: **Anisotropies in cortical tension reveal the physical basis of polarizing cortical flows.** *Nature* 2010, **467**:617–621.
42. Goehring NW, Trong PK, Bois JS, Chowdhury D, Nicola EM, Hyman AA, Grill SW: **Polarization of PAR proteins by**

- advective triggering of a pattern-forming system.** *Science* 2011, **334**:1137–1141.
43. Mittasch M, Gross P, Nestler M, Fritsch AW, Iserman C, Kar M, Munder M, Voigt A, Alberti S, Grill SW, *et al.*: **Non-invasive perturbations of intracellular flow reveal physical principles of cell organization.** *Nat Cell Biol* 2018, <https://doi.org/10.1038/s41556-017-0032-9>.
 44. Steinberg MS: **Reconstruction of tissues by dissociated cells. Some morphogenetic tissue movements and the sorting out of embryonic cells may have a common explanation.** *Science* 1963, **141**:401–408.
 45. Brodland G: **The Differential Interfacial Tension Hypothesis (DITH): a comprehensive theory for the self-rearrangement of embryonic cells and tissues.** *J Biomech Eng* 2002, **124**: 188–197.
 46. Manning ML, Foty RA, Steinberg MS, Schoetz E-M: **Coaction of intercellular adhesion and cortical tension specifies tissue surface tension.** *Proc Natl Acad Sci USA* 2010, **107**: 12517–12522.
 47. Goel NS, Doggenweiler CF, Thompson RL: **Simulation of cellular compaction and internalization in mammalian embryo development as driven by minimization of surface energy.** *Bull Math Biol* 1986, **48**:167–187.
 48. Kidder GM, McLachlin JR: **Timing of transcription and protein synthesis underlying morphogenesis in preimplantation mouse embryos.** *Dev Biol* 1985, **112**:265–275.
 49. Levy JB, Johnson MH, Goodall H, Maro B: **The timing of compaction: control of a major developmental transition in mouse early embryogenesis.** *J Embryol Exp Morphol* 1986, **95**: 213–237.
 50. Winkler GK, Ferguson JE, Takeichi M, Nuccitelli R: **Activation of protein kinase C triggers premature compaction in the four-cell stage mouse embryo.** *Dev Biol* 1990, **138**:1–15.
 51. O'Sullivan DM, Johnson MH, McConnell JM: **Staurosporine advances interblastomeric flattening of the mouse embryo.** *Zygote* 1993, **1**:103–112.
 52. Clayton L, Hall A, Johnson MH: **A role for Rho-like GTPases in the polarisation of mouse eight-cell blastomeres.** *Dev Biol* 1999, **205**:322–331.
 53. Laeno AMA, Tamashiro DAA, Alarcon VB: **Rho-associated kinase activity is required for proper morphogenesis of the inner cell mass in the mouse Blastocyst1.** *Biol Reprod* 2013, **89**.
 54. Samarage CR, White MD, Álvarez YD, Fierro-González JC, Henon Y, Jesudason EC, Bissiere S, Fouras A, Plachta N: **Cortical tension allocates the first inner cells of the mammalian embryo.** *Dev Cell* 2015, **34**:435–447.
 55. Kamijo H, Matsumura Y, Thumkeo D, Koike S, Masu M, Shimizu Y, Ishizaki T, Narumiya S: **Impaired vascular remodeling in the yolk sac of embryos deficient in ROCK-I and ROCK-II.** *Gene Cell* 2011, **16**:1012–1021.
 56. Dard N, Le T, Maro B, Louvet-Vallée S: **Inactivation of aPKC λ reveals a context dependent allocation of cell lineages in preimplantation mouse embryos.** *PLoS One* 2009, **4**, e7117.
 57. Elosegui-Artola A, Andreu I, Beedle AEM, Lezamiz A, Uroz M, Kosmalska AJ, Oriá R, Kechagia JZ, Rico-Lastres P, Le Roux A-L, *et al.*: **Force triggers YAP nuclear entry by regulating transport across nuclear pores.** *Cell* 2017, <https://doi.org/10.1016/j.cell.2017.10.008>.
 58. Xia P, Gütl D, Zheden V, Heisenberg C-P: **Lateral inhibition in cell specification mediated by mechanical signals modulating TAZ activity.** *Cell* 2019, <https://doi.org/10.1016/j.cell.2019.01.019>.
 59. Dupont S, Morsut L, Aragona M, Enzo E, Giulitti S, Cordenonsi M, Zanconato F, Le Dıgabel J, Forcato M, Bicciato S, *et al.*: **Role of YAP/TAZ in mechanotransduction.** *Nature* 2011, **474**:179–183.
 60. Straight AF, Cheung A, Limouze J, Chen I, Westwood NJ, Sellers JR, Mitchison TJ: **Dissecting temporal and spatial control of cytokinesis with a myosin II inhibitor.** *Science* 2003, **299**:1743–1747.
 61. Zhu M, Zernicka-Goetz M: **Building an apical domain in the early mouse embryo: lessons, challenges and perspectives.** *Curr Opin Cell Biol* 2020, **62**:144–149.
 62. Saitoh M, Ishikawa T, Matsushima S, Naka M, Hidaka H: **Selective inhibition of catalytic activity of smooth muscle myosin light chain kinase.** *J Biol Chem* 1987, **262**:7796–7801.
 63. Hyafil F, Morello D, Babinet C, Jacob F: **A cell surface glycoprotein involved in the compaction of embryonal carcinoma cells and cleavage stage embryos.** *Cell* 1980, **21**:927–934.
 64. Ratheesh A, Gomez GA, Priya R, Verma S, Kovacs EM, Jiang K, Brown NH, Akhmanova A, Stehbens SJ, Yap AS: **Central-spindlin and α -catenin regulate Rho signalling at the epithelial zonula adherens.** *Nat Cell Biol* 2012, **14**:818–828.
 65. Pinheiro D, Hannezo E, Herszterg S, Bosveld F, Gaugue I, Balakireva M, Wang Z, Cristo I, Rigaud SU, Markova O, *et al.*: **Transmission of cytokinesis forces via E-cadherin dilution and actomyosin flows.** *Nature* 2017, **545**:103–107.
 66. Wildenberg GA, Dohn MR, Carnahan RH, Davis MA, Lobdell NA, Settleman J, Reynolds AB: **p120-catenin and p190RhoGAP regulate cell-cell adhesion by coordinating antagonism between Rac and Rho.** *Cell* 2006, **127**:1027–1039.
 67. Yu HH, Dohn MR, Markham NO, Coffey RJ, Reynolds AB: **p120-catenin controls contractility along the vertical axis of epithelial lateral membranes.** *J Cell Sci* 2016, **129**:80–94.
 68. Wang H, Ding T, Brown N, Yamamoto Y, Prince LS, Reese J, Paria BC: **Zonula occludens-1 (ZO-1) is involved in morula to blastocyst transformation in the mouse.** *Dev Biol* 2008, **318**: 112–125.
 69. Ruiz-Herrero T, Alessandri K, Gurchenkov BV, Nassoy P, Mahadevan L: **Organ size control via hydraulically gated oscillations.** *Development* 2017, **144**:4422–4427.
 70. Leonavicius K, Preece C, Davies B, Srinivas S: **Mechanics of mouse blastocyst hatching revealed by a hydrogel-based microdeformation assay.** *Proc Natl Acad Sci USA* 2018, **115**: 10375–10380.
 71. Stephenson RE, Higashi T, Erofeev IS, Arnold TR: **Rho flares repair local tight junction leaks.** *Dev Cell* 2019, <https://doi.org/10.1016/j.devcel.2019.01.016>.
 72. Strnad P, Gunther S, Reichmann J, Krzic U, Balazs B, de Medeiros G, Norlin N, Hıiragi T, Hufnagel L, Ellenberg J: **Inverted light-sheet microscope for imaging mouse pre-implantation development.** *Nat Methods* 2016, **13**:139–142.
 73. McDole K, Guignard L, Amat F, Berger A, Malandain G, Royer LA, Turaga SC, Branson K, Keller PJ: **In toto imaging and reconstruction of post-implantation mouse development at the single-cell level.** *Cell* 2018, <https://doi.org/10.1016/j.cell.2018.09.031>.

METHODS

1. MOUSE HUSBANDRY

All animal work is performed in the animal facility at the Institut Curie, with permission by the institutional veterinarian overseeing the operation (APAFIS #11054-2017082914226001). The animal facilities are operated according to international animal welfare rules.

(C57BL/6xC3H) F1 hybrid strain is used for wild-type (WT). To visualize filamentous actin, LifeAct-GFP mice (Tg(CAG-EGFP)#Rows) are used. To visualize plasma membranes, mTmG (Gt(ROSA)26Sor^{tm4}(ACTB-tdTomato,-EGFP)^{Luo}) is used. To generate Prkci^{+/-} ; Prkcz^{+/-} embryos with membrane and actin signal, Prkci^{tm1Kido} (ref.) and Prkcz^{tm1.1Cda} (ref) mice are used to breed Prkcz^{-/-} ; Prkci^{tm1.1Cda/+} ; Zp3^{Cre/+} mothers with mTmG-LifeAct-GFP fathers. Mice are used from 5 weeks old on.

2. EMBRYO MANIPULATIONS

Embryos are isolated from superovulated female mice mated with male mice. Superovulation of female mice is induced by intraperitoneal injection of 5 international units (IU) pregnant mare's serum gonadotropin (PMSG, Ceva, Syncro-part), followed by intraperitoneal injection of 5 IU human chorionic gonadotropin (hCG, MSD Animal Health, Chorulon) 44-48 hours later. Embryos are recovered at E1.5 or E2.5 by flushing oviducts from plugged females with 37°C FHM (LifeGlobal, ZEHP-050 or Millipore, MR-122-D) using a modified syringe (Acufirm, 1400 LL 23).

Embryos are handled using an aspirator tube (Sigma, A5177-5EA) equipped with a glass pipette pulled from glass micropipettes (Blaubrand intraMark or Warner Instruments).

Embryos are placed in KSOM (LifeGlobal, ZEKS-050 or Millipore, MR-107-D) or FHM supplemented with 0.1 % BSA (Sigma, A3311) in 10 μ L droplets covered in mineral oil (Sigma, M8410 or Acros Organics). Embryos are cultured in an incubator with a humidified atmosphere supplemented with 5% CO₂ at 37°C.

2.1. Blocking Cytokinesis

To block cell division, I targeted Aurora kinases that regulate cell cycle transit from G2 through cytokinesis by using VX-680 (tocris, ref: 5907), is a small molecule inhibitor of all three Aurora kinases (Harrington et al., 2004). At the time of 2nd cleavage, embryos were cultured in KSOM containing 2,5uM Vx-680 (tocris, ref: 5907, 50mM dimethyl sulfoxide (DMSO) stock) for 3 hours at 37°C followed by washes in KSOM/BSA.

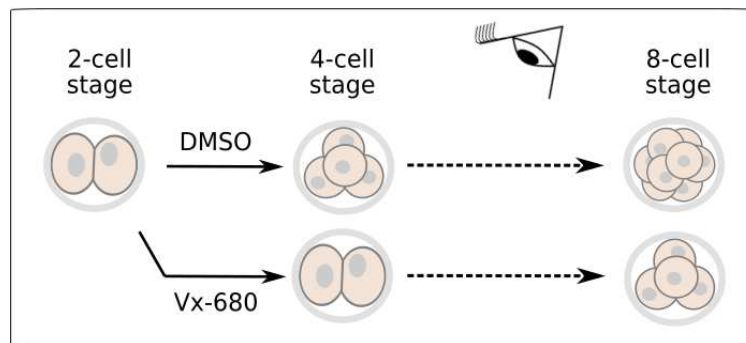


FIGURE 7: BLOCKING CELL DIVISION

Schematic diagram of the experimental design of blocking cell division from 2- to 4-cell stage with aurora kinase inhibitor Vx-680.

2.2. Blocking Zygotic genome activation

To block zygotic genome activation (ZGA), I used 5,6-dichloro-1- β -D-ribofuranosylbenzimidazole (DRB), a RNA polymerase II inhibitor (Tamm et al., 1976). Embryos with paternal mTmG allele were cultured in KSOM containing 80 μ M DRB (Sigma-Aldrich, ref: D1916, 50 mM DMSO stock from Geneviève Almouzni Lab) (Abe et al., 2018) from early 2-cell stage (1-2h after division). Control embryos were cultured in DRB-free medium that contained the appropriate amount of DMSO.

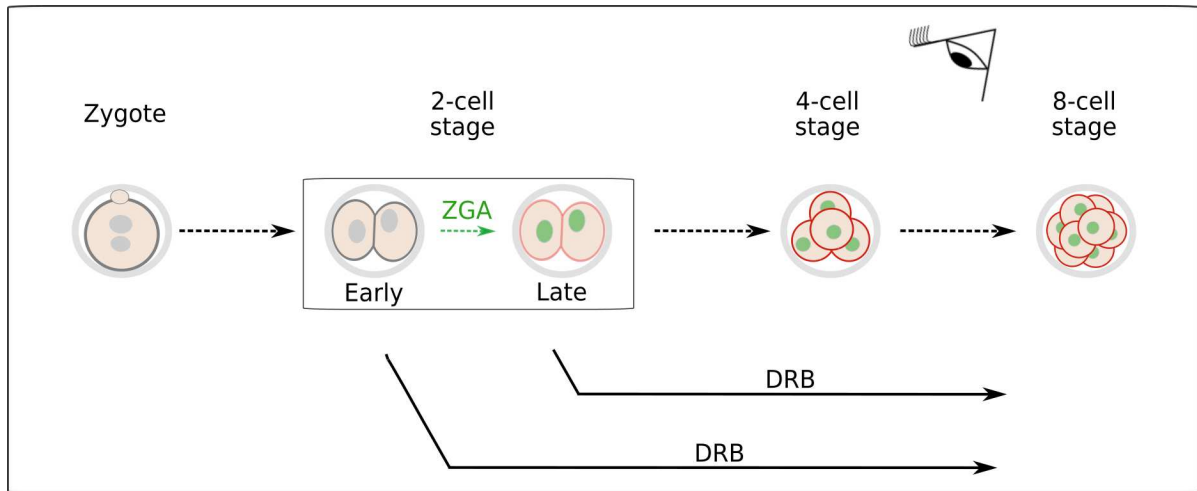


FIGURE 8: BLOCKING ZYGOTIC GENOME ACTIVATION (ZGA)

Schematic diagram of the experimental design of blocking ZGA by using RNA polymerase II inhibitor DRB.

2.3. Zona pellucida removal

To remove the Zona Pellucida (ZP), embryos are incubated for 45-60 s in pronase (Sigma, P8811), a mixture of several nonspecific endo- and exoproteases that digest proteins down to single amino acids.

2.4. Dissociation

ZP-free 2- and 4-cell-stage embryos aspirated multiple times (typically between 3–5 times) through a narrow glass pipette (with a radius that of a 2-cell-stage and of a 4-cell-stage blastomere) until dissociation of cells.

ZP-free 16-cell-stage embryos are placed into Ca²⁺ free KSOM (ref. 36) for 8–10 min before being aspirated multiple times (typically between 3–5 times) through a narrow glass pipette (with a radius that of a 1/16th blastomere) until dissociation of cells. Cells are then washed with KSOM for 1 hour before experiment.

2.5. Cellular Fragmentation

In order to fragment cells, I first made their actomyosin cortex weaker by culturing cells in KSOM containing 10 μM Cytochalasin D, inhibitor of actin polymerization (CytD; sigma, ref C2618-200UL, 10 mM DMSO stock) (Korotkevich et al., 2017). After 20 min treatment of 10mM CytD, cells were deformed by suction into a smoothed glass pipette $\sim 30 \mu\text{m}$ and $\sim 5 \mu\text{m}$ in diameter for 2-cell-stage and 16-cell-stage respectively until they clipped into two.

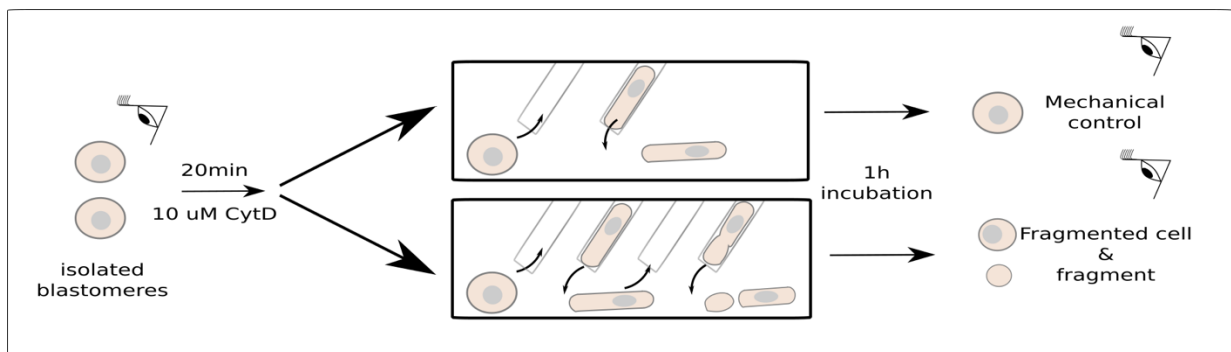


FIGURE 9: CELLULAR FRAGMENTATION

Schematic diagram of the experimental design of fragmentation using actin polymerization inhibitor CytD and small glass capillaries.

2.6. Cellular Fusion

To create different cell sizes at a fixed embryonic stage, I used the GenomONE-CF FZ SeV-E cell fusion kit (CosmoBio, ISK-CF-001-EX). This cell fusion kit contains HVJ Envelope which is a purified product prepared through complete inactivation of Sendai virus (HVJ: Hemagglutinating virus of Japan). It is a vesicle in which only the cell membrane-fusing capability of the envelope protein of Sendai virus is retained (Kaneda et al., 2002).

HVJ envelope is resuspended following manufacturer's instructions and diluted in FHM for use. To achieve a broad range of cell radii (15-40 μm) by fusing different number of 16-cell stage blastomeres, I first dissociated 4-cell stage embryos into 1/4th and 2/4th. When isolated blastomeres and doublets reached to 8-cell stage, I

dissociated 1/4th into 1/8th. this dissociations allowed me to have 2/16th, 4/16th and 8/16th embryos when they reached to 16 cell stage. To fuse half/ quarter/ eighth embryos at the 16-cell stage, they are incubated in 1:50 HVJ envelope / FHM for 15 min at 37°C followed by washes in KSOM as described in figure 10.

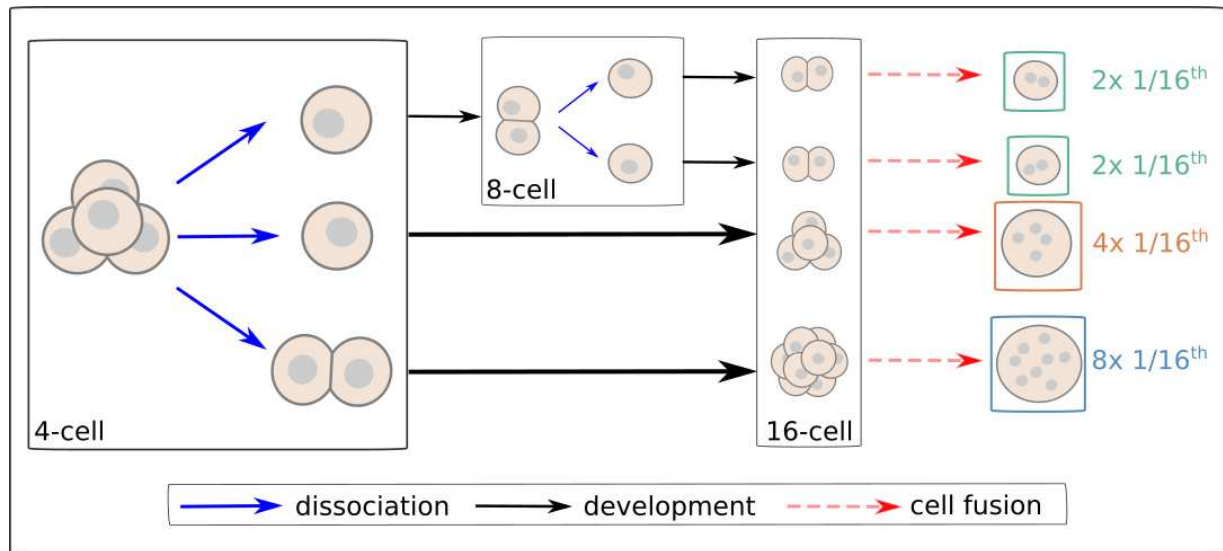


FIGURE 10: CELLULAR FUSION

Schematic diagram of the experimental design of cellular fusion by using HVJ-E

2.7. Micropipette Aspiration and surface tension measurements

As described previously (Guevorkian et al., 2010; J.-L. Maître et al., 2015) a microforged micropipette coupled to a microfluidic pump (Fluigent, MFCS EZ) is used to measure the surface tension of embryos. In brief, micropipettes of radii 8-16 μm are used to apply step-wise increasing pressures against the cell surface until reaching a deformation which has the radius of the micropipette (R_p). At steady-state, the surface tension (γ) of the cell calculated from the Young-Laplace's law applied between the cell and the micropipette: $\gamma = P_c / 2 (1/R_p - 1/R)$, where P_c is the critical pressure used to deform the cell of radius R . Based on this measurement, we then use the Young-Laplace law between the blastocyst and the outside medium to calculate the hydrostatic pressure (P) of the embryo: $P = 2\gamma / R$.

To change shape of the blastomeres, I used the same micropipette aspiration system. After reaching P_c , 20 mbar extra pressure added for few seconds and

changed back to Pc in order to manipulate the cell shape by creating a long stable tongue inside the micropipette. These cells were imaged for PeCoWaCo before the aspiration and during the aspiration.

2.8. Pharmacological manipulations of contractility

Blebbistatin (+), an inactive enantiomere of the inhibitor, or (-), the selective inhibitor myosin II ATPase activity, (Tocris, ref 1853 & 1852) 50 mM DMSO stocks are diluted to 10 μ M in KSOM. Isolated 16-cell-stage blastomeres are incubated in medium containing Blebbistatin (+ or -) without covering with mineral oil for 30 min before imaging.

ML-7 , an inhibitor of inhibitor of myosin light chain kinase, (Sigma, ref I2764) 10mM ethanol:water (1:1) stock diluted to 10 μ M in KSOM. Isolated 16-cell-stage blastomeres are incubated in medium containing ML-7 without covering with mineral oil for 30 min before imaging.

LatrunculinA, an actin polymerization inhibitor (LatA; Tocris, ref 3973) 10mM DMSO stock diluted to 100 and 500 nM in KSOM. 100nM LatA is used for 2-cell stage embryos and they are imaged for 2 hours. Isolated 16-cell-stage blastomeres are incubated in medium containing LatA covered with mineral oil for 15 min before imaging.

C3 transferase, RhoA, B, C inhibitor (Cytoskeleton; Cat # CT04, Lot 117) 100 μ g/ml distilled water stock diluted to 0.75 μ g/ml and 1 μ g/ml in KSOM. Isolated 16-cell-stage blastomeres are incubated in medium containing LatA covered with mineral oil for 30 min before imaging.

2.9. Microinjection

Glass capillaries (Harvard Apparatus glass capillaries with 780 μ m inner diameter) are pulled using a needle puller and micro forged to make “holding pipette” and “injection needle”. The resulting injection needles are filled with mRNA solution. The filled needle is positioned on a micromanipulator (Narishige MMO-4) and connected to a pressure device (Eppendorf FemtoJet 4i). Embryos are placed in FHM drops covered

with mineral oil under Leica TL Led microscope. Single blastomere of 2-cell-stage embryos were injected with the mRNA solution after stabilizing them by creating suction with holding pipette attached connected to a Micropump CellTram Oil and to micromanipulator (Narishige, MMO-4).

3. MRNA PREPARATION

pRN₃-EGFP_{C1}-aPKC λ (K273E) Kinase dead mutant plasmid (Dard et al., 2009) was kindly gifted by Sophie LOUVET-VALLEE. First the plasmid was linearized with Sfi1, by combining 2 μ L Cutsmart buffer (NEB), 1 μ L Sfi1 (NEB) and 2 μ L from plasmid solution in a 20 μ L reaction at 50°C for overnight. This was followed by the purification of the linearized plasmid by using the QIAquick PCR Purification Kit (Qiagen) according to manufacturer's instructions. For the in vitro transcription the mMessage mMachine T3 kit was used. 1 μ L of NTP/CAP Solution, 2 μ L Reaction buffer, 2 μ L T3 Enzyme Mix was combined with 50ng of template DNA and incubated at 37°C for 2hr. This was followed by a 15min TURBO DNase (Ambion) treatment with 1 μ L Enzyme. The RNA was then precipitated and purified by using 30 μ L LiCl and 1ml 50% EtOH. The RNA was then resuspended on 20 μ L water.

4. FLUORESCENT IMMUNOSTAINING

Embryos were fixed in 2% PFA (Euromedex, 2000-C) for 10 min at 37°C, washed in PBS and left in PBS at 4°C till the full collection of the stages were achieved. Once all stages (zygote, 2-cell, 4-cell and 8-cell) are fixed and washed in PBS, they are permeabilized in 0.01% Triton X-100 (Euromedex, T8787) in PBS (PBT) at room temperature before being placed in blocking solution (PBT with 3% BSA) at 4°C for 3 h. Ecad (eBioscience™, rat, 1:500) primary antibody was applied in blocking solution at 4°C overnight. After washes in PBT at room temperature, embryos were incubated with anti-rat 594 (ThermoFisher, 1:200), DAPI (ThermoFisher, 1:1000), and phalloidin-488 (ThermoFisher, 1:500, gifted by Dureen Samandar and Julie Plastino) in blocking solution at room temperature for 1 hr. Embryos were washed in PBT and imaged immediately after.

5. MICROSCOPY

5.1. Zeiss cell discoverer

For live imaging, embryos are placed in 5 cm glass-bottom dishes (MatTek) under a Celldiscoverer 7 (Zeiss) equipped with a 20x/0.95 objective and a ORCA-Flash 4.0 camera (C11440, Hamamatsu) or a 506 axiovert (Zeiss) camera.

Using the experiment designer tool of ZEN (Zeiss), we set up a nested time-lapse in which all embryos are imaged every 5 hours for 10 min long acquisitions with an image taken every 5 s at 2 focal planes positioned 10 μm apart to catch 2-3 time points in each stage from zygote to 8-cell stage. Embryos are kept in a humidified atmosphere supplied with 5% CO₂ at 37°C.

5.2. Zeiss Observer Z1

Live mTmG embryos are imaged at 2-, 4- and 16-cell-stage using an inverted Zeiss Observer Z1 microscope with a CSU-X1 spinning disc unit (Yokogawa). Excitation is achieved using 488 and 561 nm laser lines through a 63x/1.2 C Apo Korr water immersion objective. Emission is collected through 525/50 and 595/50 band pass filters onto an ORCA-Flash 4.0 camera (C11440, Hamamatsu). The microscope is equipped with an incubation chamber to keep the sample at 37°C and supply the atmosphere with 5% CO₂.

5.3. Zeiss LSM900

Immunostained embryos are imaged on Zeiss LSM900 Inverted Laser Scanning Confocal Microscope with Airyscan detector. Excitation is achieved using 488 and 594 nm laser lines through a 63x/1.4 OIL DICII PL APO objective. Emission is collected through 525/50 and 605/70 band pass filters onto an airyscan photomultiplier (PMT). Airyscan module allowing to increase resolution up to a factor 1.7.

5.4. Leica/eppendorf inverted widefield

Leica inverted widefield microscope equipped with Motorized Micromanipulator Eppendorf and a microfluidic pump (Fluigent, MFCS EZ) is used to measure the surface tension of embryos.

6. IMAGE ANALYSIS

6.1. PeCoWaCo analysis

To analyze PeCoWaCo, I used 2 different methods : Particle Image Velocimetry (PIV) and Local Surface Deformation Tracking. Each method allowed me to work with different type of microscopy images and to address different questions.

6.1.1. Particle Image Velocimetry

Using PIVlab 2.02 running on MATLAB (Thielicke & Stamhuis, 2014). Similar to (Maître et al., 2015), time-lapse movies acquired every 5 s are processed using two successive passes through interrogation windows of 20/10 μm resulting in ~ 180 vectors per embryo.

6.1.2. Local surface deformation tracking

To obtain the local curvature of isolated blastomeres, we developed an approach similar to that of (Maître et al., 2015) and (Driscoll et al., 2015). The method used in Maître et al., 2015 was MATLAB based and it was no more working due to updates and changes in Matlab version. Therefore we needed to re-write most of the code. Instead, we wanted this new tool to be freely accessible and more user friendly therefore we made a FIJI plugin. This plugin is coded by Varoon Kapoor, an image analyst in Institut Curie microscopy platform (PICT-BDD).

In order to use this custom made FIJI plugin we first need to get segmentation of the movies. This is done by applying a Gaussian blur to membrane signal images using FIJI (Schindelin et al., 2012) and then, by using Ilastik (Sommer et al., 2011), pixels are associated with cell membrane or with background. Obtained segmentation of cells then put in the plugin for computing the local curvature information using the

start, center and end point of the selected box size (we used 10 μm region) on the cell surface to fit a circle and use the radius of the fitted circle as a measure of the local deformation. All the pixels in the region are assigned the curvature value equal to the inverse of the radius of the fitted circle. The region is then shifted by 1 pixel and a new circle is fitted. The curvature value for the boundary pixels is then averaged. This process is repeated till all the points of the cell are covered. Kymograph of local curvature values around the perimeter over time is produced for further analysis. Details of this pipeline is described in figure 11.

In addition to curvature tracking, this custom made Fiji plugin also offers signal intensity tracking and a second method to track surface deformations by computing the distance of the center of the cell to the boundary points. The Fiji plugin for local curvature analysis “WizardofOz” can be found under the *MTrack* repository.

6.1.3. Fast Fourier Transform (FFT) analysis

The x- and y-velocities of individual vectors from PIV analysis are obtained from PIVlab 2.02 (Thielicke & Stamhuis, 2014). A 2D Fast Fourier Transform (FFT) analysis of x and y directions of the vector velocities over time is performed using MATLAB’s fast Fourier transform function “FFT”. The resulting Fourier transforms are squared to obtain individual power spectra per vector. Then, squared Fourier transforms in the x and y directions of all vectors are averaged for individual embryos resulting in mean power spectra of individual embryos. The peak value between 50 s and 200 s was taken as the amplitude, as this oscillation period range is detectable by our imaging method. An embryo is considered as oscillating when the amplitude peaks 1.85 above background (taken as the mean value of the power spectrum signal of a given embryo). This threshold value was chosen to minimize false-positive and false-negative according to visual verification of time-lapse movies. For example, visual inspection suggest that 3 zygote, 8 2-cell, 0 4-cell, 3 8-cell are false positive, and 0 zygote, 2 2-cell, 1 4-cell, 5 8-cell are false negative. Therefore, the number of oscillating zygote is likely overestimated while the number of oscillating 8-cell stage is underestimated.

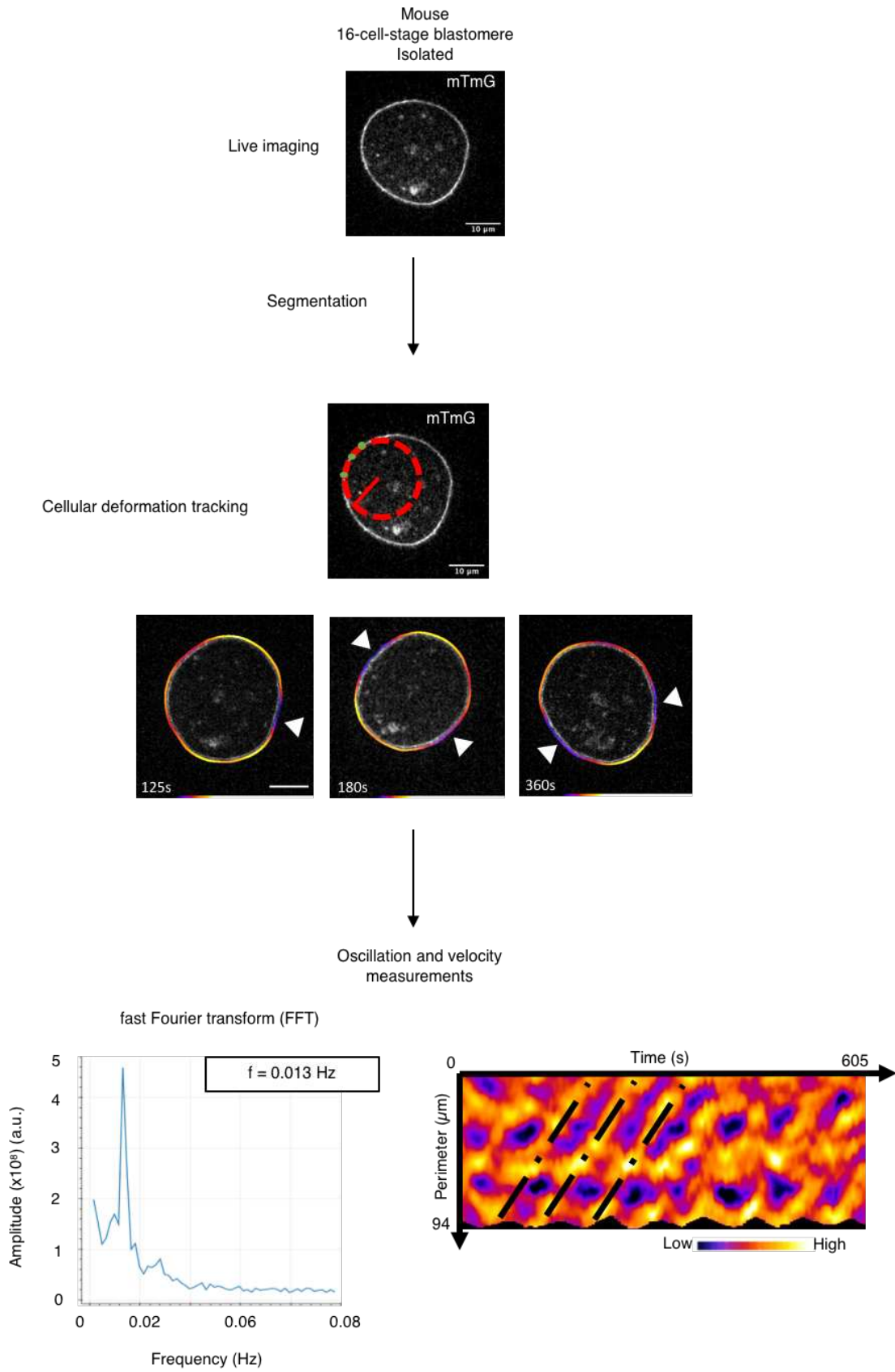


FIGURE 11: LOCAL SURFACE DEFORMATION TRACKING AND PECoWACO ANALYSIS PIPELINE

Curvature kymographs obtained from Local Curvature Tracking are then exported into a custom made Python script for 2D Fast Fourier Transform (FFT) analysis written by Varoon Kapoor (Fig. 11).

Spectra of individual cells and embryos are checked for the presence of a distinct peak to extract the oscillation period. The peak value between 50 s and 300 s was taken as the amplitude, as this oscillation period range is detectable by our imaging method. An embryo is considered as oscillating when the amplitude peaks 1.85 times above background (taken as the mean value of the power spectrum signal of a given embryo) for PIV to determine whether it has a detectable oscillation.

Code availability:

The code used to analyze the oscillation frequencies from PIV and local curvature analyses can be found at github.com/MechaBlasto/PeCoWaCo.git .

6.2. CORTEX THICKNESS

Images obtained from LSM900 airyscan are used to measure cortex thickness. The full width at half maximum (FWHM) of cortex intensity profiles was used to assess cortical thickness by using CortexThicknessAnalysis tool (Chugh et al., 2017; Clark et al., 2013) available on <https://github.com/PaluchLabUCL/CortexThicknessAnalysis> .

7. STATISTICS

Data are plotted using Excel (Microsoft) and R-based SuperPlotsOfData tool (Goedhart, 2021) Mean, standard deviation, median, one-tailed Student's *t*-test, the Fisher exact test, and Chi-squared *p* values are calculated using Excel (Microsoft) or R (<http://www.r-project.org>). Statistical significance is considered when $p < 10^{-2}$.

The sample size was not predetermined and simply results from the repetition of experiments. No sample that survived the experiment, as assessed by the continuation of cell divisions, was excluded. No randomization method was used. The investigators were not blinded during experiments.

RESULTS

1. PECoWaCo THROUGHOUT CLEAVAGE STAGES.¹

PeCoWaCo have been observed and described at the start of the morphogenetic engine at the 8-cell stage and found to be continued at the following 16-cell stage at the 32-cell stage when microlumens formed. However, when and how these oscillations start is unknown. To better understand the machinery behind we first need to understand when and why they start.

¹ This chapter is submitted as “Zygotic contractility awakening during preimplantation development” **Özge Özgüç**, Ludmilla de Plater, Varun Kapoor, Anna Francesca Tortorelli and Jean-Léon Maître. The preprint can be found at the end of the results section.

INITIATION OF PeCoWaCo

To see the initiation of PeCoWaCo, I used a nested timelapse approach. I imaged embryos every 5 s for 10 min to allow me to catch the periodic oscillations as described before (Maître et al., 2015) every 5 hours. This way, I was able to catch the early, middle, and late stages of each cleavage stage. However, imaging the early zygote stage was not feasible as they are fragile for this frequent imaging and stop developing.

I used particle image velocimetry (PIV) analysis (Thielicke & Stamhuis, 2014) followed by fast Fourier transform (FFT) to detect and analyze periodic movements (Movie 4). By looking at embryos at different cleavage stages in a short time scale, I observed that periodic contractions are visible at all the stages, starting from the late zygote. However, the percentage of the embryos showing the oscillations is around ~45 % at the zygote and 2-cell stages. When embryos reach the 4-cell stage, almost all the embryos show PeCoWaCo (85% detection rate), and it stays at high levels at the 8-cell stage as expected. I did not detect a difference in oscillation rate between the first and second half of the stages, indicating that it is not related with the cell cycle. Interestingly, when we look into the period of oscillations, we saw a gradual decrease from 200s to 80s from zygote to 8-cell-stage. The period of oscillations was also the same for the first and second half of each embryonic stage.

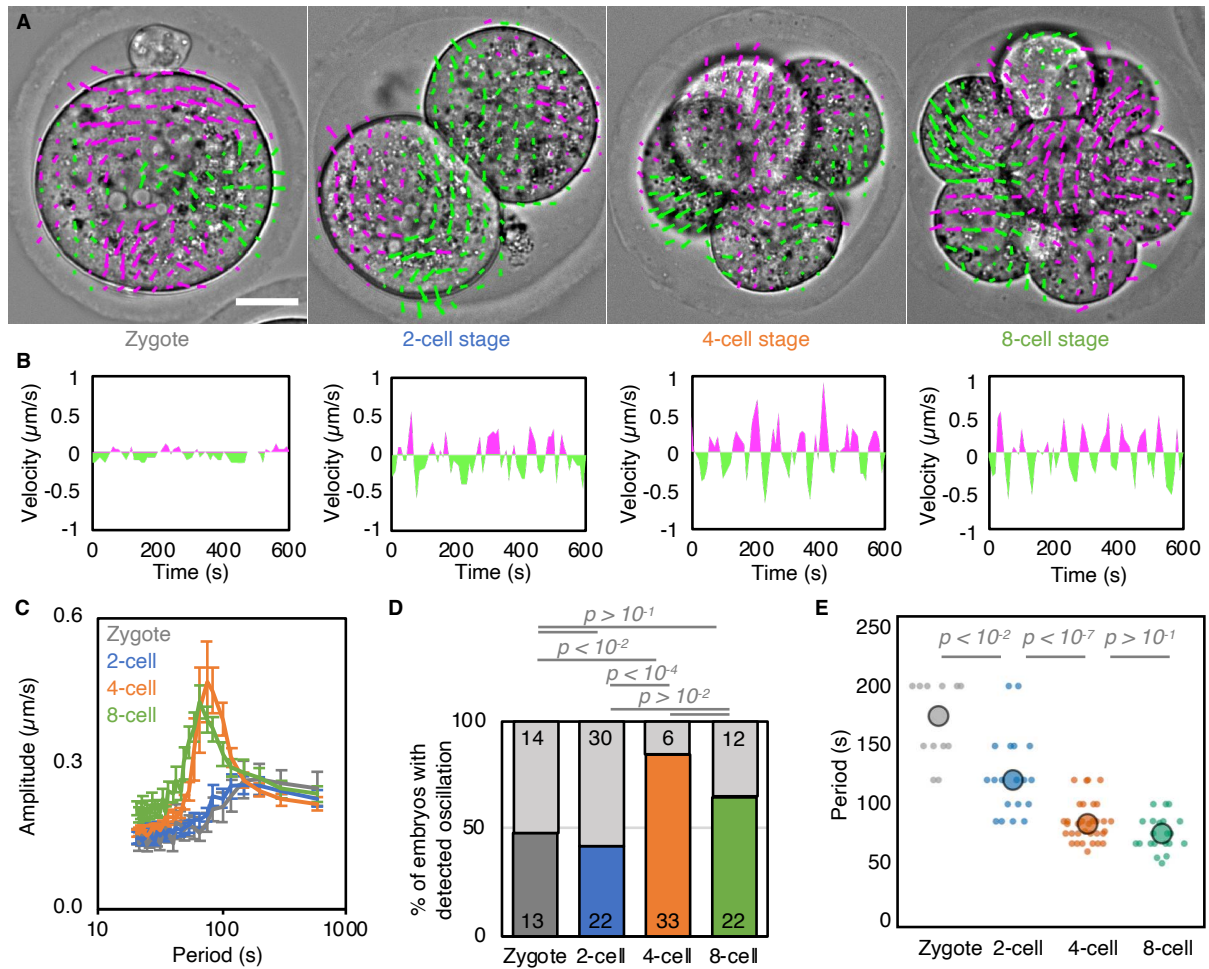


FIGURE 12: ANALYSIS OF PECoWAcO THROUGH CLEAVAGE STAGES

A) Representative images of a short-term time-lapse overlaid with a subset of velocity vectors from Particle Image Velocimetry (PIV) analysis during cleavage stages. Magenta for positive and green for negative Y directed movement. Scale bars, 20 μm .

B) Velocity over time for a representative velocity vector of each embryo shown in A.

C) Mean power spectrum resulting from Fourier transform of PIV analysis of Zygote (grey, $n = 13$), 2-cell (blue, $n = 22$), 4-cell (orange, $n = 33$) and 8-cell (green, $n = 22$) stages embryos showing detectable oscillations. Data show as mean \pm SEM.

D) Proportion of Zygote (grey, $n = 27$), 2-cell (blue, $n = 52$), 4-cell (orange, $n = 39$), 8-cell stage (green, $n = 34$) embryos showing detectable oscillations after Fourier transform of PIV analysis. Light grey shows non-oscillating embryos. Chi2 p values comparing different stages are indicated.

E) Oscillation period of Zygote (grey, $n = 13$), 2-cell (blue, $n = 22$), 4-cell (orange, $n = 33$), 8-cell (green, $n = 22$) stages embryos. Larger circles show median values. Student's t test p values are indicated.

ROLE OF CELL SIZE ON THE RISE OF PeCoWaCo DETECTION

As an embryo develops, cell size halves after each cleavage division. This brings up some questions like: Does cell size play a role in the rise of PeCoWaCo detection? Is there a critical cell size that triggers this increase in the periodic oscillations in the embryos? To answer these questions, I blocked the 2nd cleavage division by using aurora kinase inhibitor, Vx-680 (Harrington et al., 2004), to prevent 2-cell-stage embryos from cleaving and reaching the cell size 4-cell-stage. I started the 3 hours incubation in 2.5 mM Vx-680 when 1-2 embryos from the batch started turning 4-cell-stage, and at the end of 3 hours, all embryos in DMSO control were 4-cell (Fig. 13A). After several washes in the normal culture medium, I let the embryos rest for 1 hour in the incubator before starting to image. As Vx-680 is dissolved in DMSO, I used DMSO with the same dilution as a control condition. This treatment did not prevent them from further developing, and these embryos cleaved when it was time for the 3rd round of cleave. I observed that, even though Vx-680 treated embryos did not cleave and reached the size of 4-cell-stage blastomeres, most of the embryos showed PeCoWaCo (Fig. 13C, Movie 5). Interestingly, the oscillation period in both DMSO and Vx-680 treated embryos was the same (Fig. 13D). These results showed that 4-cell stage blastomere size is not required to initiate PeCoWaCo in the majority of embryos.

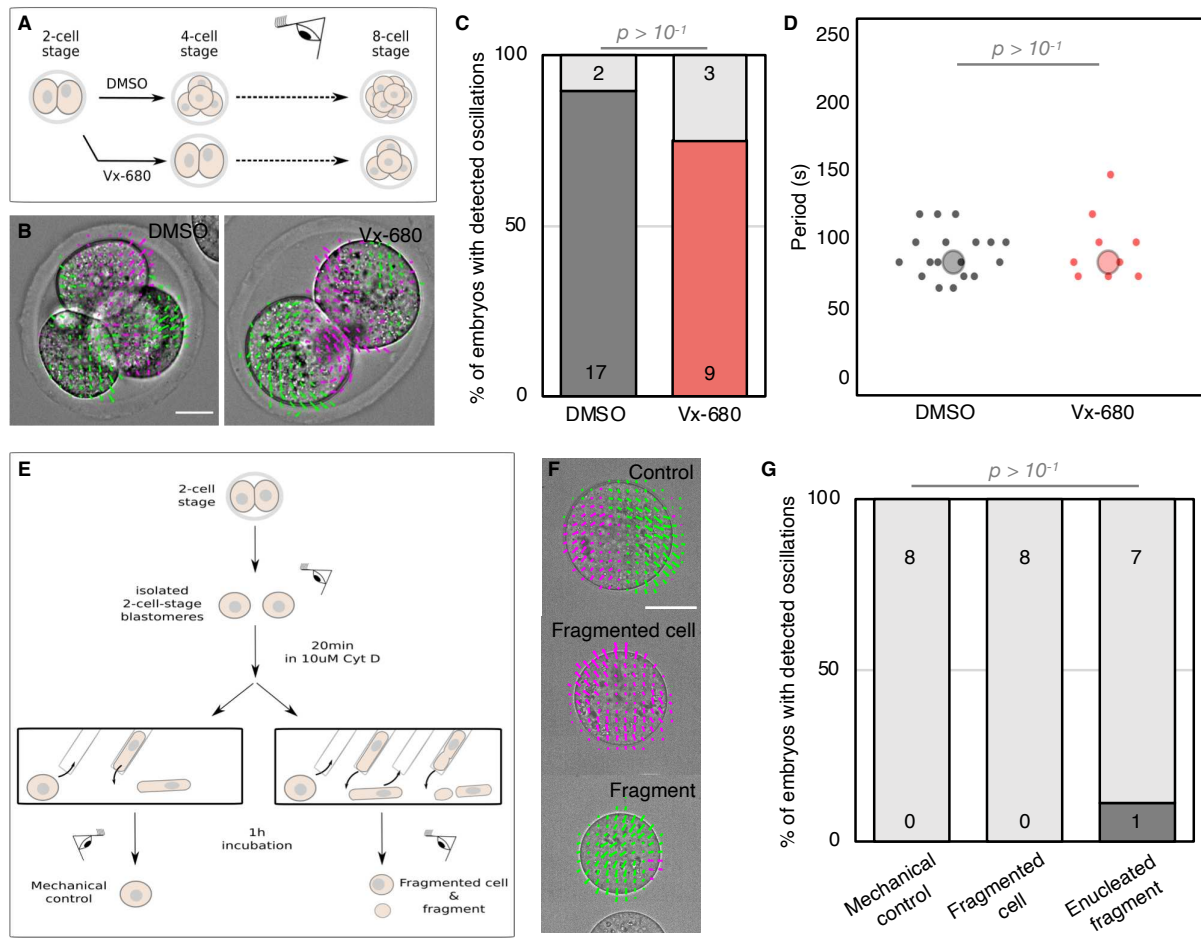


FIGURE 13: CELL SIZE IS NOT REQUIRED OR SUFFICIENT FOR PeCoWaCo

A) Schematic diagram of PeCoWaCo analysis after blocking the 2nd cleavage division with 2.5 μ M Vx680. **B)** Representative images of DMSO and Vx-680 treated embryos overlaid with a subset of velocity vectors from Particle Image Velocimetry (PIV) analysis. **C-D)** Proportion (C) of embryos showing detectable oscillations and their detected period (D, DMSO n = 19 and Vx-680 n = 12). Chi² (C) and Student's *t* test (D) *p* values comparing two conditions are indicated. Larger circles show median values. **E)** Schematic diagram of PeCoWaCo analysis after fragmentation of 2-cell stage blastomeres. **F)** Representative images of mechanical control, fragmented cell and enucleated fragments overlaid with a subset of velocity vectors from PIV analysis. **G)** Proportion of cells showing detectable oscillations in mechanical controls (n = 8), fragmented cells (n= 8) and enucleated fragments (n=9). The Fisher exact test *p* values comparing different conditions are indicated. Light grey shows non-oscillating embryos.

After seeing that reaching 4-cell-stage size is not required, I wanted to test whether PeCoWaCo could be triggered at 2-cell stage embryos by simply reducing blastomere size to a 4-cell stage size. For this, I dissociated 2-cell stage blastomeres and fragmented them with the help of the actin cytoskeleton inhibitor Cytochalasin D (CytD) (Korotkevich et al., 2017) and 30 mm size smooth glass capillaries (Fig. 13E). Aspiration into these small glass capillaries gave the blastomeres a sausage-like shape. When aspirated 1-2 times more, cells formed an artificial cleavage furrow like side causing the membranes of the two sides to fuse, resulting in fragmentation of the blastomeres into two, one with nucleus we called “fragmented cell” and the other part that is without nucleus is called “enucleated fragment”. After fragmentation, both control, fragmented cell, and the enucleated fragment is washed in the normal culture medium and left in the incubator to rebuild their cortex for one hour before looking for the presence of PeCoWaCo (Fig. 13F). While the fragmentation reduced the size of the 2-cell stage blastomeres to a 4-cell stage blastomere, it did not initiate PeCoWaCo (Fig. 13G, Movie 6). Eventually, both fragmented cells and the controls divided to the 4-cell stage, whereas enucleated fragments did not divide as expected. This suggests that the 4-cell stage blastomere size is not sufficient to trigger PeCoWaCo in the embryos.

Another important change occurring around the time of appearance of PeCoWaCo in the majority of the embryos is zygotic genome activation (ZGA) (Hamatani et al., 2004). To investigate the role of ZGA in the initiation of PeCoWaCo during the 2- to 4-cell stage transition, I blocked the major ZGA by treating 2-cell stage embryos with the inhibitor of Pol II-mediated transcription DRB (Fig. 14A) (Abe et al., 2018). To control whether ZGA is effectively blocked or not, I used embryos that express fluorescent membrane marker mTmG from a paternal allele. This signal becomes visible at the end of the 2-cell stage as paternal mTmG expression starts after the zygotic genome is activated (Fig. 14B). I started treating with DRB (and DMSO as control) at the early or late 2-cell stage. I observed that DRB treatment prevents the 2- to 4-cell stage divisions when the treatment is applied from the early 2-cell stage as expected due to the 2-cell blockage. Paternal mTmG expression is detected in embryos treated with DMSO and in embryos treated with DRB in the late 2-cell stage. This indicates that ZGA is impacted only by early 2-cell stage DRB treatment (Fig. 14C&E). When looking into PeCoWaCo, I found that treating embryos with DRB starting from the early 2-cell stage prevents their appearance when reaching the time of the 4-cell stage specifically. In contrast, it does not prevent when they are treated from the late 2-cell stage (Fig. 14D&F, Movie 7). Therefore, ZGA is required for triggering periodic contractions during preimplantation development.

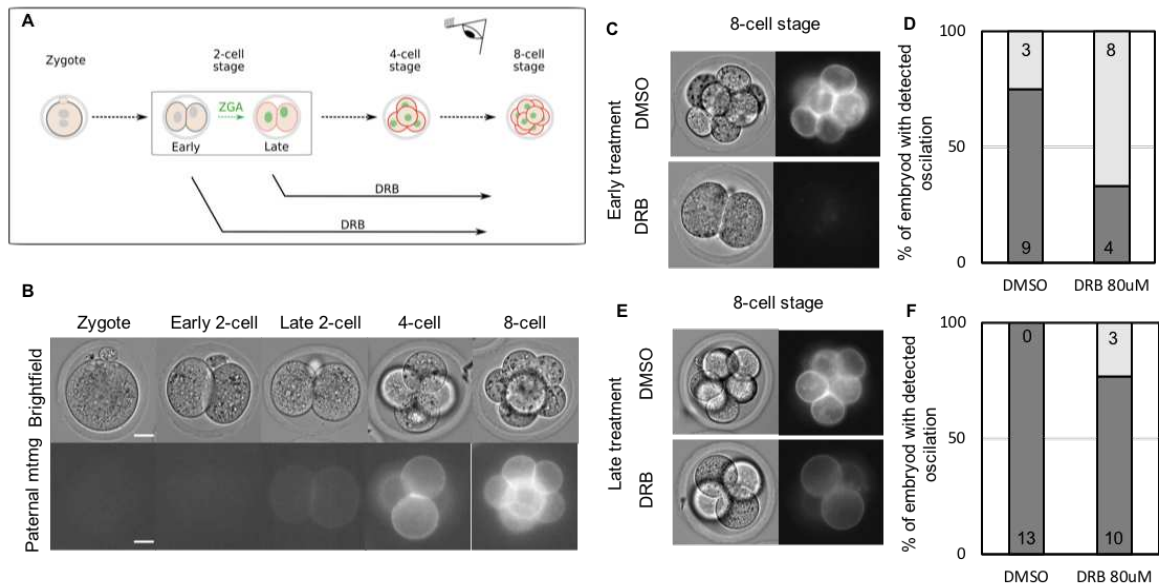


FIGURE 14: ZGA PLAYS AN IMPORTANT ROLE ON THE RISE OF PeCoWaCo DETECTION

A) Schematic diagram of PeCoWaCo analysis after blocking ZGA with DRB. **B)** Representative images of embryos expressing mTmG from their paternal allele through cleavage stages. LUT is adjusted to 8-cell stage. **C&E)** Representative images of embryos treated from early 2-cell stage (C) and from late2-cell stage (E) expressing mTmG from their paternal allele at the end of the nested timelapse imaging. LUT is adjusted to 8-cell stage DMSO. **D&F)** Proportion of embryos treated from early 2-cell stage (D) with DMSO (N = 12) and with DRB (N= 12) showing detectable oscillations and from late2-cell stage (F) with DMSO (N=13) and with DRB (N= 13) showing detectable oscillation.

CHANGES IN ACTOMYOSIN CORTEX THROUGH CLEAVAGE STAGES

To better understand how ZGA can play a role in the initiation of PeCoWaCo, we looked into the changes occurring in the actomyosin cortex over the cleavage stages. Although contractility is a major engine powering preimplantation morphogenesis, since no morphogenesis occurs before the 8-cell stage, contractility during the cleavage stages has been overlooked. To investigate this, Ludmilla De Plater, who is an engineer in our lab, measured the surface tension of cells with micropipette aspiration as a readout of contractility during cleavage stages (Fig. 15A). Mapping the surface tension through cleavage stages showed that surface tension gradually decreases from the zygote to the 8-cell stage (Fig. 15B). The surface tension levels noticeably mirror the ones of the period of PeCoWaCo during cleavage stages (Fig. 1E). Changes in cell surface tension can be accompanied by remodeling of the actomyosin cortex of the cell, which can be investigated by measuring the thickness of the cortex (Chugh et al., 2017). I measured cortex thickness across cleavage stages using Airyscan microscopy and full width at half maximum (FWHM) measurements to evaluate whether the actomyosin cortex thickness accompanies the change in surface tension. I found that cortical thickness does not vary during cleavage stages, at least to the point of resolution that I can obtain from airyscan microscopy, which is 170 nm (Fig. 15C). This suggests that despite its change in behavior and mechanical property, the cortex may not undergo major structural rearrangements that change its thickness during cleavage stages.

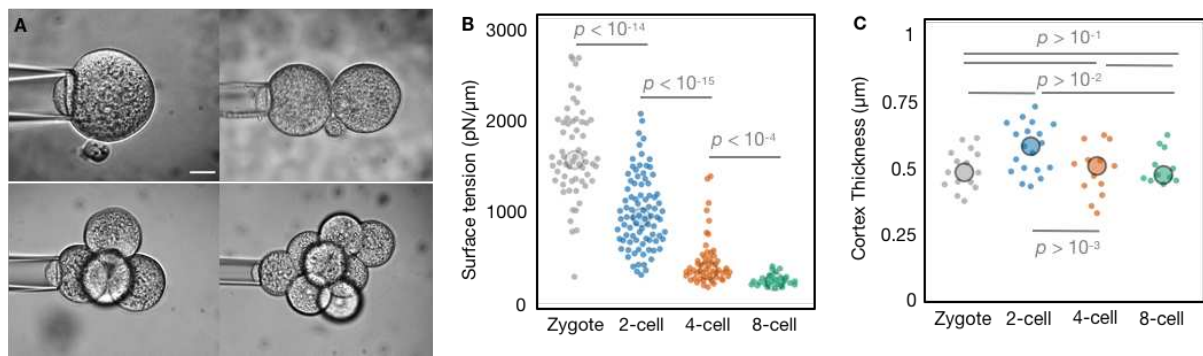


FIGURE 15: ACTOMYOSIN CORTEX MECHANICS THROUGH CLEAVAGE STAGES

A) Representative images of the tension mapping method. **B)** Surface tension of blastomeres throughout cleavage stages. Zygote (gray, $n = 60$), 2-cell (blue, $n = 86$), 4-cell (orange, $n = 55$), early 8-cell (green, $n = 28$) stages are shown. **C)** Cortex thickness of embryos throughout cleavage stages. Each point is averaged cortex thickness of blastomeres of an embryo. Zygote (gray, $n = 15$), 2-cell (blue, $n = 34$), 4-cell (orange, $n = 23$), early 8-cell (green, $n = 11$). Larger circles show median values. Student's t test p value comparing the conditions are indicated

We hypothesized that the tension of blastomeres at the zygote and 2-cell stages might be too high for PeCoWaCo to become visible. To reduce the tension of the cortex, I used a low concentration of the actin polymerization inhibitor Latrunculin A (LatA). Softening the cortex of 2-cell stage embryos with 100nM LatA increased the proportions of embryos displaying PeCoWaCo (Fig. 16B). Moreover, LatA treated embryos showed decreased oscillation period of PeCoWaCo compared to controls (Fig. 16C). This suggests that PeCoWaCo become more visible thanks to the gradual softening of the cortex of blastomeres during cleavage stages. Moreover, the polymerization rate of the actin filaments could be responsible for the decrease in the PeCoWaCo period observed during cleavage stages.

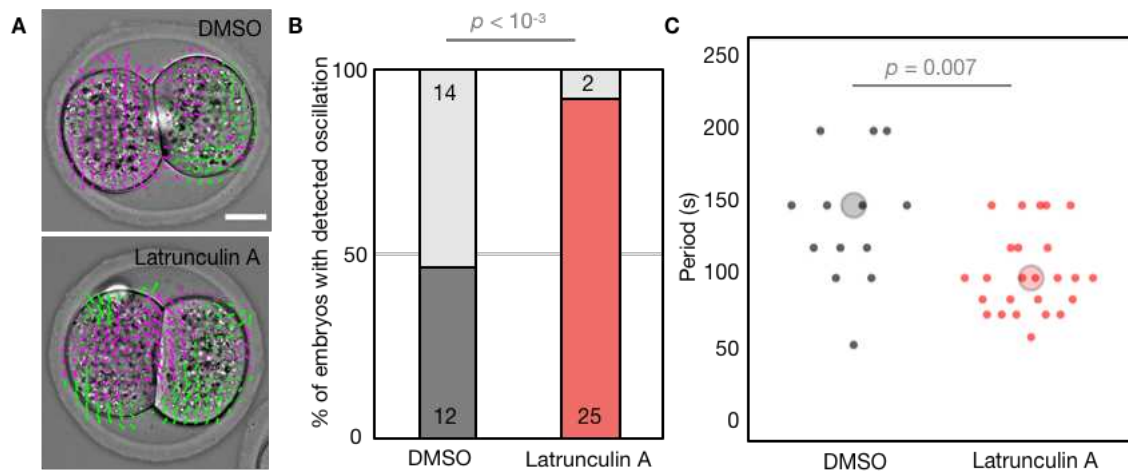


FIGURE 16: ROLE OF ACTOMYOSIN MECHANICS ON PeCoWaco DETECTION AND SCALING OF THE PERIOD

A) Representative images of Control and 100nM Latrunculin A treated embryos overlaid with a subset of velocity vectors from Particle Image Velocimetry (PIV) analysis **B-C)** Proportion (B) of embryos showing detectable oscillations and their detected period (C) of DMSO treated ($n = 26$) and 100 nM Latrunculin A treated ($n = 27$) 2-cell stage embryos. Chi² and Student's *t* test *p* value comparing two conditions is indicated. Light grey shows non-oscillating embryos. Larger circles show median values.

2. REGULATION OF PeCoWaCo

Unlike other model organisms typically used to study animal morphogenesis, the mouse embryo develops slowly. However, actomyosin keeps beating with the same tempo in the mouse as it does in fast-developing organisms. We take advantage of the slow development of the mouse embryo to study thousands of pulsed contractions and the robustness of the mouse embryo to size manipulation to explore the regulation of PeCoWaCo and fine-tuning mechanisms.

Investigating how PeCoWaCo initiate and mature over the preimplantation development revealed that the period of PeCoWaCo is decreased through development. This decrease nicely mirrors the decreasing cell size and the decreasing surface tension from zygote to early 8-cell stage. It has been previously shown that removing Myosin or Actin filaments from the system with high doses of chemical treatments such as Blebbistatin and Cytochalasin D (CytD) stop the PeCoWaCo, whereas removing cell-cell adhesion with E-cad mutants does not have any effect (Maître et al., 2015). However, what regulates and fine-tunes the period and the velocity of PeCoWaCo remains unknown. Here, I investigated geometrical and molecular regulators of PeCoWaCo, to understand the regulation of PeCoWaCo better.

2.1. GEOMETRICAL REGULATION

After three rounds of cleavage division, with the start of the morphogenesis, cells of a compacting embryo lose their sphericity and flatten towards their neighbors, increasing their cell-cell contact with their neighbors, giving them a more cubic-like shape. However, cadherin knockout embryos showed that PeCoWaCo are not affected by cellular adhesion decrease (Maître et al., 2015). Similarly, with polarization, when cells form an apical domain taking up a large portion of the cell surface the oscillation period does not seem to be different from cells in which the wave can propagate on the entire cell surface (Maître et al., 2016). This raises the question of how robust PeCoWaCo are to geometrical parameters?

CELL SIZE DOES NOT INFLUENCE THE PROPERTIES OF PeCoWaCo²

We have seen that the cell size is neither required nor sufficient to initiate PeCoWaCo. Nevertheless, the decrease in the period of PeCoWaCo over development remarkably mirrors the decrease in blastomere size (Fig. 12E). Suppose PeCoWaCo travel around the cell at a constant velocity at each of these stages. In that case, this could be the reason behind the reduced period according to the reduced distance to travel around cells. To investigate this, I manipulated the blastomere size at the specific embryonic stage, at the 16-cell-stage, to eliminate changes that might come from changing developmental stages like surface tension. To do this, I fused varying numbers of 16-cell stage blastomeres and reached to cell size equivalent to 8-, 4- and 2-cell stages (Fig. 17A). In addition, I fragmented 16-cell stage blastomeres and made smaller cells equivalent to 32-cell stage blastomeres (Fig. 17A). Together, I could image 16-cell stage blastomeres with sizes ranging from 10 to 30 μm in radius (Fig. 17B-C, Movie 8-9). To investigate how PeCoWaCo may scale with cell size, I used local curvature tracking analysis, allowing for tracking and measuring wave velocity in addition to its period. Analysis of this range of cell sizes that has the same embryonic stage, I observed that fused and fragmented 16-cell stage blastomeres show the same period, regardless of their size (Fig. 17D). Interestingly, the wave velocity also remains constant regardless of cell size (Fig. 17E). Together, using fusion and fragmentation of cells, we find that PeCoWaCo oscillation properties are robust to a large range of size perturbations. Fusion of cells at the 16-cell stage implies that blastomeres with and without apical domains are merged. The apical domain is known to influence the amplitude of contractile waves (Maître et al., 2016). Therefore, apical signals may also influence the period and velocity of PeCoWaCo. I will address this in the molecular regulation of PeCoWaCo section

² This section is included in the manuscript submitted as “Zygotic contractility awakening during preimplantation development” **Özge Özgüç**, Ludmilla de Plater, Varun Kapoor, Anna Francesca Tortorelli and Jean-Léon Maître. The preprint can be found at the end of the results section.

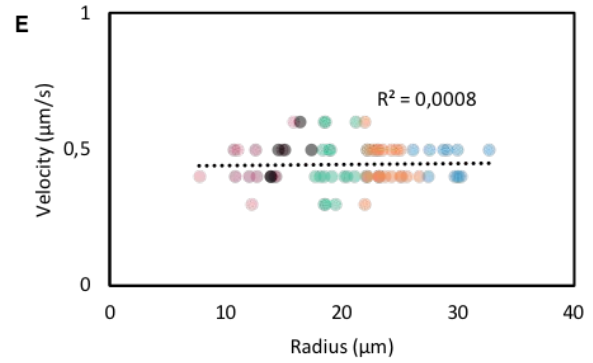
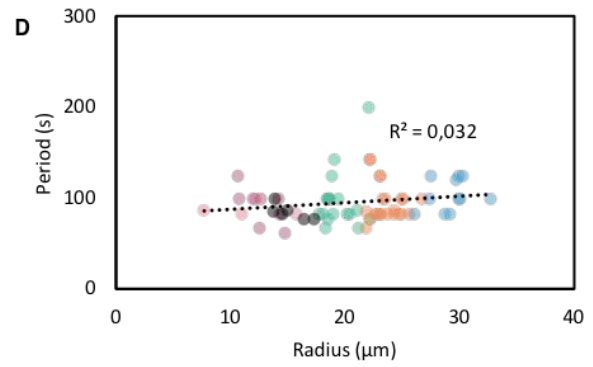
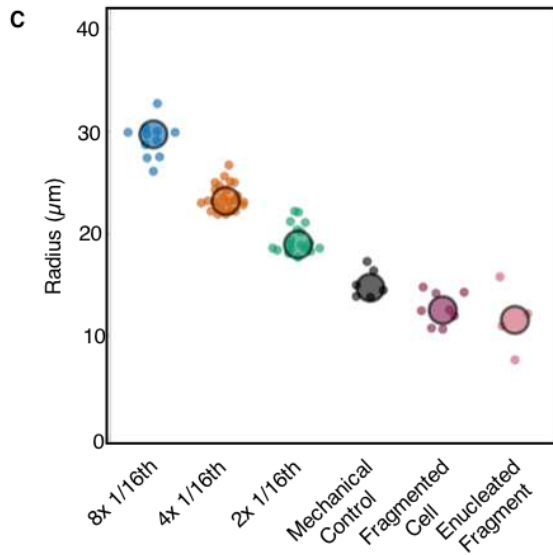
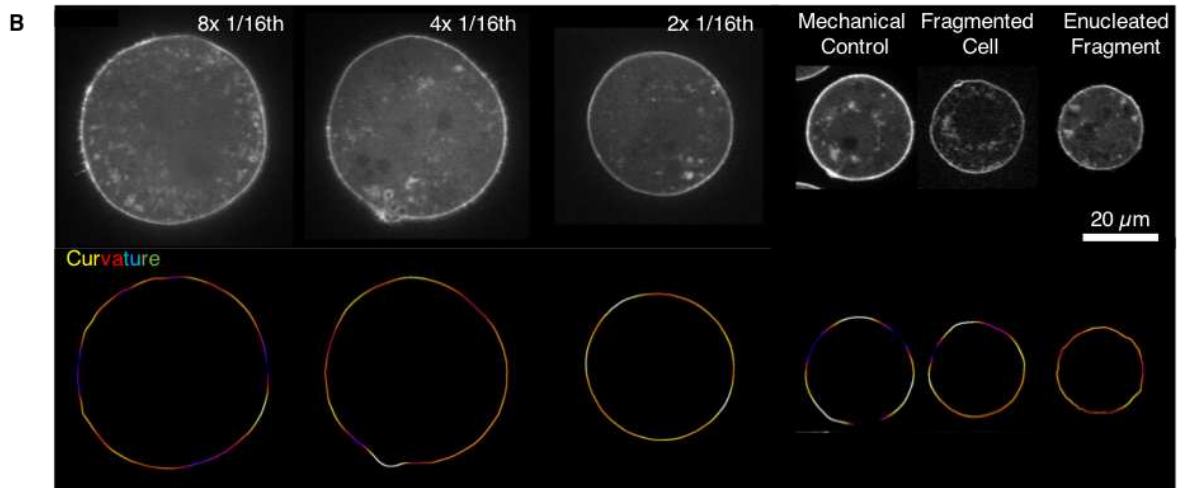
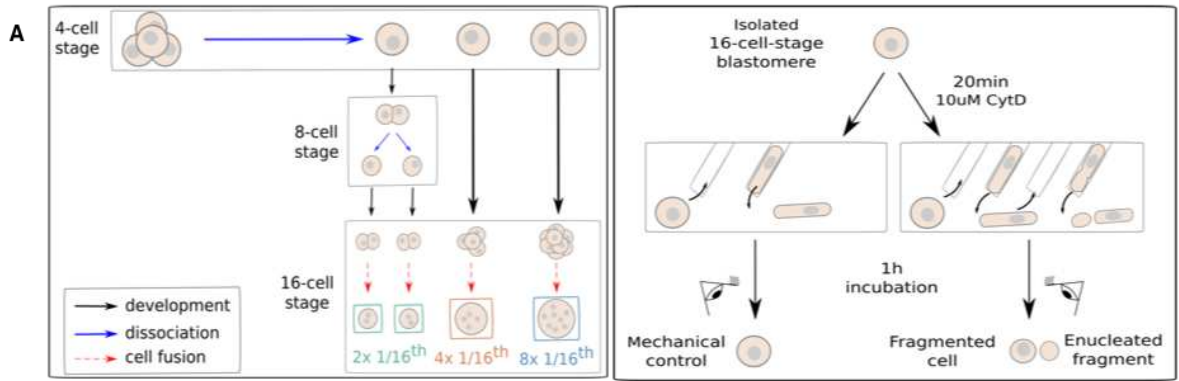


FIGURE 17: PERIOD AND VELOCITY OF PeCoWaCo ARE STABLE ACROSS A BROAD RANGE OF CELL SIZES.

A) Schematic diagram of fusion and fragmentation of 16-cell stage blastomeres.

B) Montage of mTmG (top) and local curvature measurements (bottom) of fused 8x, 4x, 2x 1/16th blastomeres and of mechanically manipulated and fragmented 2-cell stage blastomeres with and without nucleus 1/16th blastomeres showing PeCoWaCo. Scale bar, 20 μm .

C) Radius of different cell sizes obtained from fusing and fragmenting 16-cell stage blastomeres are shown. 8 x 1/16th (blue, n=6), 4 x 1/16th (orange, n = 12) and 2 x 1/16th (green, n=7) fused blastomeres, Control (black, n = 6), fragmented cell (magenta, n= 8), enucleated fragment (pink, n=4). Larger circles show median values. **D-E)** Oscillation period (D) and wave velocity (E) of PeCoWaCo over the range of radius obtained by fused and fragmented blastomeres. 8 x 1/16th (blue, n=6), 4 x 1/16th (orange, n = 12) and 2 x 1/16th (green, n=7) fused blastomeres, Control (black, n = 6), fragmented cell (magenta, n= 8), enucleated fragment (pink, n=4) are shown. Large circles show median.

CONSTRICTION OF THE AREA DOES NOT CHANGE THE PERIOD OF THE OSCILLATIONS

Although they affect the cell shape drastically, cleavage divisions are not the only shape-changing events that the blastomere of a preimplantation embryo undergoes. During compaction, for example, angles between contacting cells increase from $\sim 5^\circ$ to $\sim 150^\circ$ as blastomeres are pulled into closer contact, leaving a progressively smaller region for PeCoWaCo to be observed. To investigate the effect of cell shape changes occurring during compaction on the regulation of PeCoWaCo, I imaged at 8-cell stage embryos at different compaction levels and analyzed PeCoWaCo by using PIV analysis. By looking at 8-cell stages embryos at different compaction levels ranging between $55 - 160^\circ$ average contact angle, I observed that compaction level does not affect the oscillation period (Fig. 18A). Although it seems to affect the amplitude of the oscillations (Fig. 18B), it is hard to decipher if it is due to compaction or because PIV cannot detect the movements in the compacted embryo as nicely as in not compacted embryo.

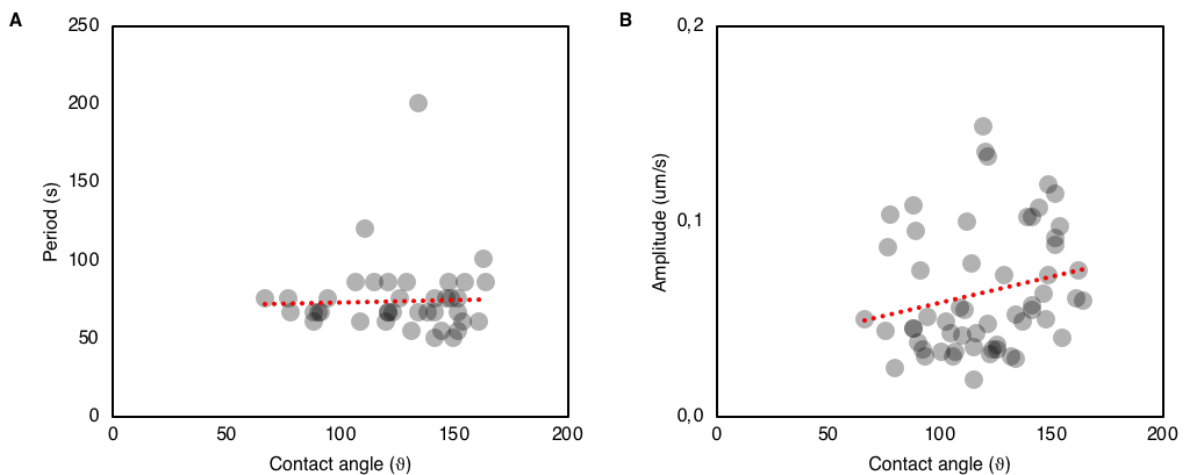


FIGURE 18 : PECoWACO PERIOD IS NOT AFFECTED FROM COMPACTION OF THE EMBRYO
A-B) Oscillation period (A) and amplitude (B) of PeCoWaCo obtained from PIV analysis over the contact angle of 8-cell stage embryos. N = 57. Red dotted line shows the trend line.

Compaction occurs over timescale of ~ 10 h (Maître et al., 2015; Zhu et al., 2017). Considering the time scale of PeCoWaCo, compaction process might be slow enough to adjust to the gradually restriction of the free area. To investigate a faster response of PeCoWaCo in detail, I used Ca²⁺ free medium and did local curvature tracking analysis (Fig. 19A). As cell-cell adhesion requires Ca²⁺ ions, when the calcium is removed from the system cell-cell contact area is decreasing. This treatment is reversible, the medium is replaced back to normal culture medium, cell-cell contacts are restored in ~ 30 min. Therefore, with this chemical treatment we can recreate compaction in much shorter time than it naturally occurs allowing us to investigate the effect of area restriction on PeCoWaCo on much shorter time scale. To be able to investigate PeCoWaCo in detail with local curvature tracking analysis I used 16-cell stage doublets instead of intact embryos due to limitations in image segmentation at embryo level. To affect cell-cell contact size, doublets are placed in Ca²⁺ free medium for 5-8min followed by washes in normal culture medium. I imaged Ca²⁺ free medium treated embryos right after the washes and after 1h of recovery. I observed that restriction of the area did not affect the oscillation period (Fig. 19B) whereas the amplitude and the velocity of the oscillations are decreased together with the decreasing free area (Fig. 19C-D).

We know that in addition to reducing the free surface area, cell-cell contacts also downregulate contractions as the cell-cell adhesion molecule E-cadherin (or Cdh1) signals to reduce contractility locally at contacts between cells (Maître et al., 2012) as well as globally (Padmanabhan 2017). This could explain the reduction of the oscillation amplitude in the doublets. It is not the case for endogenous difference, this could be explained by the global increase in actomyosin contractility at this stage (Maître et al., 2015).

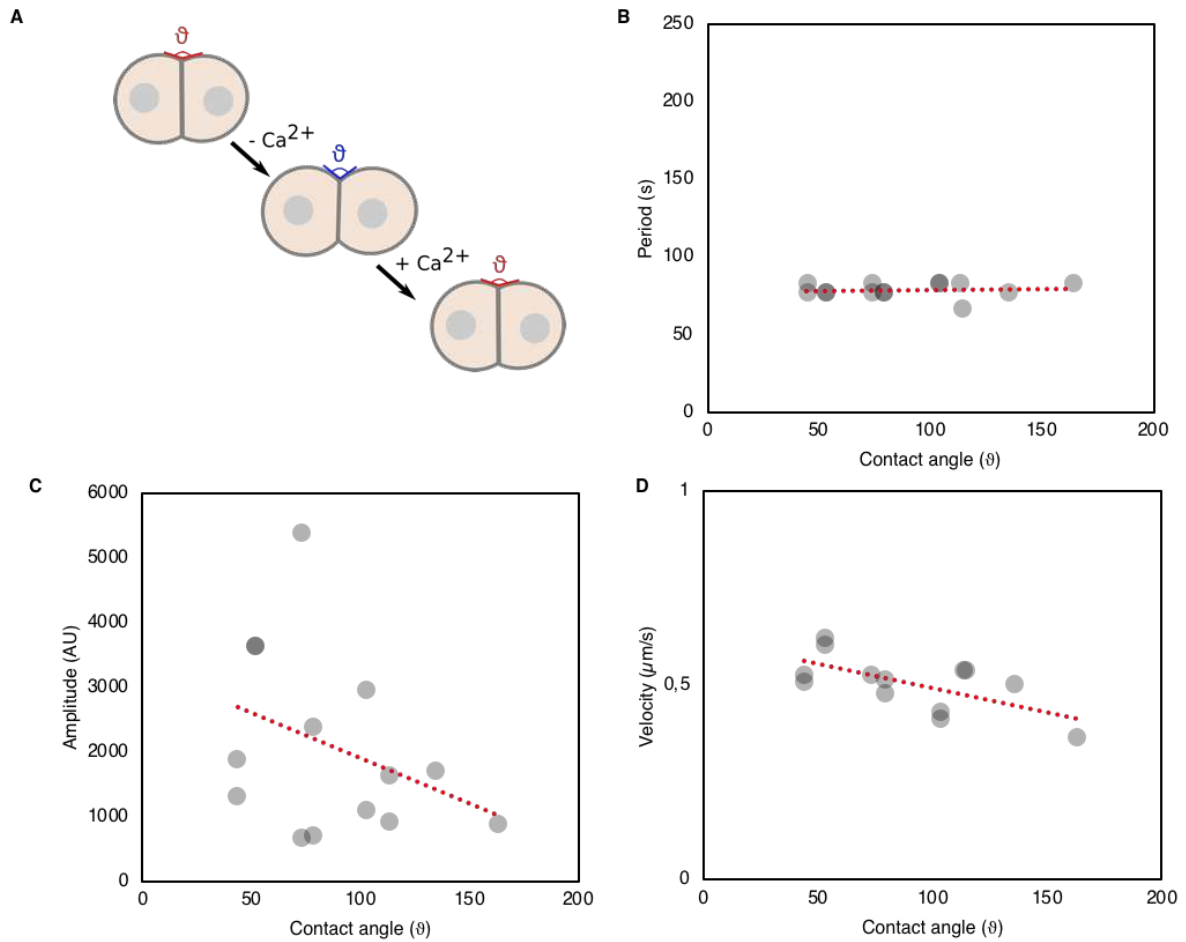


FIGURE 19: RAPID CHANGES IN CONTACT ANGLE AFFECTS PECoWAcO.

A) Schematic diagram of changing the compaction level of 16-cell-stage doublets with removing and adding Ca^{2+} from the culture medium. **B-D)** Oscillation period (B), amplitude (C), and velocity (D) of single cells over the changing contact angle of the doublets. N doublet= 5, N single cell = 10. Red dotted line shows the trend line.

MECHANICAL STRESS REDUCES WAVE VELOCITY

To test whether PeCoWaCo are affected by mechanical stress and change in sphericity, I stretched a portion of the cell surface using micropipette aspiration. After observing PeCoWaCo of a given cell, I first determined the critical pressure above which cells flow inside small micropipette (ranging between 5-50 Pa in this case). Then, I applied an additional 20 Pa to create a large deformation (ranging between 10-25 μm in length), before setting the pressure back to the critical pressure to observe PeCoWaCo in that controlled stressed configuration (Fig. 20A). I find that microaspiration does not affect the oscillation period of pulsed contractions in the aspirated or in the free part of the cell (Fig. 20B, Movie 10). However, the propagation velocity of the contractile waves are noticeably slowed down in a majority of the aspirated cells (Fig. 20C). This effect does not seem to depend on the aspiration pressure or length of the deformation.

By aspiration, we put mechanical stress onto the cells. This result shows us that, oscillation period is not affected by the additional stress whereas mechanical stress can affect the propagation of pulsed contractions, which is compatible with previous observations in other species (Goehring et al., 2011; Munjal et al., 2015; Munro et al., 2004).

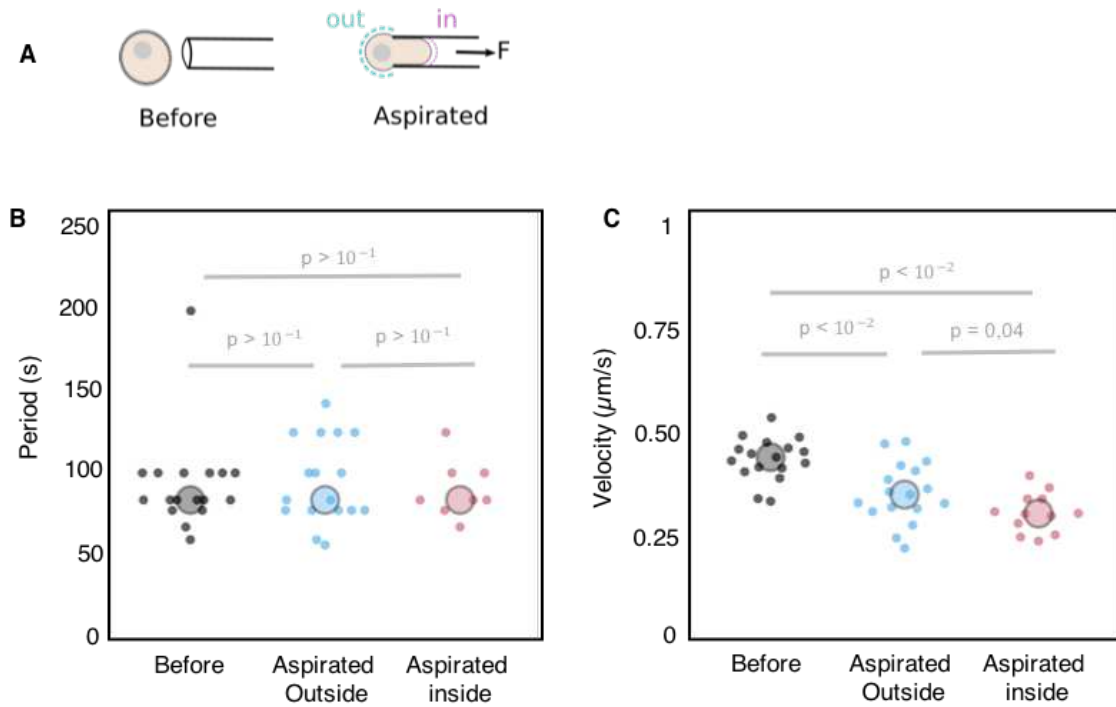


FIGURE 20: MECHANICAL STRESS CHANGES THE VELOCITY OF PeCoWaco

A) Schematic diagram of micropipette aspiration. **B-C)** Oscillation period (B), and velocity (C) of isolated 16-cell-stage blastomeres (N= 24) before (black) and during the aspiration (outside in blue, inside in pink). Student's t test p values comparing the conditions are indicated. Larger circles show median values.

2.2. MOLECULAR REGULATION

As we showed at the initiation of PeCoWaCo section, surface tension of developing mouse embryo drops from $\sim 1500 \text{ pN}/\mu\text{m}$ to $\sim 400 \text{ pN}/\mu\text{m}$ over cleavage stages from zygote to 8-cell-stage. This drop in the levels of surface tension noticeably mirrors the ones of the period of PeCoWaCo during cleavage stages. Moreover, in the geometrical regulation section we showed that period of PeCoWaCo is not affected from changing cell size and shape. On the other hand, wave velocity is reduced with increasing mechanical stress.

To better understand the regulatory machinery of PeCoWaCo, we wanted to dissect the molecular regulation of it. Preimplantation mouse embryo contains maternally deposited mRNA and proteins. Therefore one requires to specially target those mRNA and/or the protein of interest instead of their encoding genes to understand their role otherwise the essential functions of those genes during preimplantation morphogenesis remains hidden. To dissect the molecular regulation of PeCoWaCo, we first wanted to use RNAi technique by using siRNAs targeting the mRNAs of actomyosin cortex regulators. However, although many people in our lab tried the published siRNAs, we could not make this technique work and obtained published phenotypes. Therefore, I focused my investigation on using chemical inhibitors in addition to other genetic tools such as maternal zygotic mutants and mRNA injection of dominant negative form of a protein of interest. In order to quantitatively dissect the molecular regulation of PeCoWaCo we needed to affect PeCoWaCo without killing them completely so that they remain detectable. Therefore, I used titrated concentrations of inhibitors.

ROLE OF MYOSIN-II MOTOR³

To understand the molecular regulation of PeCoWaCo, we started the investigation from the non-muscle myosin-II motors that drive contractility of the actin meshwork, generating forces at different length scales that enable fast remodeling of the cell surface. Non-muscle myosin II complexes assemble from myosin regulatory light chains, myosin essential light chains (MLCs), and non-muscle myosin heavy chains (NMHCs) (Vicente-manzanares et al., 2010). The phosphorylation of MLCs by Myosin light chain kinase (MLCK) turns on the non-muscle Myosin-II motor, promoting the assembly of filaments and increasing ATPase activity (Vicente-manzanares et al., 2010). NMHCs, on the other hand, are responsible for generating the power stroke.

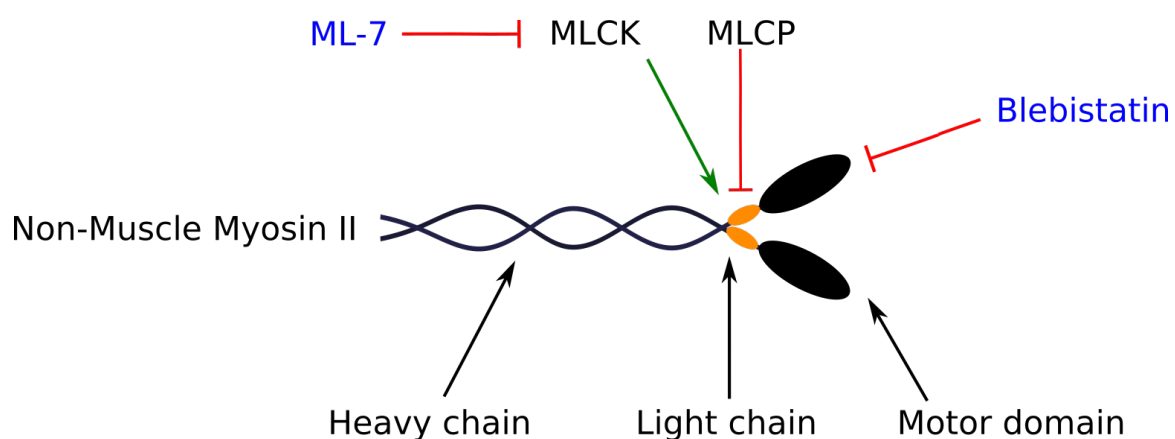


FIGURE 21: NON-MUSCLE MYOSIN II MOTOR STRUCTURE AND REGULATORS OF ITS ACTIVITY

To investigate the role of myosin-II motor in regulation of PeCoWaCo, we have used maternal zygotic mutants of NMHCs (Myh9 and Myh10) and chemical inhibition of its motor activity by using Blebbistatin to block its binding to actin filaments and ML-7 to inhibit its activation via myosin light chain kinase (MLCK).

³ First part of this section is included in the publication “Multiscale analysis of single and double maternal-zygotic Myh9 and Myh10 mutants during mouse preimplantation development”, eLife (2021), Markus Frederik Schliffka, Anna Francesca Tortorelli, **Özge Özgüç**, Ludmilla de Plater, Oliver Polzer, Diane Pelzer, Jean-Léon Maître, published manuscript can be found at the end of the results section.

Actomyosin contractility relies on the action of several subunits of non-muscle myosin II, which come in distinct isoforms. To identify their specific roles, we have generated single and double maternal zygotic knockouts of *Myh9* and *Myh10*. We carefully analyzed single and double maternal-zygotic *Myh9* and *Myh10* mutants at multiscale during mouse preimplantation development (Schliffka et al., 2021).

By using Particle Image Velocimetry (PIV) (Thielicke & Stamhuis, 2014), we found that the knockout of both *Myh9* and *Myh10* isomers separately reduces the detection rate of PeCoWaCo (Fig. 22A) and when both isomers are knocked-out, we did not observe PeCoWaCo on any of the embryos we imaged. Moreover, *Myh9* mutants (only zygotic or both maternal and zygotic) showed more severe reduction in PeCoWaCo detection rate compared to *Myh10* mutants and when both isoforms are mutated, PeCoWaCo are not detectable (Fig. 22A, Movie 11). When we looked in detail to characteristic of PeCoWaCo observed in single mutants, We found that the oscillation period was not affected in *Myh10*^{+/-}, *Myh10*^{+/+} and *Myh9*^{+/-} whereas it was increased in *Myh9*^{+/-} (Fig. 22B). On the other hand, the amplitude of the oscillations was impaired in both isoform mutants gradually where both mutants showed smaller amplitude than wildtype embryos and *Myh9* mutants showed even smaller amplitudes than *Myh10* mutants (Fig. 22C). Although our sample size for oscillating *Myh9* mutants was quite low for statistical analysis, in general the analysis of maternal zygotic mutants suggest that PeCoWaCo in mouse blastomeres result primarily from the action of the non-muscle myosin heavy chain IIA (coded by *Myh9*) rather than IIB (encoded by *Myh10*). In addition to PeCoWaCo, other contractility driven processes were also found impacted. All together these results reveal that actomyosin contractility in preimplantation mouse embryos is primarily mediated by maternal MYH9, which is found most abundantly. Comparatively, loss of *Myh10* has a mild impact on preimplantation development. Nevertheless, double maternal-zygotic mutants reveal that in the absence of MYH9, MYH10 plays a critical role in ensuring sufficient contractility to power cleavage divisions (Schliffka et al., 2021).

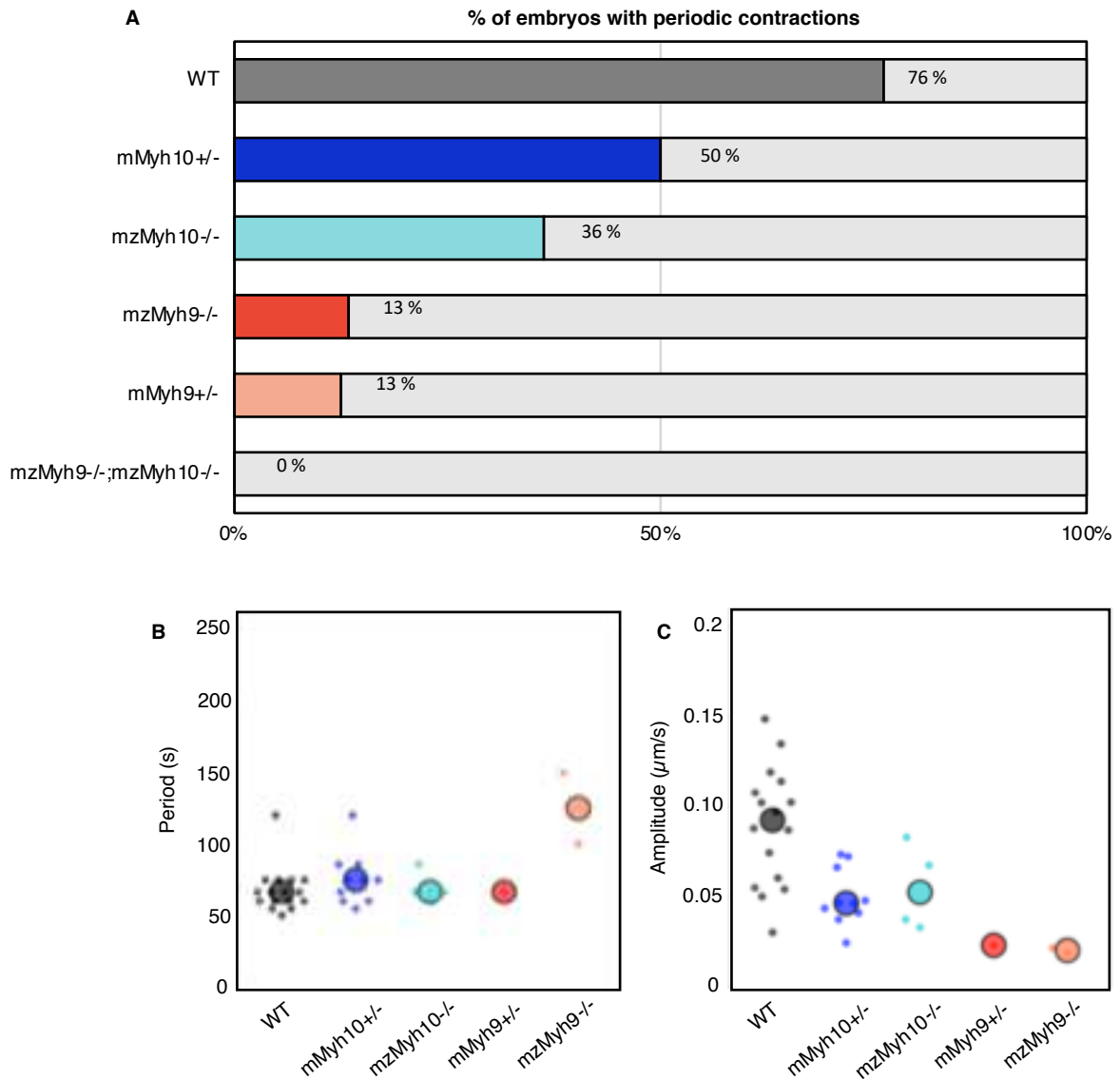


FIGURE 22: ANALYSIS OF PeCoWaCo IN MYOSIN MUTANTS AT THE ONSET OF MORPHOGENESIS.

Proportion (A) of WT (grey, $n = 21$), Myh10^{+/-} (blue, $n = 20$), and Myh10^{-/-} (light blue, $n = 11$), Myh9^{+/-} (red, $n = 17$), Myh9^{-/-} (light red, $n = 8$) embryos showing detectable oscillations and their detected period (B) and amplitude (C) of PeCoWaCo obtained from PIV analysis.

In order to investigate the role of myosin in the fine tuning machinery of PeCoWaCo we moved to chemical inhibitors as they allow to us apply titrated inhibition of myosin activity. I used Blebbistatin, a selective inhibitor of myosin 2 activity in addition to ML-7, an inhibitor of MLCK to target the Myosin activation from different levels at the pathway. I used isolated 16-cell stage blastomeres to further investigate the role of myosin on PeCoWaCo regulation in detail with local curvature tracking analysis. When I used Blebbistatin that binds to an allosteric site in the motor domain and prevents its the binding to the actin filament and therefore force generation, I observed that the oscillation period is increased (Fig. 23A) whereas the amplitude or the velocity of the PeCoWaCo was not changed (Fig 23 B-C). When I treated the cell with MLCK inhibitor ML-7, I observed that period of the oscillations were also increased (Fig. 23D) whereas amplitude and the wave velocity remained the same (Fig. 23E-F) as in the case of blebbistatin treatment.

All together, these experiments suggests that, myosin motor, and MLCK pathway that regulates its activity, is an important regulator of oscillation period and its amplitude, whereas it does not play a role in regulation of the wave velocity.

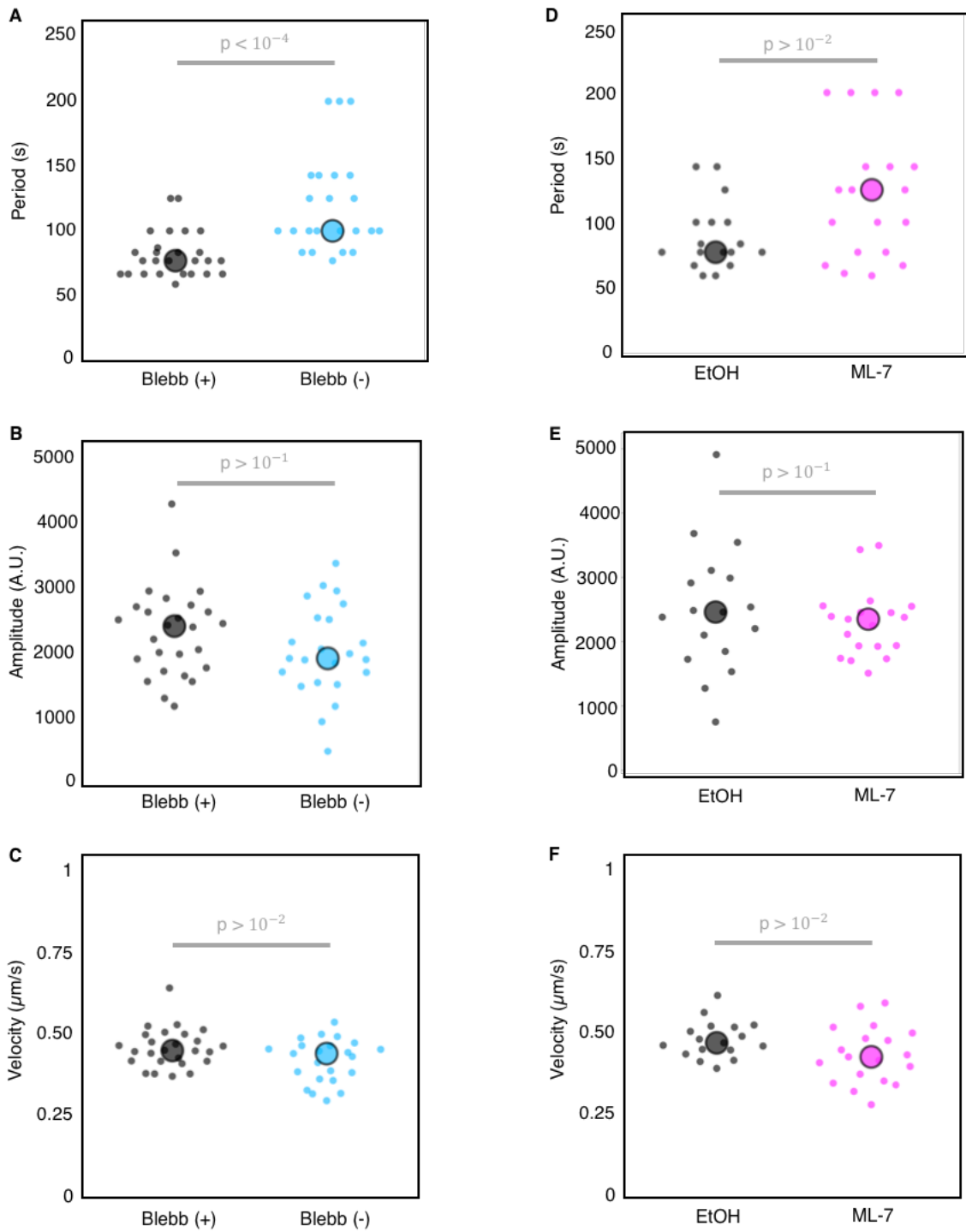


FIGURE 23: FINE TUNING OF PECOwACO PERIOD WITH MYOSIN ACTIVITY

Oscillation period (A&D), amplitude (B&E), and velocity (C&F) of isolated 16-cell-stage blastomeres treated with Blebbistatin (A-C) and ML-7 (D-F). Blebbistatin (+) (black, $n = 26$), Blebbistatin (-) (blue, $n = 23$), EtOH (black, $n = 17$), ML-7 (pink, $n = 19$). Student's t test p values comparing the conditions are indicated. Larger circles show median values.

ROLE OF ACTIN FILAMENTS

As we saw that cortex thickness is not correlating with the changes in surface tension and oscillation period of PeCoWaCo, we do not expect the architecture or the density of the actin filaments to play a role. However, what we did not learn from cortex thickness measurement is the dynamics of actin filaments as it is measured from immunofluorescence on the fixed embryos. It is known that actin filaments and associated proteins undergo wave-like movement in various types of cells. Directional polymerization and/or depolymerization of actin filaments can lead the propagation of the wave. To investigate this, I used titrated concentration of Latrunculin A (LatA), a chemical that competitively binds to globular actin preventing them to polymerize into filamentous actin. When 500nM LatA is used, I observed that period of the oscillations were almost doubled in some cells whereas it was not changed in others (Fig. 24A). On the other hand, the wave velocity remained the same in all of the cells (Fig. 24B). When I looked in detail to cells which changed their period I observed that LatA treatment cause them to change number of wave that travels from 2 to 1 (Fig. 24C, Movie 12) and this is how their period doubled whereas their velocity stayed the same.

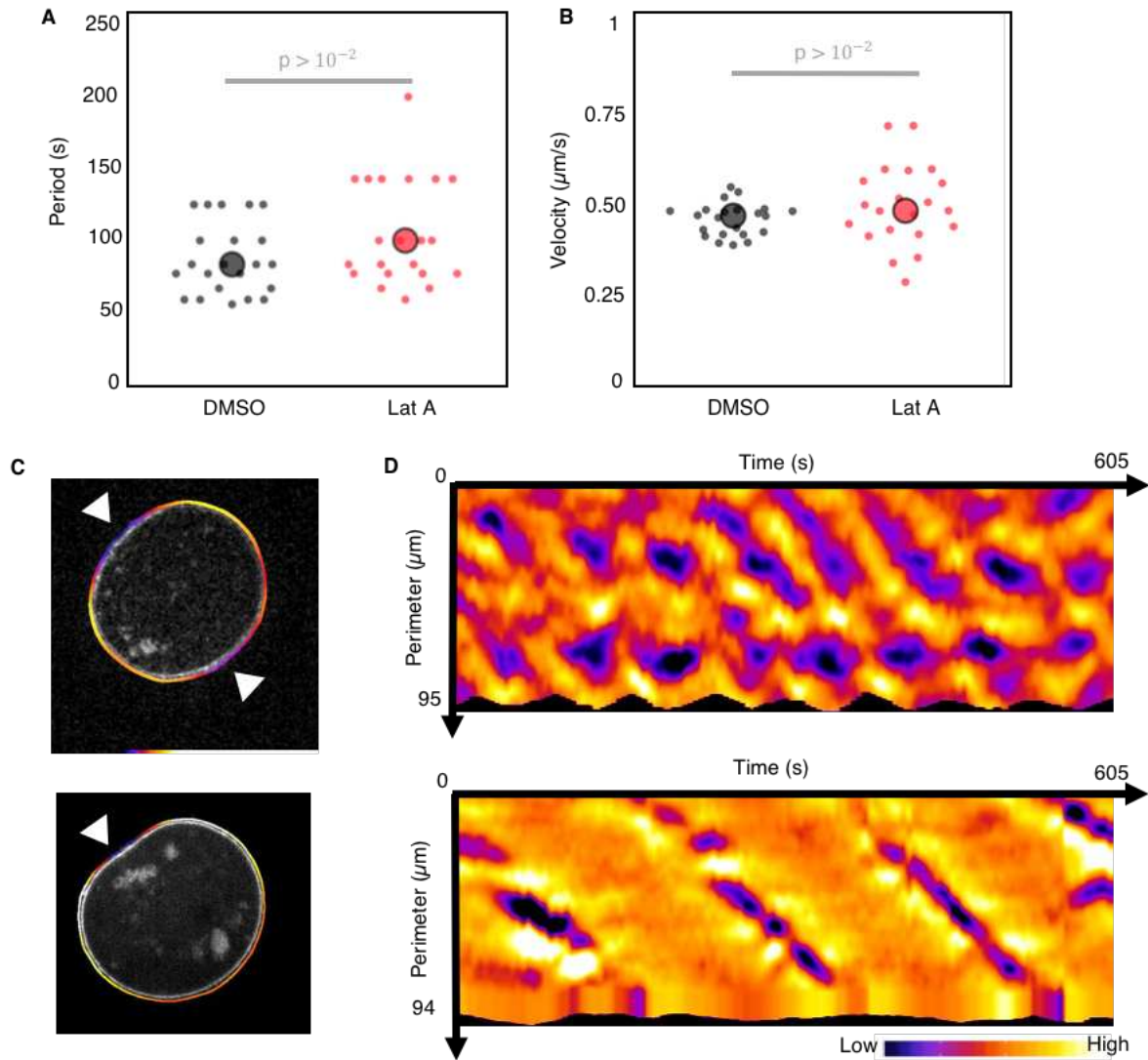


FIGURE 24: EFFECT OF LATRUCULIN A TREATMENT ON PECOwAcO

A-B) Oscillation period (A), and velocity (B) of isolated 16-cell-stage blastomeres treated with Latrunculin A (LatA). DMSO (black, $n=22$), Lat A (red, $n=21$). Student's t test p values comparing the conditions are indicated. Larger circles show median values. **C-D)** Representative images (C) of control and Latrunculin A treated cells overlaid with surface deformation heatmap and kymograph (D) obtained from surface deformation tracking for period detection and velocity measurements.

ROLE OF APKC

At the 8-cell stage, blastomeres polarize by forming an apical domain, which occupies only a portion of the contact-free surface. Atypical Protein Kinase C (aPKC) antagonizes myosin phosphorylation at the apical domain and it is essential for the stabilization of cell polarity at the 16-cell stage. In mammals, two *Prkc* genes, *aPrkcλ* and *aPrkcζ* encoding two different proteins have been identified. Double mutants for the zeta and iota isoforms of aPKC show ectopic actomyosin enrichments at what remains of their apical domain (Maître et al., 2016). Because the apical domain can be asymmetrically distributed during the 8- to 16-cell stage division, sister cells inherit distinct contractility (Maître et al., 2016). This translates into distinct amplitudes of PeCoWaCo (Maître et al., 2016). Moreover, when I fused cells at the 16-cell stage, blastomeres with and without apical domains are merged. Therefore, apical signals may also have an influence on the period and/or velocity of PeCoWaCo. To test this, I disrupted apical signaling by using *Prkci*^{+/-} ; *Prkcz*^{+/-} maternal mutants (aPKC^{+/-}) as well as injection of dominant negative Kinase dead aPKC (aPKC-Kd-DN) (Dard et al., 2009). To be able to analyze PeCoWaCo in detail, I dissociated the embryos at 16-cell stage and imaged at the equatorial plane for every 5s for 10 min and analyzed the movies by using local curvature tracking. When compared to wildtype embryos and not injected side of the embryo, neither *Prkcz* and *Prkci* maternal mutants nor kinase dead aPKC containing blastomeres showed a difference in oscillation period (Fig. 25A-B). Period was also not different between blastomeres with or without apical domain in aPKC^{+/-} blastomeres (Fig. 25C).

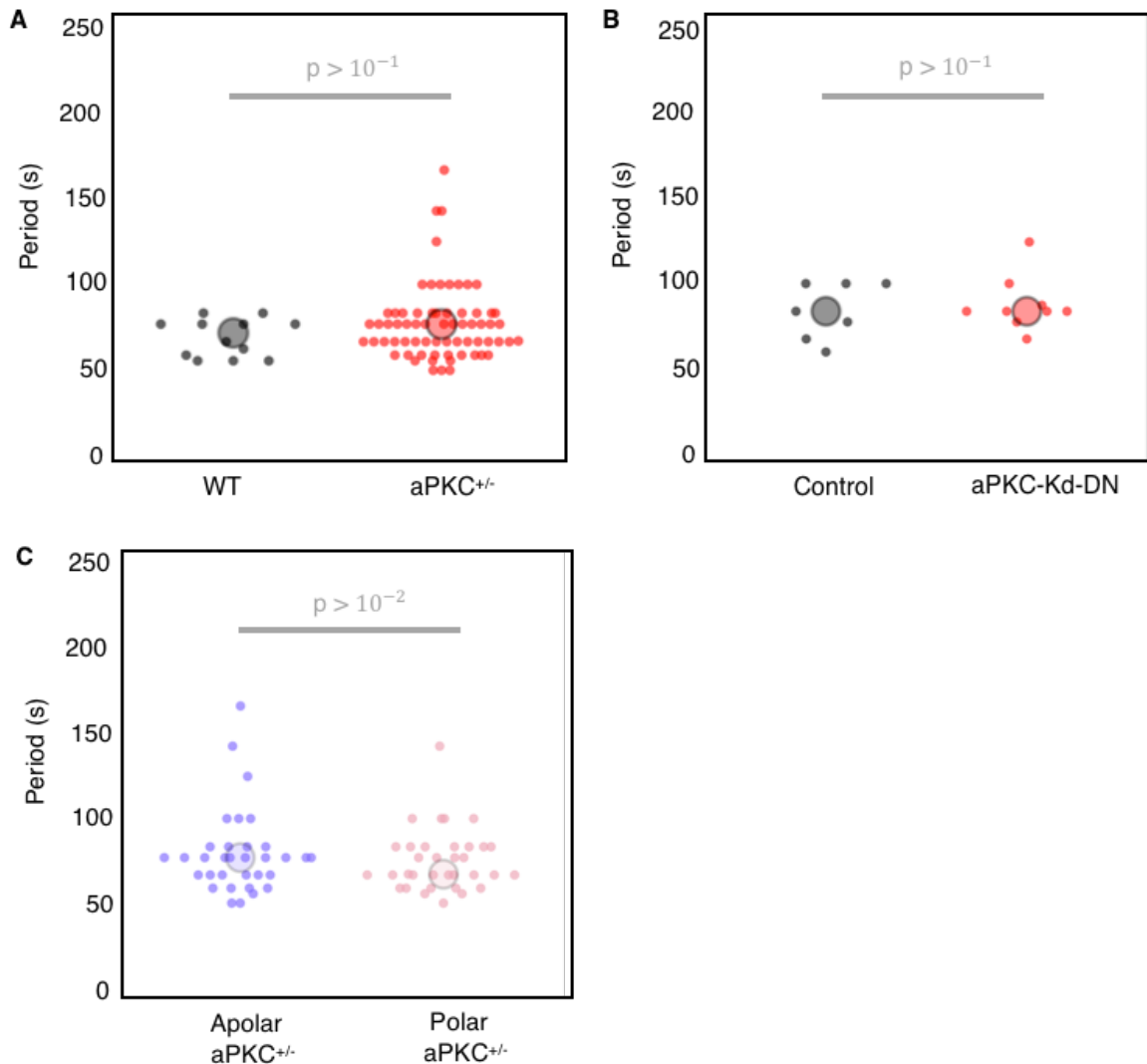


FIGURE 25: APKC PATHWAY DOES NOT AFFECT PECoWACo.

A-C) Oscillation period of 16-cell- stage isolated blastomeres of aPKC^{+/-} (A) embryos, aPKC kinase dead dominant negative (aPKC-Kd-DN) form injected embryos (B). WT (black, n = 12), aPKC^{+/-} (red, n = 68), uninjected control (black, n = 7), aPKC-Kd-DN (red, n = 9). **C)** Oscillation period of apolar and polar 16-cell- stage isolated blastomeres of aPKC^{+/-} embryos compared. Apolar (purple, n = 33), polar (pink, n= 35) Student's *t* test *p* values comparing the conditions are indicated. Larger circles show median values.

ROLE OF RHO PATHWAY

The cycling of contractile pulses is typically regulated by the Rho GTPase signaling module, which controls both actin filaments nucleation via formins and non-muscle myosin II activation via kinases (Zaidel-Bar et al., 2015). Moreover, the control of contractility by cadherins can be mediated via regulators of the small GTPase Rho. As we observed in our previous experiments, increasing cell-cell contact formation correlated with decrease in oscillation amplitude. We also know that during compaction, actomyosin levels decrease at cell-cell contacts as compared with the cell medium interface in a Cdh1-dependent manner (Maître et al., 2015). Therefore, this pathway is likely to be a regulator of the period of PeCoWaCo during development. However, Rho kinase (Rock), the usual suspect for controlling actomyosin contractility, does not seem to be involved in compaction as neither Rock inhibitors (Kono et al., 2014; Laeno et al., 2013; Samarage et al., 2015; Zenker et al., 2018), nor Rock knockout (Kamijo et al., 2011) shows a compaction phenotype (or other signs of contractility inhibition). Therefore, I wanted to inhibit this pathway from upstream of Rock and used RhoA, B, C inhibitor C3 transferase. Preliminary results with this inhibitor showed, inhibiting Rho A, B, and C does reduce the amplitude of the oscillation but does not affect the period or the velocity (Fig. 26A-C).

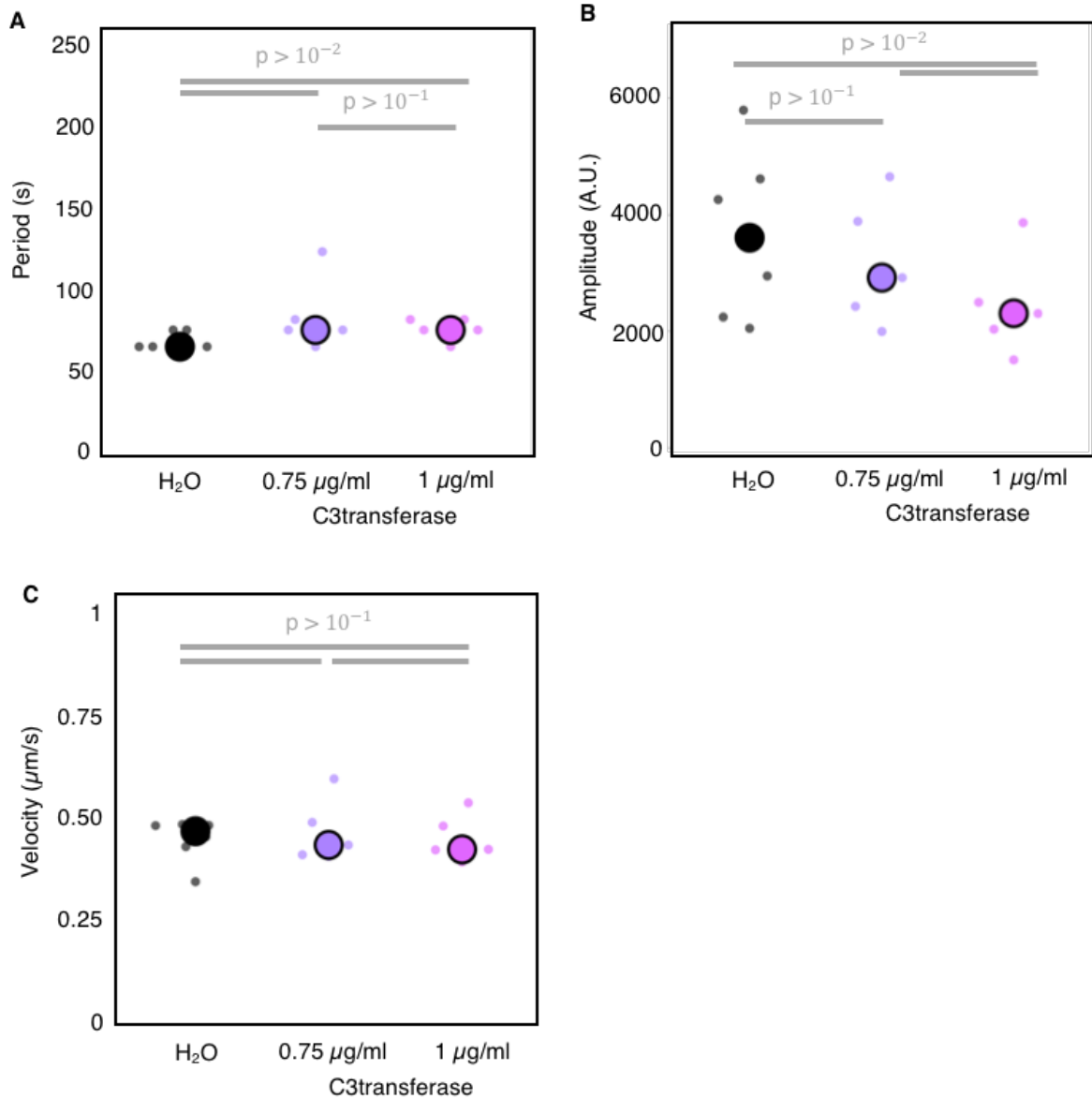


FIGURE 26: RHO A INHIBITION DOES NOT AFFECT PECOwACO.

A-C) Oscillation period (A), amplitude (B), and velocity (C) of isolated 16-cell-stage blastomeres treated with RhoA, B, and C inhibitor C3 transferase. Control (H₂O, black, n = 6) 0.75 μg/ml C3 transferase (purple, n = 5), 1 μg/ml C3 transferase (pink, n= 4). Student's *t* test *p* values comparing the conditions are indicated. Larger circles show median values.

RESEARCH PAPER 1 : ZYGOTIC CONTRACTILITY
AWAKENING DURING MOUSE PREIMPLANTATION
DEVELOPMENT

Zygotic contractility awakening during mouse preimplantation development

Özge Özgüç¹, Ludmilla de Plater¹, Varun Kapoor¹, Anna Francesca Tortorelli¹ and Jean-Léon Maître^{1*}

¹ Institut Curie, PSL Research University, Sorbonne Université, CNRS UMR3215, INSERM U934, Paris, France.

*Correspondence to jean-leon.maitre@curie.fr

Abstract

Actomyosin contractility is a major engine of preimplantation morphogenesis, which starts at the 8-cell stage during mouse embryonic development. Contractility becomes first visible with the appearance of periodic cortical waves of contraction (PeCoWaCo), which travel around blastomeres in an oscillatory fashion. How contractility of the mouse embryo becomes active remains unknown. We have taken advantage of PeCoWaCo to study the awakening of contractility during preimplantation development. We find that PeCoWaCo become detectable in most embryos only after the 2nd cleavage and gradually increase their oscillation frequency with each successive cleavage. To test the influence of cell size reduction during cleavage divisions, we use cell fusion and fragmentation to manipulate cell size across a 20-60 μm range. We find that the stepwise reduction in cell size caused by cleavage divisions does not explain the presence of PeCoWaCo or their accelerating rhythm. Instead, we discover that blastomeres gradually decrease their surface tensions until the 8-cell stage and that artificially softening cells enhances PeCoWaCo prematurely. Therefore, during cleavage stages, cortical softening awakens zygotic contractility before preimplantation morphogenesis.

Introduction

During embryonic development, the shape of animal cells and tissues largely relies on the contractility of the actomyosin cortex (Coravos et al., 2017; Murrell et al., 2015; Özgüç and Maître, 2020). The actomyosin cortex is a sub-micron-thin layer of crosslinked actin filaments, which are put under tension by non-muscle myosin II motors (Kelkar et al., 2020). Tethered to the plasma membrane, the actomyosin cortex is a prime determinant of the stresses at the surface of animal cells (Clark et al., 2014; Kelkar et al., 2020). Contractile stresses of the actomyosin cortex mediate crucial cellular processes such as the ingression of the cleavage furrow during cytokinesis (Fujiwara and Pollard, 1976; Straight et al., 2003; Yamamoto et al., 2021), the advance of cells' back during migration (Eddy et al., 2000; Tsai et al., 2019) or the retraction of blebs (Charras et al., 2006; Taneja and Burnette, 2019). At the tissue scale, spatiotemporal changes in actomyosin contractility drive apical constriction (Martin et al., 2009; Solon et al., 2009) or the remodeling of cell-cell contacts (Bertet et al., 2004; Maitre et al., 2012). Although tissue remodeling takes

place on timescales from tens of minutes to hours or days, the action of the actomyosin cortex is manifest on shorter timescales of tens of seconds (Coravos et al., 2017; Michaud et al., 2021; Özgüç and Maître, 2020). In fact, actomyosin is often found to act via pulses of contraction during morphogenetic processes among different animal species from nematodes to human cells (Baird et al., 2017; Bement, 2015; Blanchard et al., 2010; Kim and Davidson, 2011; Maître et al., 2015; Martin et al., 2009; Munro et al., 2004; Roh-Johnson et al., 2012; Solon et al., 2009). A pulse of actomyosin begins with the polymerization of actin filaments and the sliding of myosin mini-filaments until maximal contraction of the local network within about 30 s (Dehapiot et al., 2020; Ebrahim et al., 2013; Martin et al., 2009). Then, the actin cytoskeleton disassembles, and myosin is inactivated, which relaxes the local network for another 30 s (Mason et al., 2016; Munjal et al., 2015; Vasquez et al., 2014). These cycles of contractions and relaxations are governed by the turnover of the Rho GTPase and its effectors, which are well-characterized regulators of actomyosin contractility

(Bement, 2015; Graessl et al., 2017; Munjal et al., 2015). In instances where a sufficient number of pulses occur, pulses of contraction display a clear periodicity. The oscillation period of pulsed contractions ranges from 60 to 200 s (Baird et al., 2017; Bement, 2015; Maître et al., 2015; Solon et al., 2009). The period appears fairly defined for cells of a given tissue but can vary between tissues of the same species. What determines the oscillation period of contraction is poorly understood, although the Rho pathway may be expected to influence it (Bement, 2015; Munjal et al., 2015; Vasquez et al., 2014). Finally, periodic contractions can propagate into travelling waves. Such periodic cortical waves of contraction (PeCoWaCo) were observed in cell culture, starfish, and frog oocytes as well as in mouse preimplantation embryos (Bement, 2015; Driscoll et al., 2015; Kapustina et al., 2013; Maître et al., 2015). In starfish and frog oocytes, mesmerizing Turing patterns of Rho activation with a period of 80 s and a wavelength of 20 μm appear in a cell cycle dependent manner (Bement, 2015; Wigbers et al., 2021). Interestingly, experimental deformation of starfish oocytes revealed that Rho activation wave front may be coupled to the local curvature of the cell surface (Bischof et al., 2017), which was proposed to serve as a mechanism for cells to sense their shape (Wigbers et al., 2021). In mouse embryos, PeCoWaCo with a period of 80 s were observed at the onset of blastocyst morphogenesis (Maître et al., 2015; Maître et al., 2016). What controls the propagation velocity, amplitude, and period of these waves is unclear and the potential role of such evolutionarily conserved phenomenon remains a mystery.

During mouse preimplantation development, PeCoWaCo become visible before compaction (Maître et al., 2015), the first morphogenetic movements leading to the formation of the blastocyst (Maître, 2017; Özgüç and Maître, 2020; White et al., 2018). During the second morphogenetic movement, prominent PeCoWaCo are displayed in prospective inner cells before their internalization (Maître et al., 2016). In contrast, cells remaining at the surface of the embryo display PeCoWaCo of lower amplitude due to the presence of a domain of

apical material that inhibits the activity of myosin (Maître et al., 2016). Then, during the formation of the blastocoel, high temporal resolution time-lapse hint at the presence of PeCoWaCo as microlumens coarsen into a single lumen (Dumortier et al., 2019). Therefore, PeCoWaCo appear throughout the entire process of blastocyst formation (Özgüç and Maître, 2020). However, little is known about what initiates and regulates PeCoWaCo. The analysis of maternal zygotic mutants suggests that PeCoWaCo in mouse blastomeres result primarily from the action of the non-muscle myosin heavy chain IIA (encoded by *Myh9*) rather than IIB (encoded by *Myh10*) (Schliffka et al., 2021). Dissociation of mouse blastomeres indicates that PeCoWaCo are cell-autonomous since they persist in single cells (Maître et al., 2015). Interestingly, although removing cell-cell contacts free-up a large surface for the contractile waves to propagate, the oscillation period seems robust to the manipulation (Maître et al., 2015). Similarly, when cells form an apical domain taking up a large portion of the cell surface, the oscillation period does not seem to be different from cells in which the wave can propagate on the entire cell surface (Maître et al., 2016). This raises the question of how robust PeCoWaCo are to geometrical parameters, especially in light of recent observations in starfish oocytes (Bischof et al., 2017; Wigbers et al., 2021). This question becomes particularly relevant when considering that, during preimplantation development, cleavage divisions halve cell volume with each round of cytokinesis (Aiken et al., 2004; Niwayama et al., 2019).

In this study, we investigate how the contractility of the cleavage stages emerges before initiating blastocyst morphogenesis. We take advantage of the slow development of the mouse embryo to study thousands of pulsed contractions and of the robustness of the mouse embryo to size manipulation to explore the geometrical regulation of PeCoWaCo. We discover that the initiation, maintenance, or oscillatory properties of PeCoWaCo do not depend on cell size. Instead, we discover a gradual softening of blastomeres with each successive cleavage, which conceals PeCoWaCo. Together, this study reveals how preimplantation

contractility is robust to the geometrical changes of the cleavage stages during which the zygotic contractility awakens.

Results

PeCoWaCo during cleavage stages

PeCoWaCo have been observed at the 8-, 16-cell, and blastocyst stages. To know when PeCoWaCo first appear, we imaged embryos during the cleavage stages

and performed Particle Image Velocimetry (PIV) and Fourier analyses (Fig 1A-C, Movie 1). This reveals that PeCoWaCo are detectable in fewer than half of zygote and 2-cell stage embryos and become visible in most embryos from the 4-cell stage onwards (Fig 1D). Furthermore, PeCoWaCo only display large amplitude from the 4-cell stage onwards (Fig 1B-C). Interestingly, the period of oscillations of the detected PeCoWaCo

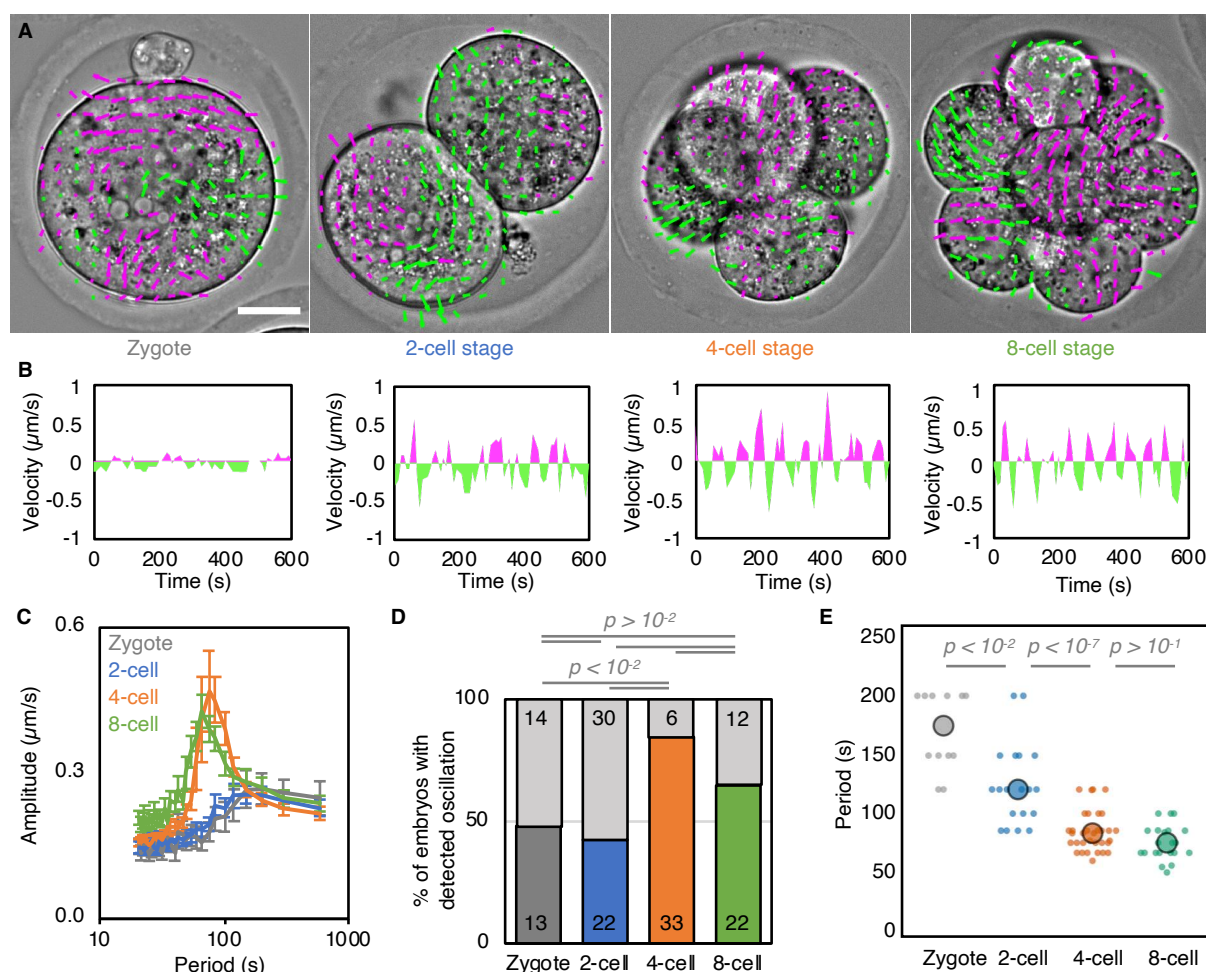


Figure 1: Analysis of PeCoWaCo during cleavage stages. A) Representative images of a short-term time-lapse overlaid with a subset of velocity vectors from Particle Image Velocimetry (PIV) analysis during cleavage stages (Movie 1). Magenta for positive and green for negative Y directed movement. Scale bars, 20 μm . **B)** Velocity over time for a representative velocity vector of each embryo shown in A. **C)** Mean power spectrum resulting from Fourier transform of PIV analysis of Zygote (grey, $n = 13$), 2-cell (blue, $n = 22$), 4-cell (orange, $n = 33$) and 8-cell (green, $n = 22$) stages embryos showing detectable oscillations. Data show as mean \pm SEM. **D)** Proportion of Zygote (grey, $n = 27$), 2-cell (blue, $n = 52$), 4-cell (orange, $n = 39$), 8-cell stage (green, $n = 34$) embryos showing detectable oscillations after Fourier transform of PIV analysis. Light grey shows non-oscillating embryos. χ^2 p values comparing different stages are indicated. **E)** Oscillation period of Zygote (grey, $n = 13$), 2-cell (blue, $n = 22$), 4-cell (orange, $n = 33$), 8-cell (green, $n = 22$) stages embryos. Larger circles show median values. Student's t test p values are indicated.

shows a gradual decrease from 200 s to 80 s between the zygote and 8-cell stages (Fig 1E). The acceleration of PeCoWaCo rhythm could simply result from the stepwise changes of cell size after cleavage divisions. Indeed, we reasoned that if the contractile waves travel at constant velocity, the period will scale with cell size and shape. This is further supported by the fact that PeCoWaCo are detected at the same rate and with the same oscillation period during the early or late halves of the 2-, 4- and 8-cell stages (Fig S1).

Therefore, we set to investigate the relationship between cell size and periodic contractions.

Cell size is not critical for the initiation or maintenance of PeCoWaCo

First, to test whether the initiation of PeCoWaCo in most 4-cell stage embryos depends on the transition from the 2- to 4-cell stage blastomere size, we prevented cytokinesis. Using transient exposure to Vx-680 to inhibit the activity of Aurora kinases

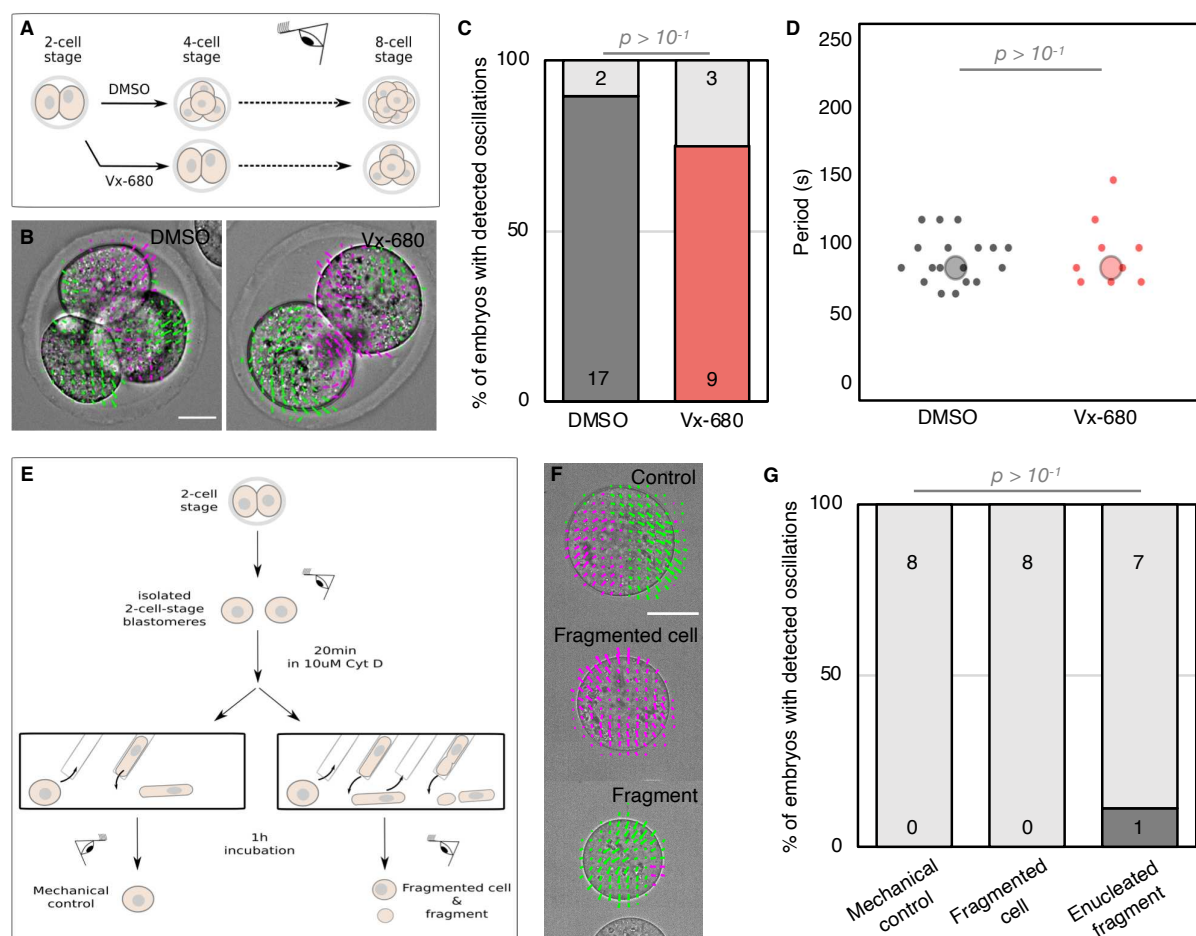


Figure 2: Initiation of PeCoWaCo is independent of cell size. **A)** Schematic diagram of PeCoWaCo analysis after blocking the 2nd cleavage division with 2.5 μ M Vx680. **B)** Representative images of DMSO and Vx-680 treated embryos overlaid with a subset of velocity vectors from Particle Image Velocimetry (PIV) analysis (Movie 2). **C-D)** Proportion (C) of embryos showing detectable oscillations and their detected period (D, DMSO n = 19 and Vx-680 n = 12). χ^2 (C) and Student's t test (D) p values comparing two conditions are indicated. Larger circles show median values. **E)** Schematic diagram of PeCoWaCo analysis after fragmentation of 2-cell stage blastomeres. **F)** Representative images of mechanical control, fragmented cell and enucleated fragments overlaid with a subset of velocity vectors from PIV analysis (Movie 3). **G)** Proportion of cells showing detectable oscillations in mechanical controls (n = 8), fragmented cells (n=8) and enucleated fragments (n=9). Fisher exact test p values comparing different conditions are indicated. Light grey shows non-oscillating embryos.

triggering chromosome separation, we specifically blocked the 2- to 4-cell stage cytokinesis without compromising the next cleavage to the 8-cell stage (Fig 2A-B, Movie 2). This causes embryos to reach the 4-cell stage with tetraploid blastomeres the size of 2-cell stage blastomeres. At the 4-cell stage, we detect PeCoWaCo in most embryos whether they have 4- or 2-cell stage size blastomeres (Fig 2C). Furthermore, the period of oscillation is identical to 4-cell stage embryos in both control and drug-treated conditions (Fig 2D). This suggests that 4-cell stage blastomere size is not required to initiate PeCoWaCo in the majority of embryos.

Then, we tested whether PeCoWaCo could be triggered prematurely by artificially reducing 2-cell stage blastomeres to the size of a 4-cell stage blastomere. First, we analyzed for the presence of PeCoWaCo in dissociated 2-cell stage blastomeres and then proceeded to reduce their size (Fig 2E-F, Movie 3). To reduce cell size, we treated dissociated 2-cell stage blastomeres with the actin cytoskeleton inhibitor Cytochalasin D before deforming repeatedly them into a narrow pipette (Fig 2E, Fig S2). By adapting the number of aspirations of softened blastomeres, we could carefully fragment blastomeres while keeping their sister cell mechanically stressed but intact. While the fragmented cell was reduced to the size of a 4-cell stage blastomere, both fragmented and manipulated cells eventually succeeded in dividing to the 4-cell stage. After waiting 1 h for cells to recover from this procedure, we examined for the presence of PeCoWaCo. At the 2-cell stage, PeCoWaCo were rarely detected in either control or fragmented cells (Fig 2G). This suggests that 4-cell stage blastomere size is not sufficient to trigger PeCoWaCo in the majority of embryos.

Cell size does not influence the properties of PeCoWaCo

The transition from 2- to 4-cell stage blastomere size is neither required nor sufficient to initiate PeCoWaCo. Nevertheless, the decrease in period of PeCoWaCo remarkably scales with the stepwise decrease in blastomere size (Fig 1E). Given a constant propagation velocity,

PeCoWaCo may reduce their period according to the reduced distance to travel around smaller cells. To test whether cell size determines PeCoWaCo oscillation period, we set out to manipulate cell size over a broad range. By fusing varying numbers of 16-cell stage blastomeres, we built cells equivalent in size to 8-, 4- and 2-cell stage blastomeres (Fig 3A-D, Movie 4). In addition, by fragmenting 16-cell stage blastomeres, we made smaller cells equivalent to 32-cell stage blastomeres (Fig 3E-G, Movie 5)(Niwayama et al., 2019). Together, we could image 16-cell stage blastomeres with sizes ranging from 10 to 30 μm in radius (Fig 3H-I). Finally, to identify how the period may scale with cell size by adjusting the velocity of the contractile wave, we segmented the outline of cells to compute the local curvature, which, unlike PIV analysis, allows us to track contractile waves and determine their velocity in addition to their period (Fig 3A) (Maître et al., 2015; Maître et al., 2016). We find that fused and fragmented 16-cell stage blastomeres show the same period, regardless of their size (Fig 3H). This could be explained if the wave velocity would scale with cell size. However, we find that the wave velocity remains constant regardless of cell size (Fig 3I). Therefore, both the oscillation period and wave velocity are properties of PeCoWaCo that are robust to changes in cell size and associated curvature.

Fusion of cells causes blastomeres to contain multiple nuclei, while cell fragmentation creates enucleated fragments. Interestingly, enucleated fragments continued oscillating with the same period and showing identical propagation velocities as the nucleus-containing fragments (Fig 3F). These measurements indicate that PeCoWaCo are robust to the absence or presence of single or multiple nuclei and their associated functions.

Together, using fusion and fragmentation of cells, we find that PeCoWaCo oscillation properties are robust to a large range of size perturbations. Therefore, other mechanisms must be at play to regulate periodic contractions during preimplantation development.

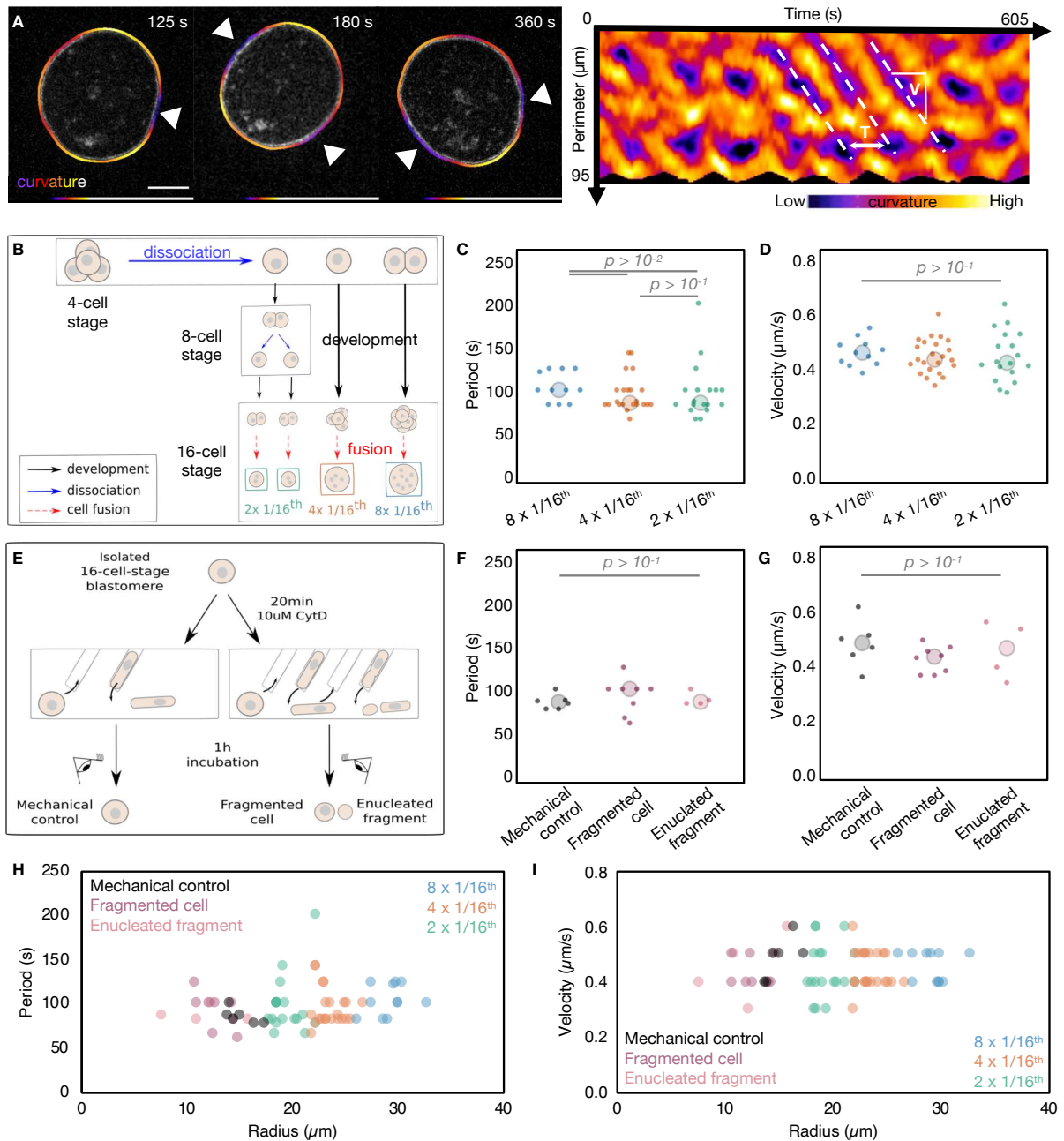


Figure 3: Period and velocity of PeCoWaCo are stable across a broad range of cell sizes. **A)** Surface deformation tracking for period detection and velocity measurements. Scale bar, 10 μm . **B)** Schematic diagram of fusion of 16-cell stage blastomeres. **C-D)** Oscillation period (C) and wave velocity (D) of fused blastomeres. 8 x 1/16th (blue, n=6), 4 x 1/16th (orange, n=12) and 2 x 1/16th (green, n=7) fused blastomeres are shown. Large circles show median. **E)** Schematic diagram of fragmentation of 16-cell stage blastomeres. **F-G)** Oscillation period (F) and wave velocity (G) of fragmented blastomeres. Control (black, n=6), fragmented cell (magenta, n=8), enucleated fragment (pink, n=4) are shown. **H-I)** Oscillation period (H) and wave velocity (I) for size-manipulated 16-cell stage blastomeres. Larger circles show median values. Student's t-test p values are indicated.

Cortical maturation during cleavage stages

Despite the apparent relationship between cell size and PeCoWaCo during preimplantation development, our experimental manipulations of cell size reveal that PeCoWaCo are not influenced by cell size. PeCoWaCo result from the activity of the actomyosin cortex, which could become stronger during cleavage stages and make PeCoWaCo more prominent as previously observed during the 16-cell stage (Maître et al., 2016). Since actomyosin contractility generates a significant portion of the surface

tension of animal cells, this would translate in a gradual increase in surface tension. To investigate this, we set to measure the surface tension of cells as a readout of contractility during cleavage stages using micropipette aspiration. Contrary to our expectations, we find that surface tension gradually decreases from the zygote to 8-cell stage (Fig 4A-B) and noticeably mirrors the behavior of the period of PeCoWaCo during cleavage stages (Fig 1E). Therefore, PeCoWaCo unlikely result simply from increased contractility. Instead, the tension of

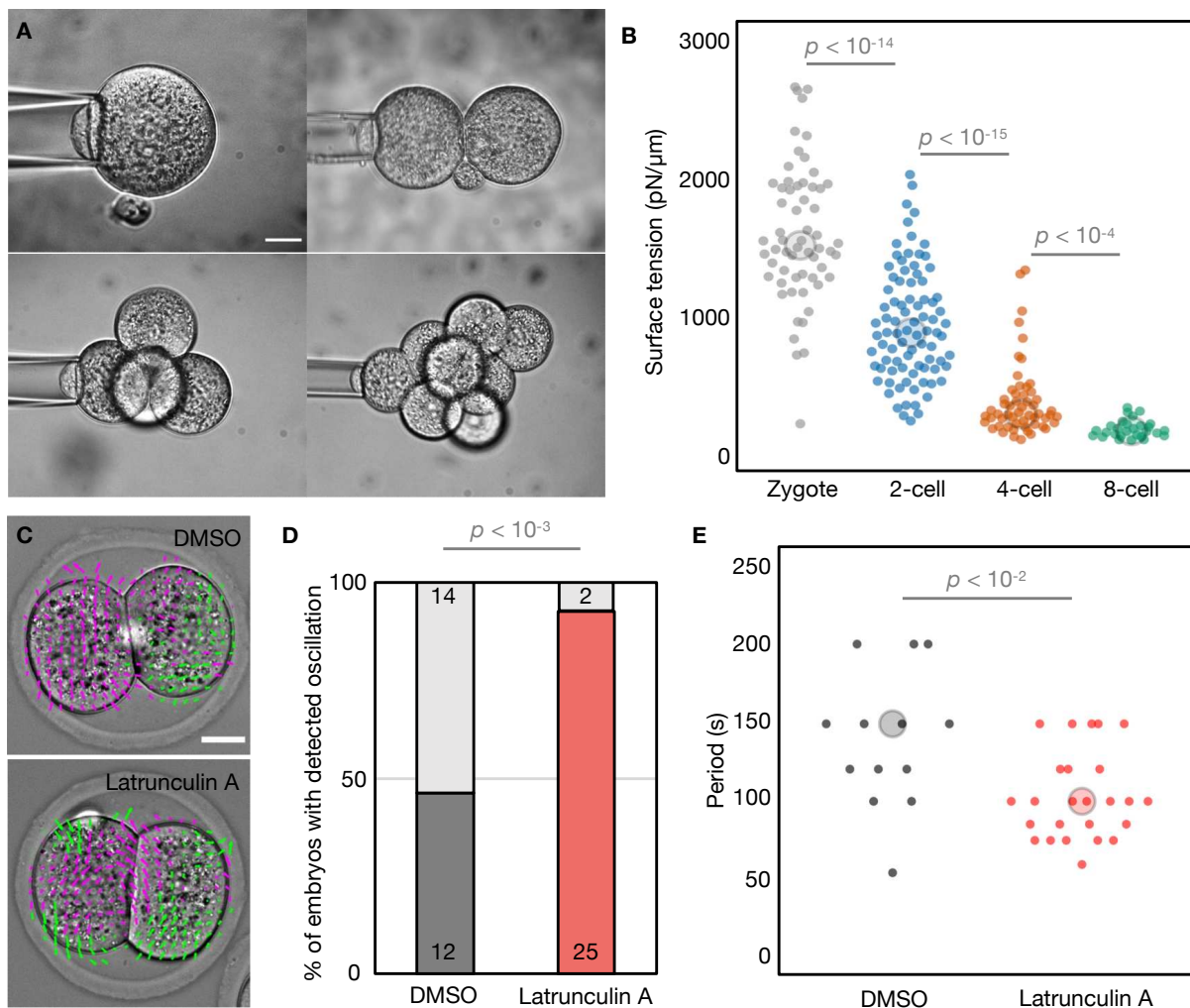


Figure 4: Cortical changes during preimplantation development. A) Representative images of the tension mapping method. **B)** Surface tension of blastomeres throughout cleavage stages. Zygote (gray, $n = 60$), 2-cell (blue, $n = 86$), 4-cell (orange, $n = 55$), early 8-cell (green, $n = 28$) stages are shown. **C)** Representative images of Control and 100nM Latrunculin A treated embryos overlaid with a subset of velocity vectors from Particle Image Velocimetry (PIV) analysis (Movie 6). **D-E)** Proportion (D) of embryos showing detectable oscillations and their detected period (E) of DMSO treated ($n = 26$) and 100 nM Latrunculin A treated ($n = 27$) 2-cell stage embryos. χ^2 p value is indicated. Light grey shows non-oscillating embryos. Larger circles show median values.

blastomeres at the zygote and 2-cell stages may be too high for PeCoWaCo to become visible in most embryos. To reduce the tension of the cortex, we used low concentrations (100 nM) of the actin polymerization inhibitor Latrunculin A (Driscoll et al., 2015). Softening the cortex of 2-cell stage embryos increased the proportions of embryos displaying PeCoWaCo (Fig 4C-D, Movie 6). This suggests that PeCoWaCo become more visible thanks to the gradual softening of the cortex of blastomeres during cleavage stages. Moreover, low concentrations of Latrunculin A decreased the oscillation period of PeCoWaCo down to ~100 s, as compared to ~150 s for the DMSO control embryos (Fig 4E). This suggests that modifications of the polymerization rate of the actin cytoskeleton could be responsible for the increase in PeCoWaCo frequency observed during cleavage stages.

Together, these experiments reveal the unsuspected maturation of the cortex of blastomeres during the cleavage stages of mouse embryonic development.

Discussion

During cleavage stages, blastomeres halve their size with successive divisions. Besides the increased number of blastomeres, there is no change in the architecture of the mouse embryo until the 8-cell stage with compaction. We find that this impression of stillness is only true on a timescale of hours since, on the timescale of seconds, blastomeres display signs of actomyosin contractility. During the first two days after fertilization, contractility seems to mature by displaying more visible and frequent pulses. We further find that pulsed contractions do not rely on the successive reductions in cell size but rather on the gradual decrease in surface tension of the blastomeres. Therefore, during cleavage stages, cortical softening awakens zygotic contractility before preimplantation morphogenesis.

Previous studies on the cytoskeleton of the early mouse embryo revealed that both the microtubule and intermediate filaments networks mature during cleavage stages. Keratin intermediate filaments appear at the

onset of blastocyst morphogenesis (Schwarz et al., 2015) and become preferentially inherited by prospective TE cells (Lim et al., 2020). The microtubule network is initially organized without centrioles around microtubule bridges connecting sister cells (Zenker et al., 2017). The spindle of early cleavages also organizes without centrioles similarly to during meiosis (Courtois et al., 2012; Schuh and Ellenberg, 2007). As centrioles form *de novo*, cells progressively transition from meiosis-like to mitosis-like divisions (Courtois et al., 2012). We find that the actomyosin cortex also matures during cleavage stages by decreasing its oscillation period (Fig 1E) and its surface tension (Fig 4B). Interestingly, this decrease in cortical tension seems to be in continuation with the maturation of the oocyte. Indeed, the surface tension of mouse oocytes decreases during their successive maturation stages (Larson et al., 2010). The softening of the oocyte cortex is associated with architectural rearrangements that are important for the cortical movement of the meiotic spindle (Chaigne et al., 2013; Chaigne et al., 2015). Therefore, similarly to the microtubule network, the zygotic actomyosin cortex awakens progressively from an egg-like state.

The maturation of zygotic contractility is likely influenced by the activation of the zygotic genome occurring partly at the late zygote stage and mainly during the 2-cell stage (Schulz and Harrison, Melissa M, 2018; Svoboda, 2018). Recent studies in frog and mouse propose that reducing cell size could accelerate zygotic genome activation (ZGA) (Chen et al., 2019; Zhu et al., 2020). We find that manipulating cell size is neither sufficient to trigger PeCoWaCo prematurely in most embryos, nor required to initiate or maintain them in a timely fashion with the expected oscillation period of the corresponding cleavage stage (Fig 2 and 3). Instead, we find that the surface of blastomeres in the cleavage stages is initially too tense to allow for PeCoWaCo to be clearly displayed (Fig 4). This is also suggested by previous studies in starfish oocytes, in which removing an elastic jelly surrounding the egg softens them and renders contractile waves more pronounced (Bischof et al., 2017). Interestingly, the

changes in surface curvature caused by cortical waves of contraction may influence the signaling and cytoskeletal machinery controlling the wave (Bischof et al., 2017; Wu et al., 2018). Such mechano-chemical feedback has been proposed to regulate the period of contractions via the advection of regulators of actomyosin contractility (Munjal et al., 2015). As a result, the curvature of cells and tissues is suspected to regulate contractile waves (Bailles et al., 2019; Bischof et al., 2017). Using cell fragmentation and fusion, we have manipulated the curvature of the surface over which PeCoWaCo travel (Fig 3). From radii ranging between 10 and 30 μm , we find no change in the period or travelling velocity of PeCoWaCo (Fig 3). This indicates that, in the mouse embryo, the actomyosin apparatus is robust to the changes in curvature taking place during preimplantation development. Therefore, the cleavage divisions per se are unlikely regulators of preimplantation contractility. The robustness of PeCoWaCo to changes of radii ranging from 10 to 30 μm is puzzling since neither the oscillation period nor the wave velocity seem affected (Fig 3H-I). One explanation would be that the number of waves present simultaneously changes with the size of the cells. Using our 2D approach, we could not systematically analyze this parameter. Nevertheless, we did note that some portions of the fused blastomeres did not display PeCoWaCo. These may be corresponding to apical domains, which do not show prominent PeCoWaCo (Maître et al., 2016). Therefore, the relationship between the total area of the cell and the “available” or “excitable” area for PeCoWaCo may not be straightforward (Bement, 2015). In the context of the embryo, in addition to the apical domain, cell-cell contacts also downregulate actomyosin contractility and do not show prominent contractions (Maître et al., 2015). As cell-cell contacts grow during compaction and apical domains expand (Korotkevich et al., 2017; Zenker et al., 2018), the available excitable cortical area for PeCoWaCo eventually vanishes.

Together, our study uncovers the maturation of the actomyosin cortex, which softens and speeds up the rhythm of contractions during the cleavage stages of

the mouse embryo. Importantly, zebrafish embryos also soften during their cleavage stages, enabling doming, the first morphogenetic movement in zebrafish (Morita et al., 2017). It will be interesting to see whether cell and tissue softening during cleavage stages is conserved in other animals. Finally, what controls the maturation of the cortex during cleavage stages will require further investigation to understand how embryos prepare for morphogenesis.

Acknowledgements

We thank the imaging platform of the Genetics and Developmental Biology unit at the Institut Curie (PICT-IBiSA@BDD) for their outstanding support; the animal facility of the Institut Curie for their invaluable help. We thank Victoire Cachoux for help with image analysis and Ido Lavi, Sophie Louvet-Vallée, and members of the Maître lab for discussions. We thank Julie Plastino and Markus Schliffka for critical reading of the manuscript. Research in the lab of J.-L.M. is supported by the Institut Curie, the Centre National de la Recherche Scientifique (CNRS), the Institut National de la Santé Et de la Recherche Médicale (INSERM), and is funded by grants from the ATIP-Avenir program, the Fondation Schlumberger pour l'Éducation et la Recherche via the Fondation pour la Recherche Médicale, the European Research Council Starting Grant ERC-2017-StG 757557, the European Molecular Biology Organization Young Investigator program (EMBO YIP), the INSERM transversal program Human Development Cell Atlas (HuDeCA), Paris Sciences Lettres (PSL) “nouvelle équipe” and QLife (17-CONV-0005) grants and Labex DEEP (ANR-11-LABX-0044) which are part of the IDEX PSL (ANR-10-IDEX-0001-02). Ö. Ö. is funded from the European Union's Horizon 2020 research and innovation program under the Marie Skłodowska-Curie grant agreement No 666003, the Fondation pour la Recherche Médicale (FDT202001010796), and benefitted from the EMBO YIP COVID bridging fund.

Author contributions

Ö. Ö., L. P. and A. F. T. performed experiments and prepared data for analyses.

V. K. wrote the curvature analysis code following Ö. Ö. and J.-L.M. initial plans. Ö. Ö. and J.-L.M. acquired funding, analyzed the data, designed the project and wrote the manuscript.

Methods

Embryo work

Recovery and culture

All animal work is performed in the animal facility at the Institut Curie, with permission by the institutional veterinarian overseeing the operation (APAFIS #11054-2017082914226001). The animal facilities are operated according to international animal welfare rules.

Embryos are isolated from superovulated female mice mated with male mice. Superovulation of female mice is induced by intraperitoneal injection of 5 international units (IU) pregnant mare's serum gonadotropin (PMSG, Ceva, Syncro-part), followed by intraperitoneal injection of 5 IU human chorionic gonadotropin (hCG, MSD Animal Health, Chorulon) 44-48 hours later. Embryos are recovered at E0.5 by dissecting in 37°C FHM (LifeGlobal, ZEHP-050 or Millipore, MR-122-D) from the oviduct the ampulla, from which embryos are cleared with a brief (5-10 s) exposure to 37°C hyaluronidase (Sigma, H4272).

Embryos are recovered at E1.5 or E2.5 by flushing oviducts from plugged females with 37°C FHM using a modified syringe (Acufirm, 1400 LL 23).

Embryos are handled using an aspirator tube (Sigma, A5177-5EA) equipped with a glass pipette pulled from glass micropipettes (Blaubrand intraMark or Warner Instruments). Embryos are placed in KSOM (LifeGlobal, ZEKS-050 or Millipore, MR-107-D) or FHM supplemented with 0.1 % BSA (Sigma, A3311) in 10 µL droplets covered in mineral oil (Sigma, M8410 or Acros Organics) unless stated otherwise. Embryos are cultured in an incubator with a humidified atmosphere supplemented with 5% CO₂ at 37°C.

To remove the Zona Pellucida (ZP), embryos are incubated for 45-60 s in pronase (Sigma, P8811).

For imaging, embryos are placed in 5 or 10 cm glass-bottom dishes (MatTek).

Only embryos surviving the experiments were analyzed. Survival is assessed by continuation of cell division as normal when embryos are placed in optimal culture conditions.

Mouse lines

Mice are used from 5 weeks old on.

(C57BL/6xC3H) F1 hybrid strain is used for wild-type (WT). To visualize plasma membranes, mTmG (Gt(ROSA)26Sor^{tm4}(ACTB-tdTomato,-EGFP)^{Luo}) is used (Muzumdar et al., 2007).

Isolation of Blastomeres

ZP-free 2-cell or 4-cell stages embryos are aspirated multiple times (typically between 3–5 times) through a smoothed glass pipette (narrower than the embryo but broader than individual cells) until dissociation of cells.

For 16-cell-stage embryos, they are placed into EDTA containing Ca²⁺ free KSOM (Biggers et al., 2000) for 8–10 min before dissociation. Cells are then washed with KSOM for 1 h before experiment.

Chemical reagents and treatments

Vx-680 (Tocris, 5907) 50 mM dimethyl sulfoxide (DMSO) stock was diluted to 2.5 µM in KSOM. To prevent mitosis, 2-cell-stage embryos are cultured in 2.5 µM Vx-680 for 3 h shortly prior to the 2nd cleavage and then washed in KSOM.

Cytochalasin D (Sigma, C2618-200UL) 10 mM DMSO stock is diluted to 10 µM in KSOM. To fragment cells, isolated 2- or 16-cell stage blastomeres were treated with Cytochalasin D for 20 min before being gently aspirated into a smoothed glass pipette of diameter about 30 or 5-10 µm respectively (Korotkevich et al., 2017). 2-3 repeated aspirations are typically sufficient to clip cells into to 2 large fragments, one containing the nucleus and one without. Cells that did not fragment after 2 aspirations are used as control.

GenomONE-CF FZ SeV-E cell fusion kit (CosmoBio, ISK-CF-001-EX) is used to fuse blastomeres (Schliffka et al., 2021). HVJ envelope is resuspended following manufacturer's instructions and diluted in FHM for use. To fuse blastomeres of embryos at the 16-cell stage, embryos are incubated in

1:50 HVJ envelope for 15 min at 37°C followed by washes in KSOM.

Latrunculin A (Tocris, ref 3973) 10mM DMSO stock is diluted to 100 nM in KSOM. To soften cells, 2-cell stage embryos are imaged in medium containing Latrunculin A covered with mineral oil for 2 h.

Micropipette aspiration

As described previously (Guevorkian, 2017; Maître et al., 2015), a microforged micropipette coupled to a microfluidic pump (Fluigent, MFCS EZ) is used to measure the surface tension of embryos. In brief, micropipettes of radii 8-16 μm are used to apply step-wise increasing pressures on the cell surface until reaching a deformation, which has the radius of the micropipette (R_p). At steady-state, the surface tension γ of the cell is calculated from the Young-Laplace's law applied between the cell and the micropipette: $\gamma = P_c / 2 (1/R_p - 1/R)$, where P_c is the critical pressure used to deform the cell of radius R .

8-cell stage embryos are measured before compaction (all contact angles $< 105^\circ$), during which surface tension would increase (Maître et al., 2015).

Microscopy

For live imaging, embryos are placed in 5 cm glass-bottom dishes (MatTek) under a CellDiscoverer 7 (Zeiss) equipped with a 20x/0.95 objective and an ORCA-Flash 4.0 camera (C11440, Hamamatsu) or a 506 axiovert (Zeiss) camera.

Using the experiment designer tool of ZEN (Zeiss), we set up nested time-lapses in which all embryos are imaged every 5 h for 10 min with an image taken every 5 s at 2 focal planes positioned 10 μm apart. Embryos are kept in a humidified atmosphere supplied with 5% CO₂ at 37°C.

mTmG embryos are imaged at the 2- and 16-cell stage using an inverted Zeiss Observer Z1 microscope with a CSU-X1 spinning disc unit (Yokogawa). Excitation is achieved using a 561 nm laser through a 63x/1.2 C Apo Korr water immersion objective. Emission is collected through 595/50 band pass filters onto an ORCA-Flash 4.0 camera (C11440, Hamamatsu). The microscope is equipped with an incubation chamber to keep the

sample at 37°C and supply the atmosphere with 5% CO₂.

Surface tension measurements are performed on a Leica DMI6000 B inverted microscope equipped with a 40x/0.8 DRY HC PL APO Ph2 (11506383) objective and Retina R3 camera and 0,7x lens in front of the camera. The microscope is equipped with an incubation chamber to keep the sample at 37°C and supply the atmosphere with 5% CO₂.

Data analysis

Image analysis

Manual shape measurements

FIJI (Schindelin et al., 2012) is used to measure cell, embryo, pipette sizes, and wave velocity. The circle tool is used to fit a circle onto cells, embryos and pipettes. The line tool is used to fit lines onto curvature kymographs.

Particle image velocimetry (PIV) analysis

To detect PeCoWaCo in phase contrast images of embryos, we use Particle Image velocimetry (PIV) analysis followed by a Fourier analysis.

As previously (Maître et al., 2015; Schliiffka et al., 2021), PIVlab 2.02 running on Matlab (Thielicke and Eize J. Stamhuis, 2020; Thielicke and Stamhuis, 2010) is used to process 10 min long time lapses with images taken every 5 s using 2 successive passes through interrogation windows of 20/10 μm resulting in ~ 180 vectors per embryo.

The x- and y-velocities of individual vectors from PIV analysis are used for Fourier analysis. A Fourier transform of the vector velocities over time is performed using Matlab's fast Fourier transform function. The resulting Fourier transforms are squared to obtain individual power spectra. Squared Fourier transforms in the x and y directions of all vectors are averaged for individual embryos resulting in mean power spectra of individual embryos.

Spectra of individual embryos are checked for the presence of a distinct amplitude peak to extract the oscillation period. The peak value between 50 s and 200 s was taken as the amplitude, as this oscillation period range is detectable by our imaging method. An embryo is considered as oscillating when the

amplitude peaks 1.85 times above background (taken as the mean value of the power spectrum signal of a given embryo). This threshold value was chosen to minimize false-positive and false-negative according to visual verification of time-lapse movies. For example, visual inspection of embryos shown in Fig 1D suggest that three zygote, eight 2-cell, zero 4-cell, three 8-cell are false positive, and zero zygote, two 2-cell, one 4-cell, five 8-cell are false negative. Therefore, the number of oscillating zygote is likely overestimated while the number of oscillating 8-cell stage is underestimated.

2-cell, 4-cell and 8-cell stages are considered early during the first half of the corresponding stage and late during the second half.

Local curvature analysis

To measure PeCoWaCo period, amplitude and velocity, we analyze the associated changes in surface curvature and perform Fourier analysis.

To obtain the local curvature of isolated blastomeres, we developed an approach similar to that of (Driscoll et al., 2012; Maître et al., 2015; Maître et al., 2016). First, a Gaussian blur is applied to mTmG images using FIJI (Schindelin et al., 2012). Then, using Ilastik (Sommer et al., 2011), pixels are associated with cell membrane or background. Segmentation of cells are then used in a custom made Fiji plugin (called *WizardofOz*, found under the *Mtrack* repository) for computing the local curvature information using the start, center and end point of a 10 μm strip on the cell surface to fit a circle. The strip is then moved by 1 pixel along the segmented cell and a new circle is fitted. This process is repeated till all the points of the cell are covered. The radius of curvature of the 10 μm strip boundaries are averaged. Kymograph of local curvature values around the perimeter over time is produced by plotting the perimeter of the strip over time.

Curvature kymographs obtained from local curvature tracking are then exported into a custom made Python script for 2D Fast Fourier Transform analysis.

Spectra of individual cells are checked for the presence of a distinct amplitude peak to extract the oscillation period. The peak value

between 50 s and 200 s was taken as the amplitude, as this oscillation period range is detectable by our imaging method.

To measure the wave velocity a line is manually fitted on the curvature kymograph using FIJI.

Statistics

Data are plotted using Excel (Microsoft) and R-based SuperPlotsOfData tool (Goedhart, 2021). Mean, standard deviation, median, one-tailed Student's *t*-test, Fisher exact test, and Chi² *p* values are calculated using Excel (Microsoft) or R (R Foundation for Statistical Computing). Statistical significance is considered when $p < 10^{-2}$.

The sample size was not predetermined and simply results from the repetition of experiments. No sample that survived the experiment, as assessed by the continuation of cell divisions, was excluded. No randomization method was used. The investigators were not blinded during experiments.

Code availability

The code used to analyze the oscillation frequencies from PIV and local curvature analyses can be found at github.com/MechaBlasto/PeCoWaCo.git.

The Fiji plugin for local curvature analysis *WizardofOz* can be found under the *MTrack* repository.

Movie legends

Movie 1: Particle image velocimetry (PIV) analysis during cleavage stages. Time-lapse imaging of zygote, 2-, 4- and 8-cell stage embryos showing PeCoWaCo. Pictures are taken every 5 s and PIV analysis is performed between two consecutive images. PIV vectors are overlaid on top of the images with vectors pointing upward in magenta and downward in green. Scale bar, 20 μm .

Movie 2: PIV analysis of 4-cell stage embryos treated with DMSO or Vx-680. Time-lapse imaging of 4-cell stage embryos showing PeCoWaCo after treatment with DMSO or 2.5 μM Vx680 at the time of the 2nd cleavage division. Pictures are taken every 5 s and PIV analysis is performed between two

consecutive images. PIV vectors are overlaid on top of the images with vectors pointing upward in magenta and downward in green. Scale bar, 20 μm .

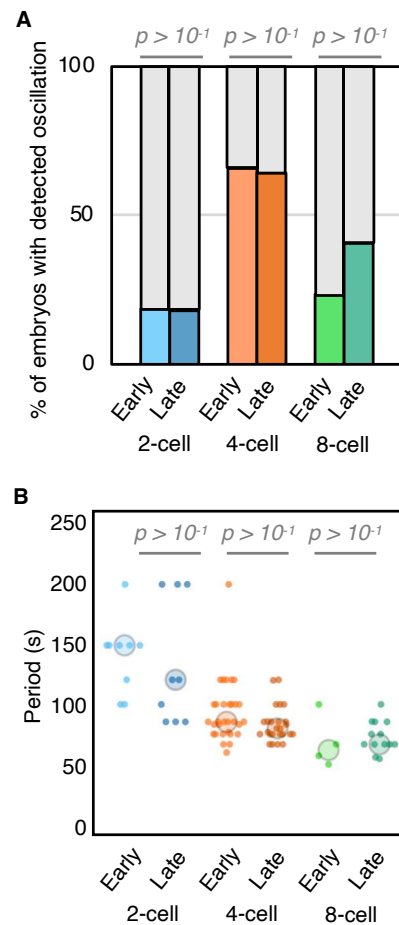
Movie 3: PIV analysis of fragmented 2-cell stage blastomeres. Time-lapse imaging of mechanically manipulated and fragmented 2-cell stage blastomeres with and without nucleus. Pictures are taken every 5 s and PIV analysis is performed between two consecutive images. PIV vectors are overlaid on top of the images with vectors pointing upward in magenta and downward in green. Scale bar, 20 μm .

Movie 4: Surface deformation tracking of fused cells. Montage of mTmG (top) and local curvature measurements (bottom) of fused 8x, 4x, 2x 1/16th blastomeres showing PeCoWaCo. Scale bar, 20 μm .

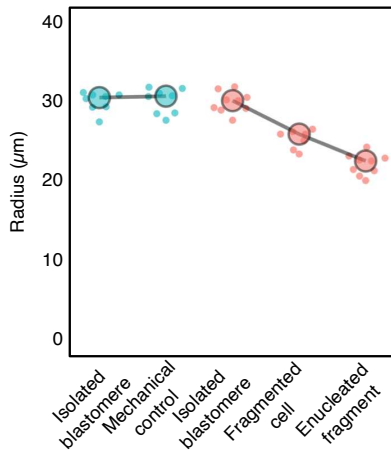
Movie 5: Surface deformation tracking of fragmented 16-cell-stage blastomeres. Montage of mTmG (top) and local curvature measurements (bottom) of mechanically manipulated and fragmented 16-cell stage blastomeres with and without nucleus 1/16th blastomeres showing PeCoWaCo. Scale bar, 10 μm .

Movie 6: PIV analysis of 2-cell stage embryos treated with DMSO or Latrunculin A. Time-lapse imaging of 2-cell stage embryos treated with DMSO or 100 nM Latrunculin A (LatA) showing PeCoWaCo. Pictures are taken every 5 s and PIV analysis is performed between two consecutive images. PIV vectors are overlaid on top of the images with vectors pointing upward in magenta and downward in green. Scale bar, 20 μm .

Supplementary figures



Supplementary Figure related to Figure 1: Analysis of PeCoWaCo within cleavage stages. **A)** Proportion of early and late 2-cell (blue, $n = 43$ and 50), 4-cell (orange, $n = 38$ and 28), 8-cell stage (green, $n = 17$ and 32) embryos showing detectable oscillations after Fourier transform of PIV analysis. χ^2 p values comparing different stages are indicated. Light grey shows non-oscillating embryos. **B)** Oscillation period of early and late 2-cell (blue, $n = 22$), 4-cell (orange, $n = 33$), 8-cell (green, $n = 22$) stages embryos. Larger circles show median values. Student's t test p values are indicated.



Supplementary Figure related to Figure 2: size of cells before and after fragmentation. Radius of 16-cell stage blastomeres before and after mechanical manipulation ($n = 8$), fragmentation into fragmented cells ($n = 8$) or enucleated fragments ($n = 9$). Larger circles show median values.

References

- Aiken, C. E. M., Swoboda, P. P. L., Skepper, J. N. and Johnson, M. H.** (2004). The direct measurement of embryogenic volume and nucleocytoplasmic ratio during mouse pre-implantation development. *Reproduction (Cambridge, England)* **128**, 527–535.
- Bailles, A., Collinet, C., Philippe, J.-M., Lenne, P.-F., Munro, E. and Lecuit, T.** (2019). Genetic induction and mechanochemical propagation of a morphogenetic wave. *Nature* **572**, 467–473.
- Baird, M. A., Billington, N., Wang, A., Adelstein, R. S., Sellers, J. R., Fischer, R. S. and Waterman, C. M.** (2017). Local pulsatile contractions are an intrinsic property of the myosin 2A motor in the cortical cytoskeleton of adherent cells. *Molecular Biology of the Cell* **28**, 12.
- Bement, W. M.** (2015). Activator-inhibitor coupling between Rho signalling and actin assembly makes the cell cortex an excitable medium. *Nature cell biology* **17**, 1471–1483.
- Bertet, C., Sulak, L. and Lecuit, T.** (2004). Myosin-dependent junction remodelling controls planar cell intercalation and axis elongation. *Nature* **429**, 667–671.
- Biggers, J. D., McGinnis, L. K. and Raffin, M.** (2000). Amino Acids and Preimplantation Development of the Mouse in Protein-Free Potassium Simplex Optimized Medium. *Biology of reproduction*.
- Bischof, J., Brand, C. A., Somogyi, K., Májer, I., Thome, S., Mori, M., Schwarz, U. S. and Lénárt, P.** (2017). A cdk1 gradient guides surface contraction waves in oocytes. *Nat Commun* **8**, 849.
- Blanchard, G., Murugesu, S., Adams, R., Martinez-Arias, A. and Gorfinkiel, N.** (2010). Cytoskeletal dynamics and supracellular organisation of cell shape fluctuations during dorsal closure. *Development (Cambridge, England)* **137**, 2743–2752.
- Chaigne, A., Campillo, C., Gov, N. S., Voituriez, R., Azoury, J., Umaña-Diaz, C., Almonacid, M., Queguiner, I., Nassoy, P., Sykes, C., et al.** (2013). A soft cortex is essential for asymmetric spindle positioning in mouse oocytes. *Nat Cell Biol* **15**, 958–966.
- Chaigne, A., Campillo, C., Gov, N. S., Voituriez, R., Sykes, C., Verlhac, M. H. and Terret, M. E.** (2015). A narrow window of cortical tension guides asymmetric spindle positioning in the mouse oocyte. *Nature communications* **6**, 6027.
- Charras, G., Hu, C., Coughlin, M. and Mitchison, T.** (2006). Reassembly of contractile actin cortex in cell blebs. *The Journal of cell biology* **175**, 477–490.
- Chen, H., Einstein, L. C., Little, S. C. and Good, M. C.** (2019). Spatiotemporal Patterning of Zygotic Genome Activation in a Model Vertebrate Embryo. *Developmental Cell* **49**, 852–866.e7.
- Clark, A. G., Wartlick, O., Salbreux, G. and Paluch, E. K.** (2014). Stresses at the cell surface during animal cell morphogenesis. *Curr Biol* **24**, R484–94.
- Coravos, J. S., Mason, F. M. and Martin, A. C.** (2017). Actomyosin Pulsing in Tissue Integrity Maintenance during Morphogenesis. *Trends in Cell Biology* **27**, 276–283.
- Courtois, A., Schuh, M., Ellenberg, J. and Hiiragi, T.** (2012). The transition from meiotic to mitotic spindle assembly is gradual during early mammalian development. *The Journal of cell biology* **198**, 357–370.
- Dehapiot, B., Clément, R., Alégot, H., Gzásó-Gerhát, G., Philippe, J.-M. and Lecuit, T.** (2020). Assembly of a persistent apical actin network by the formin Frl/Fmnl tunes epithelial cell deformability. *Nat Cell Biol* **22**, 791–802.
- Driscoll, M. K., McCann, C., Kopace, R., Homan, T., Fourkas, J. T., Parent, C. and Losert, W.** (2012). Cell shape dynamics: from waves to migration. *PLoS computational biology* **8**, e1002392.
- Driscoll, M. K., Losert, W., Jacobson, K. and Kapustina, M.** (2015). Spatiotemporal relationships between the cell shape and the actomyosin cortex of periodically protruding cells. *Cytoskeleton (Hoboken, N.J.)* **72**, 268–281.
- Dumortier, J. G., Le Verge-Serandour, M., Tortorelli, A. F., Mielke, A., de Plater, L., Turlier, H. and Maître, J.-L.** (2019). Hydraulic fracturing

and active coarsening position the lumen of the mouse blastocyst. *Science* **365**, 465–468.

Ebrahim, S., Fujita, T., Millis, B. A., Kozin, E., Ma, X., Kawamoto, S., Baird, M. A., Davidson, M., Yonemura, S., Hisa, Y., et al. (2013). NMII forms a contractile transcellular sarcomeric network to regulate apical cell junctions and tissue geometry. *Curr Biol* **23**, 731–736.

Eddy, R. J., Pierini, L. M., Matsumura, F. and Maxfield, F. R. (2000). Ca²⁺-dependent myosin II activation is required for uropod retraction during neutrophil migration. *J Cell Sci* **113 (Pt 7)**, 1287–1298.

Fujiwara, K. and Pollard, T. D. (1976). Fluorescent antibody localization of myosin in the cytoplasm, cleavage furrow, and mitotic spindle of human cells. *The Journal of cell biology* **71**, 848–875.

Goedhart, J. (2021). SuperPlotsOfData—a web app for the transparent display and quantitative comparison of continuous data from different conditions. *MBoC* **32**, 470–474.

Graessl, M., Koch, J., Calderon, A., Kamps, D., Banerjee, S., Mazel, T., Schulze, N., Jungkurth, J. K., Patwardhan, R., Solouk, D., et al. (2017). An excitable Rho GTPase signaling network generates dynamic subcellular contraction patterns. *The Journal of cell biology* **216**, 4271–4285.

Guevorkian, K. (2017). Micropipette aspiration: A unique tool for exploring cell and tissue mechanics in vivo. *Methods in cell biology* **139**, 187–201.

Kapustina, M., Elston, T. C. and Jacobson, K. (2013). Compression and dilation of the membrane-cortex layer generates rapid changes in cell shape. *The Journal of cell biology* **200**, 95–108.

Kelkar, M., Bohec, P. and Charras, G. (2020). Mechanics of the cellular actin cortex: From signalling to shape change. *Current Opinion in Cell Biology* **66**, 69–78.

Kim, H. Y. and Davidson, L. A. (2011). Punctuated actin contractions during convergent extension and their permissive regulation by the non-canonical Wnt-signaling pathway. *Journal of cell science* **124**, 635–646.

Korotkevich, E., Niwayama, R., Courtois, A., Friese, S., Berger, N., Buchholz, F. and Hiiragi, T. (2017). The Apical Domain Is Required and Sufficient for the First Lineage Segregation in the Mouse Embryo. *Dev Cell* **40**, 235–247.e7.

Larson, S. M., Lee, H. J., Hung, P., Matthews, L. M., Robinson, D. N. and Evans, J. P. (2010). Cortical mechanics and meiosis II completion in mammalian oocytes are mediated by myosin-II and Ezrin-Radixin-Moesin (ERM) proteins. *Mol Biol Cell* **21**, 3182–3192.

Lim, H. Y. G., Alvarez, Y. D., Gasnier, M., Wang, Y., Tetlak, P., Bissiere, S., Wang, H., Biro, M. and Plachta, N. (2020). Keratins are asymmetrically inherited fate determinants in the mammalian embryo. *Nature*.

Maitre, J.-L. (2017). Mechanics of blastocyst morphogenesis. *Biology of the Cell* **109**, 323–338.

Maitre, J.-L., Berthoumieux, H., Krens, S. F. G., Salbreux, G., Julicher, F., Paluch, E. and Heisenberg, C.-P. (2012). Adhesion Functions in Cell Sorting by Mechanically Coupling the Cortices of Adhering Cells. *Science* **338**, 253–256.

Maitre, J.-L., Niwayama, R., Turlier, H., Nédélec, F. and Hiiragi, T. (2015). Pulsatile cell-autonomous contractility drives compaction in the mouse embryo. *Nature cell biology* **17**, 849–855.

Maitre, J.-L., Turlier, H., Illukkumbura, R., Eismann, B., Niwayama, R., Nédélec, F. and Hiiragi, T. (2016). Asymmetric division of contractile domains couples cell positioning and fate specification. *Nature* **536**, 344–348.

Martin, A., Kaschube, M. and Wieschaus, E. (2009). Pulsed contractions of an actin-myosin network drive apical constriction. *Nature* **457**, 495–499.

Mason, F. M., Xie, S., Vasquez, C. G., Tworoger, M. and Martin, A. C. (2016). RhoA GTPase inhibition organizes contraction during epithelial morphogenesis. *The Journal of cell biology* **214**, 603–617.

Michaud, A., Swider, Z. T., Landino, J., Leda, M., Miller, A. L., von Dassow, G., Goryachev, A. B. and Bement, W. M. (2021). Cortical excitability and cell division. *Current Biology* **31**, R553–R559.

Morita, H., Grigolon, S., Bock, M., Krens, S. F. G., Salbreux, G. and Heisenberg, C.-P. (2017). The Physical Basis of Coordinated Tissue Spreading in Zebrafish Gastrulation. *Developmental Cell* **40**, 354–366.e4.

Munjal, A., Philippe, J.-M., Munro, E. and Lecuit, T. (2015). A self-organized biomechanical network drives shape changes during tissue morphogenesis. *Nature* **524**, 351–355.

Munro, E., Nance, J. and Priess, J. (2004). Cortical flows powered by asymmetrical contraction transport PAR proteins to establish and maintain anterior-posterior polarity in the early *C. elegans* embryo. *Dev Cell* **7**, 413–424.

Murrell, M., Lenz, M. and Gardel, M. L. (2015). Forcing cells into shape: the mechanics of actomyosin contractility. *Nat Rev Mol Cell Biol* **16**, 486–498.

Muzumdar, M. D., Tasic, B., Miyamichi, K., Li, L. and Luo, L. (2007). A global double-fluorescent Cre reporter mouse. *genesis* **45**, 593–605.

Niwayama, R., Moghe, P., Liu, Y.-J., Fabrèges, D., Buchholz, F., Piel, M. and Hiiragi, T. (2019).

- A Tug-of-War between Cell Shape and Polarity Controls Division Orientation to Ensure Robust Patterning in the Mouse Blastocyst. *Developmental Cell* 1–18.
- Özgüç, Ö. and Maître, J.-L.** (2020). Multiscale morphogenesis of the mouse blastocyst by actomyosin contractility. *Current Opinion in Cell Biology* **66**, 123–129.
- Roh-Johnson, M., Shemer, G., McClellan, J. H., Werts, A. D., Tulu, U. S., Gao, L., Betzig, E., Kiehart, D. P. and Goldstein, B.** (2012). Triggering a cell shape change by exploiting preexisting actomyosin contractions. *Science (New York, NY)* **335**, 1232–1235.
- Schindelin, J., Arganda-Carreras, I., Frise, E., Kaynig, V., Longair, M., Pietzsch, T., Preibisch, S., Rueden, C., Saalfeld, S. and Schmid, B.** (2012). Fiji: an open-source platform for biological-image analysis. *Nature Methods* **9**, 676–682.
- Schliffka, M. F., Tortorelli, A.-F., Özgüç, Ö., de Plater, L., Polzer, O., Pelzer, D. and Maître, J.-L.** (2021). Multiscale analysis of single and double maternal-zygotic Myh9 and Myh10 mutants during mouse preimplantation development. *eLife* **10**, e68536.
- Schuh, M. and Ellenberg, J.** (2007). Self-Organization of MTOCs Replaces Centrosome Function during Acentrosomal Spindle Assembly in Live Mouse Oocytes. *Cell* **130**, 484–498.
- Schulz, K. N. and Harrison, Melissa M** (2018). Mechanisms regulating zygotic genome activation. *Nat Rev Genet* 221–234.
- Schwarz, N., Windoffer, R., Magin, T. M. and Leube, R. E.** (2015). Dissection of keratin network formation, turnover and reorganization in living murine embryos. *Sci Rep* **5**, 9007.
- Solon, J., Kaya-Copur, A., Colombelli, J. and Brunner, D.** (2009). Pulsed forces timed by a ratchet-like mechanism drive directed tissue movement during dorsal closure. *Cell* **137**, 1331–1342.
- Sommer, C., Straehle, C., Kothe, U. and Hamprecht, F. A.** (2011). Ilastik: Interactive learning and segmentation toolkit. In (0.5), pp. 230–233. IEEE.
- Straight, A. F., Cheung, A., Limouze, J., Chen, I., Westwood, N. J., Sellers, J. R. and Mitchison, T. J.** (2003). Dissecting temporal and spatial control of cytokinesis with a myosin II inhibitor. *Science (New York, NY)* **299**, 1743–1747.
- Svoboda, P.** (2018). Mammalian zygotic genome activation. *Developmental Biology* **9**.
- Taneja, N. and Burnette, D. T.** (2019). Myosin IIA drives membrane bleb retraction. *Mol Biol Cell* **30**, 1051–1059.
- Thielicke, W. and Eize J. Stamhuis** (2020). PIVlab v2.36 - Time-Resolved Digital Particle Image Velocimetry Tool for MATLAB. figshare.
- Thielicke, W. and Stamhuis, E. J.** (2010). PIVlab - Time-Resolved Digital Particle Image Velocimetry Tool for MATLAB (version: 1.35).
- Tsai, T. Y.-C., Collins, S. R., Chan, C. K., Hadjitheodorou, A., Lam, P.-Y., Lou, S. S., Yang, H. W., Jorgensen, J., Ellett, F., Irimia, D., et al.** (2019). Efficient Front-Rear Coupling in Neutrophil Chemotaxis by Dynamic Myosin II Localization. *Developmental Cell* **49**, 189–205.e6.
- Vasquez, C. G., Tworoger, M. and Martin, A. C.** (2014). Dynamic myosin phosphorylation regulates contractile pulses and tissue integrity during epithelial morphogenesis. *The Journal of cell biology* **206**, 435–450.
- White, M. D., Zenker, J., Bissiere, S. and Plachta, N.** (2018). Instructions for Assembling the Early Mammalian Embryo. *Developmental Cell* **45**, 667–679.
- Wigbers, M. C., Tan, T. H., Brauns, F., Liu, J., Swartz, S. Z., Frey, E. and Fakhri, N.** (2021). A hierarchy of protein patterns robustly decodes cell shape information. *Nat. Phys.* **17**, 578–584.
- Wu, Z., Su, M., Tong, C., Wu, M. and Liu, J.** (2018). Membrane shape-mediated wave propagation of cortical protein dynamics. *Nat Commun* **9**, 136.
- Yamamoto, K., Miura, H., Ishida, M., Sawai, S., Kondo, Y. and Aoki, K.** (2021). *Optogenetic relaxation of actomyosin contractility uncovers mechanistic roles of cortical tension during cytokinesis.* Cell Biology.
- Zenker, J., White, M. D., Templin, R. M., Parton, R. G., Thorn-Seshold, O., Bissiere, S. and Plachta, N.** (2017). A microtubule-organizing center directing intracellular transport in the early mouse embryo. *Science (New York, NY)* **357**, 925–928.
- Zenker, J., White, M. D., Gasnier, M., Álvarez, Y. D., Lim, H. Y. G., Bissiere, S., Biro, M. and Plachta, N.** (2018). Expanding Actin Rings Zipper the Mouse Embryo for Blastocyst Formation. *Cell* 1–34.
- Zhu, M., Cornwall-Scoones, J., Wang, P., Handford, C. E., Na, J., Thomson, M. and Zernicka-Goetz, M.** (2020). Developmental clock and mechanism of de novo polarization of the mouse embryo. *Science* **370**, eabd2703.

RESEARCH PAPER 2: MULTISCALE ANALYSIS OF
SINGLE AND DOUBLE MATERNAL-ZYGOTIC MYH9 AND
MYH10 MUTANTS DURING MOUSE PREIMPLANTATION
DEVELOPMENT

Multiscale analysis of single and double maternal-zygotic *Myh9* and *Myh10* mutants during mouse preimplantation development

Markus Frederik Schliffka^{1,2†}, Anna Francesca Tortorelli^{1†}, Özge Özgüç¹, Ludmilla de Plater¹, Oliver Polzer¹, Diane Pelzer¹, Jean-Léon Maître^{1*}

¹Institut Curie, PSL Research University, Sorbonne Université, Paris, France; ²Carl Zeiss SAS, Marly-le-Roy, France

Abstract During the first days of mammalian development, the embryo forms the blastocyst, the structure responsible for implanting the mammalian embryo. Consisting of an epithelium enveloping the pluripotent inner cell mass and a fluid-filled lumen, the blastocyst results from a series of cleavage divisions, morphogenetic movements, and lineage specification. Recent studies have identified the essential role of actomyosin contractility in driving cytokinesis, morphogenesis, and fate specification, leading to the formation of the blastocyst. However, the preimplantation development of contractility mutants has not been characterized. Here, we generated single and double maternal-zygotic mutants of non-muscle myosin II heavy chains (NMHCs) to characterize them with multiscale imaging. We found that *Myh9* (NMHC II-A) is the major NMHC during preimplantation development as its maternal-zygotic loss causes failed cytokinesis, increased duration of the cell cycle, weaker embryo compaction, and reduced differentiation, whereas *Myh10* (NMHC II-B) maternal-zygotic loss is much less severe. Double maternal-zygotic mutants for *Myh9* and *Myh10* show a much stronger phenotype, failing most of the attempts of cytokinesis. We found that morphogenesis and fate specification are affected but nevertheless carry on in a timely fashion, regardless of the impact of the mutations on cell number. Strikingly, even when all cell divisions fail, the resulting single-celled embryo can initiate trophoctoderm differentiation and lumen formation by accumulating fluid in increasingly large vacuoles. Therefore, contractility mutants reveal that fluid accumulation is a cell-autonomous process and that the preimplantation program carries on independently of successful cell division.

*For correspondence:
jean-leon.maitre@curie.fr

†These authors contributed
equally to this work

Competing interest: See
page 23

Funding: See page 23

Received: 18 March 2021

Accepted: 28 March 2021

Published: 19 April 2021

Reviewing editor: Edward E
Morrisey, University of
Pennsylvania, United States

© Copyright Schliffka et al. This
article is distributed under the
terms of the [Creative Commons
Attribution License](https://creativecommons.org/licenses/by/4.0/), which
permits unrestricted use and
redistribution provided that the
original author and source are
credited.

Introduction

During embryonic development, cells execute their genetic program to build organisms with the correct cell fate, shape, position, and number. In this process, the coordination between cell proliferation, differentiation, and morphogenesis is crucial. In mice, the early blastocyst initially consists of 32 cells distributed among the trophoctoderm (TE) and inner cell mass (ICM), with squamous TE cells enveloping the ICM and a lumen called the blastocoel (*Frankenberg et al., 2016; Plusa and Piliszek, 2020; Rossant, 2016*). Starting from the zygote, the early blastocyst forms after five cleavage divisions, three morphogenetic movements, and two lineage commitments (*Maître, 2017; White et al., 2018; Zhang and Hiragi, 2018*). Differentiation and morphogenesis are coupled by the formation of a domain of apical material after the third cleavage (*Ziomek and Johnson, 1980*). The apical domain promotes differentiation into TE by counteracting signals from cell-cell contacts, which control the nuclear localization of the co-transcriptional activator Yap (*Hirate et al., 2013; Nishioka et al., 2009; Wicklow et al., 2014*). The apical domain also guides cell division orientation

(Dard et al., 2009; Korotkevich et al., 2017; Niwayama et al., 2019) and contact rearrangements (Maître et al., 2016), which is key for positioning cells at the embryo surface or interior. Morphogenesis and cleavages are concomitant and appear synchronized with compaction starting after the third cleavage, internalization after the fourth, and lumen opening after the fifth. Beyond this apparent coordination, the existence of a coupling between cleavages and morphogenesis requires further investigations.

Actomyosin contractility is a conserved instrument driving animal morphogenesis (Heisenberg and Bellaïche, 2013; Lecuit and Yap, 2015) and cytokinesis (Ramkumar and Baum, 2016). Recent studies have suggested key contributions of actomyosin contractility during all the morphogenetic steps leading to the formation of the blastocyst (Özgüç and Maître, 2020). During the 8-cell stage, increased contractility at the cell-medium interface pulls blastomeres together and compacts the embryo (Maître et al., 2015). Also, cells form an apical domain that inhibits actomyosin contractility (Maître et al., 2016; Zhu et al., 2017). During the fourth cleavage, the asymmetric inheritance of this domain leads sister cells to exhibit distinct contractility (Anani et al., 2014; Maître et al., 2016). This causes the most contractile blastomeres to internalize and adopt ICM fate, while weakly contractile cells are stretched at the surface of the embryo and become TE (Maître et al., 2016; Samarage et al., 2015). When the blastocoel fluid starts to accumulate, these differences in contractility between ICM and TE cells guide the fluid away from ICM-ICM cell-cell contacts (Dumortier et al., 2019). Finally, contractility has been proposed to control the size of the blastocoel negatively by increasing the tension of the TE and positively by reinforcing cell-cell adhesion via mechanosensing (Chan et al., 2019). Together, these findings highlight actomyosin as a major engine powering blastocyst morphogenesis.

To change the shape of animal cells, myosin motor proteins contract a network of cross-linked actin filaments, which can be tethered to the plasma membrane, adherens junctions, and/or focal adhesions (Murrell et al., 2015). This generates tension, which cells use to change shape and tissue topology (Clark et al., 2013; Salbreux et al., 2012). Among myosin motors, non-muscle myosin II are the key drivers of cell shape changes (Zaidel-Bar et al., 2015). Non-muscle myosin II complexes assemble from myosin regulatory light chains, myosin essential light chains, and non-muscle myosin heavy chains (NMHCs) (Vicente-Manzanares et al., 2009). NMHCs are responsible for generating the power stroke and exist in three distinct paralogs in mice and humans: NMHC II-A, II-B, and II-C, encoded by the genes *Myh9/MYH9*, *Myh10/MYH10*, and *Myh14/MYH14* (Conti et al., 2004). Distinct paralogs co-assemble into the same myosin mini-filaments (Beach et al., 2014) and, to some extent, seem to have redundant actions within the cells. However, several in vitro studies point to specific roles of NMHC paralogs. For example, MYH9 plays a key role in setting the speed of furrow ingression during cytokinesis (Taneja et al., 2020; Yamamoto et al., 2019) and is essential to drive bleb retraction (Taneja and Burnette, 2019). During cell-cell contact formation, MYH9 was found essential for cadherin adhesion molecule clustering and setting contact size while MYH10 would be involved in force transmissions across the junction and would influence contact rearrangements (Heuzé et al., 2019; Smutny et al., 2010).

These studies at the subcellular level and at a short timescale complement those at the organismal level and at a long timescale. In mice, the zygotic knockout of *Myh14* causes no obvious phenotype with animals surviving to adulthood with no apparent defect (Ma et al., 2010), whereas the loss of either *Myh9* (Conti et al., 2004) or *Myh10* (Tullio et al., 1997) is embryonic lethal. *Myh9* zygotic knockout embryos die at E7.5 due to visceral endoderm adhesion defects (Conti et al., 2004). *Myh10* zygotic knockout mice die between E14.5 and P1 because of heart, brain, and liver defects (Tullio et al., 1997). In addition, knocking out both *Myh10* and *Myh14* can lead to abnormal cytokinesis (Ma et al., 2010). Elegant gene replacement experiments have also revealed insights into partial functional redundancy between *Myh9* and *Myh10* during development (Wang et al., 2010). However, despite the prominent role of actomyosin contractility during preimplantation development (Ma et al., 2010), the specific functions of NMHC paralogs remain largely unknown. Previous genetic studies have relied on zygotic knockouts (Conti et al., 2004; Ma et al., 2010; Tullio et al., 1997), which do not remove the maternally deposited mRNA and proteins of the deleted genes. This often hides the essential functions of genes during preimplantation morphogenesis, as is the case, for example, with the cell-cell adhesion molecule CDH1 (Stephenson et al., 2010). Moreover, NMHCs could have redundant functions, and gene deletions may trigger compensation mechanisms, which would obscure the function of essential genes (Rossi et al., 2015).

In this study, we generated maternal-zygotic deletions of single or double NMHC genes to investigate the molecular control of contractile forces during preimplantation development. We used nested time-lapse microscopy to quantitatively assess the effect of maternal-zygotic deletions at different timescales. This reveals the dominant role of MYH9 over MYH10 in generating the contractility that shapes the mouse blastocyst. In addition, double maternal-zygotic *Myh9* and *Myh10* knockout reveals compensatory mechanisms provided by MYH10 in generating enough contractility for cytokinesis when MYH9 is absent. Moreover, the maternal-zygotic knockout of both *Myh9* and *Myh10* can cause embryos to fail all five successive cleavages, resulting in syncytial single-celled embryos. These single-celled embryos nevertheless initiate lineage specification and blastocoel formation by accumulating fluid into intracellular vacuoles. Therefore, double maternal-zygotic NMHC mutants reveal that fluid accumulation in the blastocyst is a cell-autonomous process. Finally, we confirm this surprising finding by fusing all blastomeres of wild-type (WT) embryos, thereby forming single-celled embryos, which accumulate fluid into inflating vacuoles.

Results

NMHC paralogs during preimplantation development

As in humans, the mouse genome contains three genes encoding NMHCs: *Myh9*, *Myh10*, and *Myh14*. To decipher the specific contributions of NMHC paralogs to preimplantation development, we first investigated the expression of *Myh9*, *Myh10*, and *Myh14*.

We performed real-time quantitative PCR (qPCR) at four different stages in order to cover the levels of transcripts at key steps of preimplantation development. We detected high levels of *Myh9* mRNA throughout preimplantation development (**Figure 1A**). Importantly, transcripts of *Myh9* are by far the most abundant among NMHCs at the zygote stage (E0.5), which suggests that *Myh9* is the main NMHC paralog provided maternally. *Myh10* mRNA is detected at very low levels in zygotes before it reaches comparable levels to *Myh9* mRNA at the morula stage (**Figure 1A**). We found that *Myh14* is not expressed during preimplantation stages (**Figure 1A**). Since *Myh14* homozygous mutant mice are viable and show no apparent defects (*Ma et al., 2010*), *Myh14* is unlikely to play an

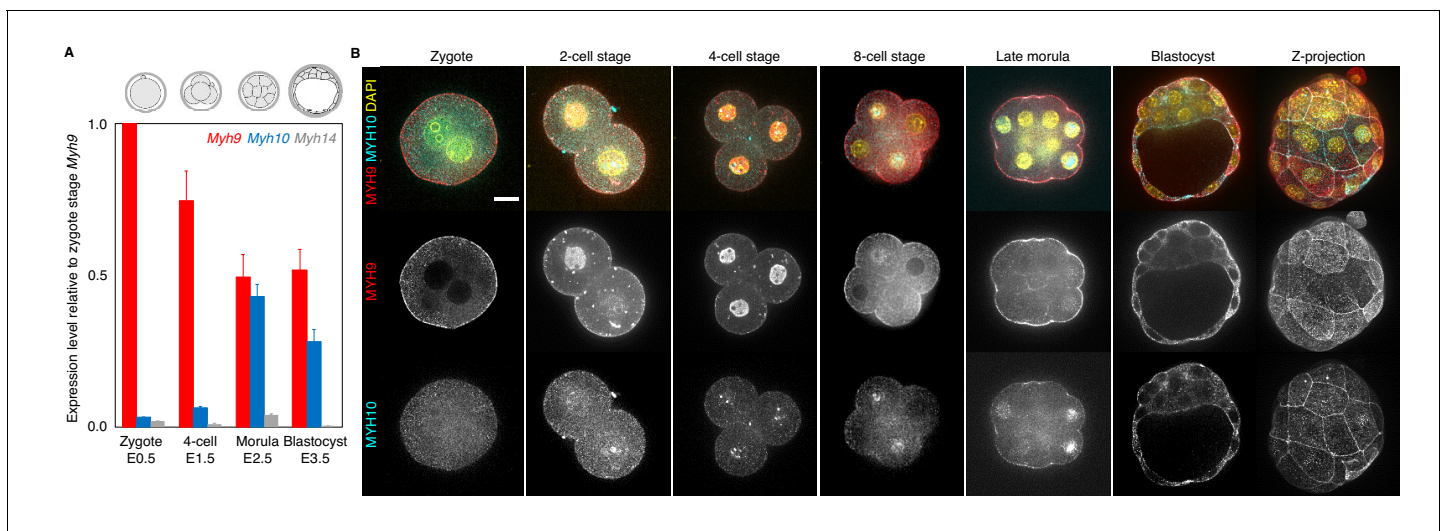


Figure 1. Expression of non-muscle myosin II heavy chain (NMHC) paralogs during preimplantation development. (A) RT-qPCR of *Myh9* (red), *Myh10* (blue), and *Myh14* (grey) at the zygote (E0.5, n = 234), four-cell (E1.5, n = 159), morula (E2.5, n = 189), and blastocyst (E3.5, n = 152) stages from six independent experiments. Gene expression is normalized to *Gapdh* and shown as the mean \pm SEM fold change relative to *Myh9* at the zygote stage. (B) Representative images of immunostaining of NMHC paralogs MYH9 (red) and MYH10 (cyan) throughout preimplantation development. DAPI in yellow. Scale bar, 20 μ m.

The online version of this article includes the following figure supplement(s) for figure 1:

Figure supplement 1. Analysis of the expression of non-muscle myosin II heavy chain (NMHC) paralogs during preimplantation development based on single cell RNA sequencing and MYH9-GFP fluorescence.

important role in preimplantation development. These qPCR measurements show similar trends to available mouse single cell RNA sequencing (scRNA-seq) data (**Figure 1—figure supplement 1A**; [Deng et al., 2014](#)). In humans, scRNA-seq data indicate similar expression levels between *MYH9* and *MYH10* during preimplantation development and, as in mice, the absence of *MYH14* expression (**Figure 1—figure supplement 1B**; [Yan et al., 2013](#)). This points to a conserved regulation of NMHC paralogs in mouse and human preimplantation development.

At the protein level, immunostaining of MYH9 becomes visible at the cortex of blastomeres from the zygote stage onwards (**Figure 1B**). On the other hand, MYH10 becomes detectable at the earliest at the 16-cell stage (**Figure 1B**). Finally, we used transgenic mice expressing endogenously tagged MYH9-GFP to assess the relative parental contributions of MYH9 protein (**Figure 1—figure supplement 1C–D**). Embryos coming from MYH9-GFP females show highest levels of fluorescence at the zygote stage, consistent with our qPCR measurement and scRNA-seq data (**Figure 1A, Figure 1—figure supplement 1A**). MYH9-GFP produced from the paternal allele is detected at the 4-cell stage and increases until blastocyst stage, reaching levels comparable to blastocyst coming from MYH9-GFP females (**Figure 1—figure supplement 1C–D**).

Together, we conclude that MYH9 and MYH10 are the most abundant NMHCs during mouse and human preimplantation development and that MYH9 is heavily maternally provided at both the transcript and protein level in the mouse embryo (**Figure 1, Figure 1—figure supplement 1**).

Preimplantation development of single maternal-zygotic *Myh9* or *Myh10* mutant embryos

Initial studies of *Myh9* or *Myh10* zygotic knockouts have reported that single zygotic knockouts are able to implant, suggesting they are able to form a functional blastocyst ([Conti et al., 2004](#); [Tullio et al., 1997](#)). A potential lack of phenotype could be due to maternally provided products, which are most abundant in the case of *Myh9* (**Figure 1, Figure 1—figure supplement 1**). To eliminate this contribution, we used *Zp3^{Cre/+}* mediated maternal deletion of conditional knockout alleles of *Myh9* and *Myh10*. This generated either maternal-zygotic (mz) homozygous or maternal only (m) heterozygous knockout embryos for either *Myh9* or *Myh10*. Embryos were recovered at E1.5, imaged throughout the rest of their preimplantation development, stained, and genotyped once WT embryos reached the blastocyst stage. We implemented a nested time-lapse protocol to image each embryo at the long (every 30 min for about 50 hr) and short (every 5 s for 10 min twice for each embryo around the time of their 8-cell stage) timescales. This imaging protocol allowed us to visualize the effect of actomyosin contractility at multiple timescales, as it is involved in pulsatile contractions, cytokinesis, and morphogenesis, which take place on timescales of tens of seconds, minutes, and hours, respectively ([Maître et al., 2015](#); [Maître et al., 2016](#)).

The first visible phenotype concerns the zona pellucida (ZP), which encapsulates the preimplantation embryo. WT and maternal *Myh10* mutants have a spherical ZP, whereas maternal *Myh9* mutants show an irregularly shaped ZP (**Figure 2—figure supplement 1A,B**). This suggests a previously unreported role of contractility in the formation of the ZP during oogenesis that is mediated specifically by maternal MYH9. The abnormally shaped ZP could cause long-term deformation of the embryo, as previous studies indicate that the ZP can influence the shape of the embryo at the blastocyst stage ([Kurotaki et al., 2007](#); [Motosugi et al., 2005](#)).

During compaction, angles formed at the surface of contacting cells increase as blastomeres are pulled into closer contact (**Figure 2A**). In WT embryos, contact angles increase from $87 \pm 3^\circ$ to $147 \pm 2^\circ$ during the 8-cell stage between the third and the fourth cleavage (mean \pm SEM from the end of the last cleavage of the third wave to the first one of the fourth wave, 23 embryos, **Figure 2A–B, Appendix 1—table 1–2, Figure 2—video 1**), as measured previously ([Maître et al., 2015](#); [Zhu et al., 2017](#)). In mzMyh9 embryos, contact angles only grow from $85 \pm 2^\circ$ to $125 \pm 4^\circ$ (mean \pm SEM, 15 embryos, **Figure 2A–B, Appendix 1—table 1–2**). This reduced ability to compact is in agreement with previous measurements on heterozygous mMyh9 embryos, which generate a lower surface tension, and therefore cannot efficiently pull cells into closer contact ([Maître et al., 2016](#)). During the 8-cell stage, mzMyh10 embryos initially grow their contacts from $87 \pm 5^\circ$ to $121 \pm 4^\circ$, similarly to mzMyh9 embryos (mean \pm SEM, 11 embryos, **Figure 2A–B, Appendix 1—table 1**). However, unlike mzMyh9 embryos, mzMyh10 embryos continue to increase their contact size and reach compaction levels identical to WT embryos by the end of the 16-cell stage ($148 \pm 4^\circ$, mean \pm SEM, 11 embryos, **Figure 2A–B, Appendix 1—table 1**). Importantly, heterozygous mMyh9

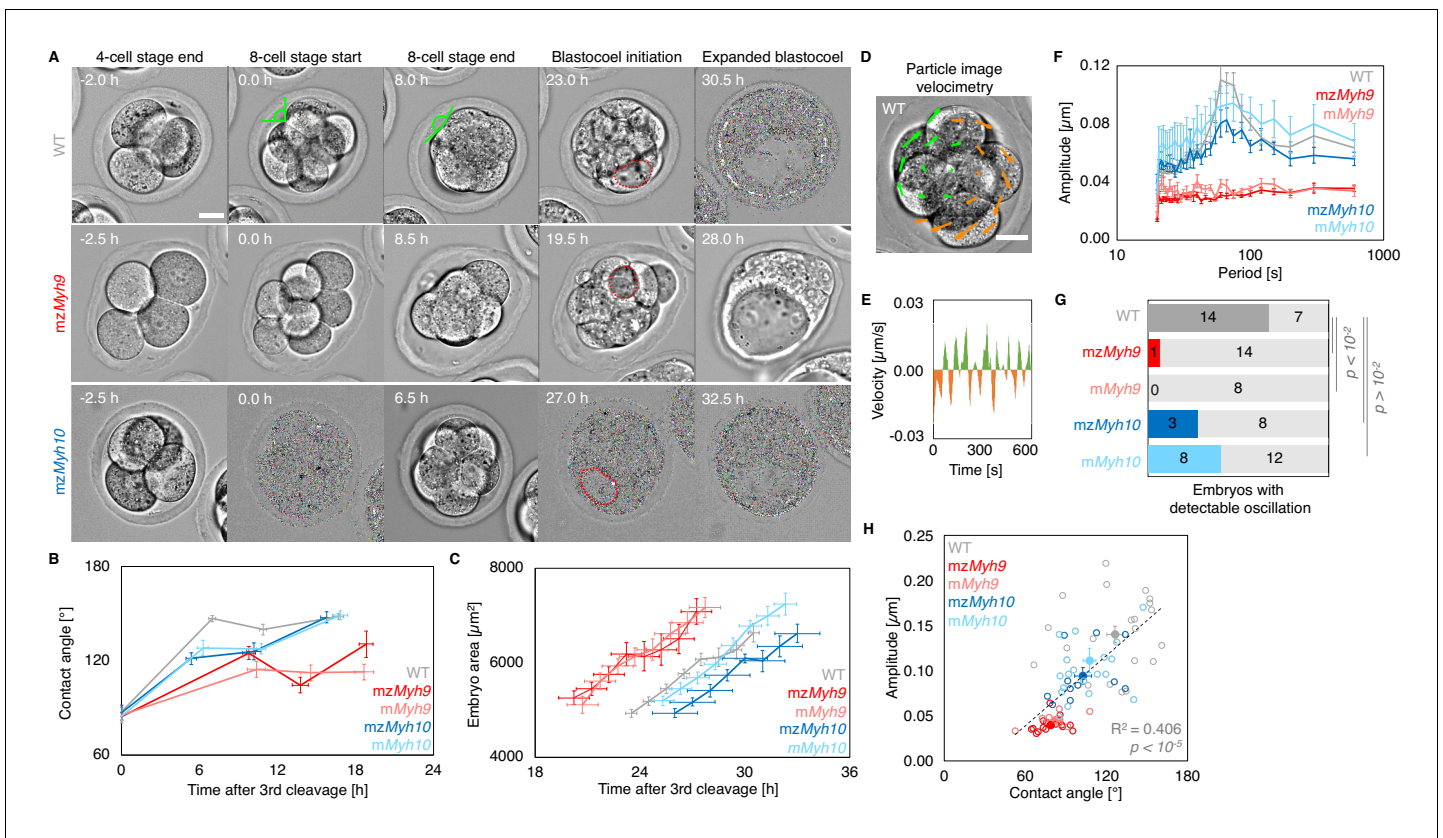


Figure 2. Multiscale analysis of morphogenesis in single maternal-zygotic *Myh9* or *Myh10* mutant embryos. (A) Representative images of long-term time-lapse of WT, *mzMyh9*, and *mzMyh10* embryos at the end of the 4-cell stage, start and end of the 8-cell stage, at the initiation of blastocoel formation and early blastocyst stage (see also **Figure 2—video 1**). Scale bar, 20 μm . Time in hours after the third cleavage. Green lines mark the contact angles increasing during compaction. Dotted red lines indicate the nascent lumen. (B) Contact angle of WT (grey, $n = 23, 23, 21, 22$), *mzMyh9* (red, $n = 15, 15, 10, 8$), *mMyh9* (light red, $n = 8, 8, 8, 3$), *mzMyh10* (blue, $n = 11, 11, 11, 11$), and *mMyh10* (light blue, $n = 20, 20, 20, 20$) embryos after the third cleavage, before and after the fourth cleavage and before the fifth cleavage. Data show mean \pm SEM. Statistical analyses are provided in **Appendix 1—table 1–2**. (C) Embryo growth during lumen formation of WT (grey, $n = 20$), *mzMyh9* (red, $n = 9$), *mMyh9* (light red, $n = 7$), *mzMyh10* (blue, $n = 7$), and *mMyh10* (light blue, $n = 13$) embryos measured for seven continuous hours after a lumen of at least 20 μm in diameter is observed. Data show mean \pm SEM. (D) Representative image of a short-term time-lapse overlaid with a subset of velocity vectors from Particle Image Velocimetry (PIV) analysis. Green for positive and orange for negative Y-directed movement. (E) Velocity over time for a representative velocity vector of embryo shown in D and **Figure 2—video 2**. (F) Power spectrum resulting from Fourier transform of PIV analysis of WT (grey, $n = 21$), *mzMyh9* (red, $n = 17$), *mMyh9* (light red, $n = 8$), *mzMyh10* (blue, $n = 11$), and *mMyh10* (light blue, $n = 20$) embryos. Data show mean \pm SEM. (G) Proportion of WT (grey, $n = 21$), *mzMyh9* (red, $n = 17$), *mMyh9* (light red, $n = 8$), *mzMyh10* (blue, $n = 11$), and *mMyh10* (light blue, $n = 20$) embryos showing detectable oscillations in their power spectrum (see ‘Materials and methods’). Chi² p value comparing to WT is indicated. (H) Amplitude of oscillation as a function of the mean contact angle for WT (grey, $n = 21$), *mzMyh9* (red, $n = 17$), *mMyh9* (light red, $n = 8$), *mzMyh10* (blue, $n = 11$), and *mMyh10* (light blue, $n = 20$) embryos. Open circles show individual embryos and filled circles give mean \pm SEM of a given genotype. Pearson’s R^2 and p value are indicated. Statistical analyses are provided in **Appendix 1—table 3**.

The online version of this article includes the following video and figure supplement(s) for figure 2:

Figure supplement 1. Macroscopic shape analysis of maternal-zygotic *Myh9* and *Myh10* mutant embryos.

Figure supplement 2. Morphogenesis of embryos with blastomeres fused at the 4-cell stage.

Figure 2—video 1. Preimplantation development of WT, *mzMyh9*, and *mzMyh10* embryos.

<https://elifesciences.org/articles/68536#fig2video1>

Figure 2—video 2. Periodic waves of contraction in WT, *mzMyh9*, *mzMyh10*, and *mzMyh9;mzMyh10* embryos.

<https://elifesciences.org/articles/68536#fig2video2>

Figure 2—video 3. Failed cleavage in *mzMyh9* embryos.

<https://elifesciences.org/articles/68536#fig2video3>

Figure 2—video 4. Preimplantation development of control, $\frac{3}{4}$, and $\frac{1}{2}$ cell number embryos.

<https://elifesciences.org/articles/68536#fig2video4>

or *mMyh10* embryos show similar phenotypes to their respective homozygous counterparts (**Figure 2B**, **Appendix 1—table 1–2**), suggesting that maternal loss dominates for both NMHC paralogs and that the paternal allele makes little difference. Together, we conclude that maternal MYH9 is essential for embryos to compact fully, whereas MYH10 only regulates the rate of compaction.

During the 8-cell stage, contractility becomes visible on the short timescale as periodic contractions, which we can use to gauge the specific contribution of NMHCs (**Maître et al., 2015; Maître et al., 2016**). We performed particle image velocimetry (PIV) and Fourier analysis to evaluate the period and amplitude of periodic movements (**Figure 2D–F; Maître et al., 2015**). While 14/21 WT embryos displayed periodic contractions, these were rarely detected in *Myh9* mutants (1/15 *mzMyh9* and 0/8 *mMyh9* embryos) and occasionally in *Myh10* mutants (3/11 *mzMyh10* and 8/20 *mMyh10* embryos; **Figure 2G**, **Figure 2—video 2**). This suggests that contractility is reduced after maternal loss of *Myh10* and is greatly reduced following maternal loss of *Myh9*. This hierarchy in the phenotypes of the NMHC paralog mutants parallels the one observed on the long timescale during compaction (**Figure 2B**). In fact, we found that the amplitude of periodic contractions correlates with the contact angle across the genotypes we considered (**Figure 2H**, 78 embryos, Pearson's $R = 0.637$, $p < 10^{-5}$, **Appendix 1—table 3**). This analysis across timescales reveals the continuum between the short-term impact of *Myh9* or *Myh10* loss onto contractile movements and the long-term morphogenesis, as previously observed for internalizing ICM cells (**Maître et al., 2016**).

We also noted that the duration of the 8-cell stage is longer in embryos lacking maternal *Myh9* (9.8 ± 0.5 hr from the third to the fourth wave of cleavages, mean \pm SEM, 15 embryos) as compared to WT (7.0 ± 0.3 hr, mean \pm SEM, 23 embryos; **Figure 2A,B**, **Appendix 1—tables 1–2**, **Figure 2—video 1**). This is not the case for the duration of the fourth wave of cleavages or the ensuing 16-cell stage, which are similar in these different genotypes (**Appendix 1—table 2**). On the long timescale, longer cell cycles could affect the number of cells in *Myh9* mutants. Indeed, when reaching the blastocyst stage, *mzMyh9* embryos count less than half the number of cells than WT (58.1 ± 2.9 cells in 23 WT embryos, as compared to 25.2 ± 2.8 cells in 15 *mzMyh9* embryos, Mean \pm SEM; **Figure 3B**). In the time-lapse movies, we did not observe cell death, which could, in principle, also explain a reduced cell number at the blastocyst stage. On the other hand, we did observe reverting cleavages in maternal *Myh9* mutants (**Figure 2—video 3**), effectively reducing cell number at the blastocyst stage. Loss of MYH9 is likely to cause difficulties during cytokinesis (**Taneja et al., 2020; Yamamoto et al., 2019**), which could in turn impact cell cycle progression (**Figure 2B**) and explain the significant reduction in cell number in *mzMyh9* embryos. As for *mzMyh10* embryos, we do not observe any cell cycle delay and count blastocysts with the correct cell number (**Figure 2B** and **Figure 3B**), indicating that MYH9 is the primary NMHC powering cytokinesis during mouse preimplantation development.

The second morphogenetic movement consists in the positioning of cells on the inside of the embryo after the fourth cleavage division to form the first lineages of the mammalian embryo. To see if this process is affected in NMHC mutants, we counted the number of inner and outer cells on immunostaining at the blastocyst stage (**Figure 3A–C**). Despite showing less than half the expected cell number, *mzMyh9* blastocysts show the same proportion of inner and outer cells as WT and *mzMyh10* embryos (**Figure 3C**). This suggests that the remaining contractility is sufficient to drive cell internalization or that oriented cell divisions can mitigate the loss of contractility-mediated internalization (**Korotkevich et al., 2017; Maître et al., 2016; Niwayama et al., 2019**). Outer and inner cells differentiate into TE and ICM, respectively. To assess whether differentiation is affected in NMHC mutants, we performed immunostaining of TE marker CDX2 and ICM marker SOX2 at the blastocyst stage (**Figure 3A; Avilion et al., 2003; Strumpf et al., 2005**). *mzMyh10* embryos display negligible reduction in CDX2 and SOX2 levels compared to WT embryos (**Figure 3E–G**). On the other hand, we found that *mzMyh9* embryos show lower levels of CDX2 in their outer cells, as measured here and previously for *mMyh9* embryos at the 16-cell stage (**Figure 3F; Maître et al., 2016**), and of SOX2 for inner cells compared to WT embryos (**Figure 3G**). This is caused in part by the presence of individual unspecified cells localized both inside and at the surface of *mzMyh9* embryos (**Figure 3D**). To assess whether delayed cell cycle progression may explain the reduced differentiation, we calculated the correlation between the duration of the 8-cell stage and the levels of CDX2 in the TE and of SOX2 in the ICM. This correlation is poor for all maternal *Myh9* mutants (Pearson's

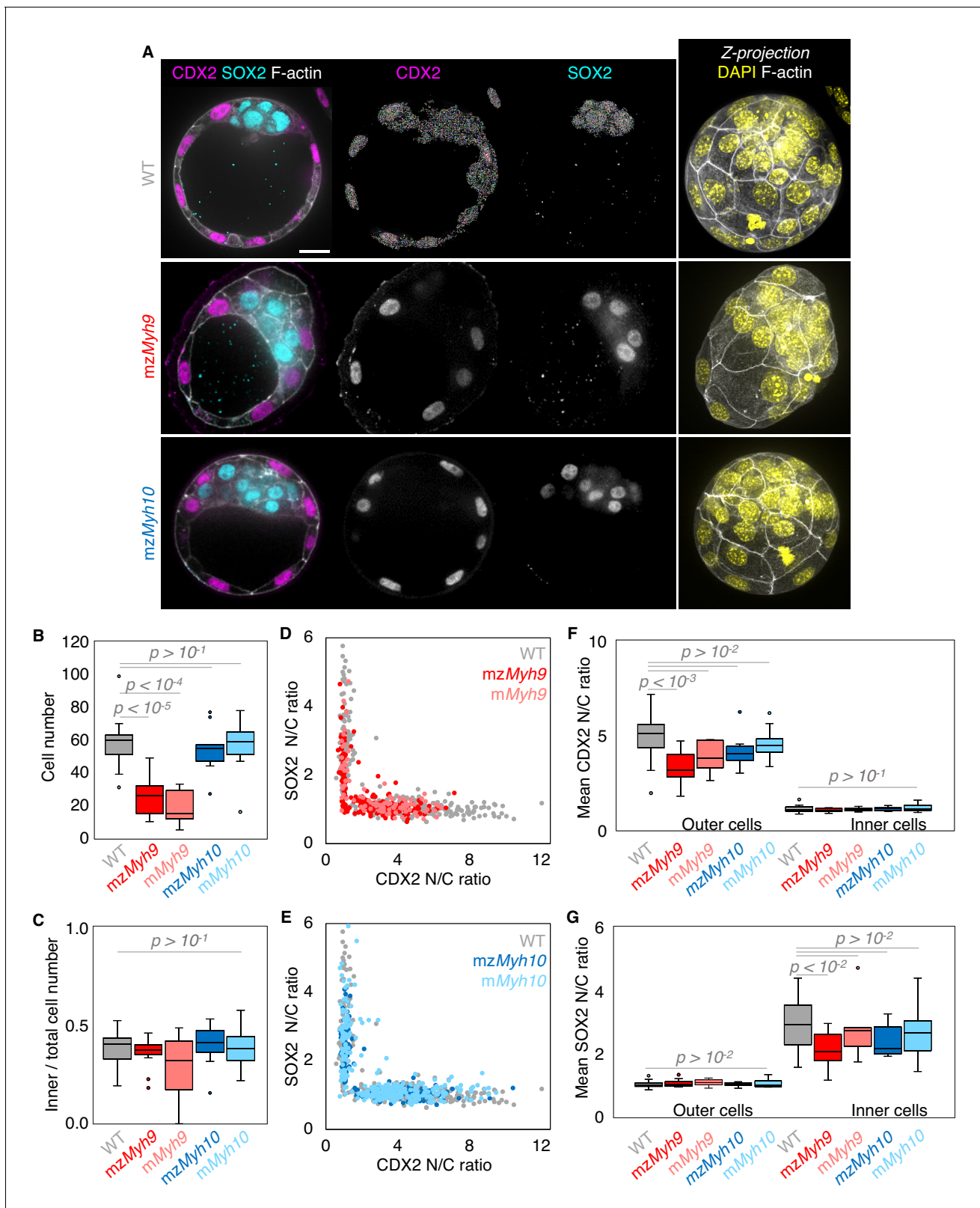


Figure 3. Analysis of TE and ICM lineages in single maternal-zygotic *Myh9* or *Myh10* mutant embryos. (A) Representative images of WT, mzMyh9, and mzMyh10 embryos stained for TE and ICM markers CDX2 (magenta) and SOX2 (cyan), DAPI (yellow), and F-actin (grey). The same mutant embryos as in **Figure 2A** are shown. Scale bar, 20 μ m. (B-C) Total cell number (B) and proportion of inner cells (C) in WT (grey, n = 23), mzMyh9 (red, n = 15), mMyh9 (light red, n = 8), mzMyh10 (blue, n = 11), and mMyh10 (light blue, n = 19) embryos. (D-E) Nuclear to cytoplasmic (N/C) ratio of CDX2 and SOX2

Figure 3 continued on next page

Figure 3 continued

staining for individual cells from WT (grey, n = 345), mzMyh9 (red, n = 204), mMyh9 (light red, n = 95), mzMyh10 (blue, n = 160), and mMyh10 (light blue, n = 300) embryos. (F-G) Average N/C ratio of CDX2 (F) and SOX2 (G) staining for outer (left) or inner (right) cells from WT (grey, n = 23), mzMyh9 (red, n = 15), mMyh9 (light red, n = 8), mzMyh10 (blue, n = 11), and mMyh10 (light blue, n = 19) embryos. Mann-Whitney U test p values compared to WT are indicated.

The online version of this article includes the following figure supplement(s) for figure 3:

Figure supplement 1. Analysis of YAP localization in maternal-zygotic Myh9 and Myh10 mutant embryos.

Figure supplement 2. Lineage specification of embryos with blastomeres fused at the 4-cell stage.

$R = -0.193$ for CDX2 and -0.076 for SOX2, 22 embryos, $p > 10^{-2}$), which does not support reduced differentiation levels due to cell cycle delay.

To assess whether signalling upstream of CDX2 and SOX2 expression is affected in NMHC mutants, we stained embryos for the co-transcriptional activator YAP (Hirate et al., 2013; Nishioka et al., 2009; Royer et al., 2020; Wicklow et al., 2014). In WT embryos, YAP is enriched specifically in the nuclei of TE cells (Figure 3—figure supplement 1; Hirate et al., 2013; Nishioka et al., 2009; Wicklow et al., 2014). Consistent with CDX2 and SOX2 levels, YAP localization is unaffected in mzMyh10 mutants and reduced in mzMyh9 mutants (Figure 3—figure supplement 1), as observed previously in mMyh9 mutants at the 16-cell stage (Maître et al., 2016). In the mouse preimplantation embryo, the nuclear localization of YAP is promoted by signals from the apical domain (Hirate et al., 2013). ML7 treatment, which inhibits the myosin light chain kinase, suggests that contractility may be required for apical domain formation (Zhu et al., 2017). However, immunostaining of apico-basal markers reveals that, as in WT, mzMyh9 and mzMyh10 embryos accumulate the apical marker PRKCz at the embryo surface (Figure 4; Hirate et al., 2013). Also, basolateral markers such as the adhesion molecule CDH1 or members of the fluid transport machinery, such as the ATP1A1 subunit of the Na/K pump and aquaporin AQP3, are enriched at basolateral membranes of WT, mzMyh9, and mzMyh10 embryos alike (Figure 4; Barcroft et al., 2003; Barcroft et al., 2004; Dumortier et al., 2019; Stephenson et al., 2010). Together, these findings suggest that MYH9-mediated contractility is required for the correct expression of lineage markers downstream of YAP but dispensable for the establishment of apico-basal polarity.

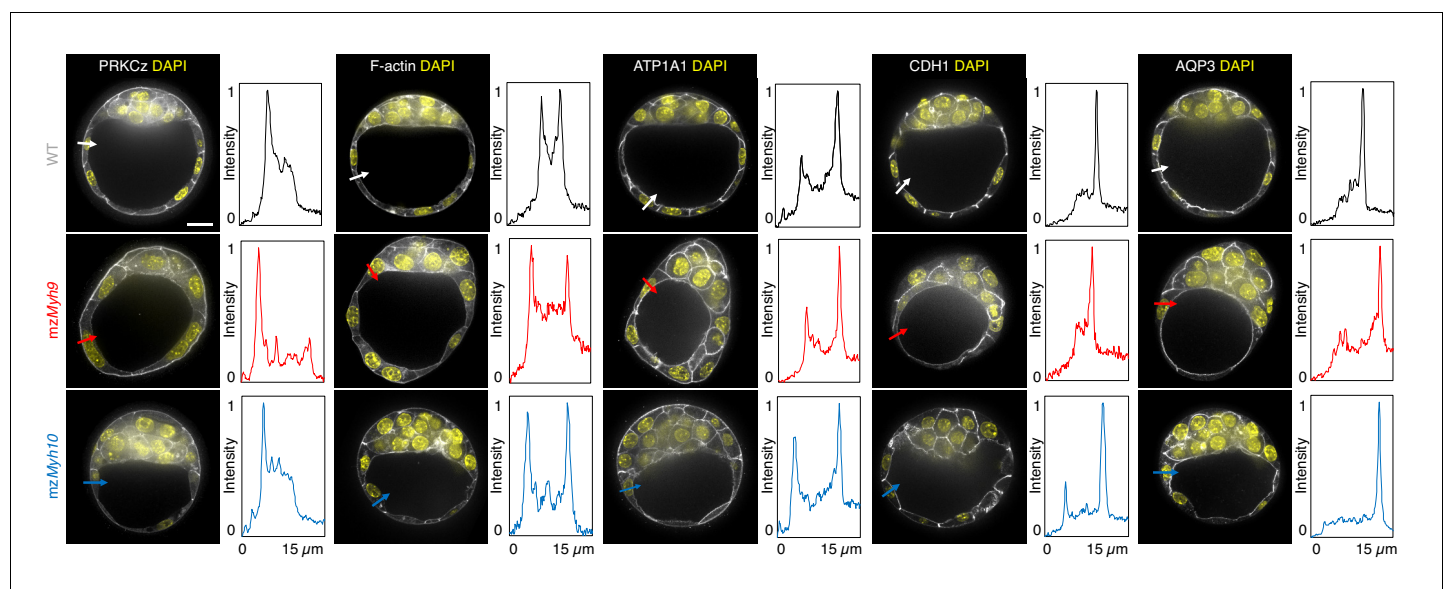


Figure 4. Apico-basal polarity of single maternal-zygotic Myh9 or Myh10 mutant embryos. Representative images of WT, mzMyh9, and mzMyh10 embryos stained for apico-basal polarity markers. From left to right: PRKCz, F-actin, ATP1A1, CDH1, and AQP3 shown in grey. Nuclei stained with DAPI are shown in yellow. Intensity profiles of a representative 15 µm line drawn from the embryo surface towards the interior are shown next to each marker and genotype (arrows). Intensities are normalized to each minimal and maximal signals. Scale bar, 20 µm.

Apico-basal polarity is essential for the final morphogenetic step shaping the blastocyst: the formation of the first mammalian lumen. After the fifth cleavage, the growth of the blastocoel inflates and increases the projected area of WT embryos steadily at $3.9 \pm 0.5 \mu\text{m}^2/\text{min}$ (mean \pm SEM, 20 embryos; **Figure 2C**, **Figure 2—video 1**). During lumen formation, *mzMyh9* and *mzMyh10* embryos inflate at 3.9 ± 1.0 and $4.0 \pm 0.5 \mu\text{m}^2/\text{min}$, respectively, which is similar to WT embryos (mean \pm SEM, 9 and 7 embryos; Student's *t* test compared to WT $p > 10^{-2}$, **Figure 2C**). This suggests that blastocoel expansion rate is unaffected in NMHC mutants. Importantly, we observe that the time of lumen opening in *mzMyh9* embryos is not delayed compared to WT embryos (**Figure 2A–C**). In fact, relative to the time of third cleavage, the lumen inflates on average at an earlier stage in *mzMyh9* embryos than in WT (**Figure 2C**). Some *mzMyh9* embryos begin inflating their lumen before the fifth wave of cleavages (5/11; **Figure 2—video 1**), while all WT and *mzMyh10* embryos begin lumen formation after the first cleavages of the fifth wave. This argues against *mzMyh9* embryos having a global delay in their development, despite their longer cell cycles, lower cell number (**Figure 2B** and **Figure 3B**), and impaired differentiation (**Figure 3D,F–G**). Finally, when the lumen becomes sufficiently large, embryos come into contact with the ZP. 3D segmentation of blastocysts reveals that embryos with mutated maternal *Myh9* alleles become less spherical than those with a WT allele (**Figure 2—figure supplement 1C–F**). In fact, the shape of the ZP of mutant embryos at the 2-cell stage correlates with the shape of embryos at the blastocyst stage (**Figure 2—figure supplement 1G**; 67 embryos from all genotypes combined but WT, Pearson's $R = -0.739$, $p < 10^{-2}$), which suggests that the misshapen ZP could deform the embryo. This is consistent with previous studies reporting on *Myh9* mutant embryos being more deformable than WT (Maître et al., 2016) and on the influence of the ZP on the shape of the blastocyst (Kurotaki et al., 2007; Motosugi et al., 2005). Experimental deformation of the embryo was reported to affect cell fate (Niwayama et al., 2019; Royer et al., 2020). In the range of deformation of the ZP observed in mutant embryos, we found weak correlations between the shape of the ZP and CDX2 or SOX2 levels (**Figure 2—figure supplement 1H–I**, CDX2 in outer cells of 77 embryos from all genotypes combined but WT, Pearson's $R = 0.315$, $p < 10^{-2}$, SOX2 in the inner cells of 58 embryos, Pearson's $R = 0.223$, $p > 10^{-1}$). This suggests that defects in lineage specification of maternal *Myh9* mutant embryos do not simply result from the deformation of these blastocysts by their ZP. From this multi-scale analysis, we conclude that maternal-zygotic loss of *Myh9* or *Myh10* has little impact on lumen formation and that maternal loss of *Myh9* impacts the shape of the blastocyst indirectly by its initial effect on the structure of the ZP.

Maternal *Myh9* mutants show defective cytokinesis and reduced cell number, which could constitute the cause for the defects in morphogenesis and lineage specification. To separate the effects of impaired contractility and defective cell divisions, we decided to reduce cell number by fusing blastomeres of WT embryos together. Reducing cell number by $\frac{1}{4}$ or $\frac{1}{2}$ at the 4-cell stage results in embryos compacting with the same magnitude and forming a lumen concomitantly to control embryos (**Figure 2—figure supplement 2A–C**, **Figure 2—video 4**, **Figure 3—figure supplement 2B**). Also, embryos with reduced cell numbers differentiate into TE and ICM identically to control embryos as far as lineage proportions and fate marker levels are concerned (**Figure 3—figure supplement 2A,C–E**). Therefore, the morphogenesis and lineage specification defects observed in maternal *Myh9* mutants are not likely to result simply from cytokinesis defects and their impact on cell number.

Together, these analyses reveal the critical role of MYH9 in setting global cell contractility on short and long timescales in order to effectively drive compaction, cytokinesis, and lineage specification. Comparably, the function of MYH10 during early blastocyst morphogenesis is less prominent. Importantly, the similarity of maternal homozygous and maternal heterozygous mutants indicates that the preimplantation embryo primarily relies on the maternal pools of MYH9. We conclude that maternally provided MYH9 is the main NMHC powering actomyosin contractility during early preimplantation development.

Preimplantation development of double maternal-zygotic *Myh9;Myh10* mutants

Despite MYH9 being the main NMHC provided maternally, the successful cleavages, shape changes, and differentiation observed in *mMyh9* and *mzMyh9* embryos suggest that some compensation by MYH10 could occur in these embryos. To test for compensations between the two NMHC paralogs

expressed during preimplantation development, we generated double maternal-zygotic *Myh9* and *Myh10* knockout (mz*Myh9*;mz*Myh10*) embryos.

Nested time-lapse revealed that mz*Myh9*;mz*Myh10* embryos fail most attempts of cytokinesis (**Figure 5A**, **Figure 5—video 1**). In addition to failed cytokinesis, mz*Myh9*;mz*Myh10* embryos show increased cell cycle durations, which are more severe than those for mz*Myh9* embryos (**Figure 5A–B**, **Appendix 1—table 1–2**). This results in mz*Myh9*;mz*Myh10* embryos with only 2.9 ± 0.5 cells when reaching the blastocyst stage (**Figure 6B**). In fact, they occasionally develop into blastocyst-stage embryos consisting of only one single cell (1/8 embryos). Of those which succeed in dividing at least once, compaction after the third cleavage is weak with contact angles for mz*Myh9*;mz*Myh10* embryos capping at $117 \pm 4^\circ$ compared to $147 \pm 2^\circ$ for WT (mean \pm SEM, 3 and 23 embryos; **Figure 5B**, **Appendix 1—table 1**, **Figure 5—video 1**). Consistent with previous observations, periodic contractions are undetectable in any of the double mutants that we analyzed (**Figure 5D–E**, **Figure 2—video 2**). Together, this indicates that double maternal-zygotic *Myh9* and *Myh10* mutants generate extremely weak contractile forces compared to WT and single maternal-zygotic *Myh9* or *Myh10* mutants.

When investigating fate specification (**Figure 6**), CDX2 is present in 5/7 embryos as compared to all the 23 WT embryos we analyzed (**Figure 6F**). SOX2 is only detected when embryos succeed in internalizing at least one cell (**Figure 6A,C–E and G**). No maternal *Myh9*;*Myh10* mutant embryo consisting of only two cells contained an inner cell, half of embryos with 3–5 cells contained a single inner cell, and all embryos with six cells or more contained inner cells (**Figure 6D**). Moreover, the levels of CDX2 in outer cells are reduced compared to WT embryos, as observed previously for single maternal-zygotic *Myh9* mutants. Consistently, YAP is enriched in the nucleus of outer cells, albeit at lower levels than in WT (**Figure 3—figure supplement 1**). As for single mutants, the apical marker PRKCz, F-actin, the cell-cell adhesion molecule CDH1, and members of the fluid-pumping machinery ATP1A1 and AQP3 are correctly apico-basally polarized in double mutants (**Figure 7**). The presence of CDX2, nuclear YAP, and the correct organization of apico-basal polarity suggest that mz*Myh9*;mz*Myh10* embryos can initiate differentiation into TE, the epithelium responsible for making the blastocoel. The ability of mz*Myh9*;mz*Myh10* embryos to create de novo a functional polarized epithelium is further supported by the fact that they can eventually proceed with polarized fluid accumulation and create a blastocoel (**Figure 5A**, **Figure 5—video 1**). As observed in single maternal *Myh9* mutants, mz*Myh9*;mz*Myh10* embryos are not delayed to initiate lumen formation despite their extended cell cycles (**Figure 5C**, **Figure 5—video 1**). Also, we measure that mutant embryos grow at rates that are similar to WT ones (5.8 ± 1.5 and $3.9 \pm 0.5 \mu\text{m}^2/\text{min}$, mean \pm SEM, 5 and 20 embryos, Student's *t* test $p > 10^{-2}$; **Figure 5C**). This indicates that contractility does not influence the initial growth rate of the blastocoel and that blastocoel formation does not require powerful actomyosin contractility.

Finally, we measure similar metrics for all single and double heterozygous *Myh9* and *Myh10* mutant embryos (**Figure 5**, **Figure 6**, **Appendix 1—table 1**), indicating once again that maternal contributions predominantly set the contractility for preimplantation development. We conclude that after the maternal loss of both *Myh9* and *Myh10*, contractility is almost entirely abolished. This effect is much stronger than that after the loss of maternal MYH9 only and suggests that, in single maternal *Myh9* mutants, MYH10 can compensate significantly, which we would not anticipate from our previous single mz*Myh10* knockout analysis. Therefore, despite MYH9 being the main engine of preimplantation actomyosin contractility, MYH10 ensures a substantial part of blastocyst morphogenesis in the absence of MYH9. The nature and extent of this compensation will need further characterization.

Preimplantation development of single-celled embryos

Embryos without maternal MYH9 and MYH10 can fail all successive cleavages when reaching the time of the blastocyst stage (18/53 embryos, all *Myh9* and *Myh10* mutant genotypes combined across seven experiments; **Figure 8A**, **Figure 8—video 1**). In single-celled embryos, multiple cleavage attempts at intervals of 10–20 hr can be observed, suggesting that the cell cycle is still operational in those embryos (**Figure 5—video 1**). This is further supported by the presence of multiple large nuclei in single-celled embryos, indicative of preserved genome replication (**Figure 8C**). Interestingly, these giant nuclei contain CDX2 and YAP, but no SOX2, suggesting that, in addition to the cell cycle, the lineage specification program is still partially operational (**Figure 8C–E**, **Figure 3—**

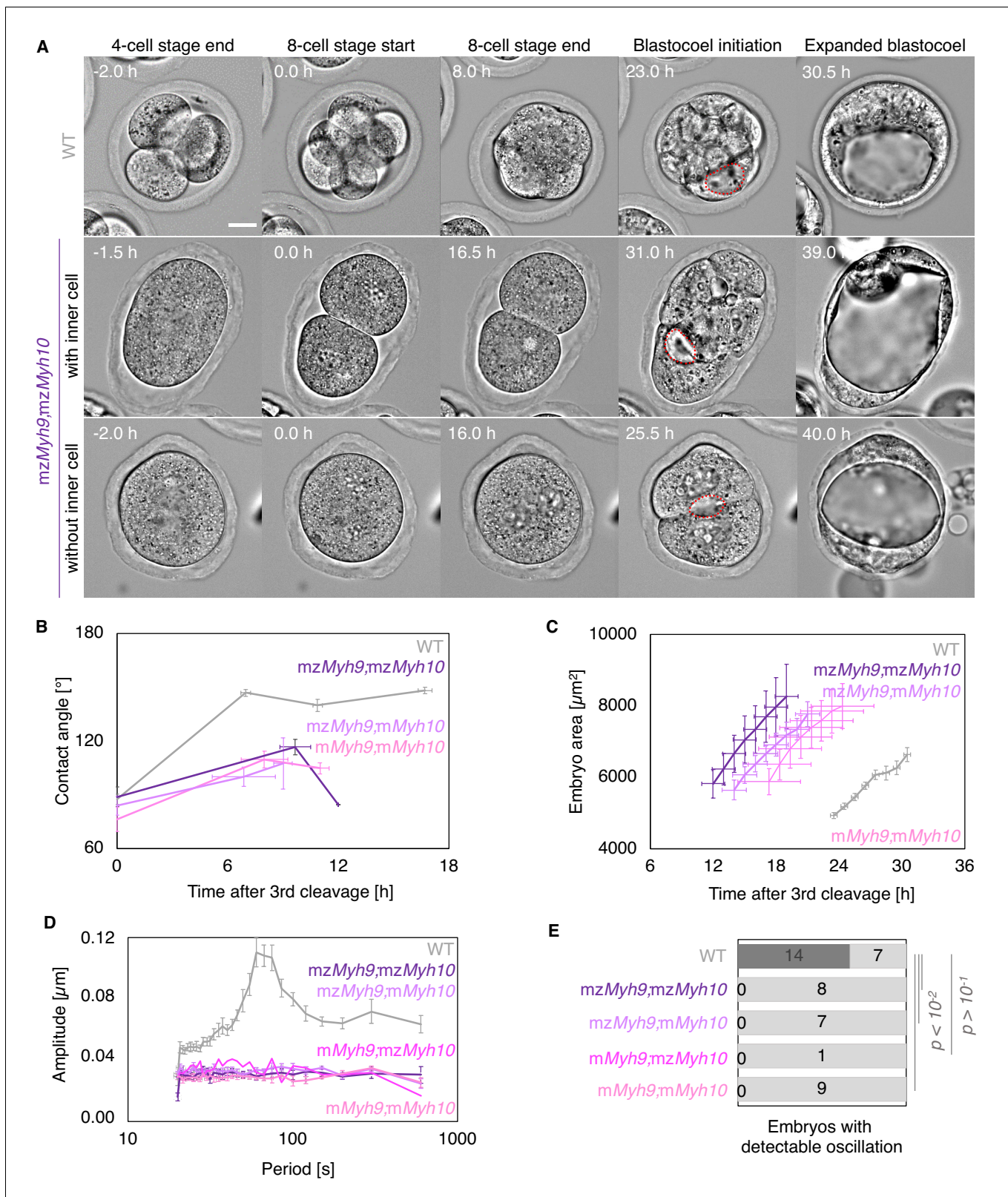


Figure 5. Multiscale analysis of morphogenesis in double maternal-zygotic *Myh9* and *Myh10* mutant embryos. (A) Representative images of long-term time-lapse of WT and *mzMyh9;mzMyh10* embryos at the end of the 4-cell stage, start and end of the 8-cell stage, at the initiation of blastocoel formation, and early blastocyst stage (Figure 5—video 1). The middle row shows an embryo that cleaved once at the time of the third cleavage and twice at the time of the fourth cleavage, which produces an embryo with one inner cell. The bottom row shows an embryo that cleaved once at the

Figure 5 continued on next page

Figure 5 continued

time of the fourth cleavage, which produces an embryo without inner cell. Scale bar, 20 μm . (B) Contact angle of WT (grey, n = 23, 23, 21, 22), *mzMyh9*; *mzMyh10* (purple, n = 7, 3, 1), *mzMyh9*;*mMyh10* (lilac, n = 7, 4, 2), and *mMyh9*;*mMyh10* (bubblemum, n = 7, 5, 3) embryos after the third cleavage, before and after the fourth cleavage, and before the fifth cleavage, when available. Data show mean \pm SEM. Statistical analyses are provided in **Appendix 1—table 1–2**. (C) Embryo growth during lumen formation for WT (grey, n = 20), *mzMyh9*;*mzMyh10* (purple, n = 5), *mzMyh9*;*mMyh10* (lilac, n = 6), and *mMyh9*;*mMyh10* (bubblemum, n = 6) embryos measured for seven continuous hours after a lumen of at least 20 μm is observed. Data show mean \pm SEM. (D) Power spectrum resulting from Fourier transform of PIV analysis of WT (grey, n = 21), *mzMyh9*;*mzMyh10* (purple, n = 8), *mzMyh9*;*mMyh10* (lilac, n = 7), *mMyh9*;*mzMyh10* (pink, n = 1), and *mMyh9*;*mMyh10* (bubblemum, n = 9) embryos. Data show mean \pm SEM. (E) Proportion of WT (grey, n = 21), *mzMyh9*;*mzMyh10* (purple, n = 8), *mzMyh9*;*mMyh10* (lilac, n = 7), *mMyh9*;*mzMyh10* (pink, n = 1), and *mMyh9*;*mMyh10* (bubblemum, n = 9) embryos showing detectable oscillations in their power spectrum. Chi² test p value compared to WT is indicated.

The online version of this article includes the following video for figure 5:

Figure 5—video 1. Preimplantation development of *mzMyh9*;*mzMyh10* embryos.

<https://elifesciences.org/articles/68536#fig5video1>

figure supplement 1). Strikingly, we also observed that at the time of blastocoel formation, single-celled maternal *Myh9* and *Myh10* mutant embryos begin to swell to sizes comparable to normal blastocysts (**Figure 8A–B**, **Figure 8—video 1**). Single-celled embryos then form, within their cytoplasm, tens of fluid-filled vacuolar compartments, which can inflate into structures comparable in size to the blastocoel (**Figure 8A and C**, **Figure 8—video 1**). The membrane of these cytoplasmic vacuoles contains the fluid pumping machinery ATP1A1 and AQP3, which is specific of basolateral membranes in multicellular embryos of all considered genotypes (**Figure 7**; **Barcroft et al., 2003**; **Barcroft et al., 2004**). This indicates that single-celled embryos are able to establish apico-basal polarity and to direct fluid pumping into a basolateral compartment despite the absence of neighbouring cells. When measuring the growth rates of single-celled embryos, we found that they are comparable to the ones of multiple-celled mutant embryos or WT (4.1 ± 0.8 , 5.8 ± 1.5 , and 3.9 ± 0.5 $\mu\text{m}^2/\text{min}$, mean \pm SEM, 4, 5, and 20 embryos, Student's t test $p > 10^{-2}$; **Figure 8B**), indicating that they are able to accumulate fluid as fast as embryos composed of multiple cells. Therefore, single-celled embryos are able to initiate TE differentiation and display some attributes of epithelial function. Unexpectedly, this also indicates that fluid accumulation during blastocoel formation is cell-autonomous. Together, this further indicates that the developmental program entailing morphogenesis and lineage specification carries on independently of successful cleavages.

To further test whether fluid accumulation is cell-autonomous without disrupting actomyosin contractility, we fused all blastomeres at the late morula stage before lumen formation (**Figure 8—figure supplement 1A**, **Figure 8—video 2**). The nuclei from the fused cells displayed high CDX2 and low SOX2 levels, which indicates that fused embryos retain a TE phenotype (**Figure 8—figure supplement 1C–E**). Moreover, similarly to single-celled embryos resulting from the loss of contractility, single-celled embryos resulting from cell fusion grew in size at rates similar to those of control embryos while forming large fluid-filled vacuoles (3.3 ± 0.4 and 3.7 ± 0.4 $\mu\text{m}^2/\text{min}$, 7 and 8 embryos, Student's t test $p > 10^{-2}$; **Figure 8—figure supplement 1A–B**, **Figure 8—video 2**). This further confirms that the initiation of fluid accumulation and its rate during blastocoel morphogenesis can rely entirely on transcellular transport and are independent from cell-cell contacts and its associated paracellular transport.

Together, our experiments with single and double maternal-zygotic NMHC knockout embryos reveal that, while MYH9 is the major NMHC powering sufficient actomyosin contractility for blastocyst morphogenesis, MYH10 can significantly compensate the effect of MYH9 loss onto cytokinesis and compaction. Mutant and fused embryos also reveal that even blastocyst-stage embryos made out of a single cell can proceed with the preimplantation program in a timely fashion, as they differentiate into TE and build features of the blastocyst, such as the inflation of fluid-containing compartments. Finally, myosin mutants and fused embryos reveal that the developmental program entailing morphogenesis and lineage specification carries on independently of successful cleavages. This further demonstrates the remarkable regulative capacities of the early mammalian embryo.

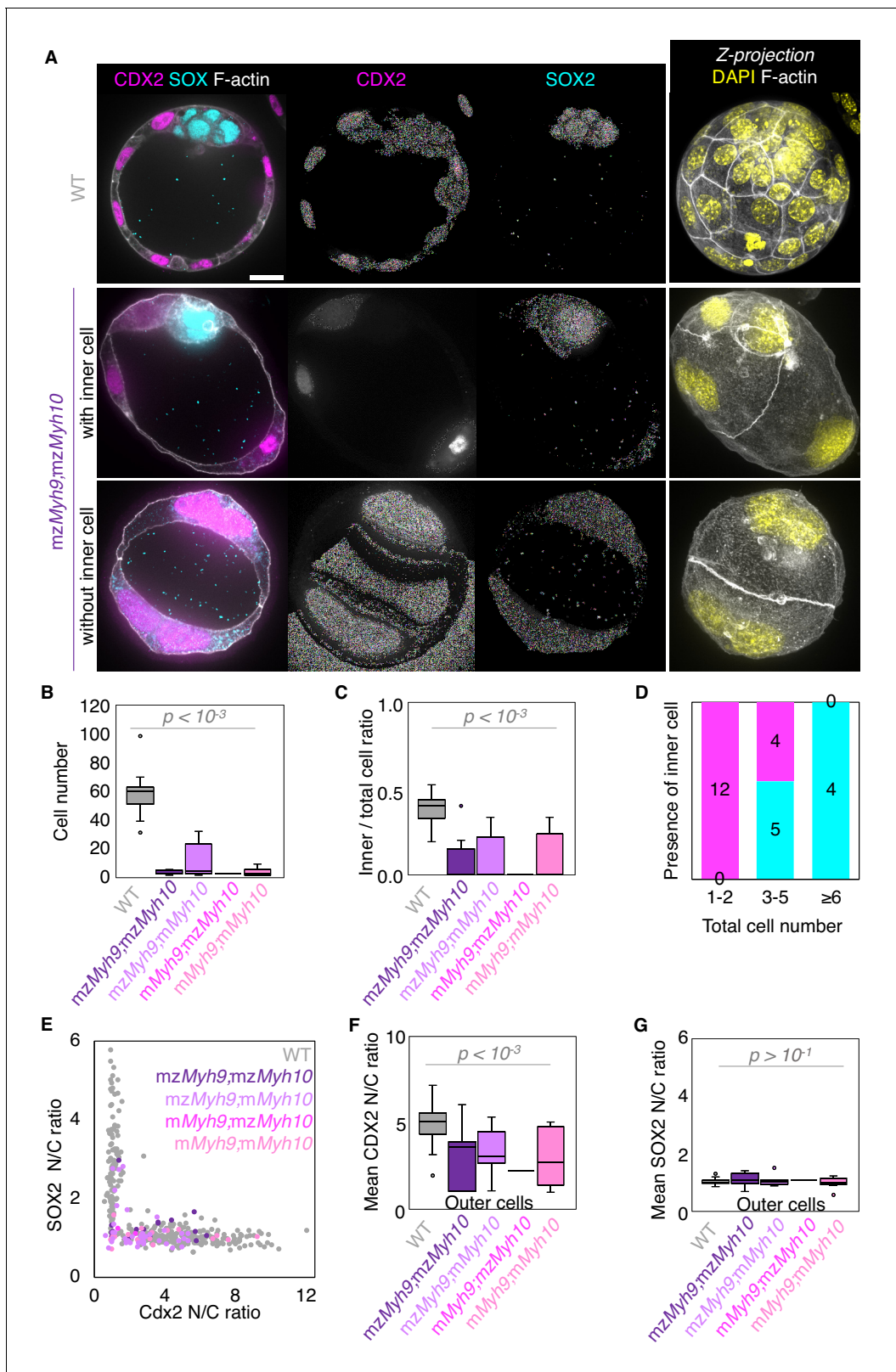


Figure 6. Analysis of TE and ICM lineage in double maternal-zygotic *Myh9* and *Myh10* mutant embryos. (A) Representative images of WT and *mzMyh9;mzMyh10* embryos stained for TE and ICM markers CDX2 (magenta) and SOX2 (cyan), DAPI (yellow), and F-actin (grey). The same mutant embryos as in **Figure 5A** are shown. Scale bar, 20 μ m. (B-C) Total cell number (B) and proportion of inner cells (C) in WT (grey, n = 23), *mzMyh9;mzMyh10* (purple, n = 8), *mzMyh9;mMyh10* (lilac, n = 7), *mMyh9;mzMyh10* (pink, n = 1), and *mMyh9;mMyh10* (bubblegum, n = 9) embryos. (D) Number

Figure 6 continued on next page

Figure 6 continued

of maternal *Myh9*/*Myh10* mutant embryos with (cyan) or without (magenta) inner cells as a function of the total number of cells. (E) Nuclear to cytoplasmic (N/C) ratio of CDX2 and SOX2 staining for individual cells from WT (grey, n = 345), *mzMyh9*/*mzMyh10* (purple, n = 17), *mzMyh9*/*mMyh10* (lilac, n = 41), *mMyh9*/*mzMyh10* (pink, n = 2), and *mMyh9*/*mMyh10* (bubblegum, n = 21) embryos. (F-G) N/C ratio of CDX2 (F) and SOX2 (G) staining for outer cells from averaged WT (grey, n = 23), *mzMyh9*/*mzMyh10* (purple, n = 8), *mzMyh9*/*mMyh10* (lilac, n = 7), *mMyh9*/*mzMyh10* (pink, n = 1), and *mMyh9*/*mMyh10* (bubblegum, n = 9) embryos. Mann-Whitney U test p values compared to WT are indicated.

Discussion

Recent studies have described the critical role of actomyosin contractility in establishing the blastocyst (Anani et al., 2014; Chan et al., 2019; Dumortier et al., 2019; Maître et al., 2015; Maître et al., 2016; Samarage et al., 2015; Zenker et al., 2018; Zhu et al., 2017). To understand the molecular regulation of this crucial engine of preimplantation development, we have eliminated the maternal and zygotic sources of the NMHCs MYH9 and MYH10 individually and jointly. Maternal-zygotic mutants reveal that actomyosin contractility is primarily mediated by maternal MYH9, which is found most abundantly. Comparatively, loss of *Myh10* has a mild impact on preimplantation development. Nevertheless, double maternal-zygotic mutants reveal that in the absence of MYH9, MYH10 plays a critical role in ensuring sufficient contractility to power cleavage divisions. Furthermore, double maternal-zygotic mutants bring to light the remarkable ability of the preimplantation embryo to carry on with its developmental program even when reduced to a single-celled embryo. Indeed, single-celled embryos, obtained from NMHC mutants or from the fusion of all cells of WT embryos, display evident signs of differentiation and initiate lumen formation by accumulating fluid in a timely fashion. Therefore, NMHC mutants and fused embryos reveal that the developmental program entailing morphogenesis and lineage specification carries on independently of successful cleavages.

Despite the importance of contractility during the formation of the blastocyst, maternal-zygotic mutants of NMHCs are yet to be characterized. The phenotypes we report here further confirm some of the previously proposed roles of contractility during preimplantation development and provide molecular insights on which NMHC paralog powers contractility. We observed reduced compaction when *Myh9* is maternally deleted and slower compaction when *Myh10* is deleted (Figure 2A–B). This is in agreement with cell culture studies, in which *Myh9* knockdown reduces

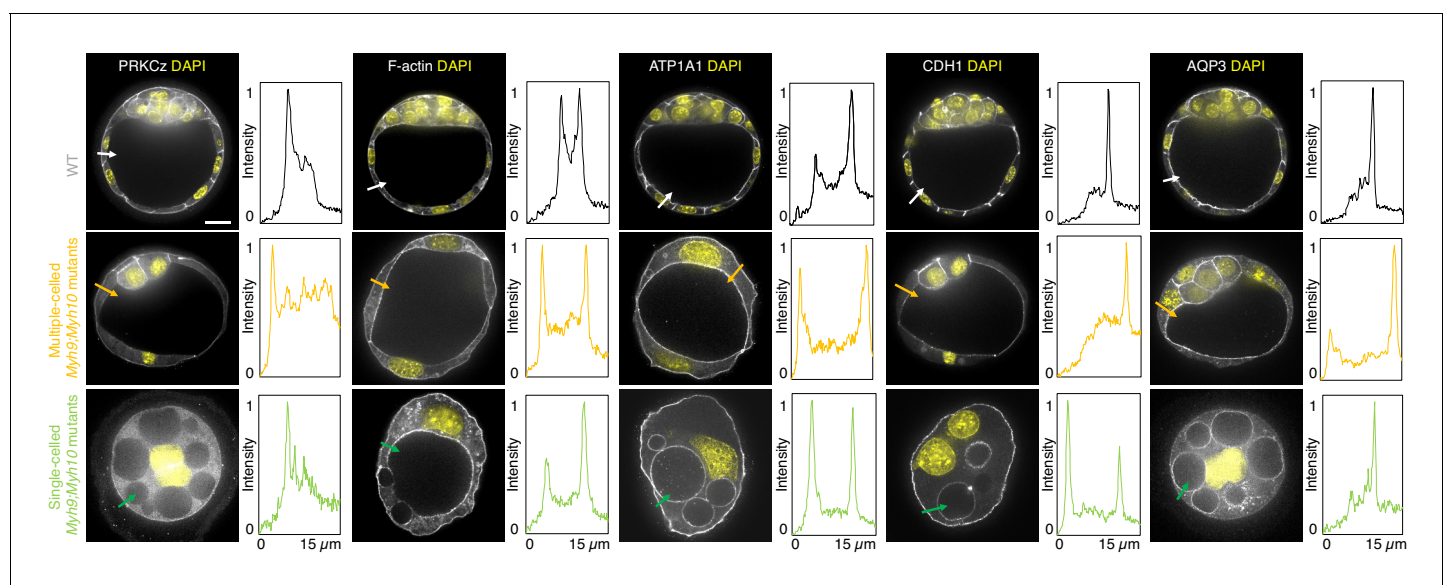


Figure 7. Apico-basal polarity of maternal *Myh9*/*Myh10* mutant embryos composed of multiple cells or a single cell. Representative images of WT, multiple- or single-celled *Myh9*/*Myh10* mutant embryos stained for apico-basal polarity markers. From left to right: PRKcz, F-actin, ATP1A1, CDH1, and AQP3 shown in grey. Nuclei stained with DAPI shown in yellow. Intensity profiles of a representative 15 μ m line drawn from the embryo surface towards the interior are shown next to each marker and genotype (arrows). Intensities are normalized to each minimal and maximal signals. Scale bar, 20 μ m.

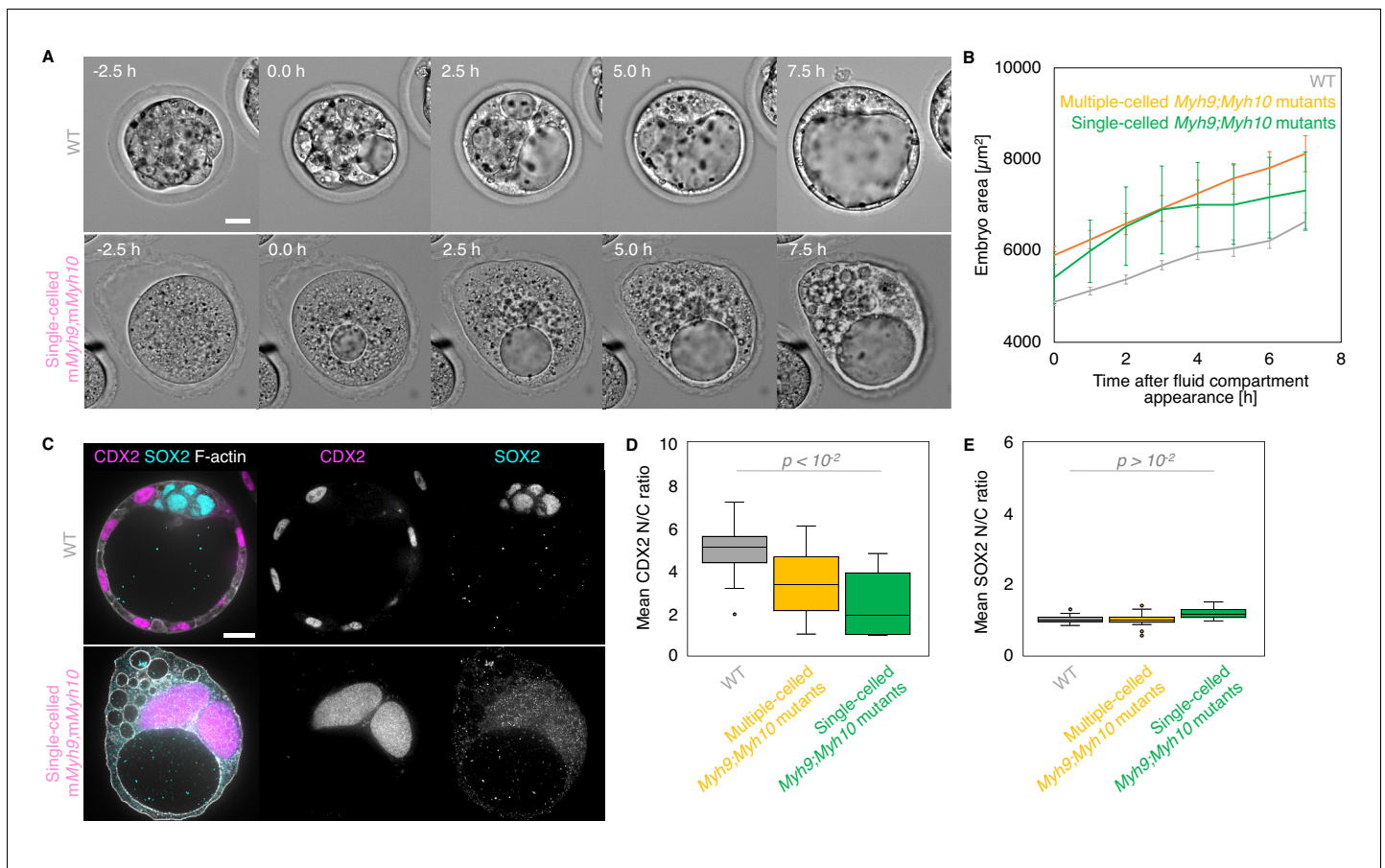


Figure 8. Single-celled embryos at the blastocyst stage. (A) Representative images of long-term time-lapse of WT and single-celled *mMyh9;mMyh10* embryos at the onset of fluid accumulation (**Figure 8—video 1**). Scale bar, 20 μm . (B) Embryo growth curves during fluid accumulation for WT (grey, $n = 20$) and multiple- (yellow, $n = 13$) or single-celled *Myh9;Myh10* (green, $n = 4$) mutant embryos measured for seven continuous hours after a lumen of at least 20 μm is observed. Data show mean \pm SEM. (C) Representative images of WT and single-celled *mMyh9;mMyh10* embryos stained for TE and ICM markers CDX2 (magenta) and SOX2 (cyan), DAPI (yellow), and F-actin (grey). The same mutant embryos as in A are shown. Scale bar, 20 μm . (D–E) N/C ratio of CDX2 (D) and SOX2 (E) staining for outer cells from WT (grey, $n = 23$) and multiple- (yellow, $n = 18$) or single-celled *Myh9;Myh10* (green, $n = 6$) embryos. Mann-Whitney U test p values compared to WT are indicated.

The online version of this article includes the following video and figure supplement(s) for figure 8:

Figure supplement 1. Morphogenesis and lineage specification of embryos with all blastomeres fused at the late morula stage.

Figure 8—video 1. Preimplantation development of an *mMyh9;mMyh10* embryo failing all successive cleavages.

<https://elifesciences.org/articles/68536#fig8video1>

Figure 8—video 2. Fluid accumulation in control and single-celled fused embryos.

<https://elifesciences.org/articles/68536#fig8video2>

contact size whereas *Myh10* knockdown does not (Heuzé et al., 2019; Smutny et al., 2010). This is also in agreement with previous studies using inhibitory drugs on the preimplantation embryo. Compaction is prevented, and even reverted, when embryos are treated with blebbistatin, a drug directly inhibiting NMHC function (Maître et al., 2015), or ML7, an inhibitor of the myosin light chain kinase (Zhu et al., 2017). However, zygotic injection of siRNA targeting *Myh9* did not affect compaction (Samarage et al., 2015; Zenker et al., 2018), further indicating that MYH9 acts primarily via its maternal pool. Similarly, siRNA-mediated knockdown of a myosin regulatory light chain *My12b* did not affect compaction (Zhu et al., 2017). Therefore, for efficient reduction of contractility with molecular specificity, maternal depletion is required.

The phenotypes of the maternal-zygotic NMHC mutants can also appear in contradiction with other conclusions from previous studies. Drugs were used to test the role of contractility in apico-basal polarity establishment with contradictory results. ML7, but not blebbistatin, was reported to

block de novo cell polarization (Zhu et al., 2017). This discrepancy might be due to ML7 inhibiting other kinases than MLCK such as PKC (Bain et al., 2003), which is required for apical domain formation (Zhu et al., 2017). Also, blebbistatin was reported to block the maturation of the apical domain (Zenker et al., 2018). The apical domain is essential for TE differentiation and for polarized fluid transport (Laeno et al., 2013; Hirate et al., 2013). We observed that even the most severely affected NMHC mutant embryos are able to establish and maintain apico-basal polarity, specific expression of TE markers and, most importantly, a functional polarized fluid transport (Figure 8). This argues against the requirement of contractility for de novo polarization and apical domain maturation.

Besides compaction defects, reduced cell number is one of the major effects caused by reduced contractility in the maternal-zygotic knockout of NMHCs. Loss of MYH9 alone, but not of MYH10 alone, causes cytokinesis defects (Figures 2–3, Figure 2—videos 1 and 3). This could simply be explained by the higher levels of maternal MYH9 (Figure 1). In vitro studies also noted that MYH9, but not MYH10, is key to power the ingression of the cleavage furrow (Taneja et al., 2020). This recent study also noted that MYH10 can compensate the absence of MYH9 with increased cortical recruitment (Taneja et al., 2020). Consistently, we observed much more severe division failures when both *Myh9* and *Myh10* are maternally removed (Figures 5, 6 and 8). This reveals significant compensation between NMHCs during preimplantation development. Whether this compensation takes place by a change in subcellular localization or by changes in expression level will require further studies.

Reduced cell number could have a major impact during very early development, when the zygote needs to produce enough cells for developmental patterning and morphogenesis. During normal development, the mouse embryo paces through the successive morphogenetic steps of compaction, internalization, and lumen formation at the rhythm of the third, fourth, and fifth waves of cleavage (Maître, 2017; Plusa and Piliszek, 2020; Rossant, 2016; White et al., 2018). Such concomitance may initially suggest that the preimplantation program is tightly linked to cleavages and cell number. However, seminal studies have established that the mammalian embryo is regulative and can build the blastocyst correctly with either supernumerary or fewer cells (Smith and McLaren, 1977; Snow, 1973; Tarkowski, 1959; Tarkowski, 1961; Tarkowski and Wróblewska, 1967). For example, aggregating multiple embryos results in compaction and lumen formation after the third and fifth cleavage, respectively, rather than when the chimeric embryos are composed of 8 and 32 cells (Tarkowski, 1961). Disaggregation leads to the same result with halved or quartered embryos compacting and forming a lumen at the correct embryonic stages rather than when reaching a defined cell number (Tarkowski, 1959; Tarkowski and Wróblewska, 1967). Contrary to disaggregated embryos, NMHC mutant embryos show reduced cell numbers without affecting the amount of cellular material (Figure 2—figure supplement 1). As observed in other species, the pace of development during mouse cleavage stages is thought to depend on the size ratio between the nucleus and the cytoplasm (Tsichlaki and FitzHarris, 2016). Evidences of nuclear divisions are visible even in the case of single-celled embryos (Figure 8—video 1), which suggests that the nuclear to cytoplasmic ratio may increase during the development of single-celled embryos. In line with these previous studies, the present experiments further confirm that compaction, internalization, and lumen formation take place without the expected cell number. Therefore, although cleavages and morphogenetic events are concomitant, they are not linked. Importantly, affecting blastocyst cell number through maternal *Myh9* loss or fusion of blastomeres at the 4-cell stage preserves the proportion of cells allocated to TE and ICM lineages (Figure 3C and Figure 3—figure supplement 2D). A recent study proposed that this proportion is controlled by the growth of the lumen (Chan et al., 2019). This is compatible with our observation that lumen growth is not affected by the loss of *Myh9* or cell fusion (Figure 2C and Figure 2—figure supplement 2C). However, lineage proportions break down when both *Myh9* and *Myh10* are maternally lost (Figure 6C). With about three cells on an average (Figure 6C–D), a majority of double mutants fail to internalize cells. As observed for doublets of 16-cell stage blastomeres, in principle, two cells should be enough to internalize one cell by an entosis-like process (Maître et al., 2016; Overholtzer et al., 2007). With extremely low contractility, double mutants may fail to raise contractility above the tension asymmetry threshold, enabling internalisation (Maître et al., 2016). As for oriented cell division (Korotkevich et al., 2017), this mechanism needs at least two cells to push one dividing cell within the cell-cell contact area. Together, this explains the absence of inner cells in mutant embryos with fewer than three cells.

Disaggregation experiments were key to reveal some of the cell-autonomous aspects of blastocyst formation: a single 8-cell stage blastomere can polarize (Ziomek and Johnson, 1980) and increase its contractility (Maître et al., 2015). Our observations on single-celled embryos reveal that fluid accumulation is also a cell-autonomous process (Figure 8). In fact, single-celled embryos inflate at rates similar to control embryos, implying that cell-cell contacts, closed by tight junctions at the embryo surface, are not required for accumulating fluid within blastomeres. Therefore, blastocoel components may be transported exclusively transcellularly, whereas paracellular transport through tight junctions may be negligible.

Whether single-celled embryos resulted from systematically failed cytokinesis or from cell fusion, these embryos grow at a similar rate, which is also the same as control embryos and other embryos composed of a reduced cell number (Figure 2C, Figure 5C, Figure 8B, Figure 8—figure supplement 1B, and Figure 2—figure supplement 2C). This suggests that fluid accumulation is a robust machinery during preimplantation development. Interfering with aquaporins, ion channels and transporters affect fluid accumulation, but the transcellular and paracellular contributions remain unclear (Barcroft et al., 2003; Kawagishi et al., 2004; Schliffka and Maître, 2019). Future studies will be needed to understand what sets robust transcellular fluid accumulation during preimplantation development. The ability of single cells to polarize and inflate a lumen was recently demonstrated in vitro by plating hepatocytes onto CDH1-coated substrates (Zhang et al., 2020). In this study, fluid accumulation in single-celled embryos does not result in the formation of a lumen but in the formation of inflating vacuoles. Vacuoles were also reported to appear occasionally in mutant mouse embryos with defective cell-cell adhesion (Bedzhov et al., 2012; Stephenson et al., 2010). Similarly, vacuole formation in case of acute loss of cell-cell adhesion has been studied in vitro (Vega-Salas et al., 1988). When apical lumens are disrupted, the apical compartment is internalized, and this can result in fluid accumulation within the vacuolar apical compartment (VAC) (Vega-Salas et al., 1988). Analogous VACs were proposed to coalesce into the lumen of endothelial tubes upon cell-cell contact in vivo (Kamei et al., 2006). The molecular characteristics and dynamics of these structures and their empty counterparts, the so-called apical membrane initiation sites, have been extensively studied in vitro and proven helpful to better understand apical lumen formation (Bryant et al., 2010; Overeem et al., 2015). In the case of the blastocyst, which forms a lumen on its basolateral side (Dumortier et al., 2019; Schliffka and Maître, 2019), such vacuoles may constitute an equivalent *vacuolar basolateral compartment*. Similar to apical lumen, further characterization of the molecular identity and dynamic behaviors of these vacuoles may prove useful to better understand fluid accumulation during basolateral lumen formation. Studying transcellular fluid transport and the molecular machinery of basolateral lumen formation will be greatly facilitated by the fusion approach reported in the present study (Figure 8—figure supplement 1).

Materials and methods

Embryo work

Recovery and culture

All the animal works were performed in the animal facility at the Institut Curie, with permission from the institutional veterinarian overseeing the operation (APAFIS #11054–2017082914226001). The animal facilities are operated according to international animal welfare rules.

Embryos were isolated from superovulated female mice mated with male mice. Superovulation of female mice was induced by intraperitoneal injection of 5 international units (IU) pregnant mare's serum gonadotropin (Ceva, Syncro-part), followed by intraperitoneal injection of 5 IU human chorionic gonadotropin (MSD Animal Health, Chorulon) 44–48 hr later. Embryos at E0.5 were recovered from plugged females by opening the ampulla followed by a brief treatment with 37°C 0.3 mg/mL hyaluronidase (Sigma, H4272-30MG) and washing in 37°C FHM. Embryos were recovered at E1.5 by flushing oviducts and at E2.5 and E3.5 by flushing oviducts and uteri from plugged females with 37°C FHM (Millipore, MR-122-D) using a modified syringe (Acufirm, 1400 LL 23).

Embryos were handled using an aspirator tube (Sigma, A5177-5EA) equipped with a glass pipette pulled from glass micropipettes (Blaubrand intraMark or Warner Instruments).

Embryos were placed in KSOM (Millipore, MR-107-D) supplemented with 0.1% BSA (Sigma, A3311) in 10 μ L droplets covered in mineral oil (Acros Organics). Embryos are cultured in an incubator under a humidified atmosphere supplemented with 5% CO₂ at 37°C.

To remove the ZP, embryos were incubated for 45–60 s in pronase (Sigma, P8811).

Blastomeres were fused using the GenomONE-CF FZ SeV-E cell fusion kit (CosmoBio, ISK-CF-001-EX). HVJ envelope was resuspended following manufacturer's instructions and diluted in FHM for use. To fuse the blastomeres of embryos at the 4-cell stage, embryos were incubated in 1:60 HVJ envelope/FHM for 15 min at 37°C followed by washes in KSOM. To fuse blastomeres at the morula stage, embryos were treated in the same manner in 1:50 HVJ envelope/FHM. Fusion typically completes ~30 min after the treatment.

For imaging, embryos were placed in 3.5 or 5 cm glass-bottom dishes (MatTek).

Mouse lines

Mice used were of 5 weeks old and above.

(C57BL/6xC3H) F1 hybrid strain was used for WT.

To remove LoxP sites specifically in oocytes, *Zp3^{Cre/+}* (*Tg(Zp3-cre)93Knw*) mice were used (*de Vries et al., 2000*).

To generate *mzMyh9* embryos, *Myh9^{tm5RSad}* mice were used (*Jacobelli et al., 2010*) to breed *Myh9^{tm5RSad/tm5RSad}; Zp3^{Cre/+}* females with *Myh9^{+/-}* \pm . To generate *mzMyh10* embryos, *Myh10^{tm7R-sad}* mice were used (*Ma et al., 2009*) to breed *Myh10^{tm7R-sad/tm7R-sad}; Zp3^{Cre/+}* females with *Myh10^{+/-}* \pm . To generate *mzMyh9;mzMyh10* embryos, *Myh9^{tm5RSad/tm5RSad}; Myh10^{tm7R-sad/tm7R-sad}; Zp3^{Cre/+}* females were mated with *Myh9^{+/-}*; *Myh10^{+/-}* males. To generate embryos with a maternal *Myh9-GFP* allele, *Myh9^{tm8.1RSad}* (*Gt(ROSA)26Sor^{tm4(ACTB-tdTomato,-EGFP)Luo}*) females were mated with WT males; to generate embryos with a paternal *Myh9-GFP* allele, WT females were mated with *Myh9^{tm8.1RSad}* (*Gt(ROSA)26Sor^{tm4(ACTB-tdTomato,-EGFP)Luo}*) males (*Muzumdar et al., 2007*; *Zhang et al., 2012*). For fusion at the morula stage, *Gt(ROSA)26Sor^{tm4(ACTB-tdTomato,-EGFP)Luo}* mice were used (*Muzumdar et al., 2007*).

Mouse strain	RRID
(C57BL/6xC3H) F1	MGI:5650923
<i>Tg(Zp3-cre)93Knw</i>	MGI:3835429
<i>Myh9^{tm5RSad/tm5RSad}</i>	MGI:4838530
<i>Myh10^{tm7R-sad/tm7R-sad}</i>	MGI:4443040
<i>Myh9^{tm8.1RSad}</i>	MGI:5499741
<i>Gt(ROSA)26Sor^{tm4(ACTB-tdTomato,-EGFP)Luo}</i>	IMSR_JAX:007676

Immunostaining

Embryos were fixed in 2% PFA (Euromedex, 2000-C) for 10 min at 37°C, washed in PBS, and permeabilized in 0.1% (SOX2, CDX2, and YAP primary antibodies) or 0.01% (all other primary antibodies) Triton X-100 (Euromedex, T8787) in PBS (PBT) at room temperature before being placed in blocking solution (PBT with 3% BSA) at 4°C for 2–4 hr. Primary antibodies were applied in blocking solution at 4°C overnight. After washes in PBT at room temperature, embryos were incubated with secondary antibodies, DAPI, and/or phalloidin in blocking solution at room temperature for 1 hr. Embryos were washed in PBT and imaged immediately after.

Primary antibodies	Dilution	Provider	RRID
CDX2	1:200	Abcam, ab157524	AB_2721036
SOX2	1:100	Abcam, ab97959	AB_2341193
YAP	1:100	Abnova, H00010413-M01	AB_535096
Phospho-MYH9 (Ser1943)	1:200	Cell Signaling, 5026	AB_10576567

Continued on next page

Continued

Primary antibodies	Dilution	Provider	RRID
MYH10	1:200	Santa Cruz, sc-376942	
PRKCz (H-1)	1:50	Santa Cruz, sc-17781	AB_628148
AQP3	1:500	Novusbio, NBP2-33872	
CDH1	1:500	eBioscience, 14-3249-82	
ATP1A1	1:100	Abcam, ab76020	AB_1310695

Secondary antibodies and dyes	Dilution	Provider	RRID
Alexa Fluor Plus 488 anti-mouse	1:200	Invitrogen, A32723	AB_2633275
Alexa Fluor 546 anti-mouse	1:200	Invitrogen, A11003	AB_2534071
Alexa Fluor Plus 488 anti-rabbit	1:200	Invitrogen, A32731	AB_2633280
Alexa Fluor Plus 546 anti-rabbit	1:200	Invitrogen, A11010	AB_2534077
Alexa Fluor 633 anti-rat	1:200	Invitrogen, A21094	AB_141553
Alexa Fluor 488 anti-rat	1:200	Invitrogen, A11006	AB_2534074
Alexa Fluor 633 phalloidin	1:200	Invitrogen, A22284	
4',6-diamidino-2-phenylindole (DAPI)	1:1000	Invitrogen, D1306	AB_2629482

Single embryo genotyping

DNA extraction was performed on single fixed embryos, in 10 μ L of DNA extraction buffer containing 10 mM Tris-HCl (pH 8, Sigma, T2694), 50 mM KCl (Sigma, 60142), 0.01% gelatine (Sigma, G1393), 0.1 mg/mL proteinase K (Sigma, P2308) at 55°C for 90 min, followed by deactivation of the proteinase K at 90°C for 10 min. 2 μ L of this DNA extract was used in PCR reactions.

To assess the *Myh9* genotype, a preamplification PCR was performed using forward (fw) primer GGGACCCACTTTCCCCATAA/reverse (rev) primer GTTCAACAGCCTAGGATGCG at a final concentration of 0.4 μ M. The PCR program is as follows: denaturation at 94°C 4 min; 35 cycles of 94°C 1 min, 58°C 1 min, 72°C 3:30 min, 72°C 1 min; final elongation step at 72°C 7 min. Subsequently, 2 μ L of the PCR product was directly used as a template for two independent PCR amplifications to detect either a 592 bp amplicon for the WT allele, with fw primer GGGACACAGTTGAATCCCTT/rev primer ATGGGCAGGTTCTTATAAGG or a 534 bp amplicon for a mutant allele, with fw primer GGGACACAGTTGAATCCCTT/rev primer CATCCTGTGGAGAGTGAGAGCAC at a final concentration of 0.4 μ M. PCR program is as follows: denaturation at 94°C for 4 min; 35 cycles of 94°C 1 min, 58°C 2 min, 72°C 1 min; final elongation step at 72°C 7 min.

To assess the *Myh10* genotype, a preamplification PCR was performed using fw primer GGCCCCATGTTACAGATTA/rev primer TTTCTCAACATCCACCCTCTG at a final concentration of 0.4 μ M. The PCR program is as follows: denaturation at 94°C for 4 min; 35 cycles of 94°C 1 min, 58°C 1 min, 72°C 2 min, 72°C 1 min; final elongation step at 72°C 7 min. Subsequently, 2 μ L of the PCR product was directly used as a template for a PCR amplification using fw primer 1 TAGC-GAAGGTCTAGGGGAATTG/fw primer 2 GACCGCTACTATTCAGGACTTATC/rev primer CAGA-GAAACGATGGGAAAGAAAGC at a final concentration of 0.4 μ M. PCR program is as follows: denaturation at 94°C for 4 min; 35 cycles of 94°C 1 min, 58°C 1:30 min, 72°C 1 min; final elongation step at 72°C 7 min, resulting in a 230 bp amplicon for a WT allele and a 630 bp amplicon for a mutant allele.

Quantitative RT-PCR

To extract total RNA, embryos were collected in 3 μ L of PBS, frozen on ice or snap-frozen on dry ice and stored at -80°C until further use. Total RNA extraction was performed using the PicoPure RNA Isolation Kit (ThermoFisher Scientific, KIT0204) according to manufacturer's instructions. DNase treatment was performed during the extraction, using RNase-Free DNase Set (QIAGEN, 79254).

cDNA was synthesized with random primers (ThermoFisher Scientific, 48190011), using the SuperScript III Reverse Transcriptase kit (ThermoFisher Scientific, 18080044) on all the extracted RNA, according to manufacturer's instructions. The final product could be used immediately or stored at -20°C until further use.

All the RT-qPCR reactions were performed using the ViiA 7 Real-Time PCR machine (Applied Biosystems) according to the instruction of the manufacturer. For each target sample, amplifications were run in triplicate in 10 μL reaction volume containing 5 μL of 2x Power SYBR Green PCR Master Mix (Applied Biosystems, 4367659), 1.4 μL of cDNA, 0.5 μL of each primer at 2 μM , and 2.6 μL of nuclease-free water. The PCR program is as follows: denaturation at 95°C 10 min; 40 cycles of 95°C 15 s, 60°C 1 min; 1 cycle of 95°C 15 s, 60°C 1 min, 95°C 15 s. The last cycle provides the post PCR run melt curve, for assessment of the specifics of the amplification. Each couple of primers was designed in order to anneal on consecutive exons of the cDNA sequence, far from the exon-exon junction regions, except for the *Gapdh* gene. The size of amplicons varied between 84 bp and 177 bp. *Gapdh* housekeeping gene was used as internal control to normalize the variability in expression levels of each target gene, according to the $2^{-\Delta\text{CT}}$ method. For every experiment, data were further normalized to *Myh9* levels at the zygote stage.

Total RNA was extracted from 234, 159, 189, 152 embryos at zygote, four-cell, morula, and blastocyst stages, respectively, from six independent experiments.

Gene name	Primer sequence forward	Primer sequence reverse
<i>Myh9</i> (ex7–ex8)	CAATGGCTACATTGTTGGTGCC	AGTAGAAGATGTGGAAGGTCCG
<i>Myh10</i> (ex3–ex4)	GAGGGAAGAAACGCCATGAGA	GAATTGACTGGTCCTCACGAT
<i>Myh14</i> (ex25–ex26)	GAGCTCGAGGACACTCTGGATT	TTTCTTCAGCTCTGTCACTCC
<i>Gapdh</i> (ex6–ex7)	CATACCAGGAAATGAGCTTG	ATGACATCAAGAAGGTGGTG

Bioinformatic analysis

Mouse and human single cell RNA sequencing data were extracted from *Deng et al., 2014* and *Yan et al., 2013*, analyzed as in *De Iaco et al., 2017*. In brief, single cell RNAseq datasets of human and mouse embryos (GSE36552, GSE45719) were downloaded and analyzed using the online platform Galaxy (usegalaxy.org). The reads were aligned to the reference genome using TopHat (Galaxy Version 2.1.1; *Kim et al., 2013*) and read counts generated with htseq-count (Galaxy Version 0.9.1; *Anders et al., 2015*). Normalized counts were determined with limma-voom (Galaxy Version 3.38.3 + galaxy3; *Law et al., 2014*).

Microscopy

For live imaging, embryos were placed in 5 cm glass-bottom dishes (MatTek) under a Celldiscoverer 7 (Zeiss) equipped with a 20x/0.95 objective and an ORCA-Flash 4.0 camera (C11440, Hamamatsu) or a 506 axiovert (Zeiss) camera.

Embryos were imaged from E1.5 to E3.5 until the establishment of a stable blastocoel in WT control embryos. Using the experiment designer tool of ZEN (Zeiss), we set up a nested time-lapse in which all embryos were imaged every 30 min at three focal planes positioned 10 μm apart for 40–54 hr and each embryo was subjected to two 10 min-long acquisitions with an image taken every 5 s at two focal planes positioned 10 μm apart that were set 12 and 19 hr after the second cleavage division of a reference WT embryo. Embryos were kept in a humidified atmosphere supplied with 5% CO_2 at 37°C . After imaging, mutant embryos were tracked individually for immunostaining and genotyping.

Live MYH9-GFP embryos were imaged at the zygote, four-cell, morula, and blastocyst stages. Live imaging was performed using an inverted Zeiss Observer Z1 microscope with a CSU-X1 spinning disc unit (Yokogawa). Excitation was achieved using 488 and 561 nm laser lines through a 63x/1.2 C Apo Korr water immersion objective. Emission was collected through 525/50 and 595/50 band pass filters onto an ORCA-Flash 4.0 camera (C11440, Hamamatsu). The microscope was equipped with an incubation chamber to keep the sample at 37°C and supply the atmosphere with 5% CO_2 .

Immunostainings were imaged on the same microscope using 405, 488, 561, and 642 nm laser lines through a 63x/1.2 C Apo Korr water immersion objective; emission was collected through 450/50 nm, 525/50 nm, 595/50 band pass or 610 nm low pass filters.

Data analysis

Time-lapse of preimplantation development

Based on the time-lapses of preimplantation development from E1.5 to E3.5, we assessed the timing of the third, fourth, and fifth cleavage divisions as well as the dynamics of compaction and lumen growth following these definitions:

(1) Cleavages are defined as part of the same wave when they occur within 30 min of the cleavage of another cell within the same embryo. As embryos are recovered at E1.5, time-lapse imaging starts around the time of the second cleavage. As cell divisions are affected by the mutations of *Myh9* and/or *Myh10*, the cell number of recovered embryos is not necessarily equal to WT cell number. Therefore, we used the entire time-lapse to determine whether the first observed division corresponds to the second, third, fourth, or fifth wave. Failed cytokinesis is counted as part of cleavage waves. (2) Timing of maximal compaction is defined as the time when embryos stop increasing their contact angles. (3) Timing of blastocoel formation is taken as the time when a fluid compartment with a diameter of at least 20 μm is visible.

The timings of all cleavage divisions and morphogenetic events were normalized to the end of the third cleavage division (beginning of the 8-cell stage in WT embryos).

Surface contact angles were measured using the angle tool in Fiji. Only the contact angles formed by two adjacent blastomeres with their equatorial planes in focus were considered. For each embryo, between one and six contact angles were measured after completion of the third cleavage, just before the onset of the fourth cleavage, after completion of the fourth cleavage, and just before the onset of the fourth cleavage.

Lumen growth was assessed by an increase in the area of the embryo. Using FIJI, an ellipse was manually fitted around the embryo every hour starting from the time of blastocoel formation (defined here as when a lumen of at least 20 μm becomes visible) until the end of the time-lapse. Growth rates of individual embryos were calculated over a 7 hr time window following the time of blastocoel formation. Measured projected areas from different embryos were synchronized to the time of blastocoel formation and averaged. For a fused single-celled embryo, the mean blastocoel formation time of the control embryos from each experiment was calculated to synchronize the fused embryos (1 hr of deviation from the mean blastocoel formation time can be allowed to accommodate cell divisions and sampling time). For control embryos, only blastocyst growing by at least 35% of their projected area were considered.

The shape of the zona pellucida was measured by fitting an ellipse on the outer edge of the zona pellucida and measuring the long and short axes.

Time-lapse of periodic contractions

Particle image velocimetry (PIV) analysis was performed using PIVlab 2.02 running on Matlab (Thielicke and Stamhuis, 2020; Thielicke and Stamhuis, 2014). Similar to Maître et al., 2015, time-lapse movies acquired every 5 s were processed using two successive passes through interrogation windows of 20/10 μm resulting in ~180 vectors per embryo. Vector velocities were then exported to Matlab for Fast Fourier Transform (FFT) analysis. The power spectrum of each embryo was then analyzed to assess the presence of a clear oscillation peak. The peak value between 50 and 120 s was taken as the amplitude, as this oscillation period range corresponds to the one where WT show oscillations (Maître et al., 2015; Maître et al., 2016). An embryo is considered as oscillating when the amplitude peaks 1.7 above background (taken as the mean value of the power spectrum signal of a given embryo) to determine whether it has a detectable oscillation. Power spectra of embryos from the same genotype were averaged.

Time-lapse of Myh9-GFP embryos

Myh9-GFP intensity was measured in FIJI by fitting a circle with a radius of 50 μm over the sum projection of each embryo and measuring the mean gray value. Background intensity was measured in a

circular area with radius 5 μm and subtracted to the embryonic value. The corrected intensities were normalized to the zygote stage of maternal Myh9-GFP embryos.

Immunostaining

We used FIJI to measure the levels of SOX2, CDX2, and YAP expression and localization by measuring the signal intensity of immunostainings. For each embryo, 15 cells (five ICM, five polar TE, five mural TE) were measured. In case an embryo had fewer than five ICM cells, a corresponding number of TE cells were added. If the embryo had fewer than 15 cells, all cells were measured. For each cell, the signal intensity was measured in a representative 3.7 μm^2 circular area of the equatorial nuclear plane and in a directly adjacent cytoplasmic area. Mitotic and apoptotic cells were excluded from analysis. We then calculated the nuclear to cytoplasmic ratio.

To obtain apico-basal intensity profiles of polarity markers, we selected confocal slices cutting through the equatorial plane of a surface cell lining the blastocoel. We drew a 15- μm -long and 0.4- μm -thick line from the cell-medium interface through the cell into the cell-lumen or cell-vacuole interface. Lowest/highest intensity values were normalized to 0 and 1, respectively.

To count cell number, we used DAPI to detect nuclei and phalloidin staining to detect cells. Cells were considered outer cells if they were in contact with the outside medium.

To measure the 3D properties of blastocysts, we manually segmented the surface of the embryo and of the blastocoel using Bitplane Imaris. Volumes and ellipticity were obtained from Imaris. The cellular volume was obtained by subtracting the blastocoel volume from the total volume of the embryo.

Statistics

Mean, standard deviation, SEM, lower and upper quartiles, median, Pearson's correlation coefficients, unpaired two-tailed Welch's *t* test, Mann-Whitney *U* test, and Pearson's χ^2 test with Yates's correction for continuity *p* values were calculated using Excel (Microsoft) and R (<http://www.r-project.org>). Pearson's correlation statistical significance was determined on the corresponding table. Statistical significance was considered when $p < 10^{-2}$. Boxplots show the median (line), interquartile range (box), 1.5 x interquartile range (whiskers), and remaining outliers (dots).

The sample size was not predetermined and simply results from the repetition of experiments. No sample was excluded. No randomization method was used. The investigators were not blinded during experiments.

Acknowledgements

We thank the imaging platform of the Genetics and Developmental Biology unit at the Institut Curie (PICT-IBISA@BDD), member of the French National Research Infrastructure France-BioImaging (ANR-10-INBS-04) for their outstanding support; the animal facility of the Institut Curie for their invaluable help. We thank Aurélie Teissendier for help with bioinformatic analysis, Victoire Cachoux for help with image analysis, and Yohanns Bellaïche for discussion and advice on the manuscript. Research in the lab of J-LM is supported by the Institut Curie, the Centre National de la Recherche Scientifique (CNRS), the Institut National de la Santé Et de la Recherche Médicale (INSERM), and is funded by grants from the ATIP-Avenir program, the Fondation Schlumberger pour l'Éducation et la Recherche via the Fondation pour la Recherche Médicale, the European Research Council Starting Grant ERC-2017-StG 757557, the European Molecular Biology Organization Young Investigator program (EMBO YIP), the INSERM transversal program Human Development Cell Atlas (HuDeCA), Paris Sciences Lettres (PSL) 'nouvelle équipe' and QLife (17-CONV-0005) grants and Labex DEEP (ANR-11-LABX-0044), which are part of the IDEX PSL (ANR-10-IDEX-0001-02). MFS is funded by a Convention Industrielle de Formation pour la Recherche (No 2019/0253) between the Agence Nationale de la Recherche and Carl Zeiss SAS. ÖÖ is funded from the European Union's Horizon 2020 research and innovation program under the Marie Skłodowska-Curie grant agreement No 666003 and benefits from the EMBO YIP bridging fund.

Additional information

Competing interests

Markus Frederik Schliffka: is employed by Carl Zeiss SAS via a public PhD programme Conventions Industrielles de Formation par la Recherche (CIFRE) co-funded by the Association Nationale de la Recherche et de la Technologie (ANRT). The other authors declare that no competing interests exist.

Funding

Funder	Grant reference number	Author
Association Nationale de la Recherche et de la Technologie	2019/0253	Markus Frederik Schliffka
H2020 Marie Skłodowska-Curie Actions	666003	Özge Özgüç
Fondation pour la Recherche Médicale		Özge Özgüç
Centre National de la Recherche Scientifique		Jean-Léon Maître
H2020 European Research Council	ERC-2017-StG 757557	Jean-Léon Maître
Schlumberger Foundation		Jean-Léon Maître
Université de Recherche Paris Sciences et Lettres	17-CONV-0005	Jean-Léon Maître
Agence Nationale de la Recherche	ANR-11-LABX-0044	Jean-Léon Maître
Institut National de la Santé et de la Recherche Médicale	HuDeCA	Jean-Léon Maître
European Molecular Biology Organization	Young Investigator Programme	Jean-Léon Maître
Agence Nationale de la Recherche	ANR-10-IDEX-0001-02	Jean-Léon Maître

The funders had no role in study design, data collection and interpretation, or the decision to submit the work for publication.

Author contributions

Markus Frederik Schliffka, Anna Francesca Tortorelli, Conceptualization, Resources, Data curation, Formal analysis, Validation, Investigation, Visualization, Methodology, Writing - review and editing; Özge Özgüç, Data curation, Software, Formal analysis, Visualization, Methodology, Writing - review and editing; Ludmilla de Plater, Resources, Methodology; Oliver Polzer, Formal analysis, Visualization; Diane Pelzer, Software, Formal analysis, Visualization, Writing - review and editing; Jean-Léon Maître, Conceptualization, Resources, Data curation, Software, Formal analysis, Supervision, Funding acquisition, Validation, Investigation, Visualization, Methodology, Writing - original draft, Project administration, Writing - review and editing

Author ORCIDs

Markus Frederik Schliffka  <https://orcid.org/0000-0002-5128-1653>

Anna Francesca Tortorelli  <https://orcid.org/0000-0002-9995-9582>

Özge Özgüç  <http://orcid.org/0000-0002-1545-1715>

Ludmilla de Plater  <http://orcid.org/0000-0002-0982-5960>

Oliver Polzer  <http://orcid.org/0000-0003-4970-6058>

Diane Pelzer  <http://orcid.org/0000-0001-6906-2451>Jean-Léon Maître  <https://orcid.org/0000-0002-3688-1474>

Ethics

Animal experimentation: All animal work is performed in the animal facility at the Institut Curie, with permission by the institutional veterinarian overseeing the operation (APAFIS #11054-2017082914226001). The animal facilities are operated according to international animal welfare rules.

Decision letter and Author response

Decision letter <https://doi.org/10.7554/eLife.68536.sa1>Author response <https://doi.org/10.7554/eLife.68536.sa2>

Additional files

Supplementary files

- Transparent reporting form

Data availability

The microscopy data, ROI and analyses are available on the following repository under a CC BY-NC-SA license: <https://ressources.curie.fr/mzmyh/>.

The following previously published datasets were used:

Author(s)	Year	Dataset title	Dataset URL	Database and Identifier
Deng Q, Ramsköld D, Reinius B, Sandberg R	2014	Single-cell RNA-Seq reveals dynamic, random monoallelic gene expression in mammalian cells	https://www.ncbi.nlm.nih.gov/geo/query/acc.cgi?acc=GSE45719	NCBI Gene Expression Omnibus, GSE45719
Tang F, Qiao J, Li R	2013	Tracing pluripotency of human early embryos and embryonic stem cells by single cell RNA-seq	https://www.ncbi.nlm.nih.gov/geo/query/acc.cgi?acc=GSE36552	NCBI Gene Expression Omnibus, GSE36552

References

- Anani S**, Bhat S, Honma-Yamanaka N, Krawchuk D, Yamanaka Y. 2014. Initiation of Hippo signaling is linked to polarity rather than to cell position in the pre-implantation mouse embryo. *Development* **141**:2813–2824. DOI: <https://doi.org/10.1242/dev.107276>, PMID: 24948601
- Anders S**, Pyl PT, Huber W. 2015. HTSeq—a Python framework to work with high-throughput sequencing data. *Bioinformatics* **31**:166–169. DOI: <https://doi.org/10.1093/bioinformatics/btu638>, PMID: 25260700
- Avilion AA**, Nicolis SK, Pevny LH, Perez L, Vivian N, Lovell-Badge R. 2003. Multipotent cell lineages in early mouse development depend on SOX2 function. *Genes & development* **17**:126–140. DOI: <https://doi.org/10.1101/gad.224503>, PMID: 12514105
- Bain J**, McLauchlan H, Elliott M, Cohen P. 2003. The specificities of protein kinase inhibitors: an update. *The Biochemical journal* **371**:199–204. DOI: <https://doi.org/10.1042/BJ20021535>, PMID: 12534346
- Barcroft LC**, Offenberg H, Thomsen P, Watson AJ. 2003. Aquaporin proteins in murine trophectoderm mediate transepithelial water movements during cavitation. *Developmental biology* **256**:342–354. DOI: [https://doi.org/10.1016/s0012-1606\(02\)00127-6](https://doi.org/10.1016/s0012-1606(02)00127-6), PMID: 12679107
- Barcroft LC**, Moseley AE, Lingrel JB, Watson AJ. 2004. Deletion of the Na/K-ATPase alpha1-subunit gene (Atp1a1) does not prevent cavitation of the preimplantation mouse embryo. *Mechanisms of development* **121**:417–426. DOI: <https://doi.org/10.1016/j.mod.2004.04.005>, PMID: 15147760
- Beach JR**, Shao L, Rimmert K, Li D, Betzig E, Hammer JA, 2014. Nonmuscle myosin II isoforms coassemble in living cells. *Current biology* : CB **24**:1160–1166. DOI: <https://doi.org/10.1016/j.cub.2014.03.071>, PMID: 24814144
- Bedzhov I**, Liszewska E, Kanzler B, Stemmler MP. 2012. Igf1r signaling is indispensable for preimplantation development and is activated via a novel function of E-cadherin. *PLOS genetics* **8**:e1002609. DOI: <https://doi.org/10.1371/journal.pgen.1002609>, PMID: 22479204

- Bryant DM**, Datta A, Rodríguez-Fraticelli AE, Peränen J, Martín-Belmonte F, Mostov KE. 2010. A molecular network for de novo generation of the apical surface and lumen. *Nature cell biology* **12**:1035–1045. DOI: <https://doi.org/10.1038/ncb2106>, PMID: 20890297
- Chan CJ**, Costanzo M, Ruiz-Herrero T, Mönke G, Petrie RJ, Bergert M, Diz-Muñoz A, Mahadevan L, Hiiragi T. 2019. Hydraulic control of mammalian embryo size and cell fate. *Nature* **571**:112–116. DOI: <https://doi.org/10.1038/s41586-019-1309-x>, PMID: 31189957
- Clark AG**, Dierkes K, Paluch EK. 2013. Monitoring actin cortex thickness in live cells. *Biophysical journal* **105**:570–580. DOI: <https://doi.org/10.1016/j.bpj.2013.05.057>, PMID: 23931305
- Conti MA**, Even-Ram S, Liu C, Yamada KM, Adelstein RS. 2004. Defects in cell adhesion and the visceral endoderm following ablation of nonmuscle myosin heavy chain II-A in mice. *The Journal of biological chemistry* **279**:41263–41266. DOI: <https://doi.org/10.1074/jbc.C400352200>, PMID: 15292239
- Dard N**, Louvet-Vallée S, Maro B. 2009. Orientation of mitotic spindles during the 8- to 16-cell stage transition in mouse embryos. *PLOS ONE* **4**:e8171. DOI: <https://doi.org/10.1371/journal.pone.0008171>, PMID: 19997595
- De Iaco A**, Planet E, Coluccio A, Verp S, Duc J, Trono D. 2017. DUX-family transcription factors regulate zygotic genome activation in placental mammals. *Nature genetics* **49**:941–945. DOI: <https://doi.org/10.1038/ng.3858>, PMID: 28459456
- de Vries WN**, Binns LT, Fancher KS, Dean J, Moore R, Kemler R, Knowles BB. 2000. Expression of Cre recombinase in mouse oocytes: a means to study maternal effect genes. *Genesis* **26**:110–112. PMID: 10686600
- Deng Q**, Ramsköld D, Reinius B, Sandberg R. 2014. Single-cell RNA-seq reveals dynamic, random monoallelic gene expression in mammalian cells. *Science* **343**:193–196. DOI: <https://doi.org/10.1126/science.1245316>, PMID: 24408435
- Dumortier JG**, Le Verge-Serandour M, Tortorelli AF, Mielke A, de Plater L, Turlier H, Maître JL2019. Hydraulic fracturing and active coarsening position the lumen of the mouse blastocyst. *Science* **365**:465–468. DOI: <https://doi.org/10.1126/science.aaw7709>, PMID: 31371608
- Frankenberg SR**, de Barros FR, Rossant J, Renfree MB. 2016. The mammalian blastocyst. *Wiley interdisciplinary reviews. Developmental biology* **5**:210–232. DOI: <https://doi.org/10.1002/wdev.220>, PMID: 26799266
- Heisenberg CP**, Bellaïche Y. 2013. Forces in tissue morphogenesis and patterning. *Cell* **153**:948–962. DOI: <https://doi.org/10.1016/j.cell.2013.05.008>, PMID: 23706734
- Heuzé ML**, Sankara Narayana GHN, D’Alessandro J, Cellerin V, Dang T, Williams DS, Van Hest JC, Marcq P, Mège RM, Ladoux B. 2019. Myosin II isoforms play distinct roles in *adherens* junction biogenesis. *eLife* **8**:e46599. DOI: <https://doi.org/10.7554/eLife.46599>, PMID: 31486768
- Hirate Y**, Hirahara S, Inoue K, Suzuki A, Alarcon VB, Akimoto K, Hirai T, Hara T, Adachi M, Chida K, Ohno S, Marikawa Y, Nakao K, Shimono A, Sasaki H. 2013. Polarity-dependent distribution of angiominin localizes Hippo signaling in preimplantation embryos. *Current biology : CB* **23**:1181–1194. DOI: <https://doi.org/10.1016/j.cub.2013.05.014>, PMID: 23791731
- Jacobelli J**, Friedman RS, Conti MA, Lennon-Dumenil AM, Piel M, Sorensen CM, Adelstein RS, Krummel MF. 2010. Confinement-optimized three-dimensional T cell amoeboid motility is modulated via myosin IIA-regulated adhesions. *Nature immunology* **11**:953–961. DOI: <https://doi.org/10.1038/ni.1936>, PMID: 20835229
- Kamei M**, Saunders WB, Bayless KJ, Dye L, Davis GE, Weinstein BM. 2006. Endothelial tubes assemble from intracellular vacuoles in vivo. *Nature* **442**:453–456. DOI: <https://doi.org/10.1038/nature04923>, PMID: 16799567
- Kawagishi R**, Tahara M, Sawada K, Morishige K, Sakata M, Tasaka K, Murata Y. 2004. Na⁺/H⁺ Exchanger-3 is involved in mouse blastocyst formation. *Journal of Experimental Zoology* **301A**:767–775. DOI: <https://doi.org/10.1002/jez.a.90>
- Kim D**, Perteu G, Trapnell C, Pimentel H, Kelley R, Salzberg SL. 2013. TopHat2: accurate alignment of transcriptomes in the presence of insertions, deletions and gene fusions. *Genome biology* **14**:R36. DOI: <https://doi.org/10.1186/gb-2013-14-4-r36>, PMID: 23618408
- Korotkevich E**, Niwayama R, Courtois A, Friese S, Berger N, Buchholz F, Hiiragi T. 2017. The Apical Domain Is Required and Sufficient for the First Lineage Segregation in the Mouse Embryo. *Developmental cell* **40**:235–247. DOI: <https://doi.org/10.1016/j.devcel.2017.01.006>, PMID: 28171747
- Kurotaki Y**, Hatta K, Nakao K, Nabeshima Y, Fujimori T. 2007. Blastocyst axis is specified independently of early cell lineage but aligns with the ZP shape. *Science* **316**:719–723. DOI: <https://doi.org/10.1126/science.1138591>, PMID: 17446354
- Laeno AM**, Tamashiro DA, Alarcon VB. 2013. Rho-associated kinase activity is required for proper morphogenesis of the inner cell mass in the mouse blastocyst. *Biology of Reproduction* **89**:122. DOI: <https://doi.org/10.1095/biolreprod.113.109470>, PMID: 23946538
- Law CW**, Chen Y, Shi W, Smyth GK. 2014. voom: Precision weights unlock linear model analysis tools for RNA-seq read counts. *Genome biology* **15**:R29. DOI: <https://doi.org/10.1186/gb-2014-15-2-r29>, PMID: 24485249
- Lecuit T**, Yap AS. 2015. E-cadherin junctions as active mechanical integrators in tissue dynamics. *Nature cell biology* **17**:533–539. DOI: <https://doi.org/10.1038/ncb3136>, PMID: 25925582
- Ma X**, Takeda K, Singh A, Yu ZX, Zerfas P, Blount A, Liu C, Towbin JA, Schneider MD, Adelstein RS, Wei Q. 2009. Conditional ablation of nonmuscle myosin II-B delineates heart defects in adult mice. *Circulation research* **105**:1102–1109. DOI: <https://doi.org/10.1161/CIRCRESAHA.109.200303>, PMID: 19815823
- Ma X**, Jana SS, Conti MA, Kawamoto S, Claycomb WC, Adelstein RS. 2010. Ablation of nonmuscle myosin II-B and II-C reveals a role for nonmuscle myosin II in cardiac myocyte karyokinesis. *Molecular biology of the cell* **21**:3952–3962. DOI: <https://doi.org/10.1091/mbc.E10-04-0293>, PMID: 20861308

- Maître JL**, Niwayama R, Turlier H, Nédélec F, Hiiragi T. 2015. Pulsatile cell-autonomous contractility drives compaction in the mouse embryo. *Nature cell biology* **17**:849–855. DOI: <https://doi.org/10.1038/ncb3185>, PMID: 26075357
- Maître JL**, Turlier H, Illukkumbura R, Eismann B, Niwayama R, Nédélec F, Hiiragi T. 2016. Asymmetric division of contractile domains couples cell positioning and fate specification. *Nature* **536**:344–348. DOI: <https://doi.org/10.1038/nature18958>, PMID: 27487217
- Maître JL**. 2017. Mechanics of blastocyst morphogenesis. *Biology of the cell* **109**:323–338. DOI: <https://doi.org/10.1111/boc.201700029>, PMID: 28681376
- Motosugi N**, Bauer T, Polanski Z, Solter D, Hiiragi T. 2005. Polarity of the mouse embryo is established at blastocyst and is not prepatterned. *Genes & development* **19**:1081–1092. DOI: <https://doi.org/10.1101/gad.1304805>, PMID: 15879556
- Murrell M**, Oakes PW, Lenz M, Gardel ML. 2015. Forcing cells into shape: the mechanics of actomyosin contractility. *Nature reviews. Molecular cell biology* **16**:486–498. DOI: <https://doi.org/10.1038/nrm4012>, PMID: 26130009
- Muzumdar MD**, Tasic B, Miyamichi K, Li L, Luo L. 2007. A global double-fluorescent Cre reporter mouse. *Genesis* **45**:593–605. DOI: <https://doi.org/10.1002/dvg.20335>, PMID: 17868096
- Nishioka N**, Inoue K, Adachi K, Kiyonari H, Ota M, Ralston A, Yabuta N, Hirahara S, Stephenson RO, Ogonuki N, Makita R, Kurihara H, Morin-Kensicki EM, Nojima H, Rossant J, Nakao K, Niwa H, Sasaki H. 2009. The Hippo signaling pathway components Lats and Yap pattern Tead4 activity to distinguish mouse trophectoderm from inner cell mass. *Developmental cell* **16**:398–410. DOI: <https://doi.org/10.1016/j.devcel.2009.02.003>, PMID: 19289085
- Niwayama R**, Moghe P, Liu YJ, Fabrèges D, Buchholz F, Piel M, Hiiragi T. 2019. A Tug-of-War between cell shape and polarity controls division orientation to ensure robust patterning in the mouse blastocyst. *Developmental Cell* **51**:564–574. DOI: <https://doi.org/10.1016/j.devcel.2019.10.012>, PMID: 31735668
- Overeem AW**, Bryant DM, van IJendoorn SC. 2015. Mechanisms of apical-basal axis orientation and epithelial lumen positioning. *Trends in cell biology* **25**:476–485. DOI: <https://doi.org/10.1016/j.tcb.2015.04.002>, PMID: 25941134
- Overholtzer M**, Maillieux AA, Mouneimne G, Normand G, Schnitt SJ, King RW, Cibas ES, Brugge JS. 2007. A nonapoptotic cell death process, entosis, that occurs by cell-in-cell invasion. *Cell* **131**:966–979. DOI: <https://doi.org/10.1016/j.cell.2007.10.040>, PMID: 18045538
- Özgüç Ö**, Maître JL. 2020. Multiscale morphogenesis of the mouse blastocyst by actomyosin contractility. *Current opinion in cell biology* **66**:123–129. DOI: <https://doi.org/10.1016/jceb.2020.05.002>, PMID: 32711300
- Plusa B**, Piliszek A. 2020. Common principles of early mammalian embryo self-organisation. *Development* **147**:dev183079. DOI: <https://doi.org/10.1242/dev.183079>, PMID: 32699138
- Ramkumar N**, Baum B. 2016. Coupling changes in cell shape to chromosome segregation. *Nature reviews. Molecular cell biology* **17**:511–521. DOI: <https://doi.org/10.1038/nrm.2016.75>, PMID: 27353479
- Rossant J**. 2016. Making the Mouse Blastocyst: Past, Present, and Future. *Current topics in developmental biology* **117**:275–288. DOI: <https://doi.org/10.1016/bs.ctdb.2015.11.015>, PMID: 26969983
- Rossi A**, Kontarakis Z, Gerri C, Nolte H, Hölper S, Krüger M, Stainier DY. 2015. Genetic compensation induced by deleterious mutations but not gene knockdowns. *Nature* **524**:230–233. DOI: <https://doi.org/10.1038/nature14580>, PMID: 26168398
- Royer C**, Leonavicius K, Kip A, Fortin D, Nandi K, Vincent A, Jones C, Child T, Coward K, Graham C, Srinivas S. 2020. Establishment of a relationship between blastomere geometry and YAP localisation during compaction. *Development* **147**:dev189449. DOI: <https://doi.org/10.1242/dev.189449>, PMID: 32928909
- Salbreux G**, Charras G, Paluch E. 2012. Actin cortex mechanics and cellular morphogenesis. *Trends in cell biology* **22**:536–545. DOI: <https://doi.org/10.1016/j.tcb.2012.07.001>, PMID: 22871642
- Samarage CR**, White MD, Álvarez YD, Fierro-González JC, Henon Y, Jesudason EC, Bissiere S, Fouras A, Plachta N. 2015. Cortical tension allocates the first inner cells of the mammalian embryo. *Developmental Cell* **34**:435–447. DOI: <https://doi.org/10.1016/j.devcel.2015.07.004>, PMID: 26279486
- Schliffka MF**, Maître JL. 2019. Stay hydrated: basolateral fluids shaping tissues. *Current opinion in genetics & development* **57**:70–77. DOI: <https://doi.org/10.1016/j.gde.2019.06.015>, PMID: 31445440
- Smith R**, McLaren A. 1977. Factors affecting the time of formation of the mouse blastocoele. *Journal of Embryology and Experimental Morphology* **41**:79–92.
- Smutny M**, Cox HL, Leerberg JM, Kovacs EM, Conti MA, Ferguson C, Hamilton NA, Parton RG, Adelstein RS, Yap AS. 2010. Myosin II isoforms identify distinct functional modules that support integrity of the epithelial zonula adherens. *Nature cell biology* **12**:696–702. DOI: <https://doi.org/10.1038/ncb2072>, PMID: 20543839
- Snow MH**. 1973. Tetraploid mouse embryos produced by cytochalasin B during cleavage. *Nature* **244**:513–515. DOI: <https://doi.org/10.1038/244513a0>, PMID: 4621127
- Stephenson RO**, Yamanaka Y, Rossant J. 2010. Disorganized epithelial polarity and excess trophectoderm cell fate in preimplantation embryos lacking E-cadherin. *Development* **137**:3383–3391. DOI: <https://doi.org/10.1242/dev.050195>
- Strumpf D**, Mao CA, Yamanaka Y, Ralston A, Chawengsaksophak K, Beck F, Rossant J. 2005. Cdx2 is required for correct cell fate specification and differentiation of trophectoderm in the mouse blastocyst. *Development* **132**:2093–2102. DOI: <https://doi.org/10.1242/dev.01801>, PMID: 15788452
- Taneja N**, Bersi MR, Baillargeon SM, Fenix AM, Cooper JA, Ohi R, Gama V, Merryman WD, Burnette DT. 2020. Precise tuning of cortical contractility regulates cell shape during cytokinesis. *Cell Reports* **31**:107477. DOI: <https://doi.org/10.1016/j.celrep.2020.03.041>, PMID: 32268086

- Taneja N**, Burnette DT. 2019. Myosin IIA drives membrane bleb retraction. *Molecular biology of the cell* **30**: 1051–1059. DOI: <https://doi.org/10.1091/mbc.E18-11-0752>, PMID: 30785846
- Tarkowski AK**. 1959. Experiments on the development of isolated blastomers of mouse eggs. *Nature* **184**:1286–1287. DOI: <https://doi.org/10.1038/1841286a0>, PMID: 13836947
- Tarkowski AK**. 1961. Mouse chimaeras developed from fused eggs. *Nature* **190**:857–860. DOI: <https://doi.org/10.1038/190857a0>, PMID: 13775333
- Tarkowski AK**, Wróblewska J. 1967. Development of blastomeres of mouse eggs isolated at the 4- and 8-cell stage. *Journal of embryology and experimental morphology* **18**:155–180. PMID: 6048976
- Thielicke W**, Stamhuis EJ. 2014. PIVlab – Towards User-friendly, Affordable and Accurate Digital Particle Image Velocimetry in MATLAB. *Journal of Open Research Software* **2**:jors.bl. DOI: <https://doi.org/10.5334/jors.bl>
- Thielicke W**, Stamhuis EJ. 2020. PIVlab v2.36 - Time-Resolved Digital Particle Image Velocimetry Tool for MATLAB. https://figshare.com/articles/code/PIVlab_version_1_35/1092508
- Tsichlaki E**, FitzHarris G. 2016. Nucleus downscaling in mouse embryos is regulated by cooperative developmental and geometric programs. *Scientific reports* **6**:28040. DOI: <https://doi.org/10.1038/srep28040>, PMID: 27320842
- Tullio AN**, Accili D, Ferrans VJ, Yu ZX, Takeda K, Grinberg A, Westphal H, Preston YA, Adelstein RS. 1997. Nonmuscle myosin II-B is required for normal development of the mouse heart. *PNAS* **94**:12407–12412. DOI: <https://doi.org/10.1073/pnas.94.23.12407>, PMID: 9356462
- Vega-Salas DE**, Salas PJ, Rodriguez-Boulan E. 1988. Exocytosis of vacuolar apical compartment (VAC): a cell-cell contact controlled mechanism for the establishment of the apical plasma membrane domain in epithelial cells. *The Journal of cell biology* **107**:1717–1728. DOI: <https://doi.org/10.1083/jcb.107.5.1717>, PMID: 3053735
- Vicente-Manzanares M**, Ma X, Adelstein RS, Horwitz AR. 2009. Non-muscle myosin II takes centre stage in cell adhesion and migration. *Nature reviews. Molecular cell biology* **10**:778–790. DOI: <https://doi.org/10.1038/nrm2786>, PMID: 19851336
- Wang A**, Ma X, Conti MA, Liu C, Kawamoto S, Adelstein RS. 2010. Nonmuscle myosin II isoform and domain specificity during early mouse development. *PNAS* **107**:14645–14650. DOI: <https://doi.org/10.1073/pnas.1004023107>, PMID: 20679233
- White MD**, Zenker J, Bissiere S, Plachta N. 2018. Instructions for Assembling the Early Mammalian Embryo. *Developmental cell* **45**:667–679. DOI: <https://doi.org/10.1016/j.devcel.2018.05.013>, PMID: 29920273
- Wicklow E**, Blij S, Frum T, Hirate Y, Lang RA, Sasaki H, Ralston A. 2014. HIPPO pathway members restrict SOX2 to the inner cell mass where it promotes ICM fates in the mouse blastocyst. *PLOS genetics* **10**:e1004618. DOI: <https://doi.org/10.1371/journal.pgen.1004618>, PMID: 25340657
- Yamamoto K**, Otomo K, Nemoto T, Ishihara S, Haga H, Nagasaki A, Murakami Y, Takahashi M. 2019. Differential contributions of nonmuscle myosin IIA and IIB to cytokinesis in human immortalized fibroblasts. *Experimental cell research* **376**:67–76. DOI: <https://doi.org/10.1016/j.yexcr.2019.01.020>, PMID: 30711568
- Yan L**, Yang M, Guo H, Yang L, Wu J, Li R, Liu P, Lian Y, Zheng X, Yan J, Huang J, Li M, Wu X, Wen L, Lao K, Li R, Qiao J, Tang F. 2013. Single-cell RNA-Seq profiling of human preimplantation embryos and embryonic stem cells. *Nature structural & molecular biology* **20**:1131–1139. DOI: <https://doi.org/10.1038/nsmb.2660>, PMID: 23934149
- Zaidel-Bar R**, Zhenhuan G, Luxenburg C. 2015. The contractome—a systems view of actomyosin contractility in non-muscle cells. *Journal of cell science* **128**:2209–2217. DOI: <https://doi.org/10.1242/jcs.170068>, PMID: 26021351
- Zenker J**, White MD, Gasnier M, Alvarez YD, Lim HYG, Bissiere S, Biro M, Plachta N. 2018. Expanding actin rings zipper the mouse embryo for blastocyst formation. *Cell* **173**:776–791. DOI: <https://doi.org/10.1016/j.cell.2018.02.035>
- Zhang Y**, Conti MA, Malide D, Dong F, Wang A, Shmist YA, Liu C, Zerfas P, Daniels MP, Chan CC, Kozin E, Kachar B, Kelley MJ, Kopp JB, Adelstein RS. 2012. Mouse models of MYH9-related disease: mutations in nonmuscle myosin II-A. *Blood* **119**:238–250. DOI: <https://doi.org/10.1182/blood-2011-06-358853>, PMID: 21908426
- Zhang Y**, De Mets R, Monzel C, Acharya V, Toh P, Chin JFL, Van Hul N, Ng IC, Yu H, Ng SS, Tamir Rashid S, Viasnoff V. 2020. Biomimetic niches reveal the minimal cues to trigger apical lumen formation in single hepatocytes. *Nature Materials* **19**:1026–1035. DOI: <https://doi.org/10.1038/s41563-020-0662-3>
- Zhang HT**, Hiiragi T. 2018. Symmetry Breaking in the Mammalian Embryo. *Annual review of cell and developmental biology* **34**:405–426. DOI: <https://doi.org/10.1146/annurev-cellbio-100617-062616>, PMID: 30095292
- Zhu M**, Leung CY, Shahbazi MN, Zernicka-Goetz M. 2017. Actomyosin polarisation through PLC-PKC triggers symmetry breaking of the mouse embryo. *Nature Communications* **8**:921. DOI: <https://doi.org/10.1038/s41467-017-00977-8>, PMID: 29030553
- Ziomek CA**, Johnson MH. 1980. Cell surface interaction induces polarization of mouse 8-cell blastomeres at compaction. *Cell* **21**:935–942. DOI: [https://doi.org/10.1016/0092-8674\(80\)90457-2](https://doi.org/10.1016/0092-8674(80)90457-2), PMID: 7438209

Appendix 1

Appendix 1—table 1. Statistical analysis of compaction data.

Mean contact angles and developmental times related to **Figure 1B** and **Figure 3B** with associated SEM, embryo number, and p value from unpaired two-tailed Welch's *t* test against WT.

		Time after last third cleavage				Time before initial fourth cleavage				Time after last fourth cleavage				Time before initial fifth cleavage			
		Mean	SEM	Embryos	P value	Mean	SEM	Embryos	p value	Mean	SEM	Embryos	p value	Mean	SEM	Embryos	P value
		WT	Time after 3rd cleavage [h]	0	0	23	NA	7.0	0.3	23	NA	10.9	0.3	21	NA	16.7	0.4
	Contact angle [°]	87	3		NA	147	2		NA	140	3		NA	148	2		NA
mzMyh9	Time after 3rd cleavage [h]	0	0	15	NA	9.8	0.5	15	0.0001	13.8	0.6	10	0.002	18.8	0.5	8	0.01
	Contact angle [°]	85	2		0.5	125	4		0.00001	104	5		0.00001	131	8		0.02
mMyh9	Time after 3rd cleavage [h]	0	0	8	NA	10.4	0.7	8	0.001	14.6	0.8	8	0.002	18.7	0.7	3	0.002
	Contact angle [°]	86	5		0.5	115	6		0.0001	112	7		0.003	113	21		0.1
mzMyh10	Time after 3rd cleavage [h]	0	0	11	NA	5.4	0.4	11	0.004	10.2	0.6	11	0.2	15.8	0.4	11	0.1
	Contact angle [°]	87	5		0.8	121	4		0.0001	126	5		0.03	148	4		0.8
mMyh10	Time after 3rd cleavage [h]	0	0	20	NA	6.3	0.4	20	0.2	10.8	0.3	20	0.5	16.8	0.6	20	0.9
	Contact angle [°]	85	3		0.3	128	5		0.0004	128	3		0.006	149	2.8		0.5
mzMyh9; mzMyh10	Time after 3rd cleavage [h]	0	0	7	NA	9.7	0.8	3	0.07	12	NA	1	NA	NA			
	Contact angle [°]	89	6		0.8	117	4		0.006	84.5	NA		NA				
mzMyh9; mMyh10	Time after 3rd cleavage [h]	0	0	7	NA	6.9	1.7	4	1.0	9	0.5	2	0.1	12	NA	1	NA
	Contact angle [°]	83	5		0.6	100	5		0.002	108	14		0.07	113	NA		NA
mMyh9; mMyh10	Time after 3rd cleavage [h]	0	0	7	NA	8	1.3	5	0.5	11	0.5	3	1.0	NA			
	Contact angle [°]	76	7		0.1	110	5		0.0006	105	3		0.002				

Appendix 1—table 2. Statistical analysis of cell cycle duration data.

Mean durations of 8-cell stage, fourth wave of cleavage, and 16-cell stage related to **Figures 2B** and **5B** with associated SEM, embryo number, and p value from unpaired two-tailed Welch's *t* test against WT.

	Duration of 8-cell stage [h]				Duration of fourth wave of cleavages [h]				Duration of 16-cell stage [h]			
	Mean	SEM	Embryos	P value	Mean	SEM	Embryos	P value	Mean	SEM	Embryos	P value
	WT	7.0	0.3	23	NA	4.0	0.3	23	NA	5.5	0.4	23
mzMyh9	9.8	0.5	15	0.0001	4.8	0.7	15	0.3	5.7	0.8	14	0.8
mMyh9	10.4	0.7	8	0.001	4.2	1.2	8	0.9	7.0	1.1	8	0.1
mzMyh10	5.4	0.4	11	0.004	4.8	0.8	11	0.2	5.6	0.5	11	0.9
mMyh10	6.3	0.4	20	0.2	4.5	0.4	20	0.3	6.1	0.5	20	0.4

Continued on next page

Appendix 1—table 2 continued

	Duration of 8-cell stage [h]				Duration of fourth wave of cleavages [h]				Duration of 16-cell stage [h]			
	Mean	SEM	Embryos	P value	Mean	SEM	Embryos	P value	Mean	SEM	Embryos	P value
mzMyh9; mzMyh10	10.3	1.4	8	0.06	2.0	0.8	3	0.1				
mzMyh9; mMyh10	8.1	1.4	6	0.5	4.3	1.1	3	0.8	NA			
mMyh9; mMyh10	9.3	1.0	8	0.06	3.6	0.7	5	0.6				

Appendix 1—table 3. Statistical analysis of periodic contraction data.

Mean amplitude of periodic movements and contact angle related to **Figure 2H** with associated SEM, embryo number, and p value from Mann-Whitney *U* test against WT.

	Embryos	Maximum amplitude within 50–120 s oscillation period range [μ m]			Contact angle [$^{\circ}$]		
		Mean	SEM	p value	Mean	SEM	p value
WT	21	0.140	0.009	NA	126	5	NA
mzMyh9	15	0.039	0.002	0.000005	78	3	0.00003
mMyh9	8	0.045	0.003	0.00005	82	6	0.001
mzMyh10	11	0.094	0.009	0.006	103	6	0.02
mMyh10	20	0.111	0.013	0.01	108	5	0.02

DISCUSSION

Actomyosin contractility is a major engine of the morphogenetic events of the preimplantation mouse development. Increase in actomyosin contractility drives embryo compaction (Maître et al., 2015). Differences in contractility trigger the sorting of blastomeres into internal or external positions; the less-contractile cells spread over the more contractile cells, which become internalized (Maître et al., 2016). Once the blastomeres are segregated into different positions they are considered to differentiate into two different cell types: the inner cell mass (ICM) and the trophectoderm (TE). Contractile forces play a role also during cavitation process where more contractile cells pushes the fluid towards the less contractile ones deciding the positioning of the lumen (Dumortier et al., 2019). Although actomyosin contractility plays such an important role, how it matures throughout cleavage stages remains unknown. Mouse embryo with its slow development compared to other model organisms used in this field allows us to look at actomyosin contractility at 2 different timescale; 1) hours-to-days: Morphogenetic events 2) seconds-to-minutes : Periodic Cortical Waves of Contraction (PeCoWaCo).

In this thesis, I discovered and studied the scaling of Periodic Cortical Waves of Contraction (PeCoWaCo) that we observe during the preimplantation development of mouse embryos. More specifically; I investigated when and why preimplantation mouse embryos start showing PeCoWaCo and how PeCoWaCo are regulated both mechanically and molecularly via mechanical manipulations of cell size and shape as well as genetic and chemical disruptions of actomyosin contractility.

1. PeCoWaCo reveals maturation of actomyosin cortex

I showed that PeCoWaCo are detectable from zygote onwards. Moreover, by looking into characteristics of PeCoWaCo, we observed the change in the period of PeCoWaCo throughout the cleavage stages. This showed us that PeCoWaCo can be used as a tool to understand the actomyosin cortex of the earlier stages. This gave us a 'map' of the mechanochemical characteristics of the actomyosin cortex that was not possible by simply looking at cell divisions or morphogenesis as there is no morphogenetic event happening till 8-cell stage.

We also showed that from zygote to early 8-cell stage surface tension drops after each round of division and this drop in the surface tension coincides with the decrease in the period of PeCoWaCo. However, when looked into stages after the initiation of morphogenesis, PeCoWaCo period stays unaffected from the changes in the surface tension. 16-cell stage, where 2 population of surface tension is observed, although there is a difference in the amplitude, there is no difference in the PeCoWaCo period between these populations (Maître et al., 2016).

Although PeCoWaCo are detectable from zygote onwards, I observed that detection rate shows a dramatic peak when embryo reaches the 4-cell-stage. After using various methods to understand the reason of this peak, I showed that the pulsed contractions do not rely on the successive reductions in cell size but rather on the gradual decrease in surface tension of the blastomeres. We hypothesize that pulsatile nature of actomyosin, or the cycling activator / inhibitor exists from the beginning, however the cortex of blastomeres at the zygote and 2-cell stages is too stiff to deform therefore this internal oscillations are not able to curve the surface for PeCoWaCo to become visible. Indeed, softening the cortex of 2-cell stage embryos with low concentrations of the actin polymerization inhibitor Latrunculin A increased the proportions of embryos displaying PeCoWaCo proving our hypothesis. Moreover, the oscillation period of softened 2-cell stage embryos is lower than the control indicating that F-actin polymerization rate could be the regulatory machinery behind the stepwise decrease in PeCoWaCo period. In addition to cortical softening awaking the PeCoWaCo, I also showed that zygotic genome activation (ZGA) that occurs at 2-cell-stage is required for the peak of PeCoWaCo detection that we observe at 4-cell-stage.

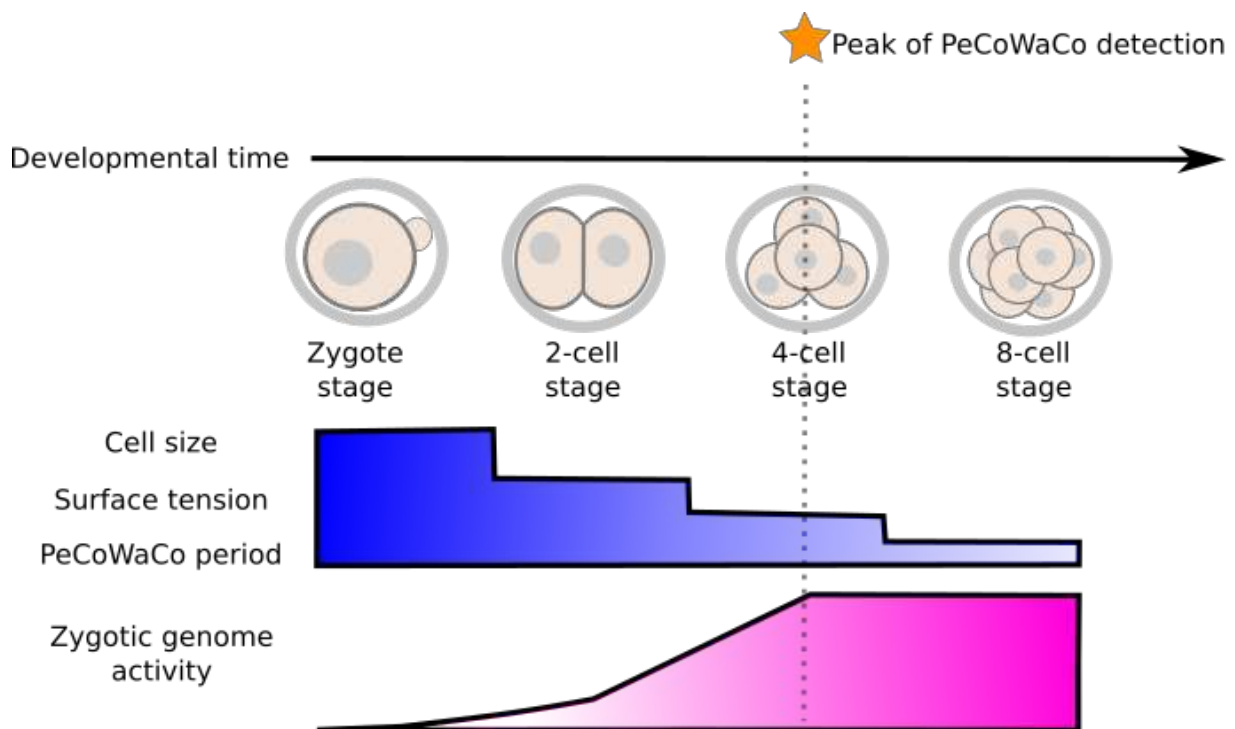


FIGURE 27: GRAPHICAL ABSTRACT

Schematic diagram of our findings on scaling of surface tension and PeCoWaCo through cleavage stages with a peak of detection rate at 4-cell stage corresponding to a critical surface tension value and zygotic genome activation.

Altogether, these might suggest that the cortex is different between cleavage stages and at the morphogenetic stage. I showed that this difference is not coming from a detectable cortex thickness with airyscan. However, cortex mechanics is also likely to be affected by the spatial organization of F-actin. To better understand the structural changes in the cortex, other superresolutive microscopes can be used to resolve better, such as STED or electron microscopy. However, as cells of the preimplantation embryo are non-adhesive and big, these methods are not optimal for the moment. Instead, the new sample preparation method called expansion microscopy can be more suitable to look into architectural changes happening during the cleavage stages. This new method works by physically magnifying the specimen directly; therefore, it enables biological samples to be imaged with nanoscale precision, even on ordinary microscopes. Magnifying an already quite big cell would cause losing the signal and the resolution of half of the volume. However, the bottom half could already be enough for deciphering the architecture of the cortex.

In addition to high-resolution imaging to decipher the architecture, we can focus on the crosslinkers and actin nucleators that shape the actin meshwork. Mining protein screening data of preimplantation development can guide us to select target proteins (Gao et al., 2017). These proteins can be targeted using inhibitors such as SMIFH2 (formin inhibitor) and CK666 (Arp2/3 inhibitor) and see whether they affect the PeCoWaCo period. However, using drugs is, most of the time, not a clear-cut experiment as they inhibit many other processes simultaneously. For cleaner experimentation, one can focus on genetic tools. Due to the maternal pool of mRNA and proteins, CRISPR/Cas9 technology is unsuitable for the cleavage stages. As we have not been successful with our attempts to replicate already published results with siRNA, this technique is also out of the list. A novel technique called TrimAway that directly targets the protein of interest would be a better option for this purpose. This method eliminates protein of interest within seconds by introducing an antibody specific to the protein of interest and a special protein called Trim21 as Trim21 recognizes antibodies and targets them (together with the protein they bind) to proteasomes (Israel et al., 2019). For our interest, selective antibodies and Trim21 can be introduced into 2-cell embryo to see if the PeCoWaCo period will increase and become more like what we observe in the zygote or decrease and become more like the ones in 4-cell-stage leading us to understand how the actomyosin cortex changes through the developmental stages. In addition to removal, overexpression experiments with mRNA injection can help as well. Altogether, these could give us how the actomyosin cortex changes over the time of cleavage stages.

The pipeline that I developed to study the cortex mechanics of cleavage stage mouse embryos could also be helpful to study the cortex and its contractility through early embryonic developments of different mammals. This pipeline is not an invasive method, and it does not require a fluorescence signal. It simply requires observing embryos under the microscope with white light. Therefore, it serves as a straightforward pipeline to be used for the embryos of other mammals that we do not have enough genetic tools (or rights to use them on) to do confocal images such as human embryos. Morphogenesis of the human blastocyst has not yet been analyzed thoroughly, and we, therefore, do not know to what extent it differs from other mammals. Preliminary observations on human embryos developing during artificial

reproductive technologies (ART) reveal quantitative differences with the mouse regarding morphogenetic progression. To further characterize the specific properties of human embryonic development, it would be key to observe if PeCoWaCo are conserved and if its features are similar. PIV analysis pipeline can quantify the period and amplitude of PeCoWaCo in human embryos. Moreover, preliminary results of Julie Firmin, a PhD student in our lab, show that preimplantation human embryos are much more stiffer than mouse embryos. Therefore, it would be interesting for our hypothesis on cortex stiffness and PeCoWaCo detection to see if PeCoWaCo are conserved in human embryos. This pipeline can be used to investigate the cortex mechanics of other animals, in addition to human embryos, such as sheep, pigs, cows, and horses. Allowing the selection of better embryos for those animals can be better for their strategic benefits (food, research) and their industries' economic impact. Supposing that PeCoWaCo are conserved and could tell us whether the quality of the embryo is good or not; then can be used as a quality check step in the reproduction technologies as a novel non-invasive method to appraise quantitatively the developmental capacity of embryos without needing hard to perform techniques.

2. Robustness of PeCoWaCo Period and Velocity.

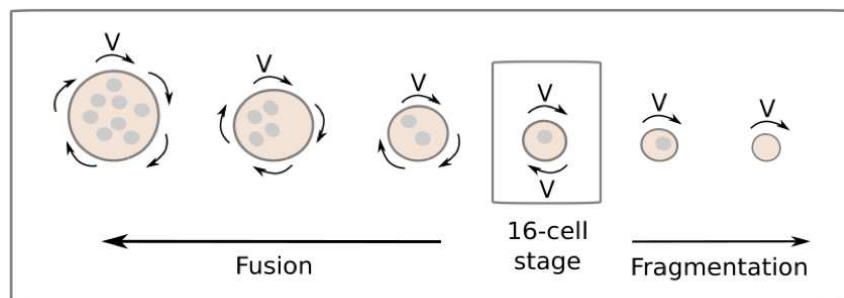
In this study, we take advantage of the slow development of the mouse embryo to study thousands of pulsed contractions and the robustness of the mouse embryo to size manipulation to explore the geometrical regulation of PeCoWaCo. Using fragmentation and fusion of cells, we find that the initiation, persistence, or properties of PeCoWaCo do not depend on a broad range of cell sizes. Furthermore, although PeCoWaCo seem insensitive to geometrical changes, aspiration of blastomeres reveals that PeCoWaCo are sensitive to mechanical stress. We confirm this by using a mild reduction of cell contractile stresses. Together, this study reveals the geometrical and mechanical regulation of PeCoWaCo during preimplantation development.

Measuring the period, amplitude, and wave velocity of 16-cell stage blastomeres over a broad range of sizes and surface curvature by fusing different numbers of cells and fragmenting cells into smaller cells. Careful analysis of the relationship between cell size and the properties of PeCoWaCo over this extensive range of cell radii showed that periodic contractions maintain their amplitude, period, and propagation velocity (Fig 12). This finding highlights the robustness of periodic contractions to a broad range of curvatures. This also makes blastomere size as an unlikely explanation for the gradually decreasing oscillation period from the zygote stage onwards (Fig 12E). The robustness of the period of PeCoWaCo to varying cell size and curvature is compatible with the proposal that contractile pulses durations are an intrinsic property of the actomyosin cytoskeleton (Baird et al., 2017) which cells can excite in space and time to change shape (Bement et al., 2015).

In addition to the robustness of the period, I also showed unsuspected robustness of the velocity to changing cell size and curvature. Interestingly, the propagation speed of Rho activation wavefront in starfish oocytes had been suggested to be coupled to the local curvature of the cell surface (Bischof et al., 2017a). Shape changing experiments done on starfish oocyte revealed that propagation speed of the Rho wavefront is changing with local curvature. However, it is not regulated by the curvature but by decaying of the concentration gradient that causes the contractions in the first place (Wigbers et al., 2021). These findings suggest that wave propagation is globally coordinated and this is proposed to serve as a mechanism for cells to sense their

shape (Wigbers et al., 2021). This is quite interesting as it could explain the behavior difference that we observe with micropipette aspiration. By aspirating the cells into a micropipette, we create a stretched surface and change the distance between the surface and the center of the cell's mass, resulting in slower PeCoWaCo.

One of our hypothesis to explain the robustness of period and the velocity of PeCoWaCo with changing cell size is the change in the number of traveling waves. At the 8-cell stage, PeCoWaCo has been characterized as a mode 2 oscillation (Maître et al., 2015). Meaning that there are two waves travelling around the cell at the same time. We hypothesize that by fusing different numbers of cells together, we might be adding more traveling waves into the system. This could explain how we observe same oscillation period at different cell sizes while the wave travels at the same speed (Fig. 28). In order to test this hypothesis, with Ido Lavi, who was a PhD student in Laboratoire Jean Perrin and received his PhD from Sorbonne Université on 2019, we looked into different oscillation modes in the fused embryos and we did not detect difference. However, we cannot exclude the fact that all these measurements were done on the images taken at the equatorial plane of the cells. It is not possible to fully understand the behavior of a wave that travels in 3D by only looking at it in 2D. Therefore, this is not sufficient to reject this hypothesis and imaging PeCoWaCo in 3D is critical for further investigation.



$$T_{(8x16)} = T_{(4x16)} = T_{(2x16)} \quad T_{(MeCon)} = T_{(Frag)}$$

FIGURE 28: MULTIPLE WAVES HYPOTHESIS

Schematic diagram of our hypothesis explaining how with changing the number of traveling waves both period and the velocity of PeCoWaCo can be staying the same with increasing and decreasing cell sizes through fusion and fragmentation experiments.

PeCoWaCo had been shown to avoid cell-cell contacts and the apical domain of the cell (Maître et al., 2015). Under the light of this information, another hypothesis on the observed robustness of period and the velocity of PeCoWaCo with changing cell size is the “Free-space to wave”. In the fusion experiment as I used 16-cell stage embryos, blastomeres with and without apical domains are merged creating multiple patches of apical domain around the perimeter (Fig. 29). This could mean that although I created different cell sizes by fusing different numbers of cells, due to different number of apical domains added to the surface at the end the space that PeCoWaCo could travel could be staying the same. This hypothesis could be easily checked from the 3D images of fused cells and measuring the surface area that apical domains cover compared to total surface area. Moreover, it is also possible that due to the labyrinth created by these apical domain patches, PeCoWaCo travel rather locally instead of all around the perimeter. Therefore, to better understand the mechanisms that provides the robustness of the PeCoWaCo characteristics it would be interesting to see how the wave travels in this labyrinth. The best way to see this would be 3D imaging and 3D analysis of PeCoWaCo in fused cells. Unfortunately, with the technologies we have we cannot image fast enough to catch the propagation of the PeCoWaCo for the full size of the fused cells.

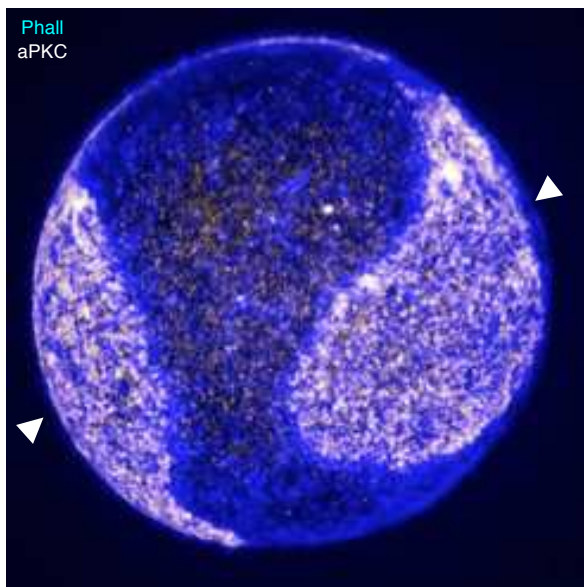


FIGURE 29: PATCHES OF APICAL DOMAIN IN FUSED CELLS

Maximum projection of a fused 4x 1/16th blastomere fixed and Immunostained with Phalloidin in blue and aPKC in white showing the patches of apical domain (shown with white arrows) at the cell surface.

3. Molecular regulation of PeCoWaCo

The robustness of the properties of PeCoWaCo to varying cell size curvature that we discussed earlier is compatible with the proposal that contractile pulses durations are an intrinsic property of the actomyosin cytoskeleton (Baird et al., 2017), which cells can excite in space and time to change shape (Bement et al., 2015). To investigate the regulatory machinery behind I first focused on the main characters : Myosin motor and F-actin and also 2 pathways Rho and aPKC.

The analysis of maternal zygotic mutants of myosin-II heavy chain 9 and 10 showed that PeCoWaCo in mouse blastomeres result primarily from the action of the Myh9 rather than Myh10. With the low numbers of Myh9 homozygous mutant indicating that myosin might play a role in fine tuning the period, I used myosin motor activity inhibitors, Blebbistatin and ML-7, to inhibit the myosin light chain kinase, the myosin heavy chain respectively at low concentrations on 16-cell-stage blastomeres. These experiments showed that the period of oscillations are regulated by Myosin motor activity whereas the velocity is not affected by it. Then I targeted the F-actin filament by using Latrunculin A at 2-cell stage and 16-cell stage. Interestingly, inhibiting F-actin polymerization showed different effects on PeCoWaCo at 2 and 16 cell stage embryo. While it decreased the period at 2-cell stage, at 16-cell stage the period was increase. This difference shows us that cortex and its contractility is working differently at different stages. More interestingly, inhibition of actin polymerization while it affects the period, like myosin motor, also did not change the wave velocity. Altogether, these results suggest that, period is representing the characteristics of the meshwork whereas the wave propagation is probably regulated globally by cytoplasmic signals.

The cycling of contractile pulses is typically regulated by the Rho GTPase signaling module, which controls both actin filaments nucleation via formins and non-muscle myosin II activation via kinases (Zaidel-Bar et al., 2015). Therefore, this pathway is a likely regulator of the period of PeCoWaCo during development. In starfish oocytes, contraction and the Rho wave front shown to be initiated with the decrease of Cdk1 gradient. Moreover, its velocity had been shown to be regulated globally by the ratio between Cdk1 and Ect2 levels in the cytoplasm (Bischof et al., 2017b; Wigbers et al., 2021). However, Cdk1 is released into cytoplasm after nuclear breakdown. This regulation is specific for cell division and we do not expect this to be involved in our

system as PeCoWaCo in mouse embryos are observed during interphase and not visible during division.

Fusion of cells at the 16-cell stage implies that blastomeres with and without apical domains are merged. The apical domain is known to influence the amplitude of contractile waves (Maître et al., 2016). Therefore, apical signals may also influence the period and/or velocity of PeCoWaCo. Moreover, PKC activation was proposed to activate actomyosin contractility via the Rho GTPase (Zhu et al., 2017), which was earlier found to be required for compaction (Clayton et al., 1999). However, Rho kinase (Rock), the usual suspect typically involved in controlling actomyosin contractility does not seem to be involved in early mouse development. Neither Rock inhibitors (Kono et al., 2014; Laeno et al., 2013; Samarage et al., 2015; Zenker et al., 2018), nor Rock knockout (Kamijo et al., 2011) show a compaction phenotype (or other contractility defects). My results with aPKC mutants and dominant negative form, together with Rho inhibitor, showed that neither aPKC nor Rho pathways play a role in the regulation of PeCoWaCo.

CONCLUSION

In the mouse, morphological changes occur on the timescale of hours when actomyosin contractility typically acts within seconds to minutes (Salbreux et al., 2012). On such short timescale, mouse blastomeres show rapid surface deformations, which propagate periodically. Initially spotted in 1980 (Lehtonen, 1980), these movements were later characterized as Periodic Cortical Waves of Contraction (Maître et al., 2015) in short “PeCoWaCo”.

The pulsatile nature of actomyosin contractility is a mysterious property of cell’s contractility, which is of widespread interest to biologists studying cell and tissue shape in physiological conditions and disease. With its relatively slow development, the mouse embryo permits observing actomyosin contractility across different time scales. PeCoWaCo are observed as a traveling wave, however, how these contractions occurred at cortex level and how they “travel” remains unknown. Understanding the mechanism of action of PeCoWaCo can help to decipher their function at cellular and at tissue level.

In this thesis, I investigated the initiation and the regulation of PeCoWaCo in pre-implantation mouse embryos. I demonstrated that **throughout cleavage divisions, actomyosin contractility matures to become the major driving force of morphogenesis and PeCoWaCo can be used as a read out of this maturation of the cortex as its frequency increases with maturing cortex.** I have also demonstrated that **PeCoWaCo characteristics (its frequency and velocity) are robust to changes in cell sizes.** Moreover, I also shed some light on the **uncoupling between the regulation of the period and the velocity of these oscillations.** Experiments with actomyosin contractility inhibitors suggest that **while the period is regulated by the properties of the cortex, velocity might be regulated at the global level.**

In addition to the scientific outcome presented in this thesis, we highlighted the importance of interdisciplinarity collaborations such as with image analysts and theoretical physicists. Our discussions led to new experimental designs, new parameters to look into and also to build new hypothesis. Moreover, the image analysis tool that we developed in collaboration would be useful for various other research outside of investigation of PeCoWaCo. With its error-prone usage on a free software like Fiji, It does not require an expertise in computer science. This is not only important

for developmental biologist or cell biologist who is interested in actomyosin cortex. As the cellular form is an important parameter in defining the well-being and functions of a cell and, therefore, can be used as a criterion for determining its state of health, our image analysis tool can serve to more translational research areas as well.

REFERENCES

- Abe, K. ichiro, Funaya, S., Tsukioka, D., Kawamura, M., Suzuki, Y., Suzuki, M. G., Schultz, R. M., & Aoki, F. (2018). Minor zygotic gene activation is essential for mouse preimplantation development. *Proceedings of the National Academy of Sciences of the United States of America*, *115*(29), E6780–E6788.
<https://doi.org/10.1073/pnas.1804309115>
- Aiken, C. E. M., Swoboda, P. P. L., Skepper, J. N., & Johnson, M. H. (2004). *The direct measurement of embryogenic volume and nucleo-cytoplasmic ratio during mouse pre-implantation development*. <https://doi.org/10.1530/rep.1.00281>
- Alsous, J. I., Romeo, N., Jackson, J. A., Mason, F. M., Dunkel, J., & Martin, A. C. (2021). Dynamics of hydraulic and contractile wave-mediated fluid transport during *Drosophila* oogenesis. *PNAS*, *118*(10).
<https://doi.org/10.1073/pnas.2019749118/-/DCSupplemental.y>
- Artus, J., & Cohen-tannoudji, M. (2008). Cell cycle regulation during early mouse embryogenesis. *Molecular and Cellular Endocrinology*, *282*, 78–86.
<https://doi.org/10.1016/j.mce.2007.11.008>
- Baird, M. A., Billington, N., Wang, A., Adelstein, R. S., Sellers, J. R., & Wang, Y. (2017). *Local pulsatile contractions are an intrinsic property of the myosin 2A motor in the cortical cytoskeleton of adherent cells*.
<https://doi.org/10.1091/mbc.E16-05-0335>
- Bement, W. M., Leda, M., Moe, A. M. M., Kita, A. M. M., Larson, M. E. E., Golding, A. E. E., Pfeuti, C., Su, K.-C. C., Miller, A. L. L., Goryachev, A. B. B., von Dassow, G., & Von Dassow, G. (2015). Activator-inhibitor coupling between Rho signalling and actin assembly makes the cell cortex an excitable medium. *Nature Cell Biology*, *17*(11), 1471–1483. <https://doi.org/10.1038/ncb3251>
- Bischof, J., Brand, C. A., Somogyi, K., Májer, I., Thome, S., Mori, M., Schwarz, U. S., & Lénárt, P. (2017a). A cdk1 gradient guides surface contraction waves in oocytes. *Nature Communications*, *8*(1), 1–10. <https://doi.org/10.1038/s41467-017-00979-6>
- Bischof, J., Brand, C. A., Somogyi, K., Májer, I., Thome, S., Mori, M., Schwarz, U. S., & Lénárt, P. (2017b). A cdk1 gradient guides surface contraction waves in oocytes. *Nature Communications*, *8*(1), 1–10. <https://doi.org/10.1038/s41467-017-00979-6>

- Bitar, K. N., Gilmont, R. R., Raghavan, S., & Somara, S. (2012). Cellular Physiology of Gastrointestinal Smooth Muscle. In *Physiology of the Gastrointestinal Tract*. <https://doi.org/10.1016/B978-0-12-382026-6.00017-8>
- Blanchard, G. B., Murugesu, S., Adams, R. J., Martinez-Arias, A., & Gorfinkiel, N. (2010). Cytoskeletal dynamics and supracellular organisation of cell shape fluctuations during dorsal closure. *Journal of Cell Science*, *123*(16), e1–e1. <https://doi.org/10.1242/jcs.078279>
- Bretschneider, T., Anderson, K., Ecke, M., Müller-Taubenberger, A., Schroth-Diez, B., Ishikawa-Ankerhold, H. C., & Gerisch, G. (2009). The three-dimensional dynamics of actin waves, a model of cytoskeletal self-organization. *Biophysical Journal*, *96*(7), 2888–2900. <https://doi.org/10.1016/j.bpj.2008.12.3942>
- Brugués, J., Nuzzo, V., Mazur, E., & Needleman, D. J. (2012). Nucleation and transport organize microtubules in metaphase spindles. *Cell*, *149*(3), 554–564. <https://doi.org/10.1016/j.cell.2012.03.027>
- Charras, G., & Paluch, E. (2008). Blebs lead the way: How to migrate without lamellipodia. *Nature Reviews Molecular Cell Biology*, *9*(9), 730–736. <https://doi.org/10.1038/nrm2453>
- Charras, G. T., Hu, C. K., Coughlin, M., & Mitchison, T. J. (2006). Reassembly of contractile actin cortex in cell blebs. *Journal of Cell Biology*, *175*(3), 477–490. <https://doi.org/10.1083/jcb.200602085>
- Cheer, A., Vincent, J. P., Nuccitelli, R., & Oster, G. (1987). Cortical activity in vertebrate eggs I: The activation waves. *Journal of Theoretical Biology*. [https://doi.org/10.1016/S0022-5193\(87\)80217-5](https://doi.org/10.1016/S0022-5193(87)80217-5)
- Chugh, P., Clark, A. G., Smith, M. B., Cassani, D. A. D., Dierkes, K., Ragab, A., Roux, P. P., Charras, G., Salbreux, G., & Paluch, E. K. (2017). Actin cortex architecture regulates cell surface tension. *Nature Cell Biology*, *19*(6), 689–697. <https://doi.org/10.1038/ncb3525>
- Chugh, P., & Paluch, E. K. (2018). The actin cortex at a glance. *Journal of Cell Science*, *131*(14), jcs186254. <https://doi.org/10.1242/jcs.186254>
- Clark, A. G., Dierkes, K., & Paluch, E. K. (2013). Monitoring actin cortex thickness in live cells. *Biophysical Journal*, *105*(3), 570–580. <https://doi.org/10.1016/j.bpj.2013.05.057>

- Clayton, L., Hall, A., & Johnson, M. H. (1999). A role for Rho-like GTPases in the polarisation of mouse eight-cell blastomeres. *Developmental Biology*, *205*(2), 322–331. <https://doi.org/10.1006/dbio.1998.9117>
- Clift, D., & Schuh, M. (2014). *Re-starting life : Fertilization and the transition from meiosis to mitosis*. *14*(9), 549–562. <https://doi.org/10.1038/nrm3643>. Re-starting
- Cockburn, K., Biechele, S., Garner, J., & Rossant, J. (2013). The hippo pathway member nf2 is required for inner cell mass specification. *Current Biology*, *23*(13), 1195–1201. <https://doi.org/10.1016/j.cub.2013.05.044>
- Coravos, J. S., Mason, F. M., & Martin, A. C. (2018). *Actomyosin pulsing in tissue integrity maintenance during morphogenesis*. *27*(4), 276–283. <https://doi.org/10.1016/j.tcb.2016.11.008>. Actomyosin
- Dard, N., Le, T., Maro, B., & Louvet-Vallée, S. (2009). Inactivation of aPKC λ reveals a context dependent allocation of cell lineages in preimplantation mouse embryos. *PLoS ONE*, *4*(9). <https://doi.org/10.1371/journal.pone.0007117>
- Dehapiot, B., Clément, R., Alégot, H., Gzásó-gerhát, G., Philippe, J., & Lecuit, T. (2020). Assembly of a persistent apical actin network by the formin Frl/Fmnl tunes epithelial cell deformability. *Nature Cell Biology*. <https://doi.org/10.1038/s41556-020-0524-x>
- Driscoll, M. K., Losert, W., Jacobson, K., & Kapustina, M. (2015). Spatiotemporal relationships between the cell shape and the actomyosin cortex of periodically protruding cells. *Cytoskeleton*, *72*(6), 268–281. <https://doi.org/10.1002/cm.21229>
- Ducibella, T., Ukena, T., Karnovsky, M., & Anderson, E. (1977). Changes in cell surface and cortical cytoplasmic organization during early embryogenesis in the preimplantation mouse embryo. *Journal of Cell Biology*, *74*(1), 153–167. <https://doi.org/10.1083/jcb.74.1.153>
- Dumortier, J. G., Le Verge-Serandour, M., Tortorelli, A. F., Mielke, A., de Plater, L., Turlier, H., & Maître, J.-L. (2019). Hydraulic fracturing and active coarsening position the lumen of the mouse blastocyst. *Science*, *August*, 1–5.
- Ebrahim, S., Fujita, T., Millis, B. A., Kozin, E., Ma, X., Kawamoto, S., Baird, M. A., Davidson, M., Yonemura, S., Hisa, Y., Conti, M. A., Adelstein, R. S., Sakaguchi, H., & Kachar, B. (2013). NMII forms a contractile transcellular sarcomeric network to regulate apical cell junctions and tissue geometry. *Current Biology*,

- 23(8), 731–736. <https://doi.org/10.1016/j.cub.2013.03.039>
- Eddy, R. J., Pierini, L. M., Matsumura, F., & Maxfield, F. R. (2000). Ca²⁺-dependent myosin II activation is required for uropod retraction during neutrophil migration. *Journal of Cell Science*, 113(7), 1287–1298. <https://doi.org/10.1242/jcs.113.7.1287>
- Fehon, R. G., McClatchey, A. I., & Bretscher, A. (2010). Organizing the cell cortex: The role of ERM proteins. *Nature Reviews Molecular Cell Biology*, 11(4), 276–287. <https://doi.org/10.1038/nrm2866>
- Fujiwara, K., & Pollard, T. D. (1976). Fluorescent antibody localization of myosin in the cytoplasm, cleavage furrow, and mitotic spindle of human cells. *Journal of Cell Biology*, 71(3), 848–875. <https://doi.org/10.1083/jcb.71.3.848>
- Gao, Y., Liu, X., Tang, B., Liao, L., Gao, S., Gao, Y., Liu, X., Tang, B., Li, C., Kou, Z., Li, L., Liu, W., Wu, Y., & Kou, X. (2017). *Protein Expression Landscape of Mouse Embryos during Pre-implantation Development Resource Protein Expression Landscape of Mouse Embryos during Pre-implantation Development*. 3957–3969. <https://doi.org/10.1016/j.celrep.2017.11.111>
- Goedhart, J. (2021). SuperPlotsOfData-a web app for the transparent display and quantitative comparison of continuous data from different conditions. *Molecular Biology of the Cell*, 32(6), 470–474. <https://doi.org/10.1091/mbc.E20-09-0583>
- Goehring, N. W., Hoegge, C., Grill, S. W., & Hyman, A. A. (2011). PAR proteins diffuse freely across the anterior-posterior boundary in polarized *C. elegans* embryos. *Journal of Cell Biology*, 193(3), 583–594. <https://doi.org/10.1083/jcb.201011094>
- Graessl, M., Koch, J., Calderon, A., Kamps, D., Banerjee, S., Mazel, T., Schulze, N., Jungkurth, J. K., Patwardhan, R., Solouk, D., Hampe, N., Hoffmann, B., Dehmelt, L., & Nalbant, P. (2017). An excitable Rho GTPase signaling network generates dynamic subcellular contraction patterns. *Journal of Cell Biology*, 216(12), 4271–4285. <https://doi.org/10.1083/jcb.201706052>
- Guevorkian, K., Colbert, M. J., Durth, M., Dufour, S., & Brochard-Wyart, F. (2010). Aspiration of biological viscoelastic drops. *Physical Review Letters*, 104(21), 1–4. <https://doi.org/10.1103/PhysRevLett.104.218101>
- Hamatani, T., Carter, M. G., Sharov, A. A., & Ko, M. S. H. (2004). Dynamics of global

- gene expression changes during mouse preimplantation development. *Developmental Cell*, 6(1), 117–131. [https://doi.org/10.1016/S1534-5807\(03\)00373-3](https://doi.org/10.1016/S1534-5807(03)00373-3)
- Harrington, E. A., Bebbington, D., Moore, J., Rasmussen, R. K., Ajose-Adeogun, A. O., Nakayama, T., Graham, J. A., Demur, C., Hercend, T., Diu-Hercend, A., Su, M., Golec, J. M. C., & Miller, K. M. (2004). VX-680, a potent and selective small-molecule inhibitor of the Aurora kinases, suppresses tumor growth in vivo. *Nature Medicine*, 10(3), 262–267. <https://doi.org/10.1038/nm1003>
- Heisenberg, C.-P., & Bellaïche, Y. (2013). Forces in Tissue Morphogenesis and Patterning. *Cell*, 153. <https://doi.org/10.1016/j.cell.2013.05.008>
- Hirate, Y., Hirahara, S., Inoue, K. I., Suzuki, A., Alarcon, V. B., Akimoto, K., Hirai, T., Hara, T., Adachi, M., Chida, K., Ohno, S., Marikawa, Y., Nakao, K., Shimono, A., & Sasaki, H. (2013). Polarity-dependent distribution of angiomin localizes hippo signaling in preimplantation embryos. *Current Biology*, 23(13), 1181–1194. <https://doi.org/10.1016/j.cub.2013.05.014>
- Hubatsch, L., Peglion, F., Reich, J. D., Rodrigues, N. T., Hirani, N., Illukkumbura, R., & Goehring, N. W. (2019). A cell size threshold limits cell polarity and asymmetric division potential. *Nature Physics*. <https://doi.org/10.1038/s41567-019-0601-x>
- Iglesias, P. A., & Devreotes, P. N. (2012). Biased excitable networks: How cells direct motion in response to gradients. *Current Opinion in Cell Biology*, 24(2), 245–253. <https://doi.org/10.1016/j.ceb.2011.11.009>
- Israel, S., Casser, E., Drexler, H. C. A., Fuellen, G., & Boiani, M. (2019). *A framework for TRIM21-mediated protein depletion in early mouse embryos: recapitulation of Tead4 null phenotype over three days*. 1–19.
- Kamijo, H., Matsumura, Y., Thumkeo, D., Koike, S., Masu, M., Shimizu, Y., Ishizaki, T., & Narumiya, S. (2011). Impaired vascular remodeling in the yolk sac of embryos deficient in ROCK-I and ROCK-II. *Genes to Cells*, 16(10), 1012–1021. <https://doi.org/10.1111/j.1365-2443.2011.01546.x>
- Kaneda, Y., Nakajima, T., Nishikawa, T., Yamamoto, S., Ikegami, H., Suzuki, N., Nakamura, H., Morishita, R., & Kotani, H. (2002). Hemagglutinating virus of Japan (HVJ) envelope vector as a versatile gene delivery system. *Molecular*

- Therapy*, 6(2), 219–226. <https://doi.org/10.1006/mthe.2002.0647>
- Kapustina, M., Elston, T. C., & Jacobson, K. (2013). Compression and dilation of the membrane-cortex layer generates rapid changes in cell shape. *Journal of Cell Biology*, 200(1), 95–108. <https://doi.org/10.1083/jcb.201204157>
- Katsuno, H., Toriyama, M., Hosokawa, Y., Mizuno, K., Ikeda, K., Sakumura, Y., & Inagaki, N. (2015). Actin migration driven by directional assembly and disassembly of membrane-anchored actin filaments. *Cell Reports*, 12(4), 648–660. <https://doi.org/10.1016/j.celrep.2015.06.048>
- Kim, H. Y., & Davidson, L. A. (2011). *Punctuated actin contractions during convergent extension and their permissive regulation by the non-canonical Wnt signaling pathway*. 635–646. <https://doi.org/10.1242/jcs.067579>
- Kono, K., Tamashiro, D. A. A., & Alarcon, V. B. (2014). Inhibition of RHO-ROCK signaling enhances ICM and suppresses TE characteristics through activation of Hippo signaling in the mouse blastocyst. *Developmental Biology*, 394(1), 142–155. <https://doi.org/10.1016/j.ydbio.2014.06.023>
- Korotkevich, E., Niwayama, R., Courtois, A., Friese, S., Berger, N., Buchholz, F., & Hiiragi, T. (2017). The Apical Domain Is Required and Sufficient for the First Lineage Segregation in the Mouse Embryo. *Developmental Cell*, 40(3), 235–247.e7. <https://doi.org/10.1016/j.devcel.2017.01.006>
- Laeno, A. M. A., Tamashiro, D. A. A., & Alarcon, V. B. (2013). Rho-Associated Kinase Activity Is Required for Proper Morphogenesis of the Inner Cell Mass in the Mouse Blastocyst¹. *Biology of Reproduction*, 89(5), 1–13. <https://doi.org/10.1095/biolreprod.113.109470>
- Lehtonen, B. E. (1980). Changes in cell dimensions and intercellular contacts during cleavage-stage cell cycles in mouse embryonic cells. *J. Embryol. Exp. Morph.*, 58, 231–249.
- Levayer, R., & Lecuit, T. (2012). Biomechanical regulation of contractility : spatial control and dynamics. *Trends in Cell Biology*, 22(2), 61–81. <https://doi.org/10.1016/j.tcb.2011.10.001>
- Madan, P., Rose, K., & Watson, A. J. (2007). Na/K-ATPase β 1 subunit expression is required for blastocyst formation and normal assembly of trophectoderm tight junction-associated proteins. *Journal of Biological Chemistry*, 282(16), 12127–

12134. <https://doi.org/10.1074/jbc.M700696200>

Maitre, J.-L., Berthoumieux, H., Krens, S. F. G., Salbreux, G., Julicher, F., Paluch, E., & Heisenberg, C.-P. (2012). Adhesion Functions in Cell Sorting by Mechanically Coupling the Cortices of Adhering Cells. *Science*, *338*(6104), 253–256.

<https://doi.org/10.1126/science.1225399>

Maître, J.-L., Niwayama, R., Turlier, H., Nedelec, F., & Hiiragi, T. (2015). Pulsatile cell-autonomous contractility drives compaction in the mouse embryo. *Nature Cell Biology*, *17*(7), 849–855. <https://doi.org/10.1038/ncb3185>

Maître, J.-L., Turlier, H., Illukkumbura, R., Eismann, B., Niwayama, R., Nédélec, F., & Hiiragi, T. (2016). Asymmetric division of contractile domains couples cell positioning and fate specification. *Nature*, *536*(7616), 344–348.

<https://doi.org/10.1038/nature18958>

Martin, A. C., Kaschube, M., & Wieschaus, E. F. (2009). Pulsed contractions of an actin-myosin network drive apical constriction. *Nature*, *457*(7228), 495–499.

<https://doi.org/10.1038/nature07522>

Mayer, M., Depken, M., Bois, J. S., Jülicher, F., & Grill, S. W. (2010). Anisotropies in cortical tension reveal the physical basis of polarizing cortical flows. *Nature*, *467*(7315), 617–621. <https://doi.org/10.1038/nature09376>

Michaud, A., Swider, Z. T., Landino, J., Leda, M., Miller, A. L., von Dassow, G., Goryachev, A. B., & Bement, W. M. (2021). Cortical excitability and cell division. *Current Biology*, *31*(10), R553–R559. <https://doi.org/10.1016/j.cub.2021.02.053>

Mittasch, M., Gross, P., Nestler, M., Fritsch, A. W., Iserman, C., Kar, M., Munder, M., Voigt, A., Alberti, S., Grill, S. W., & Kreysing, M. (2018). Non-invasive perturbations of intracellular flow Reveal Physical Principles of Cell Organization. *Nature Cell Biology*, *20*(March). <https://doi.org/10.1038/s41556-017-0032-9>

Motosugi, N., Bauer, T., Polanski, Z., Solter, D., & Hiiragi, T. (2005). Polarity of the mouse embryo is established at blastocyst and is not prepatterned. *Genes and Development*, *19*(9), 1081–1092. <https://doi.org/10.1101/gad.1304805>

Munjal, A., Philippe, J. M., Munro, E., & Lecuit, T. (2015). A self-organized biomechanical network drives shape changes during tissue morphogenesis.

Nature, *524*(7565), 351–355. <https://doi.org/10.1038/nature14603>

Munro, E., Nance, J., & Priess, J. R. (2004). Cortical flows powered by asymmetrical

- contraction transport PAR proteins to establish and maintain anterior-posterior polarity in the early *C. elegans* embryo. *Developmental Cell*, 7(3), 413–424.
<https://doi.org/10.1016/j.devcel.2004.08.001>
- Murrell, M., Oakes, P. W., Lenz, M., & Gardel, M. L. (2015). *Forcing cells into shape: the mechanics of actomyosin contractility*. 16(8), 486–498.
<https://doi.org/10.1038/nrm4012>.Forcing
- Nishioka, N., Yamamoto, S., Kiyonari, H., Sato, H., Sawada, A., Ota, M., Nakao, K., & Sasaki, H. (2008). Tead4 is required for specification of trophectoderm in pre-implantation mouse embryos. *Mechanisms of Development*, 125(3–4), 270–283.
<https://doi.org/10.1016/j.mod.2007.11.002>
- Niwayama, R., Moghe, P., Liu, Y.-J., Fabrèges, D., Buchholz, F., Piel, M., & Hiiragi, T. (2019). A Tug-of-War between Cell Shape and Polarity Controls Division Orientation to Ensure Robust Patterning in the Mouse Blastocyst. *Developmental Cell*, 51, 1–11. <https://doi.org/10.1016/j.devcel.2019.10.012>
- Özgüç, Ö., & Maître, J. (2020). Multiscale morphogenesis of the mouse blastocyst by actomyosin contractility. *Current Opinion in Cell Biology*, 66, 123–129.
<https://doi.org/10.1016/j.ceb.2020.05.002>
- Plastino, J., & Blanchoin, L. (2018). Dynamic stability of the actin ecosystem. *Journal of Cell Science*, 132(4), jcs219832. <https://doi.org/10.1242/jcs.219832>
- Plusa, B., Piliszek, A., Frankenberg, S., Artus, J., & Hadjantonakis, A.-K. (2009). Distinct sequential cell behaviours direct primitive endoderm formation in the mouse blastocyst. *Development*, 135(18), 3081–3091.
<https://doi.org/10.1242/dev.021519>.Distinct
- Roh-Johnson, M., Shemer, G., Higgins, C. D., McClellan, J. H., Werts, A. D., Tulu, U. S., Gao, L., Betzig, E., Kiehart, D. P., & Goldstein, B. (2012). Triggering a cell shape change by exploiting preexisting actomyosin contractions. *Science*, 335(6073), 1232–1235. <https://doi.org/10.1126/science.1217869>
- Royer, C., Leonavicius, K., Kip, A., Fortin, D., Nandi, K., Vincent, A., Jones, C., Child, T., Coward, K., Graham, C., & Srinivas, S. (2020). *Establishment of a relationship between blastomere geometry and YAP localisation during compaction*. <https://doi.org/10.1242/dev.189449>
- Salbreux, G., Charras, G., & Paluch, E. (2012). Actin cortex mechanics and cellular

- morphogenesis. *Trends in Cell Biology*, 22(10), 536–545.
<https://doi.org/10.1016/j.tcb.2012.07.001>
- Samarage, C. R., White, M. D., Álvarez, Y. D., Fierro-González, J. C., Henon, Y., Jesudason, E. C., Bissiere, S., Fouras, A., & Plachta, N. (2015). Cortical Tension Allocates the First Inner Cells of the Mammalian Embryo. *Developmental Cell*, 34(4), 435–447. <https://doi.org/10.1016/j.devcel.2015.07.004>
- Schindelin, J., Arganda-Carreras, I., Frise, E., Kaynig, V., Longair, M., Pietzsch, T., Preibisch, S., Rueden, C., Saalfeld, S., Schmid, B., Tinevez, J. Y., White, D. J., Hartenstein, V., Eliceiri, K., Tomancak, P., & Cardona, A. (2012). Fiji: An open-source platform for biological-image analysis. In *Nature Methods*.
<https://doi.org/10.1038/nmeth.2019>
- Schliffka, M. F., Tortorelli, A. F., Özgüç, Ö., de Plater, L., Polzer, O., Pelzer, D., & Maître, J. L. (2021). Multiscale analysis of single and double maternal-zygotic Myh9 and Myh10 mutants during mouse preimplantation development. *ELife*.
<https://doi.org/10.1101/2020.09.10.291997>
- Solon, J., Kaya-Çopur, A., Colombelli, J., & Brunner, D. (2009). Pulsed Forces Timed by a Ratchet-like Mechanism Drive Directed Tissue Movement during Dorsal Closure. *Cell*, 137(7), 1331–1342. <https://doi.org/10.1016/j.cell.2009.03.050>
- Sommer, C., Straehle, C., Kothe, U., & Hamprecht, F. A. (2011). Ilastik: Interactive learning and segmentation toolkit. *Proceedings - International Symposium on Biomedical Imaging*. <https://doi.org/10.1109/ISBI.2011.5872394>
- Stewart, M. P., Helenius, J., Toyoda, Y., Ramanathan, S. P., Muller, D. J., & Hyman, A. A. (2011). Hydrostatic pressure and the actomyosin cortex drive mitotic cell rounding. *Nature*, 469(7329), 226–231. <https://doi.org/10.1038/nature09642>
- Straight, A. F., Cheung, A., Limouze, J., Chen, I., Westwood, N. J., Sellers, J. R., & Mitchison, T. J. (2003). Dissecting temporal and spatial control of cytokinesis with a myosin II inhibitor. *Science*, 299(5613), 1743–1747.
<https://doi.org/10.1126/science.1081412>
- Svitkina, T. M. (2020). Actin Cell Cortex: Structure and Molecular Organization. *Trends in Cell Biology*, 30(7), 556–565. <https://doi.org/10.1016/j.tcb.2020.03.005>
- Tadros, W., & Lipshitz, H. D. (2009). The maternal-to-zygotic transition: A play in two acts. *Development*, 136(18), 3033–3042. <https://doi.org/10.1242/dev.033183>

- Tamm, I., Hand, R., & Caligiuri, L. A. (1976). Action of Dichlorobenzimidazole Riboside on RNA Synthesis in L-929 and HeLa Cells. *Journal of Cell Biology*, 69(31), 229–240.
- Taneja, N., & Burnette, D. T. (2019). Myosin IIA drives membrane bleb retraction. *Molecular Biology of the Cell*, 30(9), 1051–1059.
<https://doi.org/10.1091/mbc.E18-11-0752>
- Thielicke, W., & Stamhuis, E. J. (2014). PIVlab – Towards User-friendly, Affordable and Accurate Digital Particle Image Velocimetry in MATLAB. *Journal of Open Research Software*, 2. <https://doi.org/10.5334/jors.bl>
- Torres, M., Stoykova, A., Huber, O., Chowdhury, K., Bonaldo, P., Mansouri, A., Butz, S., Kemler, R., & Gruss, P. (2002). An β -catenin gene trap mutation defines its function in preimplantation development. *Proceedings of the National Academy of Sciences*, 99(3), 901–906. <https://doi.org/10.1073/pnas.99.3.901>
- Tournebise, R., Andersen, S. S. L., Verde, F., Dorée, M., Karsenti, E., & Hyman, A. A. (1997). Distinct roles of PP1 and PP2A-like phosphatases in control of microtubule dynamics during mitosis. *EMBO Journal*, 16(18), 5537–5549.
<https://doi.org/10.1093/emboj/16.18.5537>
- Tsai, T. Y. C., Collins, S. R., Chan, C. K., Hadjithodorou, A., Lam, P. Y., Lou, S. S., Yang, H. W., Jorgensen, J., Ellett, F., Irimia, D., Davidson, M. W., Fischer, R. S., Huttenlocher, A., Meyer, T., Ferrell, J. E., & Theriot, J. A. (2019). Efficient Front-Rear Coupling in Neutrophil Chemotaxis by Dynamic Myosin II Localization. *Developmental Cell*, 49(2), 189-205.e6.
<https://doi.org/10.1016/j.devcel.2019.03.025>
- Uyeda, T. Q. P., Abramson, P. D., & Spudich, J. A. (1996). The neck region of the myosin motor domain acts as a lever arm to generate movement. *Proceedings of the National Academy of Sciences of the United States of America*, 93(9), 4459–4464. <https://doi.org/10.1073/pnas.93.9.4459>
- Vallotton, P., Danuser, G., Bohnet, S., Meister, J.-J., & Verkhovskiy, A. B. (2005). Tracking Retrograde Flow in Keratocytes: News from the Front. *Mol Biol Cell*, 16(March), 1223–1231. <https://doi.org/10.1091/mbc.E04>
- Vasquez, C. G., Tworoger, M., & Martin, A. C. (2014). *Dynamic myosin phosphorylation regulates contractile pulses and tissue integrity during epithelial*

- morphogenesis*. 206(3), 435–450. <https://doi.org/10.1083/jcb.201402004>
- Vicente-manzanares, M., Ma, X., Adelstein, R. S., & Horwitz, A. R. (2010). *Non-muscle myosin II takes centre stage in cell adhesion and migration*. 10(11), 778–790. <https://doi.org/10.1038/nrm2786>. Non-muscle
- Wakatsuki, T., Wysolmerski, R. B., & Elson, E. L. (2003). Mechanics of cell spreading: Role of myosin II. *Journal of Cell Science*, 116(8), 1617–1625. <https://doi.org/10.1242/jcs.00340>
- Wang, H., Ding, T., Brown, N., Yamamoto, Y., Prince, L. S., Reese, J., & Paria, B. C. (2008). Zonula occludens-1 (ZO-1) is involved in morula to blastocyst transformation in the mouse. *Developmental Biology*, 318(1), 112–125. <https://doi.org/10.1016/j.ydbio.2008.03.008>
- Watanabe, N., & Mitchison, T. J. (2002). Single-molecule speckle analysis of actin filament turnover in lamellipodia. *Science*, 295(5557), 1083–1086. <https://doi.org/10.1126/science.1067470>
- Watson, A. J., Natale, D. R., & Barcroft, L. C. (2004). Molecular regulation of blastocyst formation. *Animal Reproduction Science*, 583–592. <https://doi.org/10.1016/j.anireprosci.2004.04.004>
- Wen, Q., & Janmey, P. A. (2012). Polymer physics of the cytoskeleton. *Curr Opin Solid State Mater Sci*, 15(5), 177–182. <https://doi.org/10.1016/j.cossms.2011.05.002>. Polymer
- Wigbers, M. C., Tan, T. H., Brauns, F., Liu, J., Swartz, S. Z., Frey, E., & Fakhri, N. (2021). A hierarchy of protein patterns robustly decodes cell shape information. *Nature Physics*, 17, 578–584. <https://doi.org/10.1038/s41567-021-01164-9>
- Windoffer, R., Wöll, S., Strnad, P., & Leube, R. E. (2004). Identification of Novel Principles of Keratin Filament Network Turnover in Living Cells. *Molecular Biology of the Cell*, 15(May), 2436–2448. <https://doi.org/10.1091/mbc.E03>
- Zaidel-Bar, R., Zhenhuan, G., & Luxenburg, C. (2015). The contractome - a systems view of actomyosin contractility in non-muscle cells. *Journal of Cell Science*, 128(12), 2209–2217. <https://doi.org/10.1242/jcs.170068>
- Zenker, J., White, M. D., Gasnier, M., Alvarez, Y. D., Lim, H. Y. G., Bissiere, S., Biro, M., & Plachta, N. (2018). Expanding Actin Rings Zipper the Mouse Embryo for Blastocyst Formation. *Cell*, 173(3), 776-791.e17.

<https://doi.org/10.1016/j.cell.2018.02.035>

Zhu, M., Leung, C. Y., Shahbazi, M. N., & Zernicka-Goetz, M. (2017). Actomyosin polarisation through PLC-PKC triggers symmetry breaking of the mouse embryo. *Nature Communications*, 8(1), 921. <https://doi.org/10.1038/s41467-017-00977-8>